Tools for numerical modelling of tunnelling interactions

Koungelis, Dimosthenis

Tools for numerical modelling of tunnelling interactions

By

Dimosthenis Koungelis

A thesis submitted for the degree of

Doctor of Philosophy

Advanced Mechanics Group

School of Engineering

University of Durham

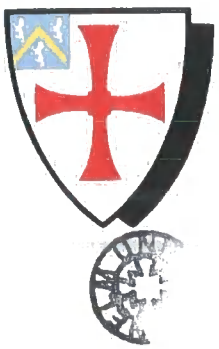

July 2007

Ithaca

When you set out for distant Ithaca,
fervently wish your journey may be long,
full of adventures and with much to learn.
Of the Laestrygones and the Cyclopes,
of the angry god Poseidon, have no fear:
these you shall not encounter, if your thought
remains at all times lofty, — if select
emotion touches you in body and spirit.
Not the Laestrygones, not the Cyclopes,
nor yet the fierce Poseidon, shall you meet,
unless you carry them within your soul,
unless your soul should raise them to confront you.

.....

At every stage bear Ithaca in mind.
The arrival there is your appointed lot.
But hurry not the voyage in the least:
'twere better if you travelled many years
and reached your island home in your old age,
being rich in riches gathered on the way,
and not expecting more from Ithaca.

Ithaca gave you the delightful voyage:
without her you would never have set out:
and she has nothing else to give you now.

And though you should find her wanting, Ithaca
will not surprise you; for you will arrive
wise and experienced, having long since perceived
the unapparent sense in Ithacas.

(*Poems by C.P.Cavafy*)

Tools for numerical modelling of tunnelling interactions

By

Dimosthenis Koungelis

Abstract

The ongoing development in the world's urban areas inevitably leads to the construction of structures in close proximity to already driven tunnels. Care should be taken to ensure that construction is carried out without damaging the tunnels or any other adjacent or overlying infrastructure. Considerable research has been undertaken for the case of a single tunnel where empirical methods for predicting tunnel induced deformations are applicable. For more complex geometries, however, empirical methods fail to make accurate predictions since they do not account for the soil-tunnel-structure interaction mechanism. The finite element method (FEM) appears to be a solution to this prediction problem, however many difficulties in its use remain. The aim of this thesis is to investigate and validate tools for numerical modelling of tunnelling related interactions in soft ground.

The generation of a suitable mesh is a major overhead in the use of three dimensional (3-D) FE analyses. Preparing and checking a complex tunnelling mesh can be extremely time consuming. Thus, a parametric scheme for automated, efficient and robust 3-D mesh generation was part of this project. FE analyses of a single driven tunnel are made for comparison with empirical methods on the direction of the surface displacement vectors. Another parametric study of twin tunnelling schemes is carried out in both 2-D and 3-D using various FE packages. The objective is to focus on the effects of surface loading on the tunnels themselves in terms of deformations and bending moments and study the changing effect as tunnel layout is altered.

The results obtained highly depend on the constitutive relations assumed, the soil properties and the discretization employed. Further to this the predictions show areas of general agreement and disagreement between the different types of analyses and FE packages used, indicating that accurate numerical modelling of this problem remains difficult and requires care.

Declaration

"The work in this thesis is based on research carried out at the Advanced Mechanics Group, School of Engineering, University of Durham. No part of the material offered has previously been submitted by me for a degree in this or in any other University. Material from the work of others has been acknowledged and quotations and paraphrases suitability indicated".

Acknowledgements

I would like to take this opportunity to acknowledge the significant help I have been given in the completion of my research presented in this thesis. I am greatly indebted to my supervisor Dr. Charles Augarde for his vivid interest, guidance and assistance in the most efficient and effective way for my research. For his patience with my English writing and his encouragement during some difficulties I faced with this project I would like to thank him too.

This work was funded by the Engineering and Physical Sciences Research Council (EPSRC), the School of Engineering at University of Durham and Halcrow Ltd. Without their support this project would not have been possible.

Some of my colleagues from the Civil Engineering Group need thanking. Cathy, Eva, Derek, Gareth, Paul and Steve in particular, for sharing the same office and for trying to introduce me into some English habits (drinking tea during the day and going to the pub on Friday night). Special thanks to Ioanna and Stergios, for our long-last Skype conversations on Monday nights while they were in Palermo, and to Viki, Antonis, Barbara and Nikos for inviting me to stay at their places during some short breaks. I would also like to thank some of my old friends from Zographou, my neighbourhood in Athens (you know who you are), most of whom I know since I was 12.

I would like to express my gratitude to my parents Lamprini and Kostas who have not just wholeheartedly supported but also encouraged me throughout. To my grandmother who passed away a year ago I just want to say that I will always remember her.

Finally, I would like to dedicate this thesis to my Fnoula mainly for her true love and encouragement but also for her patience during the writing of this thesis. Thank you!

Contents

List of Figures

List of Tables

Nomenclature

Latin symbols

A	Cross sectional area of the tunnel lining
$[B]$	Interpolation function matrix
c'	Soil cohesion
C	Cover between the surface and the tunnel crown
C'	Compressibility ratio
ChL	Characteristic length
CL	Tunnel's centre line
$\{d_E\}$	Displacements of a finite element
$\{d_G\}$	Vector containing the sum of the unknown nodal displacements of the continuum
$\{d_G\}_i$	Incremental form of the total nodal displacements
$\{d_N\}$	Vector of nodal displacements
D	Tunnel diameter
$[D]$	Constitutive matrix
E	Young's modulus of the soil
E_{inc}	Incremental value of soil stiffness
E_{ref}	Reference value of soil stiffness
E_z	Soil stiffness at any depth z
E_L	Young's modulus of the tunnel lining
EA	Normal stiffness
EI	Flexural stiffness
f_E	Applied loads of a finite element
F	Flexibility ratio
$\{F_E\}$	Total load vector for a finite element
$\{F_G\}$	Global total load vector
$\{F_G\}_i$	Incremental form of the global total load vector
$F_Y(\sigma', m_Y)$	Yield function
$F_P(\sigma', m_P)$	Plastic function
H_x	Horizontal surface movements due to tunnel excavation along the transverse direction
$H_{x,i}$	Horizontal surface movements due to tunnel excavation along the transverse direction at the point of inflection
$H_{x,\max}$	Maximum horizontal surface movement due to tunnel excavation along the transverse direction
$i,\ i_x,\ i_y$	Trough width parameters
I	Second moment of area of the tunnel lining
J	Axis to axis tunnel separation
$k1$	Tunnel inclination
K, K_1, K_2, K_3	Trough width constants
K_0	Earth pressure at rest
$[K_E]$	Stiffness matrix of a finite element
$[K_G]$	Global stiffness matrix

$[K_G]_i$	Incremental form of the global stiffness matrix
L	Maximum edge length of a finite element
M_N	Newmark's coefficient
MHI	Multiple tunnels with horizontal and inclined alignment
m_p	Plastic function parameter
m_Y	Yield function parameter
N	Stability ratio factor
N	Boussinesq's coefficient
$[N]$	Shape function matrix
p_0, p_1, p_2	Different positions of the tunnel within the domain
P	Pillar width distance
P_{crown}	Total vertical load at crown
P_D	Pillar depth distance
P_{soil}	Weight of the soil
$P_{\text{surface load}}$	Contribution of a point load at the crown
q	Surface load of a rectangular area
r	Radius of an inscribed circle
R	Tunnel radius
$[S]$	Interpolation function matrix
S'	Surface settlements due to loading
$S_{\max}$	Maximum surface settlement due to tunnel excavation
$S'_{\max}$	Maximum surface settlement due to loading
S_u	Undrained shear strength
S_x	Surface settlements due to tunnel excavation along the transverse direction
S_y	Surface settlements due to tunnel excavation along the longitudinal direction
ST	Single tunnel geometry
t	Thickness of the tunnel lining
T	Horizontal distance between the projection of the point load in the ground and the crown
TH	Twin tunnels horizontally aligned
TVD	Twin tunnels vertically and diagonally aligned
u, v	Displacement components along the x, y directions respectively
U_E	Strain energy of a finite element
Ur	Unsupported region at the face of the excavation
v	Poisson's ratio of the soil
v_L	Poisson's ratio of the tunnel lining
V	Volume of a finite element
V_E	Work done by the applied loads on a finite element
V_L	Volume loss
V_S	Volume of the settlement trough
W	Point load
$W1$ to $W6$	Surface loaded areas
x	Distance along the transverse direction
$x1$	Horizontal shift of the tunnel axis
y	Distance along the longitudinal direction

z	Depth to a sub-surface profile
$z1$	Vertical shift of the tunnel axis
z_0	Depth to the tunnel axis
z_{inc}	Increment of depth
z_{ref}	Reference depth

Greek symbols

α	Relative stiffness parameter
α_i, β_i	Constant coefficients
β	Relative stiffness parameter
γ	Soil's unit weight
γ	Aspect ratio
γ_L	Unit weight of the tunnel lining
ε_{hx}	Horizontal strains along the transverse direction
$\{\varepsilon_E\}$	Strains of a finite element
ζ, θ, ξ	Angles
λ	Unloading parameter
Π_E	Principle of the potential energy
$\sigma_1, \sigma_2, \sigma_3$	Total stresses
$\sigma_1', \sigma_2', \sigma_3'$	Effective stresses
σ_{crown}	vertical stress at the crown below the corner of the loaded area
σ_h	Horizontal stress at tunnel axis level
$\sigma_{surface\ load}$	contribution of the point load at the crown in term of stress
σ_t	Tunnel support stress
σ_v	Total overburden stress at tunnel axis level
$\{\sigma_E\}$	Stresses of a finite element
$\sum FA$	Sum of the face areas
τ	Shear stress
φ'	Angle of friction
$\varphi(y/i_y)$	Probability density of the standardised variable y with variance i
$\Phi(y/i_y)$	Cumulative distribution of the standardised variable y with variance i
ψ'	Angle of dilation

Chapter 1

Introduction

1.1 History of tunnelling

The idea of tunnelling is not new. Throughout history numerous tunnels have been built to serve different purposes (e.g. transportation, sewerage, water and power supply). The first ever tunnel was driven in Babylonia under the Euphrates River at 2180 BC. It was approximately 900m long and was used by pedestrians. At 520 BC a water tunnel was constructed in Greece (the island of Samos) by a famous engineer, Eupalinos. It was approximately 1,100m long and was entirely driven through hard rock (limestone). The extraordinary thing with this case was that excavation took place at both sides of the tunnel simultaneously and the two teams met in the middle (Britannica, 2007).

Excavation during that period was entirely made by hand. After the Middle Ages gunpowder was also used. Only in the twentieth century have more sophisticated and mechanical methods been applied. Excavation has become less time consuming and safer for the working personnel. Several different techniques have been developed and the choice of method is mainly based on ground conditions and tunnel geometry. Nowadays, with the aid of state of the art technology and the experience of the past tunnels can be built virtually in any type of ground.

The first ever shield driven tunnel (the shield providing support at the face of the excavation) was constructed at 1841 in London under the River Thames by Marc Brunel, a French engineer. It was driven through London clay and was approximately

300m long. This was the first tunnel where a toll (of one penny) was charged. This particular section was bought in 1865 by London Underground (known as East London Railway during that time) and became part of the rest railway. That was the first underground railway in the world (London's transport museum, 2007). Since then more than 100 metros have been built around the world, most of which will keep expanding while new are being built (Hellawell *et al.*, 2001).

1.2 Tunnelling in urban areas

The ongoing growth of urban areas unavoidably leads to an increased need for infrastructure. Since surface space is often limited the use of underground space is seen as the most efficient way to provide new infrastructure. Lack of surface space is not the sole reason for subsurface solutions. Tunnelling and underground transportation in general, is a more environmental friendly solution contributing to the reduction of the surface traffic congestion. The high cost of such projects may in some cases be a deterrent factor though.

In the urban environment tunnelling is a highly complex operation. The main reason being that tunnels have to be driven in close proximity to other surface structures (e.g. buildings) or sub-surface structures (e.g. pre-existing tunnels, pipes, piles and foundations). Tunnel engineers should therefore, not only ensure safe tunnel construction, which is their primary and main objective, but also take all precautionary measures so that tunnel induced ground deformations will not severely damage other adjacent or overlying structures. To do so, tunnel engineers and designers should be able to make accurate predictions regarding the ground movements followed by assessments of the possible damage to the neighbouring structures as a result of these movements. With the aid of highly sophisticated mechanical excavating machines, TBMs (Tunnel Boring Machines) surface deformations can be controlled and restricted to values of volume loss (defined in Chapter 2) less than 1% by applying a high pressure at the face of the excavation (e.g. the Earth Pressure Balance method). Bowers and Moss (2006) report that average values of settlement volume loss of 0.5% were recorded at the part of the Channel Tunnel Rail Link (CTRL) high speed railway between Channel Tunnel and St. Pancras.

Design approaches used until recently in assessing possible damage to buildings do not take into consideration the stiffness of the building. Hence, they fail to account for the complex mechanism of soil-tunnel-structure interaction. Thus, these design approaches prove to be rather conservative, increasing the cost of the projects. As reported by Mair and Taylor (1997) few published data existed in the past regarding the detailed performance of tunnel induced damage to buildings. More recently though Augarde (1997), Bloodworth (2002) and Franzius (2003), with the use of full 3-D numerical modelling, re-assessed these design approaches focusing on the complex interaction mechanisms.

The final responsibility of tunnel engineers is to ensure that the tunnel lining should be able to withstand all influences to which it may be subjected during its lifetime (Peck, 1969). The most important forces are due to gravity. According to Barratt *et al.* (1994) lining design approaches which take into consideration the full overburden weight of the surrounding soil are conservative since even after 20 years of construction only 60% to 70% of the total overburden is carried by the lining mainly due to the arching effect. Other influencing factors are the excavation of new tunnels in close proximity to existing tunnels and the surface loading due to pile loading, building construction or compensation grouting below foundations (as a protective measure against tunnel induced deformations). Possible tunnel movements or increase in the lining stresses due to the above mentioned influencing factors was identified early enough and raised concerns mainly by tunnel owners (Morgan and Bartlett, 1969). These variations from normal conditions may set a tunnel's functionality at risk. Empirical and analytical methods available, based mainly on experience and field data, are used to account for any external loading other than earth pressure. These methods fail to accommodate the complex interaction mechanism between soil-tunnel-structure. The finite element method appears to overcome this problem (Moore, 1987b). Thus, the complex interaction mechanism, the magnitude of the surface load transferred to the crown and its effects on the liners of existing tunnels can be studied while a thorough and improved understanding of the interaction problem can be achieved. Relative few recorded publications, to the author's knowledge, exist on this topic the majority of which are dealing with the response of a pipe (rather than a tunnel) to surface loads.

1.3 Aim and objectives

This research project aims to produce tools for numerical modelling of tunnelling interactions. To fulfil this aim the project has the following objectives.

- The first objective is to investigate whether it is possible to perform both detailed and accurate numerical modelling in terms of available computer resources. Apart from numerical modelling other methods such as small scale physical testing, centrifuge testing and empirical methods are available. The choice of the former method though was made in order to exploit specific advantages of numerical modelling in general and 3-D non-linear finite element analysis in particular through this project. These advantages are: *i*) the ability to model the complex interaction mechanism of soil-tunnel-structure, *ii*) the ability to model any domain in all its three dimensions without having to make any 2-D simplifications and *iii*) the ability to perform parametric studies varying geometric or material parameters.

- The next objective is to attempt to reduce the amount of time spent during the pre-processing stage (this involves the generation of a mesh) of the finite element analysis. 3-D mesh generation can be time consuming. It is essential to ensure that all required parametric studies for this project are carried out within the available time period. Hence, a fully automated fast and robust way of generating 3-D meshes is a prerequisite for such analyses.

- The third objective is to compare the different methods used in this project. A given numerical model will be analysed in particular, employing different commercial FE packages (Strand7 and Plaxis) to investigate whether these packages will produce the same predictions. Further to this the same numerical model will be analysed using different types of FE analyses (2-D and 3-D) to highlight the differences (if any) in the predictions. Neither the production of design charts (this might be part of later work) nor the comparison of the produced tools with field data, are initially amongst the project objectives. The reason for the latter is twofold. Firstly, the objective is to compare the methods and evaluate the tools themselves using the available knowledge at that time and the gradually build up experience. To make a proper evaluation one has to be

aware of how sophisticated the method used is, what simplifications have been made, the quality of the input data and how these affect the predictions made. Secondly, only already published field data are in the author's possession to evaluate the proposed tools. Numerous recorded field cases would be required to allow for conclusive evaluations. Even then, this would be a type C1 prediction[1] according to Lambe (1973) classification. Lambe (1973) states that:

"One must hold some suspicion of using type C1 predictions to prove the validity of any prediction technique".

- The final objective of this project is to attempt to clarify an unresolved conflict amongst researchers which requires investigation. This has to do with the direction of the surface deformation vectors due to tunnelling in a greenfield site.

1.4 Thesis layout

Chapter 2 reviews the literature on tunnelling induced ground deformations using empirical and numerical (both in 2-D and in 3-D) methods. It then discusses about the lining distortions due to gravity and surface loading and focuses on the interaction between soil-tunnel-structure.

Chapter 3 introduces aspects of the finite element method and the formulations used. Other numerical methods are briefly described. Details on how initial conditions, constitutive models, excavation and volume loss are modelled throughout this thesis are presented.

Chapter 4 attempts to clarify the still unresolved issue of the predicted direction of the surface displacement vectors due to tunnelling using Plaxis. The produced 2-D FE predictions are then compared and discussed with other recorded field cases and predictions made using empirical methods.

Chapter 5 focuses on the pre-processing stage of FE analysis. This chapter presents a new scheme based on parameterising analyses for the generation of 3-D

[1] The type C1 prediction takes place after the main event when the results are already known. Lambe (1973) suggests that type A predictions which take place before the main event are more valuable.

meshes using Gmsh. The generated meshes used in this thesis are then evaluated in terms of mesh quality measurements. Some issues regarding the preparation of the input and output files are also discussed.

Chapter 6 presents 2-D FE predictions of surface loading on existing tunnels driven in soft ground using different FE packages. In the first and second parts of this chapter the details of the analyses using Strand7 and Plaxis respectively are discussed. The produced predictions from each package are then compared for evaluation purposes.

Chapter 7 presents the equivalent to Chapter 6 3-D predictions using Strand7. This chapter emphasizes on the differences in the predictions using different types of analyses (2-D and 3-D).

Chapter 8 draws conclusions, summarises the achievements and contains suggestions for future research.

Chapter 2

Tunnel induced ground deformation and lining distortion

2.1 Introduction

Considerable research has been undertaken for assessing the ground deformations due to tunnelling driven in soft ground using empirical, analytical and numerical methods. Previous published work referring to this problem will be discussed in this section. Empirical and semi-empirical methods are successfully used to predict soil movements when tunnelling in a greenfield site (i.e. no other surface or subsurface structure exists prior to tunnel installation). These methods though were proved to be incapable of presenting valid and realistic predictions when other structures are present in close proximity (non-greenfield sites). To account for the interaction mechanism between the excavated tunnel and another structure (i.e. another tunnel, building or pipe) numerical methods such as the Finite Element Method (FEM) are widely used. A series of FE studies addressing this problem are presented. Finally in the last section of this chapter lining distortions due to both the overburden weight of the soil and a uniformly applied surface load, above existing tunnels are presented.

2.2 Surface deformation

2.2.1 Deformation along the transverse direction

Equation 2.1 is widely accepted and recognized among geotechnical engineers, but

has no theoretical justification and is entirely empirically based. It was first introduced by Martos (1958) who proposed it following field observations of ground deformations above mine openings. Later Peck (1969) suggested that the transverse settlement trough due to tunnelling (solid line in Fig. 2.1) seems to follow an inverted Gaussian probability curve. The same formula therefore is adequate for modelling vertical surface settlements in soft ground on greenfield sites. Equation 2.1 is used for predictive purposes before or during design and construction.

$$S_x = S_{\max} e^{-\frac{x^2}{2i_x^2}} \tag{2.1}$$

where S_x is the vertical surface settlement at a transverse distance x from the tunnel centre line (CL), $S_{\max}$ is the maximum vertical surface settlement occurring above the tunnel CL and i_x is the trough width parameter which separates the sagging from the hogging zone (Fig. 2.1).

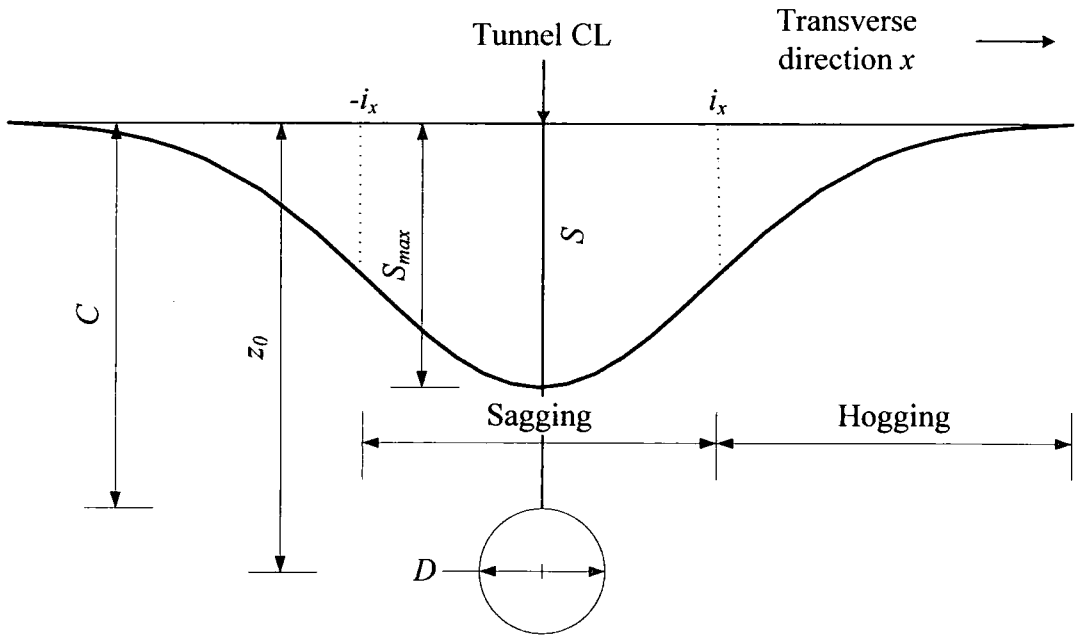

Figure 2.1. Surface settlement profile (S_x) along the transverse direction x.

The volume of the settlement trough per unit length (V_S) above the tunnel face is equal to the area enclosed by the probability curve. Attewell and Farmer (1974a) described the procedure to obtain V_S (by integration of Equation 2.1).

$$V_S = \sqrt{2\pi}\, i_x S_{max} \tag{2.2}$$

If tunnel construction takes place in low permeability materials then it can be considered that soil deforms under constant volume (undrained behaviour). In this case the extra amount of soil excavated over the initial estimated area of the opening is termed as volume loss (V_L) and is usually expressed as a percentage:

$$V_L = \frac{4V_S}{\pi D^2} \tag{2.3}$$

where D is the tunnel diameter. Combining Equations 2.2 and 2.3 the following expression can be derived for S_{max}:

$$S_{max} = 0.313\frac{V_L D^2}{i_x} \tag{2.4}$$

In order to fully determine the shape of the settlement trough of a given tunnel at least two of the following parameters need to be known from Equation 2.4: S_{max}, V_L and/or i_x. According to Peck (1969), S_{max} is empirically determined and is directly proportional to D. The properties of the normal probability curve indicate that:

$$i_x = 0.61 S_{max} \tag{2.5}$$

V_L can then be determined from Equation 2.4 by knowing the values of S_{max}, and i_x. O'Reilly and New (1982) introduced Equation 2.6 to calculate the horizontal surface movements (H_x) at a transverse distance x assuming that the total displacement vectors in the transverse direction are heading to the tunnel CL (Fig. 2.2):

$$H_x = \frac{x}{z_0} S_x \tag{2.6}$$

where z_0 is the depth of the tunnel axis and C (Fig. 2.2) is the cover between surface and crown. The horizontal strains along the transverse direction (ε_{hx}) can be calculated from Equation 2.7. The latter equation is derived by differentiating Equation 2.6. Compression then can be defined as negative while tension as positive.

Figure 2.3 shows plots of the horizontal (H_x) and vertical (S_x) surface displacements as well as the horizontal strains (ε_{hx}). Equations 2.6 and 2.7 are only valid from ground surface until the area around the tunnel within $1D$ of its periphery.

$$\varepsilon_{hx} = \frac{S_x}{z_0}\left(1 - \frac{x^2}{i_x^2}\right) \tag{2.7}$$

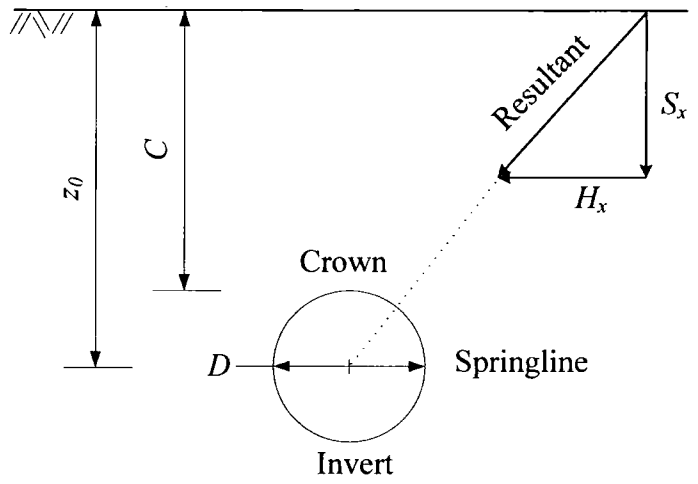

Figure 2.2. Assumption about surface deformation vectors heading to tunnel's CL (After O'Reilly and New, 1982).

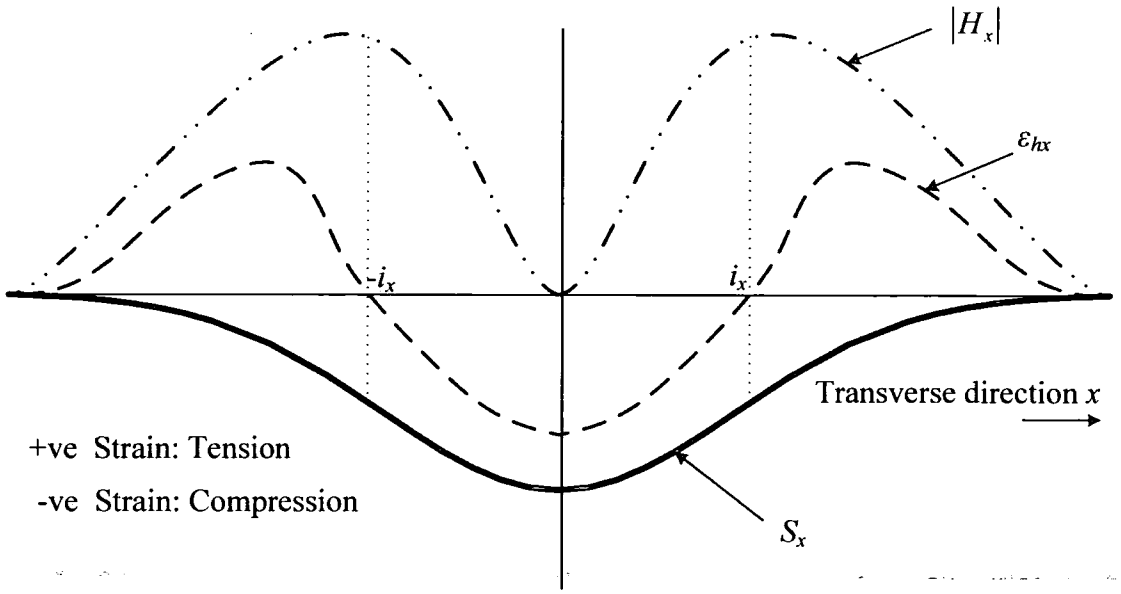

Figure 2.3. Plots of vertical (S_x) and horizontal (H_x) surface deformations as well as horizontal strains (ε_{hx}) along the transverse direction x.

2.2.2 Deformation along the longitudinal direction

Attewell and Woodman (1982) derived several equations to describe the ground movements along the longitudinal y-axis. Having accepted that the deformations along the transverse x-axis are well described by the normal probability curve, it is a logical step to say that the deformations anywhere on the longitudinal y-axis will be described by a cumulative probability function (Eq. 2.8). At $x = 0$ on the y-axis the vertical settlement profile S_y will be described by Equation 2.9.

$$S_y = \frac{V_S}{i_y\sqrt{2\pi}} e^{-\frac{x^2}{2i_x^2}} \Phi\left(\frac{y}{i_y}\right) \tag{2.8}$$

$$S_y = \frac{V_S}{i_y\sqrt{2\pi}} \Phi\left(\frac{y}{i_y}\right) \tag{2.9}$$

$$\Phi\left(\frac{y}{i_y}\right) = \int_s^f \varphi\left(\frac{y}{i_y}\right) dy = \int_s^f \frac{1}{i_y\sqrt{2\pi}} e^{-\frac{y^2}{2i_y^2}} dy \tag{2.10}$$

where i_y is the trough width parameter at the same profile, $\Phi\left(\frac{y}{i_i}\right)$ is the normal cumulative distribution function with mean $x_\mu = 0$ and variance $\sigma^2 = i_y^2$, $\varphi\left(\frac{y}{i_i}\right)$ is the probability density function, while s and f are the starting and ending positions of the tunnel face. Tabulated values of Equation 2.10 can be found in Attewell and Woodman (1982) and in many statistics texts. Figure 2.4 shows how S_y varies along the y-axis from $S_y = 0$ at $y = +\infty$ to $S_y = S_{max}$ at $y = -\infty$. For firm to stiff clay a value of 30% to 50% of S_{max} with an average value of 40% occurs above the tunnel face at $y = 0$.

Attewell et al. (1986) compared theoretical values of i_y produced from cumulative probability curves against values of i_x measured from normal probability curves. They showed that in most cases the longitudinal field settlements were slightly larger than those predicted from the cumulative probability curve assuming $i_y = i_x$. They conclude however that for most practical design problems the following assumption is valid:

$$i = i_x = i_y \tag{2.11}$$

More recently Nyren (1998) through field observation for tunnelling schemes in the Jubilee Line Extension beneath St. James's Park in London, proposed the following relation:

$$i_x = 1.3 i_y \tag{2.12}$$

For the remaining of this thesis the assumption made by Attewell et al. (1986), which is common and widely accepted by most geotechnical engineers, will be used for simplicity purposes (Eq. 2.11).

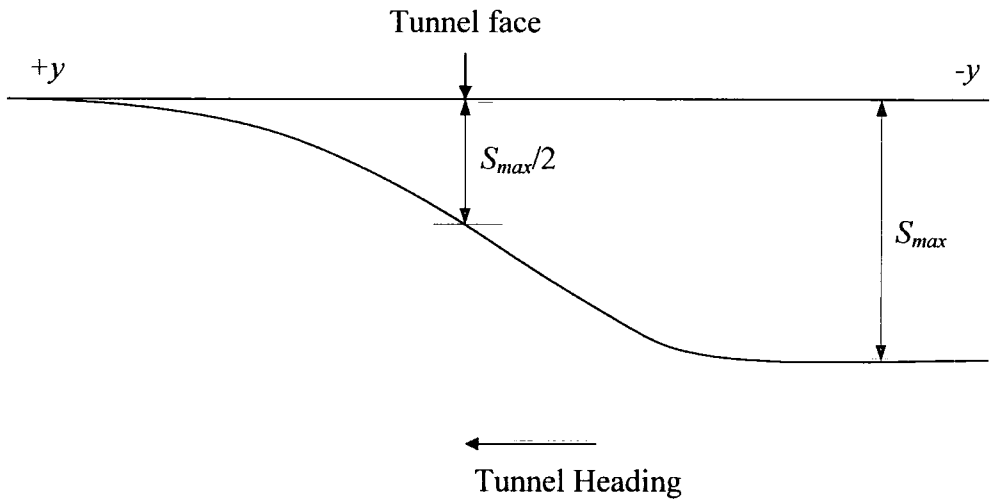

Figure 2.4. Surface settlement profile (S_y) along the longitudinal direction y.

2.2.3 Deformation above twin tunnels

In the case of twin parallel tunnelling (i.e. the same z_0) previous researchers have proposed superimposition of the two single transverse settlement troughs to obtain the final trough (see Fig. 2.5) as defined by Equations 2.13 to 2.15.

$$S_x = \frac{V_S}{i\sqrt{2\pi}}\left[e^{-\frac{x^2}{2i^2}} + e^{-\frac{(x-J)^2}{2i^2}} \right] \tag{2.13}$$

$$H_x = \frac{V_S}{z_0 i\sqrt{2\pi}}\left[x e^{-\frac{x^2}{2i^2}} + (x-J) e^{-\frac{(x-J)^2}{2i^2}} \right] \tag{2.14}$$

$$\varepsilon_{hx} = \frac{V_S}{z_0 i\sqrt{2\pi}}\left[\left(1-\frac{x^2}{i^2}\right) e^{-\frac{x^2}{2i^2}} + \left(1-\frac{(x-J)^2}{i^2}\right) e^{-\frac{(x-J)^2}{2i^2}} \right] \tag{2.15}$$

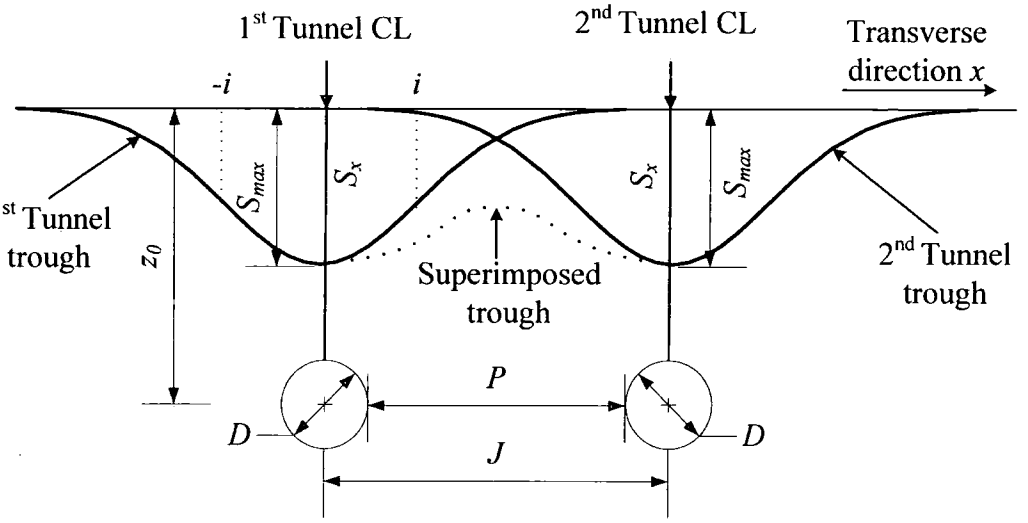

Figure 2.5. Superimposed surface settlement trough due to twin tunnelling along the transverse direction x.

where J is the axis to axis tunnel separation and P is the pillar width distance. Equations 2.14 and 2.15 are only valid if it is assumed that the surface displacement vectors head to the tunnel centre line (similar to the single tunnel case and Equations 2.6 and 2.7).

It is rare however for twin tunnel headings to advance with the same rate during construction. The trend is either to advance at a different rate or to construct the second after the first has finished. In both cases asymmetry effects have been reported. Cording and Hansmire (1975) presented field data above twin tunnels (D = 6.4m, P = 4.6m) in medium dense silty sands and gravels for the Washington Metro (see Fig. 2.6) where an asymmetric trough due to the construction of the second tunnel is formed. Burland (2001) (Fig. 2.7) presented this asymmetry effect from field data above twin tunnels (D = 5m, P = 16m) from the Jubilee Line Extension Project in London. In Figures 2.6 and 2.7 vertical surface settlements (S_x) against distance along the x-axis are plotted. These two figures show that the settlement trough due to

the second tunnel is offset towards the first trough (i.e. S_{max} does not occur above the second tunnel's CL and has a bigger value compared with the first.). This is the case regardless of the type of ground (i.e. sand or clay).

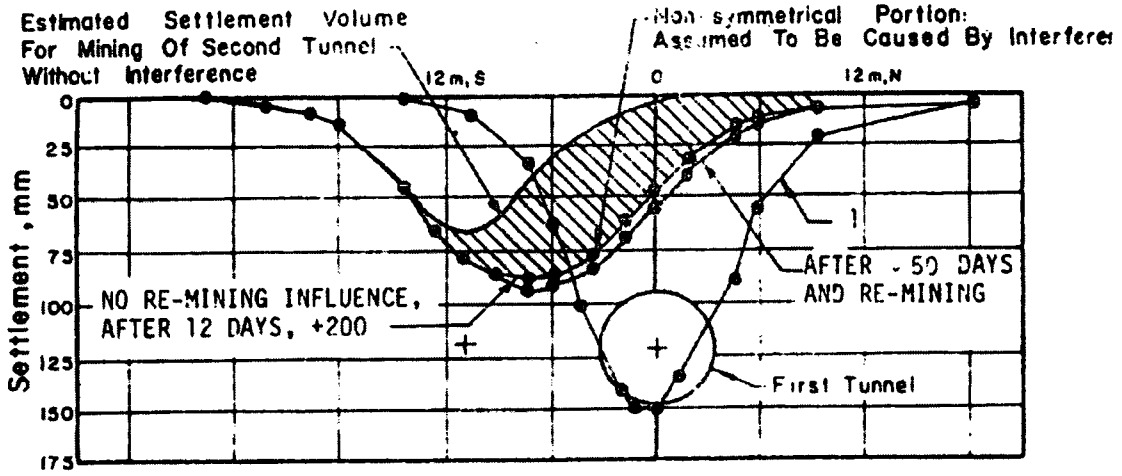

Figure 2.6. Final settlements of First and Second Tunnels, from Line C, Project A-2, Washington Metro (From Cording and Hansmire, 1975).

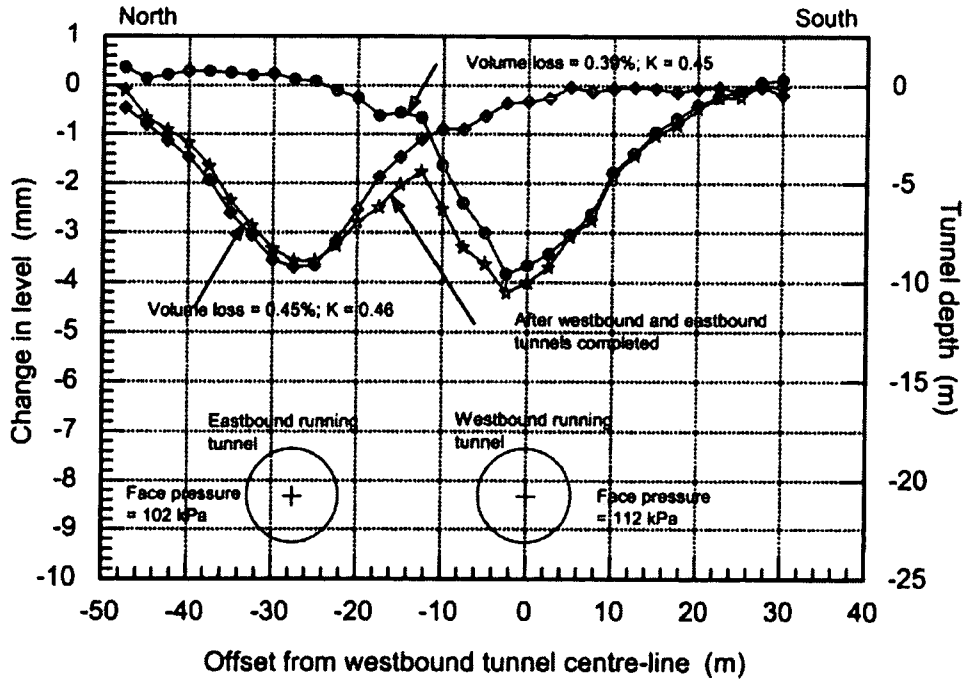

Figure 2.7. Asymmetry effects due to second tunnel construction. Surface settlements at Southwark Park Greenfield reference site (From Burland, 2001).

2.2.4 Volume Loss V_L

Stress redistribution during tunnelling and softening of the soil surrounding the face of the excavation will lead to ground movements into the opening. This extra amount of soil which has to be excavated over the originally estimated volume of the tunnel expressed as a percentage is termed volume loss (V_L). This phenomenon creates the surface settlement trough in three dimensions (Fig. 2.8).

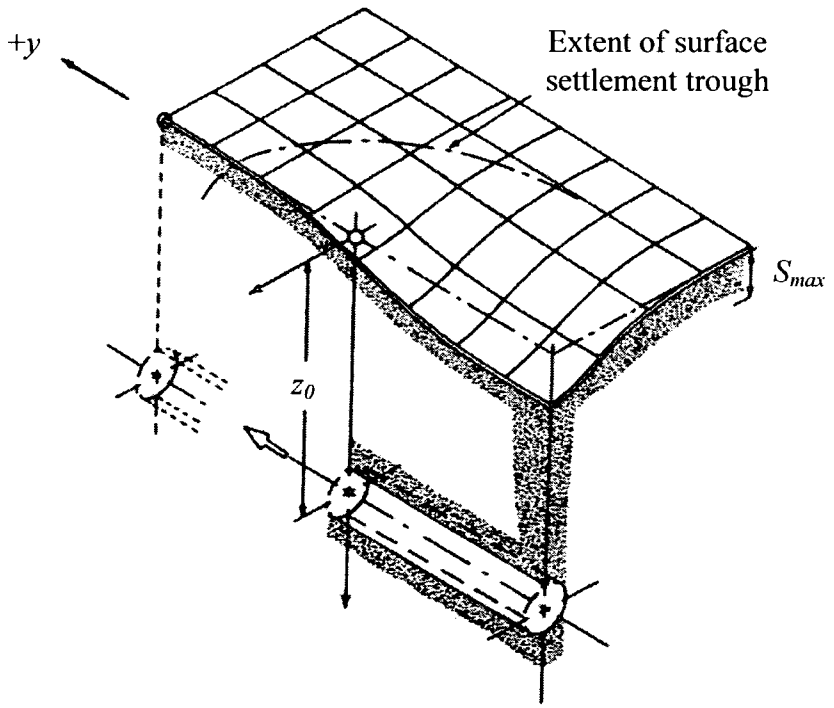

Figure 2.8. Surface deformations due to tunnelling in three dimensional space (After Attewell *et al.*, 1986).

Attewell *et al.* (1986) proposed four sources of loss due to shield tunnelling (Fig. 2.9). The sum of these four losses will produce the final value of the total volume loss:

- *Face loss*, which is the axial loss into the face. This source is very important to both transverse and longitudinal directions of the surface settlement trough
- *Shield loss*, which is the radial loss around the perimeter of the tunnel shield and at the tail
- *Post-shield loss*, which is the radial loss behind the tail after lining installation and before grouting and

- *Post-grout loss*, which is the radial loss behind the tail after grouting. This source of loss will continue until the lining stiffness will be in equilibrium with overburden stress. The latter is considered to be a long-term settlement factor contrary to the first three which are short-term factors

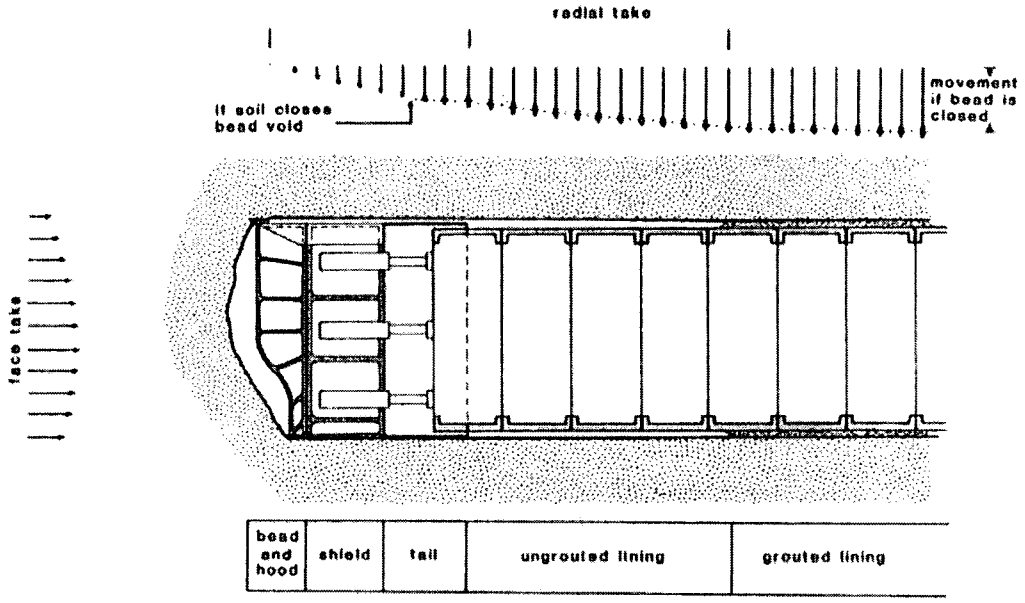

Figure 2.9. Sources of volume loss due to shield tunnelling (From Attewell *et al.*, 1986).

A different approach to determine volume loss is the "Stability Ratio Factor" (*N*). The first application of this method to the tunnelling problem is attributed to Broms and Bennermark (1967) and is defined as:

$$N = \frac{\sigma_v - \sigma_t}{S_u} \tag{2.16}$$

where σ_v is the total overburden pressure at the tunnel axis level ($\sigma_v = \gamma z_0$, and γ is the soil's unit weight), σ_t is the tunnel support pressure and S_u is the undrained shear strength of the clay at axis level. This factor N can be combined with engineering judgement from previous tunnelling schemes in the same ground conditions. Broms and Bennermark (1967) suggested that a stability ratio value greater or equal than 6 to 8 would give an unstable clay profile for tunnel excavation. This factor is independent of the tunnel diameter *D*. This method was only tested and therefore is only valid when the tunnel is excavated at a depth greater or equal to z_0 =

4*D*. Lab tests on both undisturbed and remoulded clay (Fig. 2.10a) as well as field data (Fig. 2.10b) mainly from the Chicago Subway support this theoretical approach. Figure 2.10 shows plots of stability ratio (N) against undrained shear strength (S_u). Peck (1969) concluded that in a soft to stiff clay, a stability ratio greater than 6 would produce destabilisation to the tunnel shield. According to Ward (1969), however it is safe to work in front of the tunnel lining for stability ratio values smaller than 1 to 2.

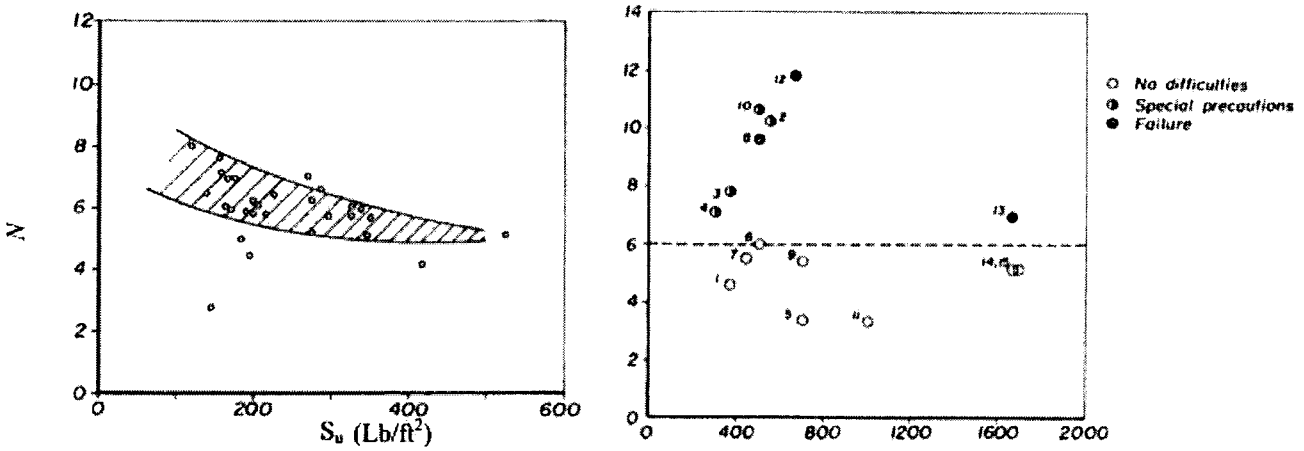

a) Lab tests on undisturbed and remoulded clay.L

b) Field data mainly from the Chicago Subway.

Figure 2.10. Plots of the stability ratio N against the undrained shear strength S_u (After Broms and Bennermark, 1967).

Davis *et al.* (1980) derived plasticity solutions by means of upper and lower bound theorems. They indicate, in contrast to Broms and Bennermark (1967) findings that the critical value of N (at collapse) varies with depth for shallow tunnels. After performing a series of centrifuge tests of tunnelling in kaolin slurry, Kimura and Mair (1981) showed that N at collapse is highly influenced by the heading geometry. Mair and Taylor (1993) plotted N with depth from field data in London clay. They proposed that the critical value of N varies from 2.5 to 3 for shallow tunnelling.

Several high quality sets of field measurements at various tunnelling schemes in London clay have been documented since the 1970s. The findings are presented in Table 2.1. It is evident that in most cases V_L ranges between 1% and 1.4% for shallow tunnels in London clay. There are however, two extreme values reported by Standing *et al.* (1996) and Bowers and Moss (2006). Standing and Burland (2006)

tried to explain why such a big value of volume loss was measured at St. James's Park (Table 2.1). They state that during design stage a value of V_L = 2% was adopted which was thought to be conservative at that time. Geological conditions and the tunnelling methods adopted were identified to be the two crucial factors contributing to such big V_L values.

Tunnelling scheme	z_0 (m)	D (m)	Method of excavation	V_L (%) from field data
Green Park, Jubilee Line (Attewell and Farmer, 1974a)	29.3	4.146	Open Shield, Hand Mined	1.3
Regent's Park, Jubilee Line (Barratt and Tyler, 1976)	34	4.146	Open Shield, Hand Mined	1.4
Heathrow Express Trial tunnel (New and Bowers, 1994)	21	8.6	New Austrian Tunnelling Method (NATM)	1.05 to 1.26
Heathrow Express Trial tunnel (Deane and Basett, 1995)	20	5.6	NATM	1.06 to 1.33
Heathrow Express (Barakat, 1996)	23	6.15	NATM	1.4
St. James's Park, Jubilee Line (Standing et al., 1996)	30.5	4.85	Open Shield	3.3 and 2.9
CTRL (Bowers and Moss, 2006)	Various depths	8.15	Earth Pressure Balance Machine (EPB)	0.5 to 1

Table 2.1. Volume loss values from tunnelling schemes in London clay.

2.2.5 Trough width parameter *i*

The distance i between the tunnel centre line and the point of inflection (i.e. the point of the maximum slope) on the transverse surface settlement trough profile (Fig. 2.1) describes the width of the settlement trough. It is thought to be related to z_0 and D. According to Rankin (1988) the size of the trough can be considered to be of total of $6i$. Beyond that distance the effects of tunnelling on the surface cease to occur.

O'Reilly and New (1982) carried out linear regression analyses of field data but did not manage directly to correlate D with i. They did however show a strong link between z_0 and i. The following linear relations were introduced to describe this correlation:

$$i = 0.43z_0 + 1.1 \quad \text{(for cohesive soils)} \tag{2.17}$$

$$i = 0.28z_0 - 0.1 \quad \text{(for cohesionless soils)} \tag{2.18}$$

where i and z_0 are both measured in metres. For practical reasons O'Reilly and New (1982) tried to simplify the above equations by introducing another which starts from the origin. Figure 2.11 shows plots of z_0 against i from *in situ* measurements.

$$i = Kz_0 \tag{2.19}$$

where K (trough width constant) varies from 0.4 for stiff clays to 0.7 for soft and silty clays and from 0.2 to 0.3 for granular materials above water table. For simplicity though K = 0.5 (constant for surface deformations) for cohesive materials and K = 0.25 for cohesionless are often used in practice. These values are empirical though and may vary depending on the ground conditions (there is a scatter in Fig. 2.11).

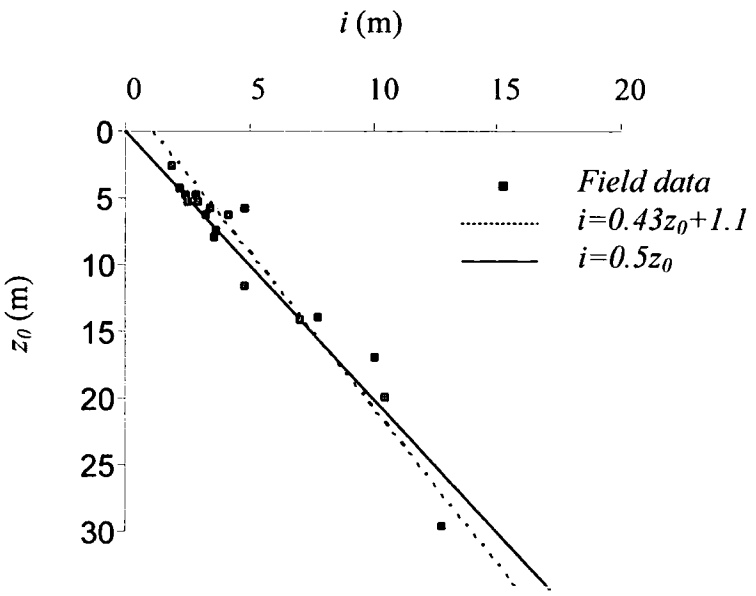

Figure 2.11. Plot of the trough width parameter i against the tunnel depth z_0 (After O'Reilly and New, 1982).

Rankin (1988) and Mair and Taylor (1997) have both plotted i against z_0 for more recent field data from U.K and worldwide. Their results confirm that a value of K = 0.5 in Equation 2.19 would fit most of the data for cohesive materials.

New and O'Reilly (1992) suggested a similar simplified formula for i for a cohesive soil profile consisting of n layers each of different thickness z and trough width constant K. They expressed their doubts for the validity of Equation 2.20 since it has not been tested for cohesionless materials.

$$i = K_1 z_1 + K_2 z_2 + ... + K_n z_n \tag{2.20}$$

2.3 Sub-surface deformation

The ruling mechanism of the surface movements due to tunnelling is well understood and described. Few results exist however to fully understand the sub-surface deformation mechanism. This is important when other structures founded at depth (e.g. pipes, tunnels and piles) exist prior to tunnel excavation (non greenfield sites).

Mair and Taylor (1993) tried to predict clay behaviour (vertical and horizontal vectors of sub-surface deformation) using simple plasticity solutions for the unloading of a cylindrical and spherical cavity. The impact of the horizontal displacement vector to the side of the tunnel at axis level appears to cease at a distance of $2D$ or greater. It seems that S_x above the crown is always bigger than H_x at the same distance (r) at springline (see Fig. 2.12). Their results seem to be in good agreement with field data. In Figure 2.12 the vectors of the vertical (S_x) and horizontal (H_x) surface deformation, as well as the tunnel radius (R), are denoted with δv, δh and α respectively.

Mair *et al.* (1993) presented field data which show the validity of the widely accepted assumption that the sub-surface settlements seem to follow an inverted Gaussian curve. To calculate the trough width parameter i for the subsurface settlement trough they suggest substituting the parameter ($z_0 - z$) for z_0 in Equation 2.19:

$$i = K(z_0 - z) \tag{2.21}$$

where z is the depth where the subsurface profile will be defined (Fig. 2.13), implying that K remains constant with depth (as it does for the surface settlement trough).

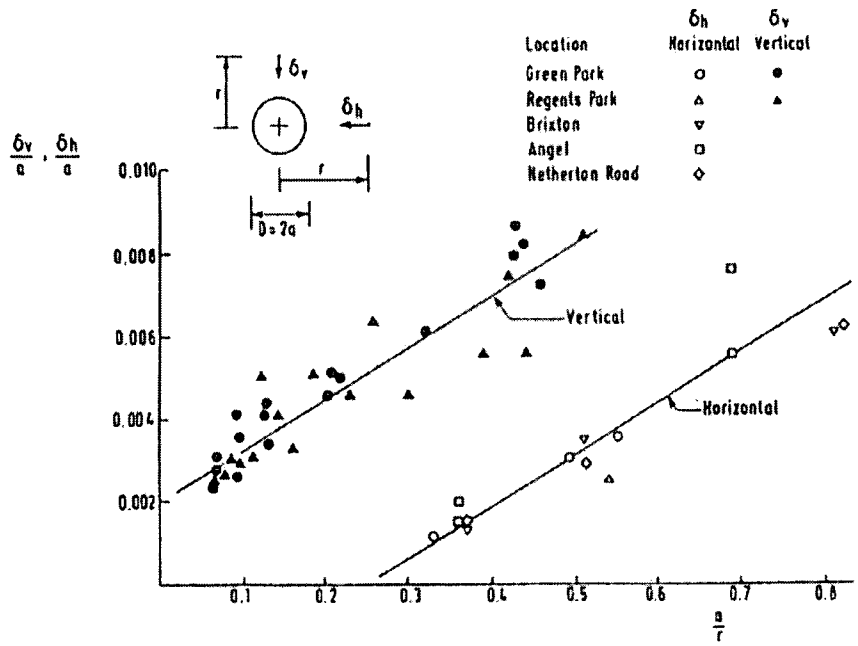

Figure 2.12. Normalised vertical and horizontal surface deformations, against the normalised tunnel radius (From Mair and Taylor, 1993).

Mair *et al.* (1993) plotted i normalized by z_0 against z normalized by z_0 with field and centrifuge data applicable for greenfield sites (Fig. 2.14). This figure illustrates that Equation 2.21 under-predicts the value of i/z_0. On the other hand a solid line which best fits the data is drawn which is defined as:

$$\frac{i}{z_0} = 0.175 + 0.325\left(1 - \frac{z}{z_0}\right) \tag{2.22}$$

Substituting Equation 2.22 to 2.21 gives:

$$K = \frac{0.175 + 0.325\left(1 - \frac{z}{z_0}\right)}{1 - \frac{z}{z_0}} \tag{2.23}$$

Equation 2.23 shows that at the surface (i.e. z = 0) K = 0.5 which is in agreement

with the assumptions made for i at the surface (Eq. 2.19). At depth though, K increases non-linearly with depth. In the case where $z = z_0$, K tends to infinity. This is clearly illustrated in Figure 2.15 where K is plotted against z/z_0 with the same data as in Figure 2.14. The assumption of $K = 0.5$ at depth underestimates the sub-surface width of the settlement trough. Equation 2.23 should be used cautiously for values of z/z_0 greater than 0.8 since it is not clear how the displacement vectors behave until a radial distance of $1D$ from the tunnel lining.

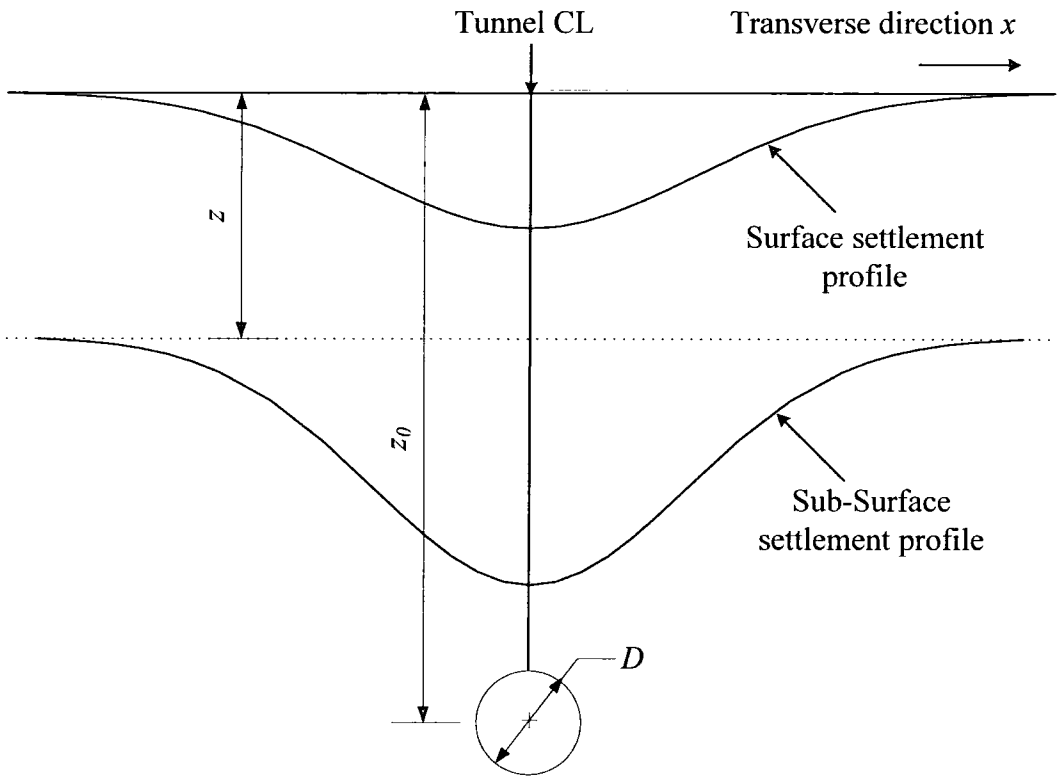

Figure 2.13. Transverse sub-surface settlement profile.

Combining Equations 2.4 and 2.22 gives:

$$\frac{S_{max}}{R} = \frac{1.25V_L \dfrac{R}{z_0}}{0.175 + 0.325\left(1 - \dfrac{z}{z_0}\right)} \tag{2.24}$$

Attewell and Farmer (1974a) presented field data from subsurface deformation measurements above tunnels in London clay, showing that S_{max} increases with depth.

This is consistent with Equation 2.24.

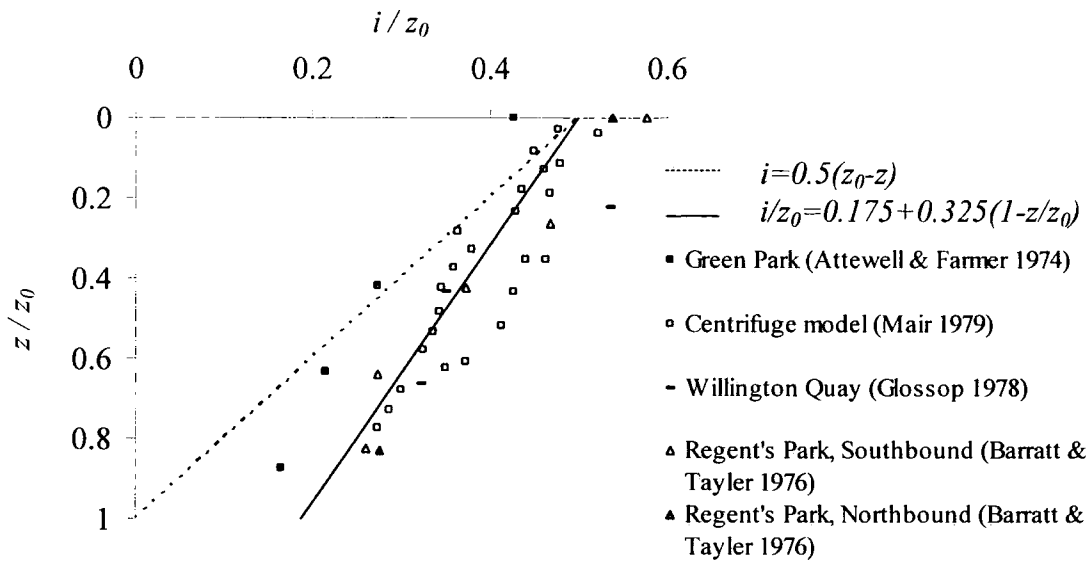

Figure 2.14. Plot of the normalised trough width parameter i against the normalised subsurface profile z (After Mair *et al.*, 1993).

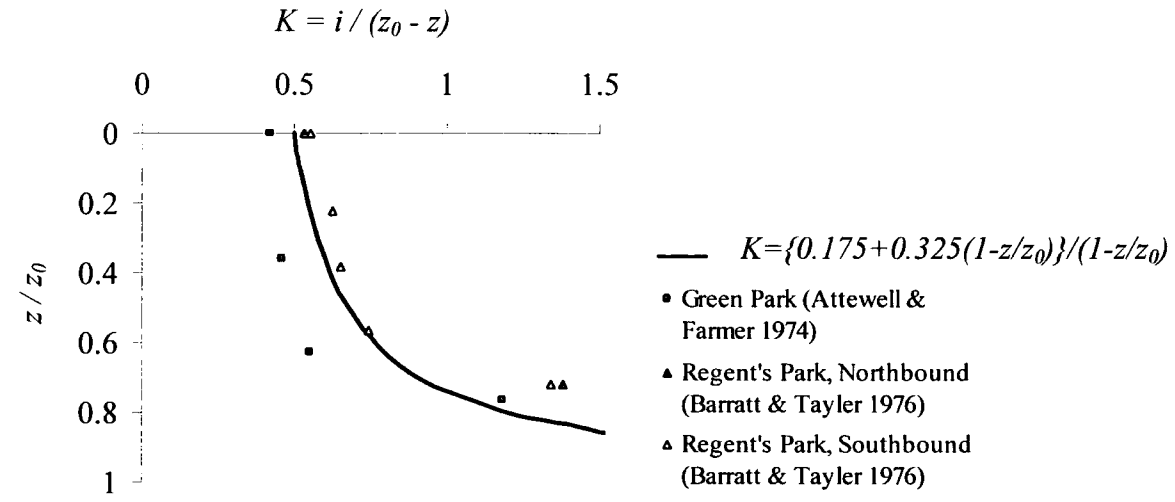

Figure 2.15. Plot of trough width constant K against the normalised subsurface profile z (Aftair Mair *et al.*, 1993).

According to Taylor (1995), in the case where K varies with depth then the surface displacement vectors are directed towards a point $0.175\,z_0/0.325$ below the tunnel axis. The results obtained for H_x are 65% less than would be expected if the ground

displacement vectors were aimed towards the tunnel axis (Fig. 2.16b). This is in contrast to the findings of O'Reilly and New (1982) (i.e. vectors heading to the tunnel CL in Fig. 2.16a).

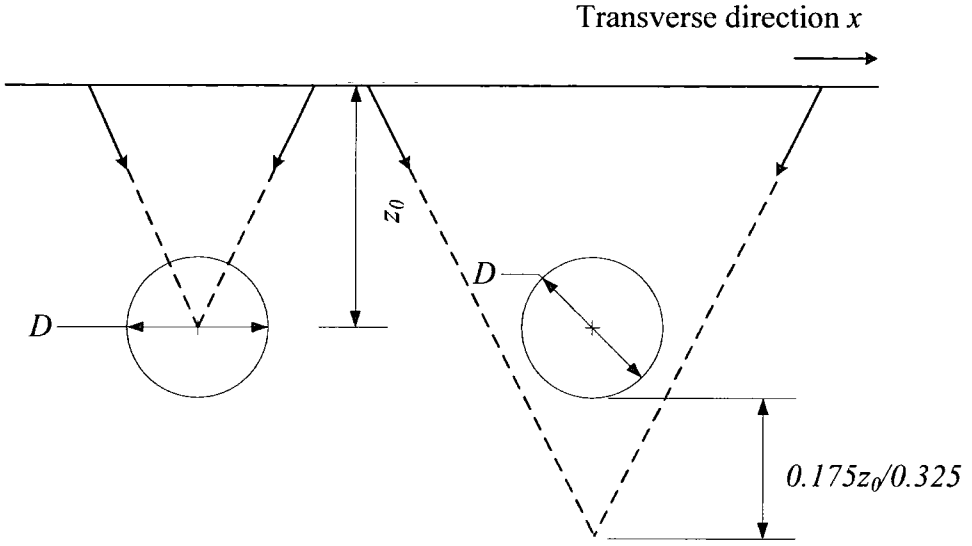

a) According to O'Reilly and New (1982) (*K* constant with depth)

b) According to Taylor (1995) (*K* varies with depth)

Figure 2.16. Different assumptions for the surface deformation vectors (After Mair and Taylor, 1997).

Through field observations at the Heathrow Express trial tunnels in London clay Deane and Bassett (1995) concluded that the displacement vectors do indeed head towards a point between the tunnel centre line and invert in one case. In another case they observed that the vectors were directed towards a point at the invert of the tunnel or below. The excavation at that scheme was performed using the NATM method (New Austrian Tunnelling Method) rather than shield tunnelling though.

Mair and Taylor (1997) suggest that the failure mechanism due to tunnelling in clays and in sands is totally different. In clays the failure mechanism develops upwards and outwards (Fig. 2.17a). On the other hand, in sands the mechanism develops only upwards (Fig. 2.17b). In clays, moreover, the zone of disturbance is wider than the tunnel diameter whereas in sand it is significantly narrow. Field observations as well as lab tests in centrifuges produced by Kimura and Mair (1981) are consistent with these findings.

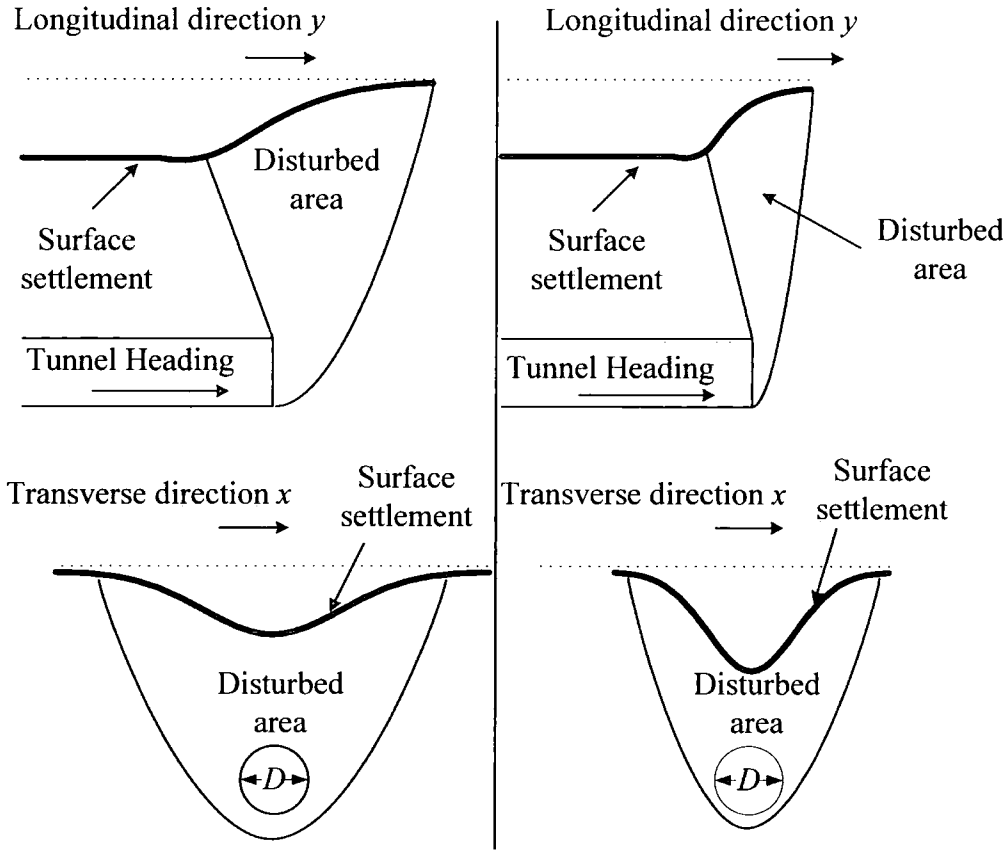

a) Clay profile b) Sand profile

Figure 2.17. Advancing tunnel and deformation mechanism for different soil profiles (After Mair and Taylor, 1997).

Summary

The most important points of the empirical and semi-empirical methods for predicting soil movements due to tunnelling operations in soft ground are summarised:

- The previously mentioned predictions, supported by field data indicate that the surface as well as the sub-surface settlement troughs along the transverse axis seem to follow a normal probability curve. On the other hand, along the longitudinal axis, the surface settlements seem to follow a cumulative probability curve.
- For twin tunnelling problems, super-imposition of the two individual settlement troughs along the transverse axis is not valid since super-imposition under-predicts the tunnel induced movements. This can be attributed to the interaction

mechanism which causes asymmetry effects.

- From the literature review a conflict amongst researchers has been revealed regarding the direction of the surface displacement vectors due to tunnelling in a greenfield site which requires further investigation.

2.4 Finite element analysis

In the previous sections empirical and analytical methods for estimating surface and subsurface deformations in three dimensions (both transverse and longitudinal axes) were presented. These methods are useful and valuable tools in every engineer's armoury. There are however some limitations in their use:

- Empirical methods are only applicable to greenfield sites. The presence of any other surface or sub-surface structure of significant stiffness cannot be considered. Thus interaction effects between tunnel and other structures are not taken into account.
- The methods are mainly used for single tunnel construction. In the case of twin tunnels, the pillar width (P) should be sufficient to ensure that no interaction occurs. In other words when the two tunnels are positioned so far apart that they can be considered as single tunnels the empirical approaches should be valid.
- The methods can only predict the immediate settlements. Consolidation (long term settlements) therefore cannot be estimated.
- Another restriction is that good engineering judgement is required for estimating some of the parameters (e.g. V_L, S_{max}).
- Finally, they are not truly three dimensional, more like a combination of two 2-D analyses.

An alternative to using empirical methods is numerical modelling (e.g. finite element method, boundary element method, and finite difference method. These are briefly described in Chapter 3). The Finite Element Method (FEM) provides substantial possibilities of modelling any geotechnical problem. In particular it deals with various types of interaction mechanisms during tunnel construction.

2.4.1 Two dimensional FE analysis

2.4.1.1 Single tunnel construction

This section will focus on different tactics of estimating tunnel induced settlements and interactions while conducting two dimensional FE (2-D) analyses. The deformation which takes place in front of the face and above an advancing tunnel is obviously a three dimensional (3-D) problem (Clough and Leca, 1989). Addressing the problem in all its three dimensions however has the following shortcomings:

- The high cost of 3-D finite element (FE) programs,
- The high memory required to run such a program,
- The amount of CPU time needed for the results and
- The more complex a program is the more parameters are required to be specified which sometimes are difficult to determine in practice.

The above disadvantages have until recently made most engineers reluctant to use 3-D FE programs. Thus, 2-D analysis has been preferred, certainly by practising engineers. Some of the most well known, validated and accepted methods of modelling 3-D effects in 2-D analyses are presented in this section.

- The Progressive Softening method proposed by Swoboda (1979). In this method soil stiffness is progressively reduced in an equivalent tunnel area in front of the face prior to excavation and lining installation. Engineering experience and judgement is required for the choice of the proper reduced stiffness value.
- The Convergence-Confinement (or λ) method described by Panet and Guenot (1982). They introduced Equation 2.25 for this purpose:

$$\sigma_r = (1-\lambda)\sigma_0 \tag{2.25}$$

where σ_r is the radial stress acting on the tunnel boundary after the lining installation, σ_0 is the initial ground stress prior to excavation and λ is an unloading parameter prior to lining installation ranging from $0 < \lambda < 1$. The factor $\lambda\sigma_0$ indicates the magnitude of the V_L. Once again engineering judgement is involved when choosing a suitable value for λ.

- The Gap method presented by Rowe *et al.* (1983) consists of allowing the tunnel

face to be uniformly shrunk and let to rest until it reaches the underlying soil. The vertical distance formed between the crown of the tunnel and its initial position is the gap parameter G (Fig. 2.18).

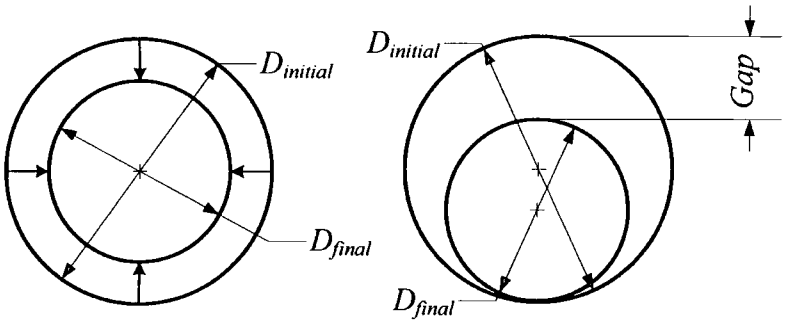

Figure 2.18. The Gap method by Rowe *et al.* (1983).

- The Volume Loss Control method introduced by Addenbrooke *et al.* (1997). Incremental removal of soil elements takes place to model excavation. When the specified value of V_L is reached at each step then the calculation is terminated.

The horizontal stresses (σ_h) prior to tunnel excavation at axis level equal to the vertical stresses (σ_v) due to the overburden weight times the coefficient of the earth pressure at rest (K_0):

$$\sigma_h = K_0 \sigma_v \tag{2.26}$$

It has been reported by Mair *et al.* (1981) that 2-D plane strain FE analysis fails accurately to predict the shape of the surface settlement trough (especially so for over-consolidated clays such as London clay where $K_0 > 1$) defined by Equation 2.1 (proposed by Peck, 1969). Instead it produces a much shallower and wider distribution. Rowe *et al.* (1983) conducted parametric studies to identify the reason for this discrepancy. They introduced non-homogeneity, anisotropy, plasticity, varied the earth pressure at rest (K_0), the Gap parameter (G), the grout pressure and the unit weight of soil (γ). According to their work the most influencing factors seem to be V_L (and consequently G), soil anisotropy, K_0 and plasticity.

Lee and Rowe (1989) performed linear elastic-perfectly plastic 2-D FE analyses using the Mohr-Coulomb failure criterion to determine the effect of soil anisotropy on the settlement trough due to tunnelling. Their findings are in good agreement with field and centrifuge data indicating that the Gauss curve is considerably affected when using values of G_{vh}/E_v between 0.2 and 0.25. G_{vh} is the shear modulus in the vertical plane while E_v is the Young's modulus in the same plane.

Gunn (1993) carried out non-linear elastic perfectly plastic analyses using the small strain constitutive models for soil by Simpson *et al.* (1979) and Jardine *et al.* (1986). The latter assumes a monotonic stress path (stresses follow the same path when loaded and unloaded) and is tested only for undrained conditions. The results seem to improve the 2-D FE predictions compared to simple linear elastic perfectly plastic models. Figure 2.19 shows plots of the error curve [i.e. Eq. 2.1, according to Gunn (1993) it is called like that because "it corresponds to the expected distribution of measurements of a physical quantity (S_x in this case) when measurement errors are random"] normalized by S_{max} against the transverse distance x normalized by i. Even with this development the shape of the trough remains shallower and wider.

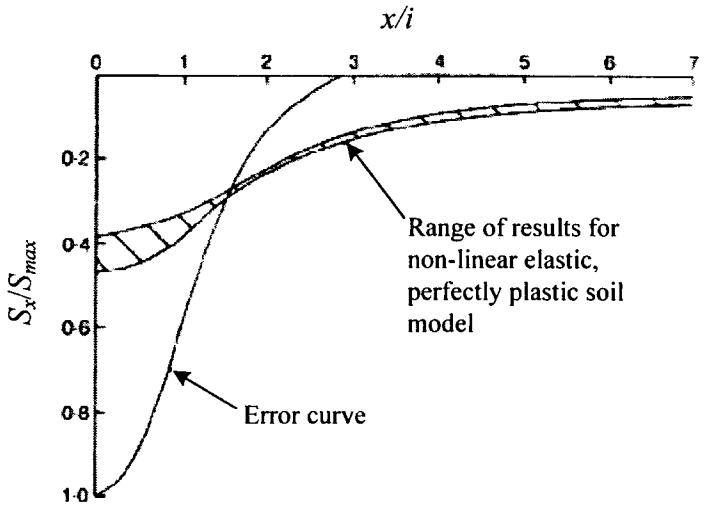

Figure 2.19. Surface settlement profiles normalized by S_{max} (From Gunn, 1993).

Simpson *et al.* (1996) appears to consider the effects of non-linear elastic behaviour of low significance. On the contrary they present FE results which agree with the field (from Heathrow Express trial tunnel) and lab data (using samples of London

clay). These indicate that by introducing anisotropy the shape of the trough resembles the Gauss curve; while non-linearity does not considerably alter the picture.

Addenbrooke (1996) investigated the effects of soil anisotropy (the findings coincide with Simpson *et al.* 1996) as well as the coefficient of the earth pressure at rest (K_0). By using reduced values of K_0 more realistic settlement troughs were obtained. For these values however, soil stiffness is unrealistically high and unrealistic for modelling London clay.

2.4.1.2 Twin tunnel construction

Experimental data and FE analyses show that tunnels excavated in close proximity interact. Due to this interaction mechanism some additional movements take place (asymmetry of the trough) which cannot be taken into account by empirical methods described in previous sections. The minimum distance between the tunnels, to avoid interaction effects, clearly varies according to tunnel position, *in situ* stresses, soil properties, support conditions and sequence of excavation. What is the minimum safe distance where no interaction effects between multiple tunnels driven in soft soil occur?

Few engineers tried to deal with this problem and as a consequence there are not so many published results. These results do not always coincide. Therefore, the answer to this problem is still debatable. According to Ward and Thomas (1965) the excavation of a second tunnel (D = 4.146m) driven in London clay at a horizontal distance of 2.4m from the first (P/D = 0.6) produces an extra distortion to the lining of the first of about 12%. Forty months later the distortion was reported to have doubled.

Cording and Hansmire (1975) presented field data from tunnels (D = 6.4m) driven in sand (excavation depth 14.6m) for the Washington D.C. Metro. It was reported that the volume of material lost in the surface for the second tunnel was greater than that lost in the tunnel face due to the interaction mechanism. The final settlement trough was therefore no longer symmetrical. The maximum displacement due to the second tunnel was not located above the second tunnel but offset towards the first. This mechanism produced an additional effect. An extra amount of deflection of the first

tunnel's lining was measured. The interaction between the two tunnels was found to increase as the distance between them (pillar width P) decreased. Figure 2.20 shows that as the ratio P/D decreases from 1.1 to 0.7 volume loss normalised by ground loss (V_S) of the first tunnel increases by a factor of approximately 3. Another point extracted from this figure is that the curve tends to become horizontal for values of $P/D > 1.1$. This is clear evidence that interaction in sand ceases beyond this distance for twin tunnel construction.

Ghaboussi and Ranken (1977) performed a parametric FE study of multiple tunnel construction using mostly linear elastic and in some cases simple elasto-plastic analyses with $K_0 = 0.5$ (Fig. 2.20). In this figure the vertical axis ($\Delta V_S / V_{S2}$) refers to the ratio of the volume loss over the volume of the settlement trough due to a single tunnel construction. Four-noded quadrilateral elements were used to model the domain. The yielding surface was described by the Drucker-Prager criterion. The varying parameters were pillar width (P), tunnel depth (z_0), sequence of excavation and support condition. They report that interaction effects are small for two adjacent and lined tunnels when they are excavated simultaneously at $P = 1D$. However, at $P > 2D$ there was no interaction at all. Therefore the tunnels could in this case be considered as independent.

Due to construction of the second tunnel, the first tunnel and the surrounding soil may move as a rigid body. The redistribution of stress creates an effect which is known as "arching" around the second tunnel. This has as a consequence the load removal from the crown of the tunnel. In other words, a reduction in earth pressure (Hansmire, 1984).

Kim *et al.* (1998) carried out reduced-scale physical model testing of deep parallel and perpendicular shield driven tunnels in clay. Small amount of FE analyses took place during this research. Consolidated kaolin slurry was used to produce the soil samples for the test. An unrealistic value of 6% was given to the imposed ground loss and a range of values from 0.49 to 0.59 for K_0. The parameters of interest were P, tunnel alignment, overconsolidation ratio (OCR) and lining stiffness. They suggested that at $P > 1.5D$ the interaction effects were found to be small. These findings are similar with Ghaboussi and Ranken (1977).

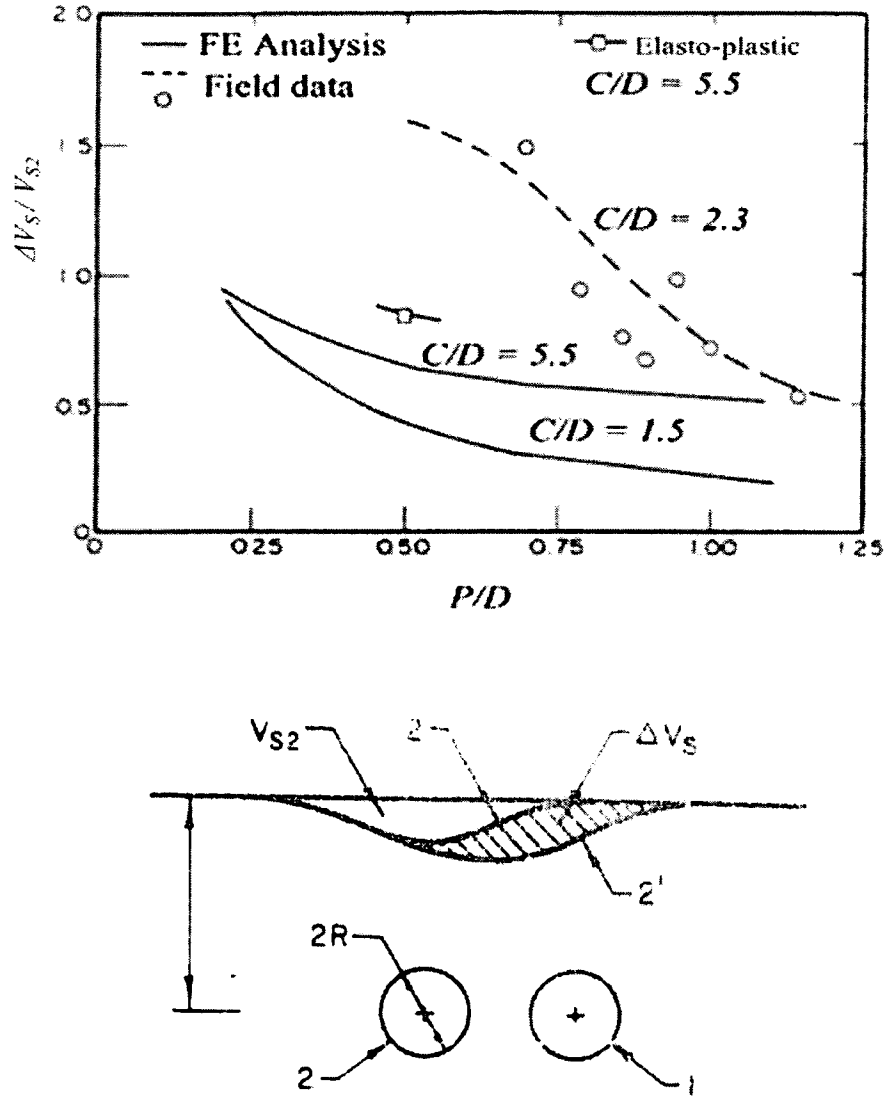

Figure 2.20. FE results (From Ghaboussi and Ranken, 1977) and field data (From Cording and Hansmire, 1975) plotted in the same graph.

Addenbrooke and Potts (2001) conducted coupled consolidation FE analyses of multiple tunnels using two different small strain non-linear soil models (Jardine *et al.*, 1986; Puzrin and Burland, 1998). Mohr Coulomb failure criterion was chosen for the plastic region. They used a soil profile similar to the one reported by Barratt and Tyler (1976) from Regent's Park in London and assigned a value of V_L = 1.4% for the first tunnel. For the second it was predicted by the analysis. The earth pressure at rest for the London clay stratum was prescribed at K_0 = 1.5. Eight node isoparametric elements were used to model the soil and three node beam elements for the tunnel lining. Time of excavation and pillar width between the two tunnels varied. The latter parameter contributes significantly to the interaction mechanism, while the

former does not. Only the effects due to the second tunnel construction were considered in their analysis. Figure 2.21 shows a plot (with just four points) of the reduction of volume loss of the second tunnel normalised by V_S against the ratio of P/D for side-by-side tunnels. For this case interaction effects became negligible for $P > 7D$ (when $D = 4.146$m). On the other hand when the tunnels are vertically aligned (piggy-back geometry) and the second tunnel is driven above an existing tunnel the minimum pillar width for no interaction is $P = 1D$. When the second tunnel is driven below an existing tunnel, there is always interaction no matter their relative locations. Limited number of numerical analyses are presented which are not enough to draw solid conclusions.

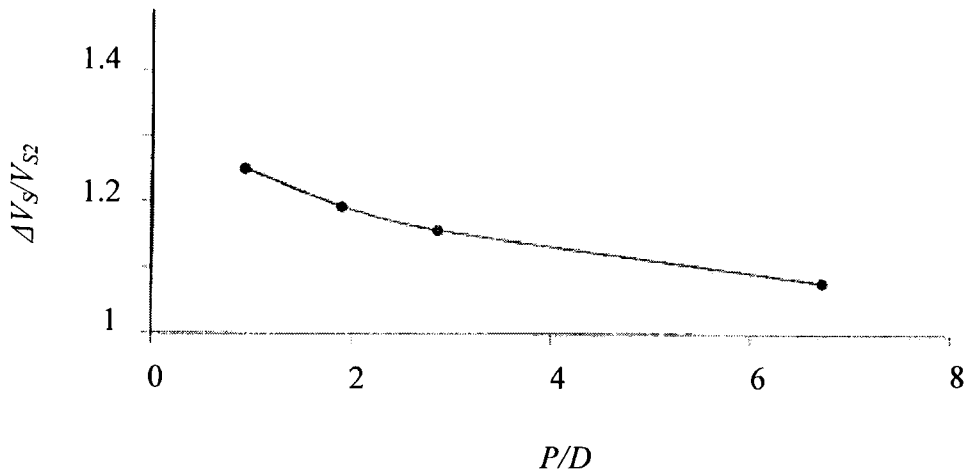

Figure 2.21. Plot of the reduction of volume loss of the second tunnel normalised by V_S against the ratio of P/D (From Addenbrooke and Potts, 2001).

Cooper *et al.* (2002) presented the experimental results taken from the existing Piccadilly line during a three station tunnel construction at the Heathrow Express Central Terminal area. They confirmed Addenbrooke and Potts (2001) results indicating that there is no extra distortion when the two tunnels have a pillar width distance between $6D$ and $7D$ or greater. Figure 2.22 shows their field data from various sites and the best fit line drawn to come up with latter mentioned result. On the vertical axis (V_{2R}/V_{2N}) the ratio of the "remote over the near limb" of the settlement trough is plotted similar to the ratio of $\Delta V_S/V_{S2}$ in Figure 2.20. Addenbrooke and Potts (2001) and Cording and Hansmire (1975) have both drawn

curves rather than straight lines when plotting similar graphs (Figs. 2.20, 2.21). Had Cooper *et al.* (2002) done the same the minimum P would be less than that recommended (around $4D$ to $5D$) since at that area the curve would become almost horizontal, indicating no further distortion. Furthermore, the best fit line drawn in Figure 2.22 is highly affected from point B (Bartlett and Bubbers, 1970) which was measured almost 37 years ago. Its accuracy thus might be debatable. A controversial technique was adopted to extract the conclusion since by ignoring point B the best fit line would cut the axis at a smaller P/D distance (around 4.5 rather than 6). This is also evident by the area enclosed between the two dotted curved lines drawn by the author of the current thesis which indicates that the interaction seems to stabilise (when curves become parallel to the horizontal axis) at a smaller pillar width distance than the one indicated by Cooper *et al.* (2002).

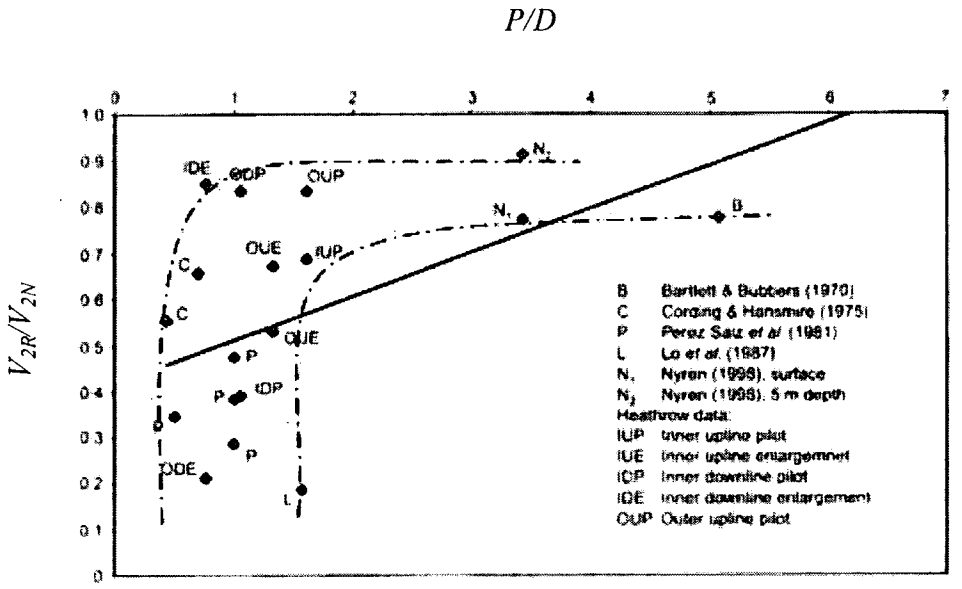

Figure 2.22. Plot of normalised volume loss against normalised pillar width (After Cooper *et al.*, 2002).

Koungelis and Augarde (2004) presented results from parametric analyses undertaken varying D, soil stiffness and tunnel position. A commercial geotechnical software package was used (Plaxis v.7) for this purpose. Similar domain and tunnel geometry with Addenbrooke and Potts (2001) was used. A simple linear elastic perfectly plastic soil model was incorporated with a Mohr-Coulomb failure criterion. For the horizontal alignment case the results indicate that from a distance of $P > 4D$ no

interaction effects seem to occur. This appears to be conservative in comparison to the values reported by Addenbrooke and Potts (2001). For the vertical alignment case though the results seem to be in agreement with the previous mentioned publication. Another interesting point is the direction of movement of the first tunnel's pillar springline due to the construction of the second. A stiff layer would force the pillar springline to move towards the tunnel centre line. A softer soil would allow the springline to expand and thus compress the pillar distance.

2.4.2 Three dimensional FE analysis

It is widely accepted that tunnel excavation is a 3-D process. It is expected therefore, that full 3-D numerical analysis would improve the 2-D FE settlement estimations. With recent advances in computing undertaking such analyses is less demanding and the number of published papers using 3-D methods is increasing.

Lee and Rowe (1991) carried out a simplified analysis using their own software (FEM3D) based on the Gap method on plane strain boundary conditions. The technique adopted seems to be reliable when tunnelling in similar conditions as the Thunder Bay tunnel (D = 2.47m) in Canada. An anisotropic simple linear elastic-perfectly plastic soil model was adopted with a value of earth pressure at rest of K_0 = 0.85. The Tresca failure criterion was used modelling undrained conditions. A two stage analysis was performed to simulate the face advance (Fig. 2.23). During the first stage, axial and radial pressures are released ahead and around the tunnel face respectively to simulate face loss. The physical gap parameter above the shield was determined. In the second stage, the total gap parameter (ground loss and physical gap) is applied over the total excavation length behind the shield. When this process finishes the lining elements are activated.

Akagi and Komiya (1996) simulated coupled 3-D FE analysis of shield tunnelling (D = 3.737m) in clay. A simple elasto-plastic constitutive model was used for the clay. Special elastic elements were employed at the face and in front of the excavation. The mesh around the shield was re-generated at every stage. The results presented seem to be in agreement with field data. However they do not provide sufficient details about volume loss and the FE program used.

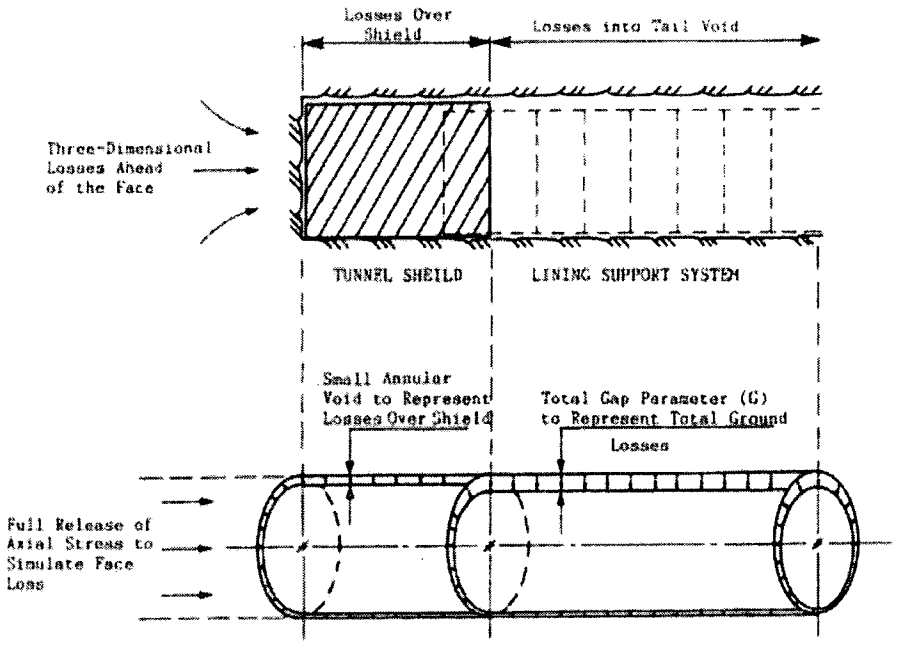

Figure 2.23. Description of the 3-D modelling of V_L (From Lee and Rowe, 1991).

Dasari *et al.* (1996) simulated tunnel construction (D = 8m) in London clay using NATM in both 2-D and 3-D incorporating the "step-by-step" (explained later in this section) approach in a FE program (CRISP) which was developed at Cambridge. They varied the sequence of construction and the elastic soil behaviour. From the results presented the importance of both construction sequence (larger settlements for larger excavation stages) and elastic non-linearities is highlighted. Dasari *et al.* (1996) state that the lining installation behind the face further restricts deformations. Plane strain analysis (2-D) along the transverse axis (2DTNLE line in Fig. 2.24a) produces approximately three times greater values of S_x than the equivalent 3-D model (3DTNLE line in Fig. 2.24a). Different types of analyses therefore give different predictions for this type of problem. The field data they present from a typical London profile (taken from Deanne and Bassett, 1986) seem to be in agreement with 3-D FE predictions.

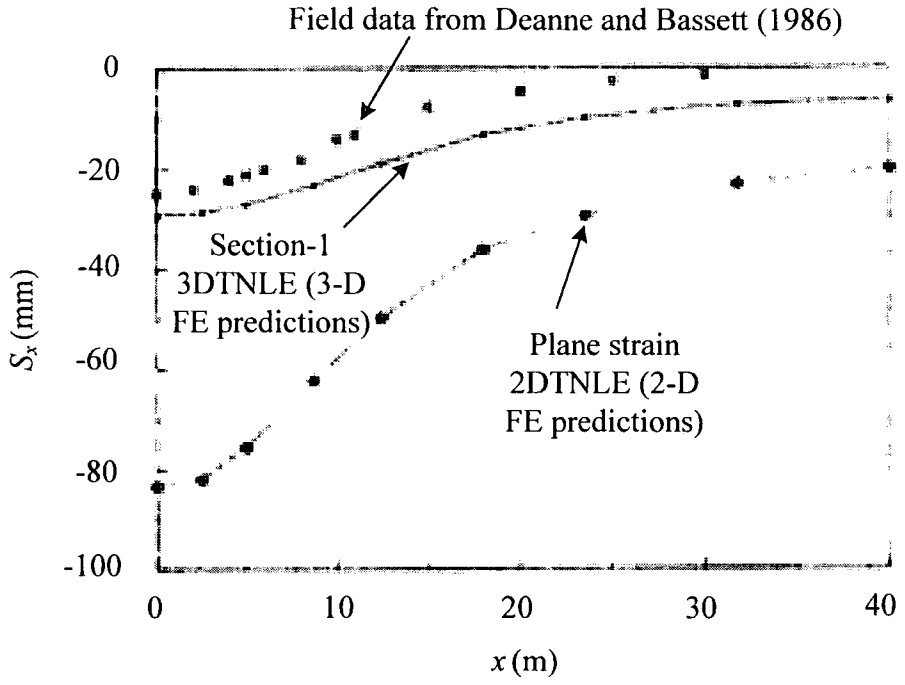

a) Field data and FE predictions from Dasari *et al.* (1996)

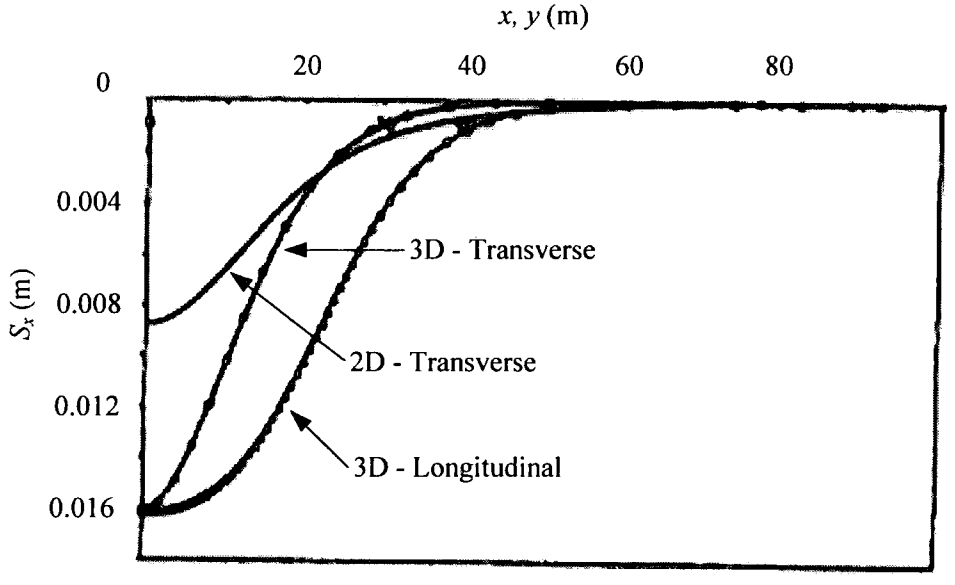

b) FE predictions from Dias *et al.* (2000)

Figure 2.24. Comparison between numerical results and field data.

Augarde *et al.* (1998) presents another method to simulate excavation where the role of the stiffness and self-weight of the elements inside the tunnel is ignored and the lining shell elements are simultaneously activated. The latter elements then are subjected to uniform hoop shrinkage by applying nodal forces in order to simulate the ground loss. This procedure is incrementally applied in every stage of excavation (Fig. 2.25). A problem highlighted by these authors was ensuring the current stage shrinkage did not create any extra amount of shrinkage to the previous lining installation stage. To overcome this difficulty Augarde *et al.* (1998) constrained the nodes which were at the face during the first stage. These constraints were then removed at the next stage. The elements used to implement this method are described in detail by Houlsby *et al.* (2000). Figure 2.25 shows how this procedure is applied. A non-linear elastic perfectly plastic model is used to represent soil behaviour with a value of K_0 = 1 and D = 5m. The research code OXFEM developed at Oxford was used to run the analyses.

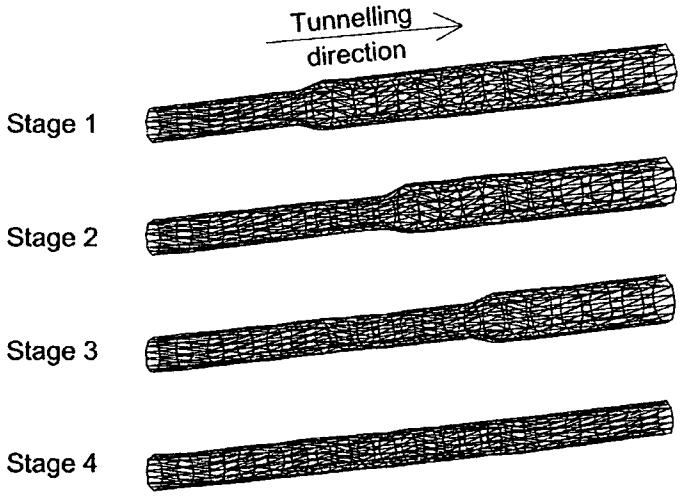

Figure 2.25. Uniform hoop shrinkage of the lining by applying nodal forces to simulate the ground loss (From Augarde *et al.*, 1998).

Dias *et al.* (2000) proposed a new 3-D finite difference model of tunnel excavation with a slurry shield TBM (Tunnel Boring Machine) using FLAC 3D. Their simulation consisted of four phases: the face support, both over cut and conical shape of the TBM, the grout injection in the annular void and finally the long term deformations. Soil was modelled using a linear elastic perfectly plastic model. Field data from the

Cairo metro (D = 9.8m) were used for evaluation with both 2-D and 3-D FE analyses. Narrower settlement troughs were produced along the transverse axis compared with the 2-D data (Fig. 2.24b). This is in contrast with the findings of Dasari *et al.* (1996) findings.

One of the most common techniques to simulate volume loss in 3-D is the so called "step-by-step" method where soil elements are removed from the face of the excavation creating an unsupported region (Ur) while lining is installed at a specific distance behind the face. The importance of the length of this region was first mentioned by Vermeer *et al.* (2002). A linear elastic perfectly plastic soil model was used with a K_0 = 0.65. Their analysis (using Plaxis 3D) revealed that the longitudinal profile is highly affected by Ur. Figure 2.26a shows the difference in modelling the first excavation step. The upper line refers to a 2m lined step while the lower refers to the unlined case of similar length. Settlements along this axis cease to increase at a distance of 35m behind the face no matter how much the shield has advanced. This condition is termed "steady state" (Fig. 2.26b). According to Vermeer *et al.* (2002) the step-by-step method is extremely time consuming. For this reason they introduced another approach (the "all in once" analysis) where in the first phase soil elements are de-activated while lining elements are activated throughout the whole length of the excavation until steady-state conditions are reached. In the second phase an unsupported region of excavation Ur is simulated while all displacements due to the first phase are set to zero. The volume of the surface deformation trough is then calculated. This volume corresponds to the volume loss of a single excavation stage. A 2-D FE analysis is then undertaken using the previous calculated value of the surface deformation trough to predict the settlement trough along the transverse axis. In their analysis the tunnel (D = 8m) is positioned very close to the horizontal boundary (just 4m). The uplift effect thus would significantly affect soil displacements.

Franzius (2003) performed 3-D FE analysis to see whether transverse settlement predictions would improve compared with 2-D. A non-linear elastic perfectly plastic soil model with a K_0 = 1.5 was used with the research code ICFEP. From the results presented only minor improvements occurred. Soil anisotropy and different K_0 values therefore, were varied to identify their impact on the trough and the distance

where the steady-state conditions appear. These studies showed that these conditions do not develop for such a high value of K_0 (Fig. 2.27a). Figure 2.27b shows that for a smaller value (K_0 = 0.5) they nearly appear at a distance of 13D (when D = 4.15m). This is in agreement with Vermeer *et al.* (2002). The significance of Ur was also identified suggesting that a higher value would decrease the number of the FE elements and calculation time. These findings indicate that only with unrealistically (for London clay) high values of soil anisotropy and V_L and low values of K_0 the settlement trough resembles with the normal probability curve.

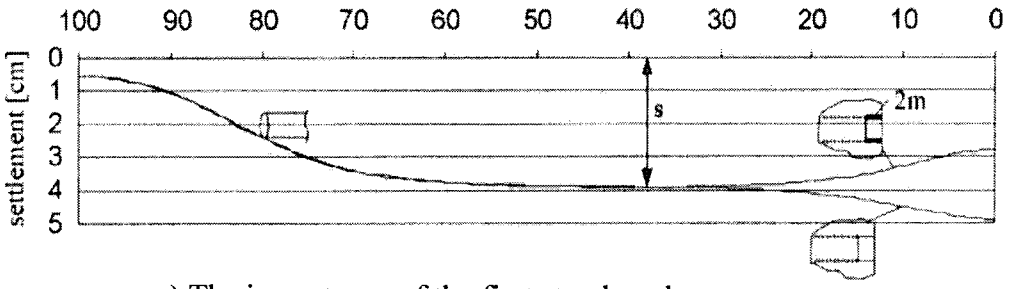

a) The importance of the first step length

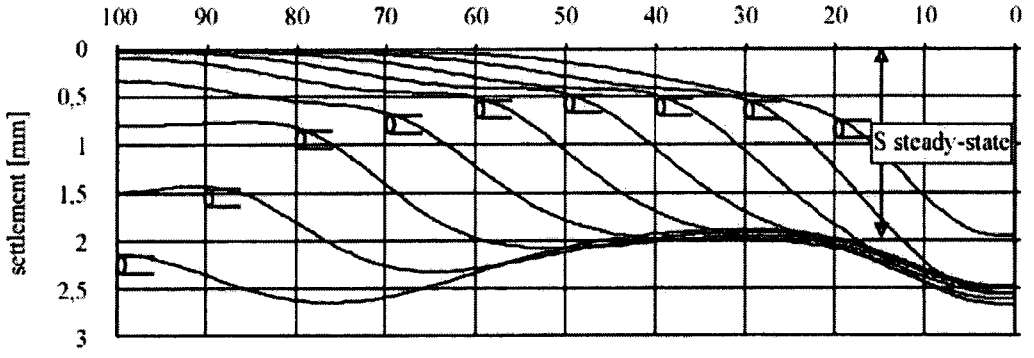

b) Steady state condition

Figure 2.26. Plots of S_y along the longitudinal y-axis (From Vermeer *et al.*, 2002).

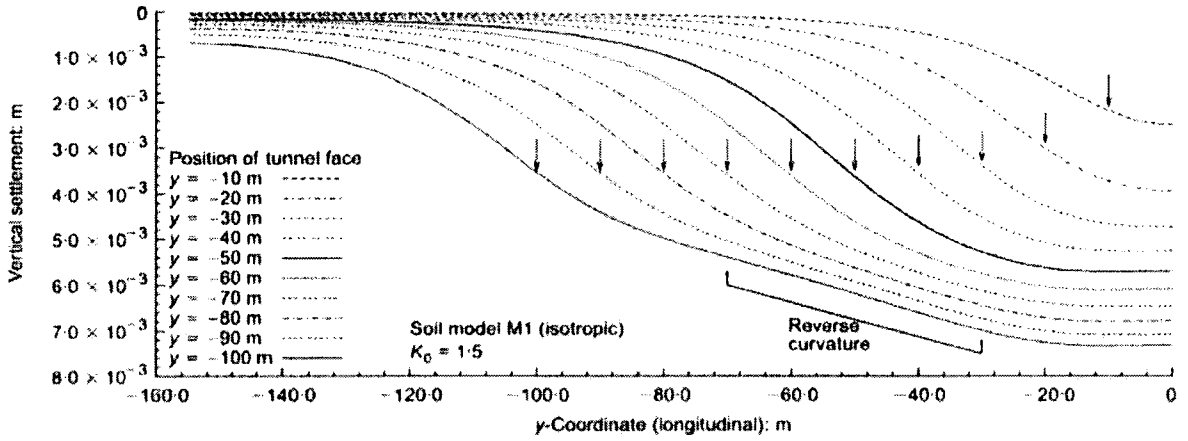

a) Steady state conditions do not develop for high values of K_0 (K_0 = 1.5)

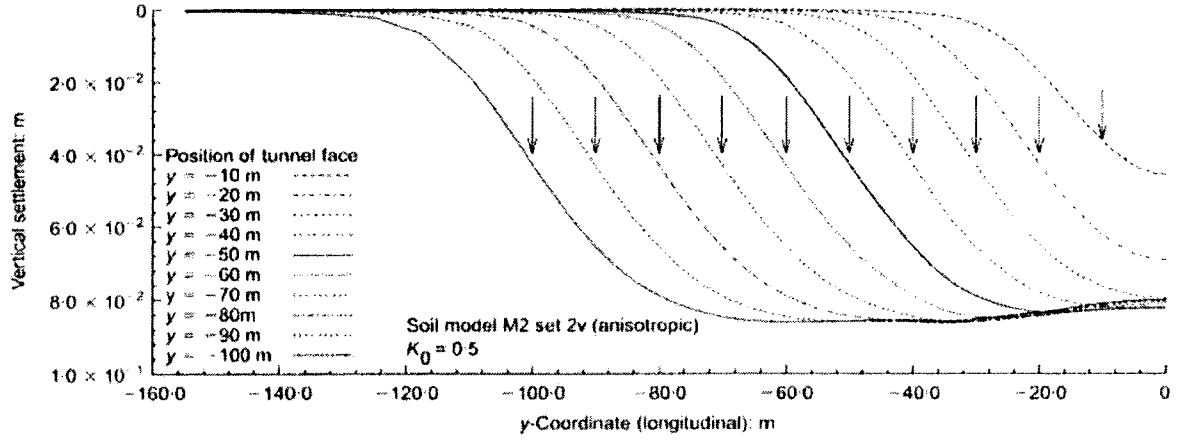

b) Steady state conditions develop for small values of K_0 (K_0 = 0.5)

Figure 2.27. Plots of S_y along the longitudinal y-axis for different K_0 values (From Franzius, 2003).

Galli *et al.* (2004) attempted to study the polycentric tunnel face (D = 11m) for both shallow and deep tunnels with temporary lining support and soil nailing by using a commercial FE package (LUSAS). Simple elasto-plastic properties with a Mohr-Coulomb failure criterion were used for the soil. Excavation and lining installation were simulated by incorporating 6 load cases for the first step. After that the last two load cases are incrementally repeated. Soil nails drastically reduced the movements in the face. The FE predictions between 2-D and 3-D analyses are in agreement.

Summary

A summary of the most important aspects regarding the use of the FEM on tunnelling related problems in both 2-D and 3-D is presented:

- Tunnelling is clearly a 3-D problem. However, due to limitations in computer resources, researchers are trying to use 2-D plane strain FE analysis instead.
- 2-D FE predictions regarding the settlement trough along the transverse axis seem to produce shallower and wider troughs compared to field data, especially so when a high value of the earth pressure at rest is used ($K_0 > 1$). Small strain constitutive models and anisotropy seem to improve these predictions.
- Another unresolved issue is the one regarding the interaction mechanism between multiple tunnels driven in close proximity. Researchers who dealt with this problem could not agree on the minimum distance where interaction reduces and tunnels act as single.
- 3-D FE predictions regarding the settlement trough along the longitudinal axis highlighted the importance of the length of the unsupported region *Ur*.

2.5 Lining distortion

Peck (1969) states three conditions for successful tunnelling. The first refers to safe operation of tunnelling works. The second requirement is the protection of adjacent structures. The final condition refers to the tunnel's ability to withstand all external loads which act upon it during its service life. In this section these loads and their influence on tunnel lining will be considered.

Various lining types (e.g. segmented, shotcrete, steel) and shapes (e.g. circular, horseshoe) can be selected by the designer depending on ground conditions and excavation method. In this thesis only circular shield driven tunnels will be studied. For the latter case a distinction should be made between temporary and permanent lining. The temporary support is employed to ensure safe working during excavation while the permanent is used for long-lasting stability.

2.5.1 Lining response to gravity

According to O'Rourke (1984) linings do not carry the total overburden weight of the overlying ground. The vertical (σ_v) and horizontal (σ_h) stresses instead, are re-distributed around the face due to mobilisation of the soil shear strength and continuity. This effect is often called as "arching". The tunnel therefore has to withstand only the stresses which are not arched.

Mair and Taylor (1997) presented field data from 12 different tunnel cases driven in London clay (Fig. 2.28). The lining load is expressed as a percentage of full overburden weight at CL. These are plotted as a *C/D* ratio. The data collection refers to one week and one year after lining installation. Figure 2.28 shows that the measured lining load even after a year is below 70% of full overburden. In most cases it varies between 40% and 60%.

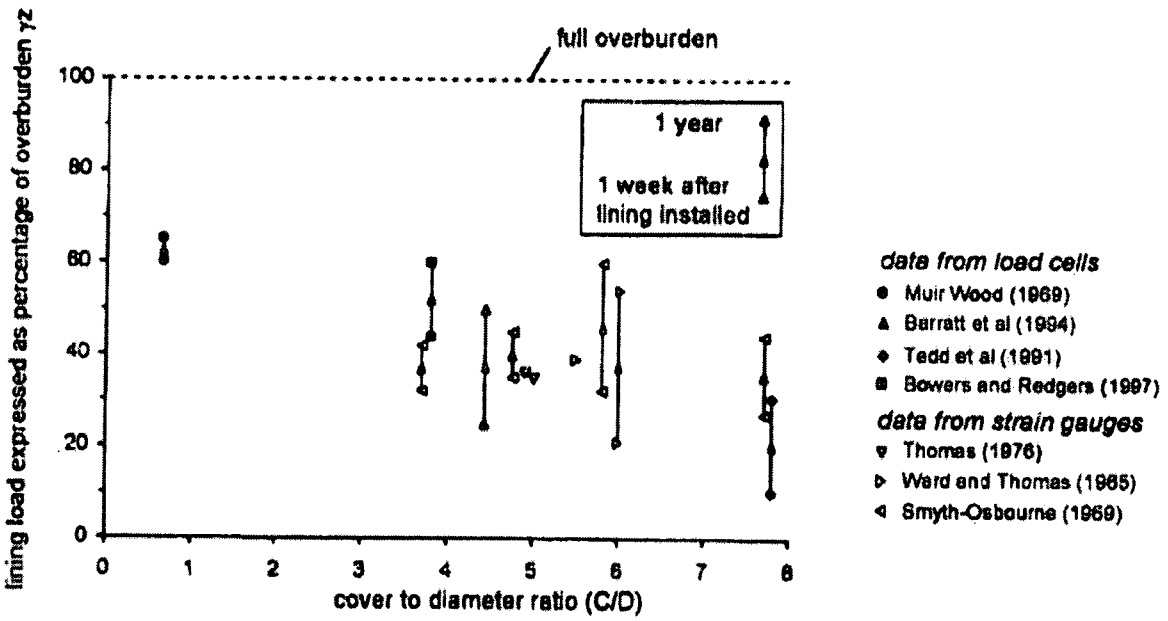

Figure 2.28. Overburden load against normalised ratio of *C/D* (From Mair and Taylor, 1997).

Similar measurements were made by Barratt *et al.* (1994) from Regent's Park in London, covering a longer period of twenty years (Fig. 2.29a). The percentage of the full overburden load is plotted against time in a semi-logarithmic scale. Figure 2.29a illustrates that the vertical load immediately after construction was approximately 30% of the total overburden. The lining load gradually increases until a value of 60%

of the overburden stress 20 years later and then it seems to stabilise. Figure 2.29b depicts data presented by Bowers and Redgers (1996) from another site in London (St. James's Park) covering a shorter period of 200 days. The same conclusions were drawn as before.

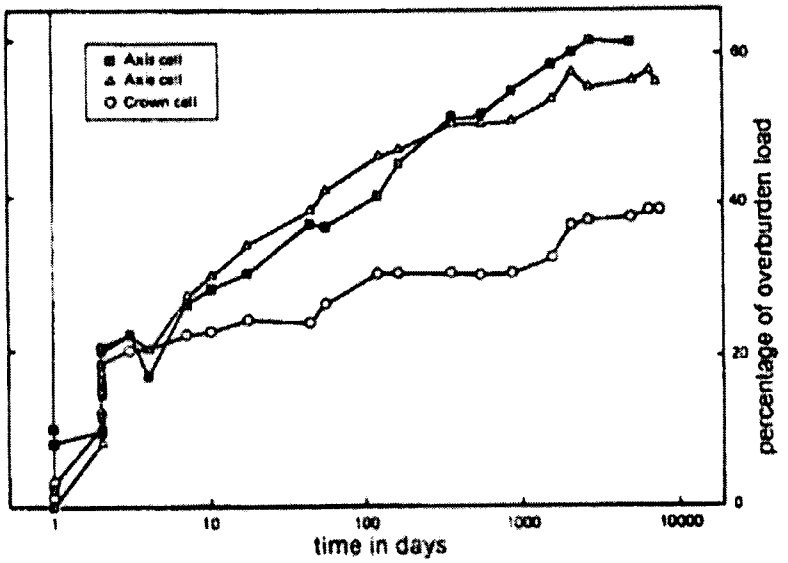

a) (From Barratt *et al.*, 1994)

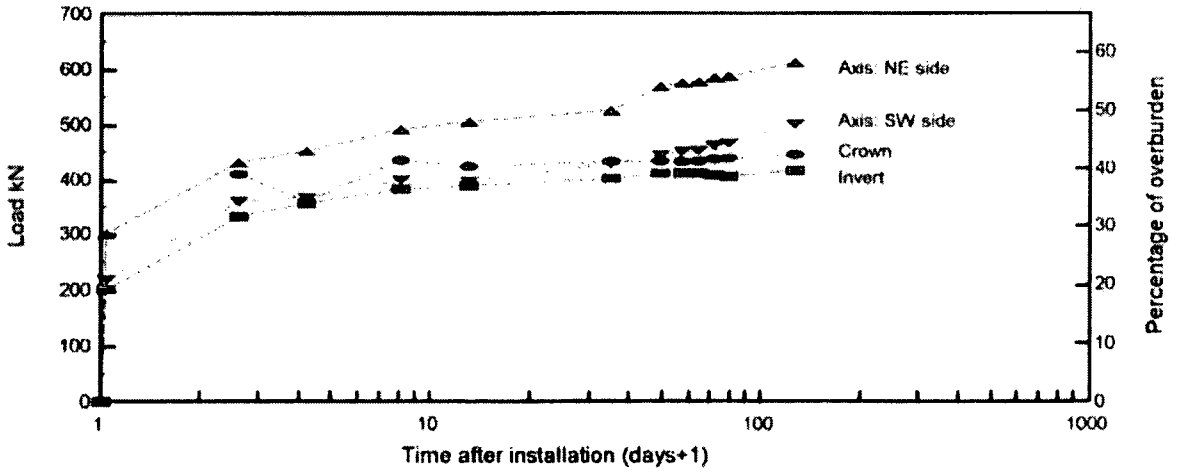

b) (From Bowers and Redgers, 1996)

Figure 2.29. Overburden load against time.

For normally consolidated clays K_0 takes values less than unity. This implies that the vertical stress acting on the tunnel lining is larger than the horizontal. Thus the original shape of the face alters from a circle to an ellipse, i.e. the vertical axis shortens while the horizontal elongates. For over-consolidated clays such as London

clay, K_0 is usually greater than one. According to Mair and Taylor (1997) it is "erroneous" to consider that the horizontal stresses acting on a tunnel are greater than the vertical. Barratt *et al.* (1994) display *in situ* measurements from Regent's Park in London, which indicate that σ_h is about 70% of σ_v (at crown) even though K_0 would range between 1.5 and 2. Bowers and Redgers (1996) point out that σ_h is about 80% of σ_v (at axis level) at St. James's Park in London, although K_0 is once more greater than unity.

Ward and Thomas (1965) made short term (just a week after tunnel installation) field observations from two different sites in London. These were from the Post Office Railway tunnel and the Victoria Line tunnel. In both of them they reported a reduction of the vertical axis dimension and an elongation of the horizontal.

Lee (2002) presented recent measurements from the London Docklands Light Railway Lewisham Extension tunnelling scheme. Elongation of the vertical axis and reduction of the horizontal became evident from the measurements. The excavation took part in the Lambeth Group-Woolwich formation which is the London clay's underlying stratum.

Peck (1969) made the following working hypothesis to acquire lining deformation. The lining is assumed to be placed without any ground disturbance. Re-distribution of stresses will take place when the soil is removed from the tunnel's interior. Further assuming that the circular lining is ideally flexible, it will deflect to an elliptical shape until equilibrium is reached. Stress distribution is almost uniform and no bending moments exist. In the case of a perfectly rigid liner though, minor deformations take place. This is because shear stresses are not mobilised as in the case of a flexible lining. *In situ* stresses do not vary appreciably thus while the lining is subjected to significant amount of bending moments (see Fig. 2.30). In reality however, linings behave between this two extreme theoretical conditions.

Einstein and Schwartz (1979) presented a simplified plane strain analytical method (Relative Stiffness Solution) for tunnel supports in an infinite purely elastic homogeneous and isotropic one-layer medium. They tried to find a quick but accurate way to calculate the soil-lining interaction effects and determine how the variation of

lining and soil properties affects tunnel deformations. Two distinct cases were identified: the stress field and the displacements prior and after the excavation. In the latter case two extreme conditions were studied; the full slip (relative movements between the lining and the ground are aloud) and the no slip (no movements between the support and the ground are permitted). Variation of thrusts, moments and displacements at springlines are plotted against compressibility (C') and flexibility (F) ratios given by Equations 2.27 and 2.28 respectively. Einstein and Schwartz (1979) state, that this method is highly depended on the right choice of the loading conditions to produce sensible results. Engineering experience and judgement are necessary when using this method.

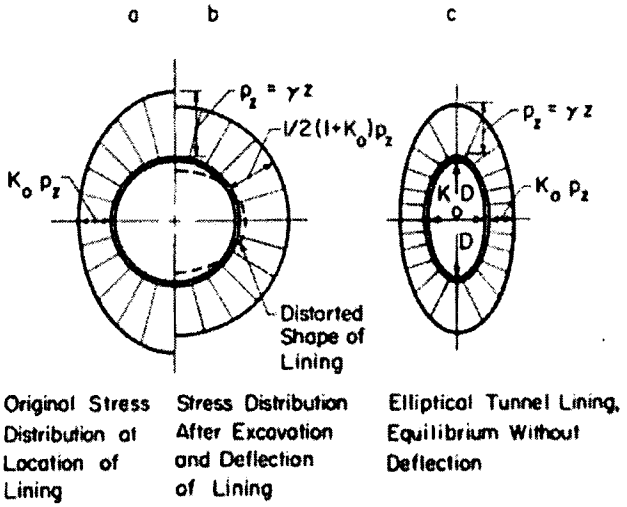

Figure 2.30. Rigid and Flexible types of lining (From Peck, 1969).

$$C' = \frac{ER\left(1-v_L^2\right)}{E_L A\left(1-v^2\right)} \tag{2.27}$$

$$F = \frac{ER^3\left(1-v_L^2\right)}{E_L I\left(1-v^2\right)} \tag{2.28}$$

where E, v and E_L, v_L are the Young's modulus and Poisson's ratio of the ground and the lining respectively. A is the cross-sectional area of the support and I is the second moment of area of the support.

Soliman *et al.* (1993) investigated how the sequence of construction of multiple tunnels interacts with the stress distribution of the soil and the lining. They conducted linear elastic 2-D and 3-D FE analyses. Equations 2.29 and 2.30 were used to calculate the relative stiffness parameters (α, β). Their results are plotted in charts that show the relative changes in stresses and deformations, in comparison with a single tunnel analysis. These results imply that a single tunnel solution can be used to find multiple tunnel solutions.

$$\alpha = \frac{ER^3}{E_L I} \tag{2.29}$$

$$\beta = \frac{ER}{E_L A} \tag{2.30}$$

2.5.2 Lining response to surface loading

Plenty of publications exist which study the interaction mechanism of soil, lining and a pre-existing structure (non-greenfield site) response during tunnelling operations. However the literature on the effect of surface loading on an existing tunnel is sparse to this author's knowledge. Most refer to the case of surface loading above pipes or pile construction and pile loading and their effects on tunnels, which is beyond the scope of the current thesis. Schroeder (2002) reviewed many relevant publications. The main reason preventing engineers from dealing with the subject of surface loading is the difficulty they face in accurately measuring the change of stresses acting on the lining due to the applied load. The lack of field data results in performing merely theoretical analysis.

Figure 2.31a shows the case of interest where a point load (W) is applied on the surface. The total vertical load at the crown in an infinite elastic medium can be estimated using Boussinesq's coefficient (N) and chart in Figure 2.31b. The total vertical load at the crown (P_{crown}) will be the sum of the soil's weight (P_{soil}) and the contribution of the point load at the crown ($P_{surface\ load}$).

$$P_{crown} = P_{soil} + P_{surface\ load} \tag{2.31}$$

If the soil profile consists of n layers then the overburden weight will be the sum of the weights imposed by every medium. Equations 2.32 and 2.33 express $P_{surface\ load}$ in

terms of stress and the Boussinesq's coefficient N respectively:

$$\sigma_{surface\ load} = \frac{NW}{C^2} \tag{2.32}$$

$$N = \frac{3\left(\frac{C}{R}\right)^5}{2\pi} \tag{2.33}$$

$$R = \sqrt{T^2 + C^2} \tag{2.34}$$

where R is the distance between the point load in the ground and the crown, C is the cover of the soil and T is the horizontal distance between the projection of the load in the ground and the crown (Figure 2.31).

In the case of a uniformly rectangular surface loaded area a different approach is adopted. The loaded area is divided into small sections and then integrated to obtain the total effect at the crown. Newmark performed such an analysis and provided analytical solutions in the case where L > B (Fig. 2.32a). The vertical stress at the crown (σ_{crown}) below the corner of the loaded area is:

$$\sigma_{crown} = M_N q \tag{2.35}$$

where M_N is Newmark's coefficient, which can be estimated from the chart of Figure 2.32b and q is the surface load.

Moore (1987b) described a semi-analytical solution that makes use of the Boussinesq method and other closed form solutions to estimate the deformation of a buried pipe (rather than a tunnel) in an infinite elastic medium due to surface loading. Boussinesq method does not account for the effect of shear stresses and strains developing in the overlying strata. It is only applicable in an infinite elastic medium and does not take into account the interaction between soil and tunnel. 2-D FE analysis therefore was also employed which can allow for these stresses to act in the medium. Provided that realistic elastic ground properties are selected the semi-analytical method compares well with the numerical results. This procedure can be used for estimations of hoop forces, bending moments and ring deformations. Clearly there are problems however with the assumption of elastic ground.

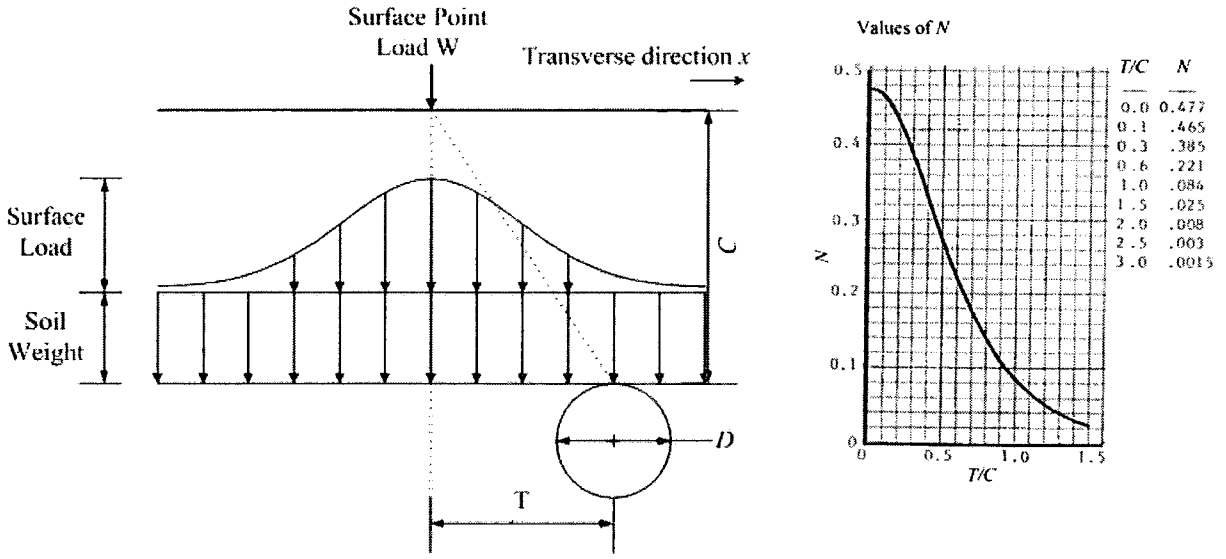

a) Point load (W) acting at a distance T from the crown

b) Boussinesq's chart for N

Figure 2.31. Surface point load and Boussinesq's chart (After Watkins and Anderson, 2000).

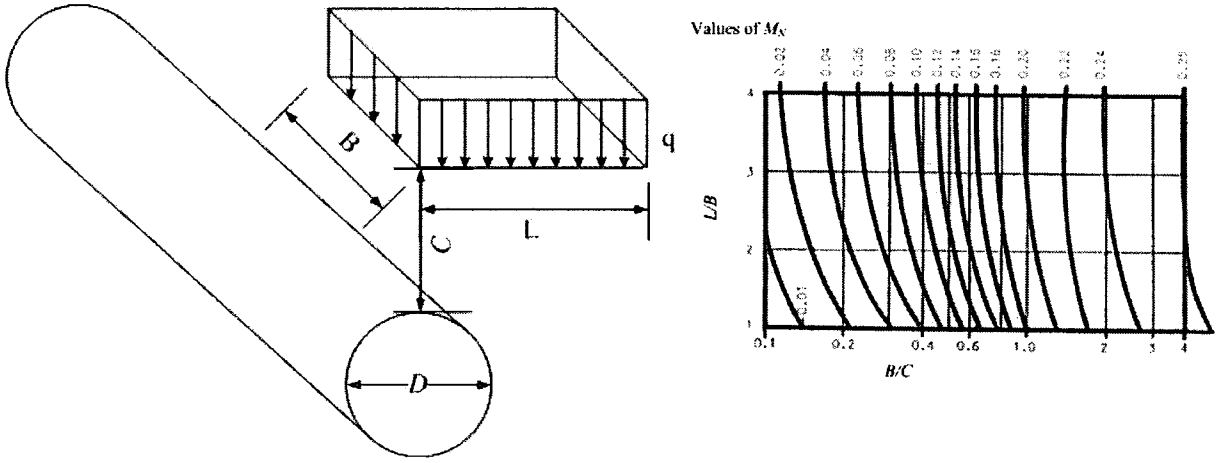

a) Rectangular surface loaded area acting above the tunnel

b) Newman's chart for M_N

Figure 2.32. Rectangular loaded surface area and Newman's chart (After Watkins and Anderson, 2000).

Moore and Brachman (1994) performed a 3-D FE analysis on the same problem described by Moore (1987b). The current method makes use of a 2-D FE mesh along the transverse x-axis and Fourier integral along the longitudinal y-axis. Firstly it was successfully tested to a problem with known solution. Then it was used to estimate thrusts from a case study. The theoretical data presented are in agreement with field data from the same site. The use of 3-D analysis further improved the accuracy of the thrust estimates compared to 2-D analysis.

Abdel-Meguid *et al.* (2002) performed 2-D and 3-D non-linear elastic perfectly plastic (Mohr-Coulomb soil model) FE analyses to model twin tunnel construction (D = 4.9m) in four stages followed by excavation of an inclined surface profile (tunnel unloading). Twenty-noded brick elements were used to model both soil and lining elements. Excavation was modelled by adopting the element removal technique described by Brown and Booker (1985). This study examines exactly the opposite problem from the one of interest (tunnel unloading). A case study from York-Mills Centre project in Toronto is used to compare the numerical results. Once more the importance of carrying out 3-D analysis (rather than 2-D) became evident since the outcome from such simulation was closer to field data (Table. 2.2). Another interesting point was that the 3-D predictions regarding surface deformation and lining distortion were almost half of the 2-D estimates. Similar conclusions were drawn from Dasari *et al.* (1996).

	2D analysis*		3D analysis*		Measured	
Point of interest	South-bound	North-bound	South-bound	North-bound	South-bound	North-bound
Maximum heave (mm)	38	39	17	18	15	17
Crown-invert Extension (mm)	6	7	5	6	4	4
Spring-line Closure (mm)	9	10	4	5	3.5	4.4

* Deformation resulting from tunnel construction is subtracted for comparison purpose.

Table 2.2. Predicted and measured maximum deformations (From Abdel-Meguid *et al.*, 2002).

Spasojevic *et al.* (2007) carried out a small scale physical model testing to study the effects of surface loading above pipes driven in sand. The data from the centrifuge tests showed that the deformations of the liner were just 0.1% of the diameter, in the case where the load resembled the weight of a heavy vehicle. Hence, only a negligible amount of the total surface load was transferred to the pipe.

Summary

In this section the most important features regarding the lining distortions due to gravity and surface loading are summarised:

- Various empirical and analytical methods exist to calculate the stresses which act upon a tunnel liner due to the overburden weight. It has been reported though that the methods which consider the full overburden weight are conservative since only the 50% to 70% of the soil's weight is transferred to the tunnel's liner even after 20 years.
- In order to calculate the initial ground stresses an appropriate value of the earth pressure at rest should be chosen. For normally consolidated clays the vertical stress is bigger than the horizontal ($K_0 < 1$). For over-consolidated clays though $K_0 > 1$, which implies that the vertical stress is smaller than the horizontal, contrary to the field measurements.
- Not many recorded data exist referring to the case of surface loading above tunnels in soft ground. Analytical methods of calculating the transfer of load from the surface to the crown (e.g. Boussinesq method) fail to make accurate predictions since they do not account for the interaction or the shear stress and they refer to an elastic medium. The use of the FEM overcomes these difficulties.

Chapter 3

Implementation of the FEM on tunnelling related problems

3.1 Introduction

In this chapter the fundamental concepts of the finite element method (FEM) are presented along with its applications to tunnelling related problems. A comparison with other numerical methods takes place in the first section followed by a brief history of the FEM. The governing equations and formulation in general, which are used to perform the finite element calculations, are then presented. Finally, important aspects of the FEM dealt with by the author during the analyses performed in Chapters 6 and 7 are discussed.

3.2 Difference between FEM and other numerical analysis methods

Numerical analysis consists of various methods, apart from the FEM. Some of the most widely used are: *i*) the finite difference method (FDM), *ii*) the boundary element method (BEM), *iii*) the discrete (or distinct) element method (DEM) and finally the most recent, and of great potential in the future, *iv*) the meshless or mesh free method (MFM).

The basic idea in the FDM is to make approximations of the partial differential equations by using finite difference equations at intersection points throughout the

generated grid. This method is used in solving flow problems (i.e. fluid dynamics) for instance. The current method has two major limitations. The first is that equal size of elements has to be generated. Thus unlike the FEM, the grid does not consist of areas or volumes of different density. Hence, instead of refining just around areas of interest, the whole grid has to be refined which makes this method computationally expensive for large problems. The second limitation refers to the restricted choice of constitutive models available.

In BEM only the boundaries (in 2-D analysis) or surfaces (in 3-D analysis) of the domain need to be subdivided, rather than the whole domain as in FEM, by using partial differential equations. In the following step, closed form solution is applied to each line or element. Usually, the formed matrices, which have to be solved, are not symmetric. Hence the matrices are full of coefficients (i.e. not sparse). Direct or iterative methods may be used to solve the system. The use of such methods confines BEM to solving small size problems. For large problems the computational time required to produce a solution is still prohibitive.

The DEM is employed to model movements of inter-connecting rigid blocks along their common surfaces by assuming an initial velocity. Forces such as friction, gravity and dumping, are then calculated at the joints of adjacent blocks following Newton's laws. The sum of these forces will define the total force vector (magnitude and direction) per block. These forces become zero in the case where the elements are no longer in contact. Solution to problems related to large scale translation and rotation is derived in a series of time steps using interpolation methods. DEM requires less computer storage to be used but is very expensive in terms of computational time, compared to the FEM.

Meshless or Mesh Free Method (MFM) is a relatively new and vastly expanding method which is used to solve linear and non-linear static or dynamic types of stress analysis similar to the FEM. The difference is that there is no need to discretise the problem domain. Instead, a set of nodes randomly distributed within the domain and on its boundaries is used to represent the investigated problem. The relation between these nodes does not have to be specified, which means that they are independent of one another. Thus the user can add, delete or transfer nodes during the procedure. The next stages (i.e. analysis and post-processing) are similar to the FEM. MFM is proven

to be time and cost saving since meshing during the pre-processing stage is omitted. However, there are issues which have not been persuadably dealt with such as modelling the interfaces and the shape functions used.

3.3 History of the FEM

The FEM as used in this research is a numerical analysis procedure for elastostatics. A German mathematician, Richard Courant (1888-1972), was the first who thought of discretising a continuum in triangular elements to deal with the torsion problem (Courant, 1943). The proposed technique was further developed during the 1960s by engineers, especially in the aerospace field. Turner *et al.* (1956) were the first to derive solutions for plane stress problems which were discretised into triangular elements. The properties of these elements were determined using the theory of elasticity. Clough (1960) was the first to actually introduce the term "finite element method" (Huebner *et al.*, 1995).

Engineers from every field, not just civil and aerospace, soon realised the potential of this method and it hence became one of the most widely used, flexible and efficient tools for prediction. The existence of specialised FE software along with available computer resources further contributed to its widespread use.

3.4 How the method works

The following steps are involved in the analysis of any continuum problem when using the FEM:

- Element discretisation
- Interpolation functions
- Element equations
- Global equations
- Boundary conditions
- Solution

The above six steps are presented in detail in the following sections.

3.4.1 Element discretisation

The geometry of the boundary problem which is under investigation is sub-divided into a series of smaller regions which are called "*finite elements*". These finite elements are connected to each other at key points called "*nodes*". The simplest forms of finite elements have straight sides and nodes located only at the vertices. 2-D elements of this type (usually called "*linear*" elements) are: *i*) three-noded triangles and *ii*) four-noded quadrilaterals. For curved sides (or straight sides with an increased required accuracy) additional nodes are required which are usually placed in the middle of each curved side. These are termed "*quadratic*" elements. The equivalent types are: *i*) six-noded (three nodes at corners and three nodes at mid-side) triangles and *ii*) eight-noded (4 nodes at corners and 4 nodes at mid-side) quadrilaterals. Finite elements can be further classified (apart from linear and quadratic) into those containing external nodes only (which lie on the sides and are connected to other elements) and those containing internal nodes (which do not connect with other elements). An example of such an element is the fifteen-noded triangle.

For the 2-D analyses presented in this thesis six-noded and the fifteen-noded triangular elements were used to model the soil in Strand7 and Plaxis respectively. The structural components (i.e. tunnel lining) were modelled with two-noded beam elements in both computer programs. For the 3-D analyses (using Strand7 only) ten-noded tetrahedral elements were used to model the soil and six-noded thin shell elements for the tunnel liner.

In this first step the FE user has to make sure that the proper type and size of elements are used. Thus engineering judgement along with expertise from published research is required.

3.4.2 Interpolation function

In the second step the primary variable [In geotechnical engineering the primary variable is usually chosen to be the displacements (u, v) for 2-D and (u, v, w) for 3-D] is interpolated through appropriate polynomial functions to every finite element of the generated mesh. The order of the polynomial depends on the number of nodes used in the finite element. Thus, for a linear element the displacement varies linearly across

the element while for a quadratic element it varies quadratically. For simplicity purposes only the polynomials used for the three-noded triangles (Eq. 3.1) in x, y space (see Figure 3.1) will be presented. These are of the following form:

$$\begin{aligned} u &= \alpha_1 + \alpha_2 x + \alpha_3 y \\ v &= \beta_1 + \beta_2 x + \beta_3 y \end{aligned} \tag{3.1}$$

where: α_i and β_i are constant coefficients. By substituting the nodal coordinates into Equation 3.1 the interpolation functions for each node can be expressed in terms of nodal displacements:

$$\begin{aligned} u_1 &= \alpha_1 + \alpha_2 x_1 + \alpha_3 y_1 \\ u_2 &= \alpha_1 + \alpha_2 x_2 + \alpha_2 y_2 \\ u_3 &= \alpha_1 + \alpha_2 x_3 + \alpha_3 y_3 \\ \\ v_1 &= \beta_1 + \beta_2 x_1 + \beta_3 y_1 \\ v_2 &= \beta_1 + \beta_2 x_2 + \beta_2 y_2 \\ v_3 &= \beta_1 + \beta_2 x_3 + \beta_3 y_3 \end{aligned} \tag{3.2}$$

Equation 3.2 can be solved for the constants α_i and β_i:

$$\begin{aligned} \alpha_1 &= \frac{u_1(x_2 y_3 - y_2 x_3) + u_2(x_3 y_1 - x_1 y_3) + u_3(x_1 y_2 - x_2 y_1)}{2\Delta} \\ \alpha_2 &= \frac{u_1(y_2 - y_3) + u_2(y_3 - y_1) + u_3(y_1 - y_2)}{2\Delta} \\ \alpha_3 &= \frac{u_1(x_3 - x_2) + u_2(x_1 - x_3) + u_3(x_2 - x_1)}{2\Delta} \end{aligned} \tag{3.3}$$

$$\text{where } 2\Delta = \begin{vmatrix} 1 & x_1 & y_1 \\ 1 & x_2 & y_2 \\ 1 & x_3 & y_3 \end{vmatrix} = 2 \text{ (area of triangle with vertices 1, 2, 3)} \tag{3.4}$$

Combining Equations 3.1 and 3.3:

$$u = \frac{b_1 + c_1 x + d_1 y}{2\Delta} u_1 + \frac{b_2 + c_2 x + d_2 y}{2\Delta} u_2 + \frac{b_3 + c_3 x + d_3 y}{2\Delta} u_3 \tag{3.5}$$

where:

$$\begin{aligned} b_1 &= x_2y_3 - x_3y_2 \quad c_1 = y_2 - y_3 \quad d_1 = x_3 - x_2 \\ b_2 &= x_3y_1 - x_1y_3 \quad c_2 = y_3 - y_1 \quad d_2 = x_1 - x_3 \\ b_3 &= x_1x_2 - x_2x_1 \quad c_3 = y_1 - y_2 \quad d_3 = x_2 - x_1 \end{aligned} \tag{3.6}$$

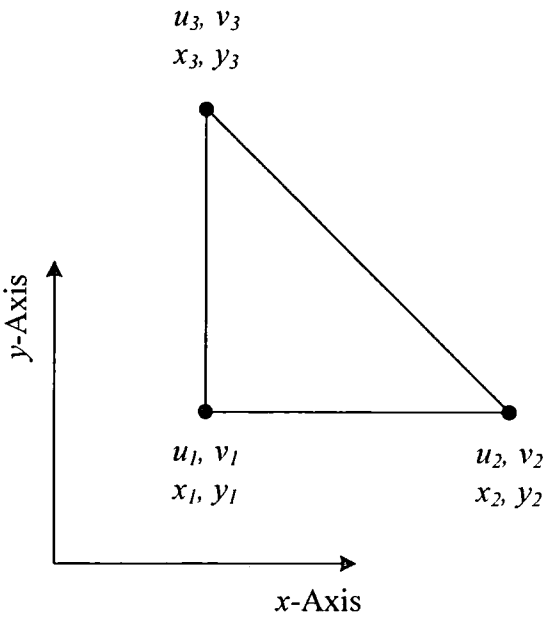

Figure 3.1. Three-noded triangle.

Similar set of equations to Equations 3.3 and 3.5 can be derived for β_i and v respectively (see Eq. 3.2). Expressed in simpler matrix format the following set of equations is produced:

$$\begin{Bmatrix} u \\ v \end{Bmatrix} = [N] \begin{Bmatrix} u_1 \\ v_1 \\ u_2 \\ v_2 \\ u_3 \\ v_3 \end{Bmatrix} \quad \text{or} \quad \{d_E\} = [N]\{d_N\} \tag{3.7}$$

where

$$[N] = \begin{bmatrix} N_1 & 0 & N_2 & 0 & N_3 & 0 \\ 0 & N_1 & 0 & N_2 & 0 & N_3 \end{bmatrix} \tag{3.8}$$

where $\{d_E\}$ provides the displacements of the finite element, $[N]$ is the interpolation

function matrix (or shape function matrix) and $\{d_N\}$ is the vector of nodal displacements. Hence, the displacement field of an element is expressed in terms of nodal displacements. From Equation 3.5 N_1, N_2, N_3 are defined as:

$$N_1 = \frac{b_1 + c_1 x + d_1 y}{2\Delta}, \quad N_2 = \frac{b_2 + c_2 x + d_2 y}{2\Delta}, \quad N_3 = \frac{b_3 + c_3 x + d_3 y}{2\Delta} \tag{3.9}$$

The corresponding strains $\{\varepsilon_E\}$ in the element for a plane strain problem can then be derived from the following equations:

$$\varepsilon_x = \frac{\partial u}{\partial x}, \quad \varepsilon_y = \frac{\partial v}{\partial y}, \quad \gamma_{xy} = \frac{\partial u}{\partial y} + \frac{\partial v}{\partial x} \tag{3.10}$$

or given in matrix format:

$$\begin{Bmatrix} \varepsilon_x \\ \varepsilon_y \\ \gamma_{xy} \end{Bmatrix} = \{\varepsilon_E\} = [S]\{d_E\} = [S][N]\{d_N\} = [B]\{d_N\} \tag{3.11}$$

where: $[S]$ is a differential operator matrix and $[B]$ is the strain-displacement matrix. $[S]$ and $[B]$ are given by the following Equations 3.12 and 3.13:

$$[S] = \begin{bmatrix} \frac{\partial}{\partial x} & 0 \\ 0 & \frac{\partial}{\partial y} \\ \frac{\partial}{\partial y} & \frac{\partial}{\partial x} \end{bmatrix} \tag{3.12}$$

$$[B] = \begin{bmatrix} \frac{\partial N_1}{\partial x} & 0 & \frac{\partial N_2}{\partial x} & 0 & \frac{\partial N_3}{\partial x} & 0 \\ 0 & \frac{\partial N_1}{\partial y} & 0 & \frac{\partial N_2}{\partial y} & 0 & \frac{\partial N_3}{\partial y} \\ \frac{\partial N_1}{\partial y} & \frac{\partial N_1}{\partial x} & \frac{\partial N_2}{\partial y} & \frac{\partial N_2}{\partial x} & \frac{\partial N_3}{\partial y} & \frac{\partial N_3}{\partial x} \end{bmatrix} \tag{3.13}$$

The corresponding stresses $\{\sigma_E\}$ in the element for the same plane strain approximation will be:

$$\begin{Bmatrix}\sigma_x\\ \sigma_y\\ \tau_{xy}\end{Bmatrix} = \{\sigma_E\} = [D]\{\varepsilon_E\} \tag{3.14}$$

where $[D]$ is the constitutive matrix which for isotropic linear elasticity will be given by Equation 3.15.

$$[D] = \frac{E}{(1+v)(1-2v)}\begin{bmatrix} 1-v & v & 0 \\ v & 1-v & 0 \\ 0 & 0 & \frac{1-2v}{2} \end{bmatrix} \tag{3.15}$$

E and v are the elastic constants (The Young's modulus and the Poisson's ratio respectively).

3.4.3 Element formulation

One of the ways of deriving the FE equations is this. The principle of the minimum potential energy has to be used along with the set of Equations 3.7, 3.11 and 3.14. For an isotropic linear elastic material the total potential energy Π_E will be:

$$\begin{aligned} \Pi_E &= U_E - V_E \\ U_E &= \frac{1}{2}\int\{\varepsilon_E\}^T\{\sigma_E\}dV = \frac{1}{2}\int\{d_N\}^T[B]^T[D][B]\{d_N\}dV \\ V_E &= \frac{1}{2}\int\{d_E\}^T\{f_E\}dV = \frac{1}{2}\int\{d_N\}^T[N]^T\{f_E\}dV \end{aligned} \tag{3.16}$$

where: U_E is the strain energy of the element while V_E is the work done by the applied loads (f_E) on the element, while dV refers to the volume of the element. The principle of the minimum potential energy states that at equilibrium, Π_E = 0. Thus from the set of Equation 3.16 the following can be written:

$$\begin{aligned} &\Pi_E = U_E - V_E = 0 \\ &\frac{1}{2}\int\{d_N\}^T[B]^T[D][B]\{d_N\}dV - \frac{1}{2}\int\{d_N\}^T[N]^T\{f_E\}dV = 0 \\ &\{d_N\}^T\left(\int[B]^T[D][B]dV\right)\{d_N\} = \{d_N\}^T\int[N]^T\{f_E\}dV \\ &[K_E]\{d_N\} = \{F_E\} \end{aligned} \tag{3.17}$$

where: $[K_E] = \int [B]^T [D][B] dV$ which calculates the element stiffness matrix and $\{F_E\} = [N]^T \{f_E\}$ which gives the total load vector for the element.

The element stiffness matrix $[K_E]$ therefore, for a given constitutive matrix $[D]$, depends only on matrix $[B]$, which is a by-product of $[N]$ (from Eq. 3.13). Hence, the interpolation function matrix will determine the element's performance.

3.4.4 Global formulation

The next step is to pass from the element level to the structure level; i.e. having defined the behaviour of the elements through interpolation functions of the nodal displacements, the behaviour of the whole domain should then be evaluated. This is achieved through the following set of equations in matrix format:

$$\{d_G\} = \sum \{d_N\} \qquad [K_G] = \sum [K_E] \qquad \{F_G\} = \sum \{F_E\} \tag{3.18}$$

where: $[K_G]$ is the global stiffness matrix, $\{d_G\}$ is a vector containing the sum of the unknown nodal displacements of the continuum and $\{F_G\}$ is the global load vector. The summations being made over the number of elements. The global equation then can be written as:

$$[K_G]\{d_G\} = \{F_G\} \tag{3.19}$$

The basic idea of the previously described procedure (see Equations 3.1 to 3.19) is that the field variable (i.e. displacements) at a common node between connecting finite elements is the same.

The way the coefficients of the global stiffness matrix $[K_G]$ are stored influences both the amount of time required to run the analysis and the computer resources for storing data. The non-zero coefficients (X in Fig. 3.2) are produced from the connection of degrees of freedom (d.o.f) belonging to the same element or from a common degree of freedom between interconnecting finite elements. Hence, each d.o.f is linked only with a small proportion of the total amount of d.o.f of the problem. Consequently many zero coefficients exist within the $[K_G]$ matrix, located

away from its leading diagonal (Figure 3.2). The matrix therefore is characterised as "*sparse*". The non-zero terms (X) on the other, are located on and around the main diagonal. Thus the matrix is also characterised as "*banded*". If an efficient algorithm is employed for node freedom numbering then the bandwidth (Figure 3.2) can be minimised. In this case computer resources for storing the matrix can be reduced. All commercial FE software can perform this process automatically to optimise storage (i.e. reduce bandwidth).

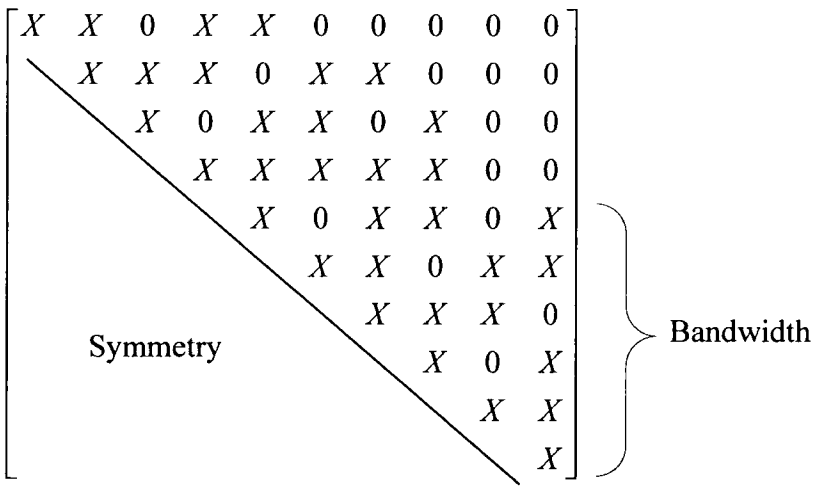

Figure 3.2. Schematic representation of the global stiffness matrix $[K_G]$. X stands for the non-zero terms.

3.4.5 Boundary conditions

A final step is necessary prior to the solution of the global equations (Equation 3.19). Boundary conditions must be imposed on the global equations in order to prevent rigid body movements. This is achieved by prescribing nodal displacements. If not, the global stiffness matrix $[K_G]$ will become non-invertible (i.e. singular). At this case the system of the global equations cannot be solved.

3.4.6 Solution

The primary unknown of the global equation is the vector $\{d_G\}$ containing the nodal displacements of the domain. Therefore, in order to solve Equation 3.19 an invertible matrix has to be created so that:

$$[K_G]^{-1}[K_G]\{d_G\} = [K_G]^{-1}\{F_G\} \tag{3.20}$$

In practise inverses are never found due to the computational cost. Other methods are used instead to solve the linear system in Equation 3.20. These methods can be broadly categorised into direct and iterative.

Direct or iterative methods may be used to solve a linear set of global equations with symmetric or un-symmetric matrices. Direct methods convert $[K_G]$ to an upper triangular and then back-substitute to obtain the solution. The most widely used direct method for solving a set of linear equations is the *Gaussian elimination*. Both Strand7 and Plaxis use this solution technique when a continuum behaves in a linear elastic way. From the set of Equations 3.17 it is clear that $[K_E]$ and hence $[K_G]$ depends on the constitutive matrix $[D]$. This implies that the constitutive model used to describe the behaviour of the continuum affects the order of the system of equations within $[K_G]$ and thus the strategy of the solution. In the case of linear elasticity, the constitutive and the global stiffness matrices are formed by linear systems of equations and they are constants throughout the analysis stage.

Iterative methods on the other hand are rarely preferred for small systems of equations. The reason is that it takes longer than the *Gaussian elimination* method to derive a solution. For larger problems though, iterative methods are often more efficient. The basic idea of the iterative methods is that an initial approximation to the solution is made, which is then improved by successive iterations until convergence according to some predefined measure. In both Strand7 and Plaxis, iterative solver has been used.

Until now, the constitutive matrix $[D]$ and hence the global stiffness matrix $[K_G]$ were supposed to be constants; meaning that the constitutive model used to describe the material behaviour was linear elasticity. However, soil behaviour is described more accurately and realistically through non-linear constitutive models. Consequently, $[D]$ and $[K_G]$ are formed by non-linear types of equations and vary with stress or strain levels throughout the analysis. Thus, different approaches should be incorporated to solve the global equations. This is usually dealt with by analysing as a series of linear increments so that the set of global equations is solved for each

increment:

$$[K_G]_i\{d_G\}_i = \{F_G\}_i \tag{3.21}$$

where: $\{d_G\}_i$ is the incremental form of the unknown nodal displacements vector, $[K_G]_i$ is the incremental form of the global stiffness matrix and $\{F_G\}_i$ is the incremental form of the global load vector. By adding the solution for each increment i the final solution can be derived. A number of solution techniques are available. However only that implemented into the two commercial FE programmes used for this research (i.e. Strand7 and Plaxis) is briefly described hereafter.

The *Modified Newton Raphson* technique is used in both Strand7 and Plaxis to deal with the solution of non-linear equations in the global stiffness matrix. In this technique, an initial approximation is made for the solution (curved thick line in Figure 3.3), knowing that this will not be exact. Thus an error $\{F_G\}_{i,1}$ is involved during the first approximation. A new approximation takes place and the new error during the second iteration $\{F_G\}_{i,2}$ is estimated (i.e. the incremental load vector, see Figure 3.3) within the i increment. From that, the incremental displacement vector per iteration $\{d_G\}_{i,2}$ is hence estimated. Solution converges after a series of successive iterations, as these vectors decrease enough in order to be within prescribed tolerance. The amount of time required for convergence depends on the size of the problem (i.e. size of the global stiffness matrix), the number of iterations and finally the load step (i.e. error approximation). A drawback of the original *Newton Raphson* scheme is that $[K_G]_i$ is not constant within every iteration. This proves to be computational costly in terms of the required time to recalculate $[K_G]_i$ for each iteration. This prompted to the *Modified Newton Raphson* scheme where $[K_G]_i$ is constant at every iteration. (Huebner *et al.*, 1995)

3.5 Constitutive models

One aspect of importance for FE analysis in soils is the appropriate choice of a constitutive model which will best describe the real behaviour of soil or structural components. In this thesis all structural components (i.e. tunnel lining) throughout the

analyses were assumed to behave in a linear elastic way regardless of the dimension of the analysis (2-D or 3-D) and the software used (Strand7 or Plaxis). On the other hand, simple elasto-plastic models were employed to model soil behaviour. The constitutive models used in this thesis are presented in the following sections.

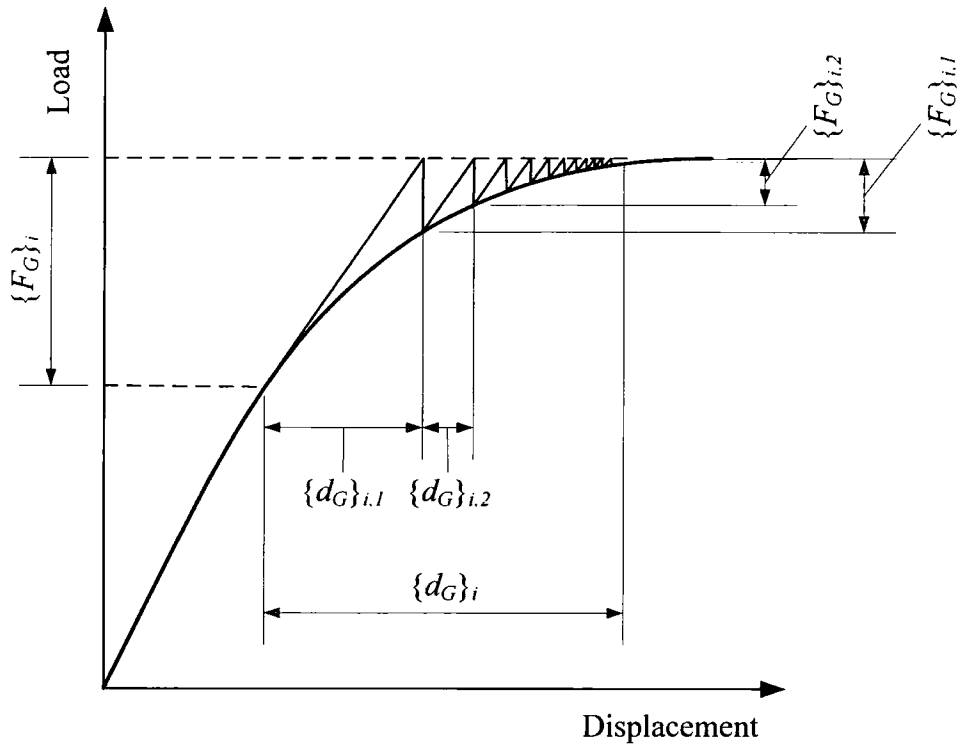

Figure 3.3. The Modified Newton-Raphson solution technique.

3.5.1 Elastic pre-yield models

Curved beam elements are used in the plane strain 2-D FE analyses using Plaxis to model the tunnel liner. This structural material behaves under the generalised Hooke's law[2] in an *isotropic linear elastic* way. In order to be fully determined, this model requires two elastic properties to be specified: e.g. the Young's modulus E and the Poisson's ratio v. The term *isotropic* implies that both of these elastic moduli are the same in all directions. The term *linear* denotes that the elastic properties are constant. Finally the term *elastic* denotes the way the tunnel liner deforms when it is unloaded.

[2] Hooke's law focuses on springs rather than continuum bodies and states that the force needed to elongate a spring is a linear function of the elongation. The generalised Hooke's law in continuum mechanics relates the strains with the stresses with a linear function.

Two-noded beam elements and six-noded triangular thin shell elements are used to model the structural components of the tunnel liner in 2-D and 3-D FE analyses respectively using Strand7. In both cases the same assumption, of *isotropic linear elasticity* was assumed, similar to the Plaxis modelling.

3.5.2 Simple elasto-plastic models

Fifteen-noded triangular finite elements are used in the 2-D FE analyses performed by Plaxis to model soil. A simple elasto-plastic constitutive soil model is used for this purpose. For elasto-plastic models the following three concepts of the theory of plasticity (Calladine, 1969) have to be defined:

- **A yield function** F_Y. A yield function has to be defined which indicates when the material becomes plastic.

$$F_Y(\{\sigma\},\{m_Y\}) = 0 \tag{3.22}$$

where F_Y is a scalar function of stress $\{\sigma\}$ and state parameter $\{m_Y\}$. Three distinct cases can be identified: *i*) when $F_Y < 0$ then the material behaves in a purely elastic behaviour, *ii*) when $F_Y = 0$ then the material becomes plastic and finally *iii*) the case where $F_Y > 0$ is impossible (Potts and Zdravkovic, 1999).

- **A plastic potential function** F_P. This function determines the direction of plastic straining at every stress state by means of the flow rule.

$$\varepsilon_i^p = \Lambda \frac{\partial F_P(\{\sigma\},\{m_P\})}{\partial \sigma_i} \tag{3.23}$$

where ε_i^p is the incremental plastic strain, Λ is a scalar multiplier and m_P is a vector of state parameters. Two distinct cases can be identified: *i*) the general case where $F_P \neq F_Y$. Then the flow rule is termed as non-associated and *ii*) the unique case where $F_P = F_Y$. The flow rule is termed as associated.

- **Hardening/Softening rules**. These rules indicate the way the state parameters vary with plastic straining. Two distinct cases can be identified: *i*) when the state

parameters vary with plastic straining, then hardening/softening occurs (Figures 3.4a and 3.4b) and *ii*) when the state parameter is constant, then perfect plasticity occurs (Figure 3.4c).

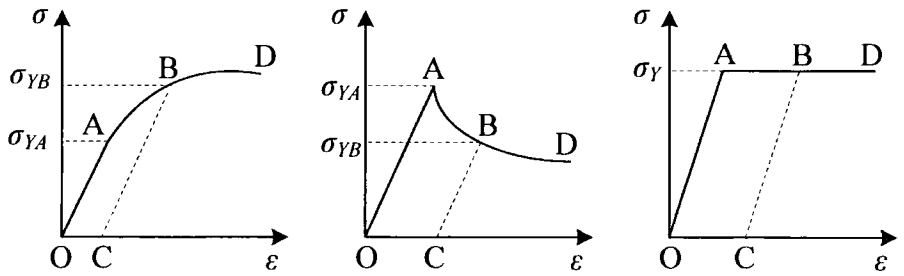

Figure 3.4. Different types of simple elasto-plastic soil behaviour under uniaxial loading.

In order to model the plastic region Plaxis provides different material models to choose from such as: *i*) the Mohr-Coulomb model, *ii*) the Soft soil model and *iii*) the Hardening soil model (described later in this section). From these, the Mohr-Coulomb model was chosen to perform the analyses in this thesis. This constitutive model can simulate soil behaviour by initialising four to five parameters, in a simple way. More sophisticated constitutive models have been developed in an attempt to simulate soil behaviour more accurately and realistically (e.g. anisotropic models, kinematic yield surface models). However, these require usually more than five parameters to be defined, some of which are extremely difficult to obtain. As a result, the frequent use of such complicated constitutive models is often prohibitive. This is why up to date most FE users in industry prefer to make use of the simple elasto-plastic soil models and Mohr-Coulomb in particular even though there are a couple of well known and identified problems. These will be discussed later in this section.

Six-noded triangles and ten-noded tetrahedra are used to model soil when conducting 2-D and 3-D FE analyses respectively in Strand7. For the plastic region Strand7 offers a variety of constitutive models to choose from (e.g. Tresca, Von Mises, Mohr-Coulomb and Drucker-Prager which are briefly described later in this chapter). From this list, the Mohr-Coulomb model was employed for consistency with the Plaxis analyses. In this way, comparison between the predictions of the two FE programs was possible.

The Mohr-Coulomb failure criterion is described by Equation 3.24 which is written in terms of effective stresses:

$$\tau = c' + \sigma' \tan\varphi' \tag{3.24}$$

where: τ and σ' are the shear and normal effective stresses respectively on the failure plane (see Figure 3.5a) while c' and φ' are the strength parameters, cohesion and angle of friction respectively.

The behaviour of an isotropic linear elastic plastic hardening material under uniaxial loading is presented in Figure 3.4a. When the material is loaded elastic behaviour occurs along the OA line. If the value of σ_{YA} (yield stress at point A) is exceeded then the yield stress increases to σ_{YB} (contrary to the perfectly plastic case where the yield stress is not increased) with $\sigma_{YA} < \sigma_{YB}$, and plastic straining occurs (OC). If the material is unloaded then elastic behaviour occurs along the BC line which is parallel to the OA line. As the stress increases to point D then the curve becomes horizontal and the stress becomes constant.

The behaviour of an isotropic linear elastic plastic softening material under uniaxial loading is presented in Figure 3.4b. Similar behaviour to the plastic hardening material occurs, only this time when σ_{YA} is exceeded the new yield stress decreases to σ_{YB} (this time $\sigma_{YA} > \sigma_{YB}$). Once more the curve becomes horizontal at D where the stress becomes constant.

3.5.3 Discussion of the Mohr-Coulomb model

The yield surface of the Coulomb failure criterion is described by Equation 3.24. This can be re-written as follows (see Craig, 1992, pp. 102-103):

$$\begin{aligned} &\sigma_1' - \sigma_3' = 2c'\cos\varphi' + (\sigma_1' + \sigma_3')\sin\varphi' \\ &F_Y(\{\sigma'\},\{m_Y\}) = \sigma_1' - \sigma_3' - 2c'\cos\varphi' - (\sigma_1' + \sigma_3')\sin\varphi' = 0 \end{aligned} \tag{3.25}$$

where: $F_Y(\{\sigma'\},\{m_Y\}) = 0$ is the yield function of the Coulomb failure criterion depending on the state of stress (σ') and the state parameter m_Y. From Equation 3.25 it can be seen that the latter parameter is related to the following two strength

parameters: cohesion and the angle of friction. Since Mohr-Coulomb is a perfectly plastic model (no hardening/softening rules) the state parameter is constant. Hence c' and φ' are constants regardless of the changes of stress or strain. Equation 3.25 forms an irregular hexagonal cone if plotted in the principal effective stress space (see Figure 3.5b). Figure 3.9 projects the same yield function $F_Y(\{\sigma'\},\{m_Y\})=0$ to the deviatoric plane (i.e. normal to the space diagonal where $\sigma'_1=\sigma'_2=\sigma'_3$).

To fully describe this simple elasto-plastic model the plastic potential function has to be specified. The state parameter m_P is related to the cohesion, the angle of friction and the angle of dilation ψ'. If *associated flow* is adopted then the plastic potential function is the same with the yield function (i.e $F_P(\{\sigma'\},\{m_P\})=F_Y(\{\sigma'\},\{m_Y\})$). This implies that the state parameters are also the same (i.e. $m_Y=m_P$). Hence, $\varphi'=\psi'$. This unique case has two serious disadvantages regarding the proper modelling of soil behaviour. The first is that the prescribed value of ψ' is unrealistic (i.e. larger) in most cases compared to real soil behaviour. The second is that if associated flow is adopted then soil will dilate for ever (Potts and Zdravkovic, 1999). By adopting a *non-associated flow*, the plastic potential function resembles to the yield function (but they are no longer equal).

$$\begin{aligned} &F_Y(\{\sigma'\},\{m_Y\})\neq F_P(\{\sigma'\},\{m_P\}) \\ &m_Y\neq m_P \\ &\varphi'\neq\psi' \end{aligned} \qquad (3.26)$$

Hence, the first of the two previously mentioned problems, associated with the value of ψ', is partly solved, since $\varphi'\neq\psi'$ with $0<\psi'<\varphi'$. Another problem arises however, since the predicted values of the new plastic volumetric strain keep increasing as long as the soil yields. This is in contrast to the real soil behaviour. To address the second problem, one strategy could be a strain dependent angle of dilation. The commercial FE packages used in this thesis do not however offer this option.

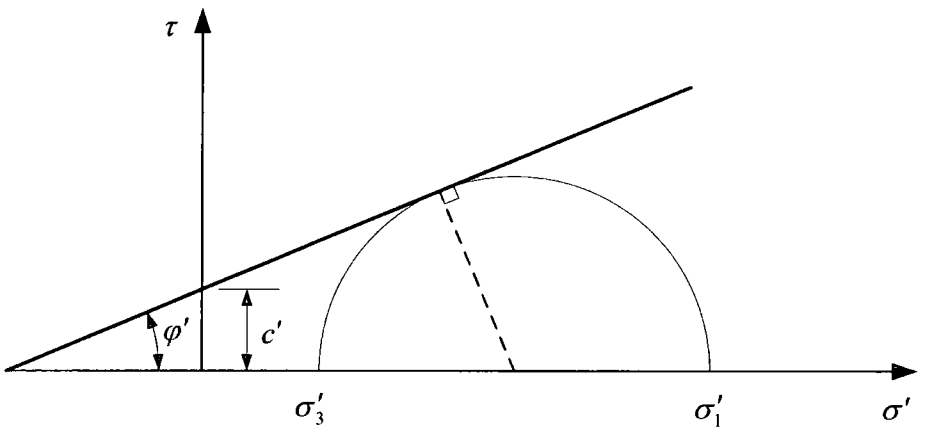

a) Mohr-Coulomb failure criterion.

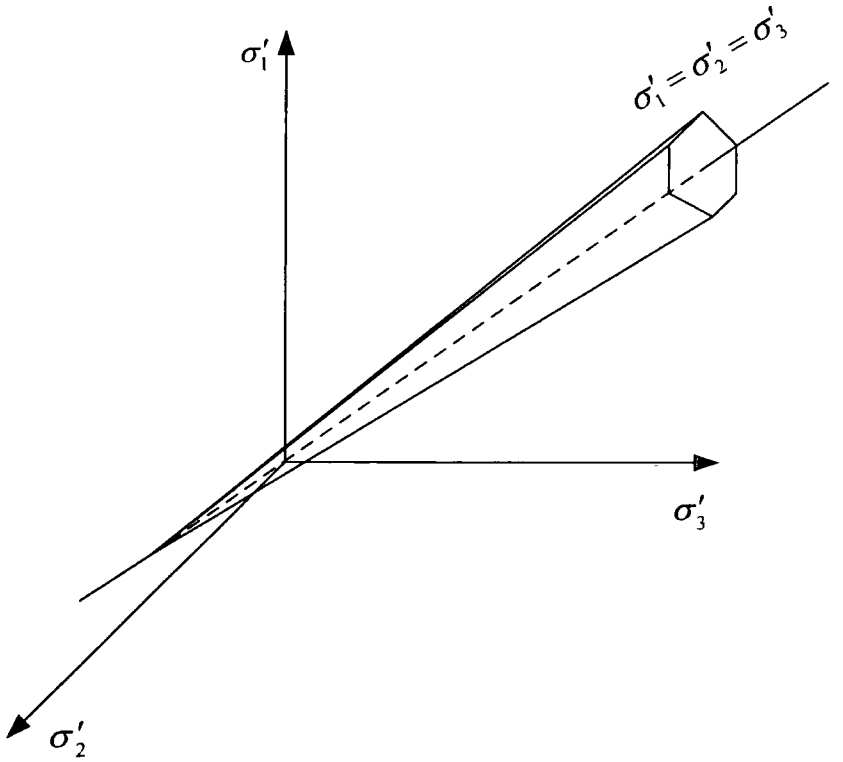

b) Mohr-Coulomb yield surface (After Potts and Zdravkovic, 1999)

Figure 3.5. Mohr-Coulomb model.

Thus, for the Mohr-Coulomb soil model, two properties need to be specified for the elastic region of the deformations. These are the Young's modulus E' and the Poison's ratio v'. For the plastic region three distinct cases exist:

i. For the case of an *associated flow* where $\varphi' = \psi'$, only two parameters need to be specified; i.e. c' and φ',

ii. For the case of *non-associated flow* where $\varphi' \neq \psi'$ with $0 < \psi' < \varphi'$, three parameters are needed; i.e. c', φ' and ψ'.

iii. Finally for the case where $\psi' = 0$, only c' and φ' need to be known.

Depending on the type of *flow rule* therefore, four to five parameters need to be specified, for this type of constitutive model. In Plaxis the user has the option of initialising the angle of dilation. Consequently, a linear elastic perfectly plastic constitutive model with non-associated flow is adopted where all five of the above mentioned parameters need to be specified. In Strand7 on the other hand, the user does not have the option of defining the value of the angle of dilation. Therefore an associated flow has to be assumed for the linear elastic perfectly plastic constitutive model. Consequently, just four parameters need to be specified.

So far, a difference in the way the two commercial FE packages model plasticity flow has been highlighted; i.e. Strand7 uses plasticity with associated flow while Plaxis uses plasticity with a non-associated flow. The predictions, from the comparative analyses presented in Chapter 6 between the two packages, should therefore differ, even slightly due to this differentiation.

3.6 Comparison of the Mohr-Coulomb yield surface to other simple elasto-plastic soil models

In the previous section the Mohr-Coulomb soil model was described in detail. In this section a comparison is made between the Mohr-Coulomb and other simple elasto-plastic constitutive models available from Strand7. These however are only briefly described since they were not used. These are: *i*) Tresca, *ii*) Von Mises and finally *iii*) Drucker-Prager. The Tresca yield criterion is best described by the following yield function:

$$F_Y(\{\sigma\},\{m_Y\}) = \sigma_1 - \sigma_3 - 2S_u = 0 \tag{3.27}$$

where σ_1, σ_3 are the maximum and minimum principal total stresses. The state parameter of the yield function is related to the undrained shear strength (S_u). Since Tresca is a perfectly plastic constitutive model, the state parameter and hence the

undrained shear strength are constant. Equation 3.27 shows that only one parameter (S_u) apart from the two elastic constants (E, v) needs to be specified (i.e. a total of three parameters). However, this is a principal total undrained stress analysis. Hence, by default $v = 0.5$. This reduces to two, the required amount of specified parameters. The yield function (Equation 3.27) plotted in the principal total stress space forms a regular hexagonal cylinder (Figure 3.6b) which is symmetric along the $\sigma_1 = \sigma_2 = \sigma_3$ line. Figure 3.7b shows the yield function plotted on the deviatoric plane, showing corners. This can prove to be a difficult task to handle in numerical analysis, since the differentials are not unique at the corners (singularities at the yield function).

The Von Mises constitutive model is considered to be an improvement to the previous. The yield function is similar to Equation 3.27. As with the Tresca criterion, only two parameters need to be specified. The plot of the yield function on the principal total stress space though, is a circular cylinder (see Figure 3.7a). Hence, no corners exist, which makes numerical analysis less demanding. Figure 3.7b shows a comparison between these two models when they are plotted on the deviatoric plane. The two Von Mises circles in Figure 3.7b refer to the inscribed and circumscribed circles of the Tresca regular hexagon.

The Mohr-Coulomb failure criterion plots as an irregular hexagonal cone in principal effective stress space (Figure 3.5) In order to overcome the difficulty of the corners (likewise Tresca and Von-Mises models), the Drucker-Prager model was introduced. The latter plots as a cylindrical cone in principal effective stress space (see Figure 3.8). Figure 3.9 depicts the difference between Mohr-Coulomb and Drucker-Prager models when they are plotted on the deviatoric plane. The two Drucker-Prager circles in Figure 3.9 refer to the inscribed and circumscribed circles of the Mohr-Coulomb irregular hexagon. The yield function is similar to the Mohr-Coulomb criterion. Hence, five parameters (two for the elastic region and three for the perfectly plastic) need to be specified. The Drucker-Prager constitutive model is perfectly plastic. Thus, the plastic parameters are not strain controlled but constants.

Tresca and Mohr-Coulomb models are preferred, compared to Von Mises and Drucker-Prager models, by most FE users even though more difficulties arise during their implementation in the FE code. The main reason for this is compatibility with

conventional soil mechanics where Tresca and Mohr-Coulomb are used.

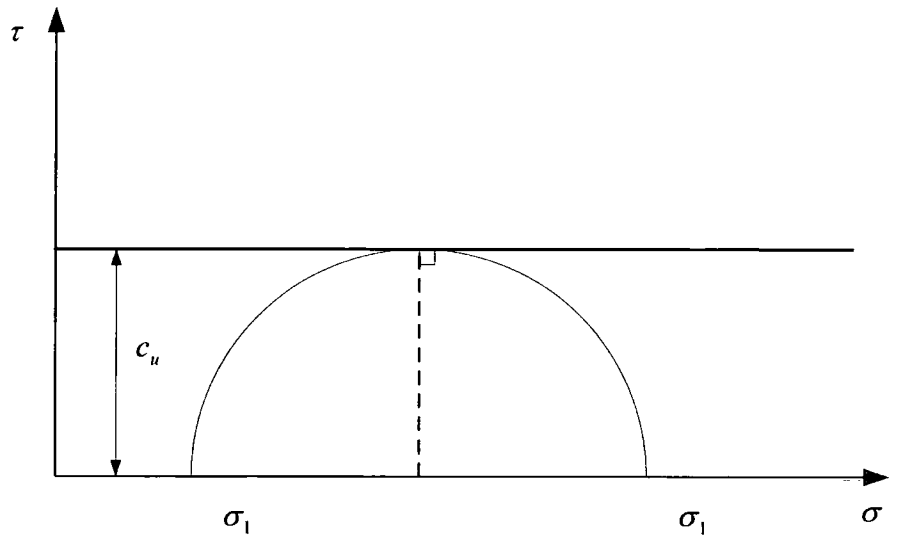

a) Tresca failure criterion

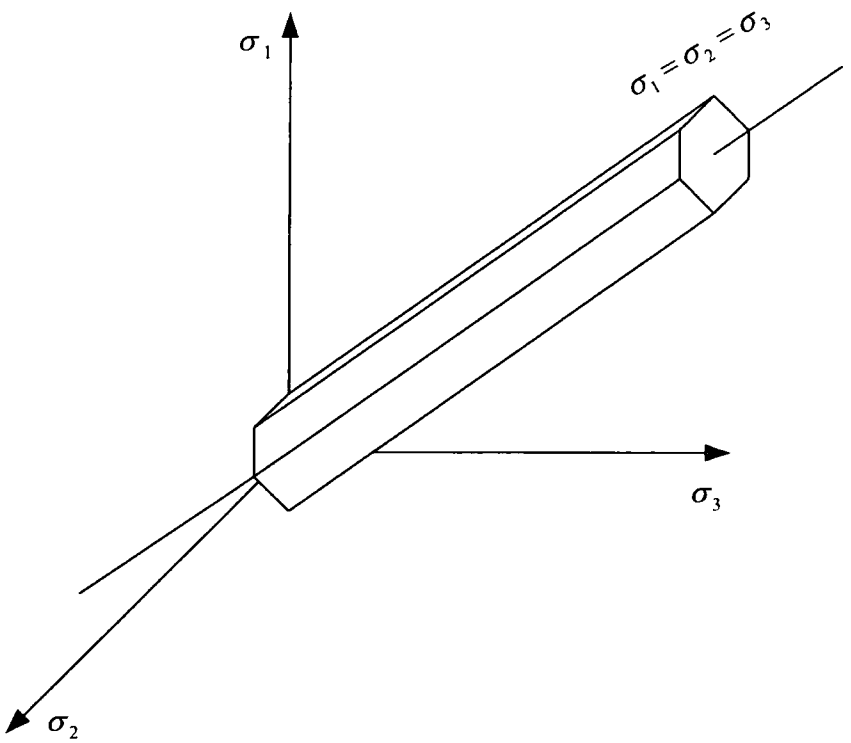

b) Tresca yield surface (After Potts and Zdravkovic, 1999)

Figure 3.6. Tresca model.

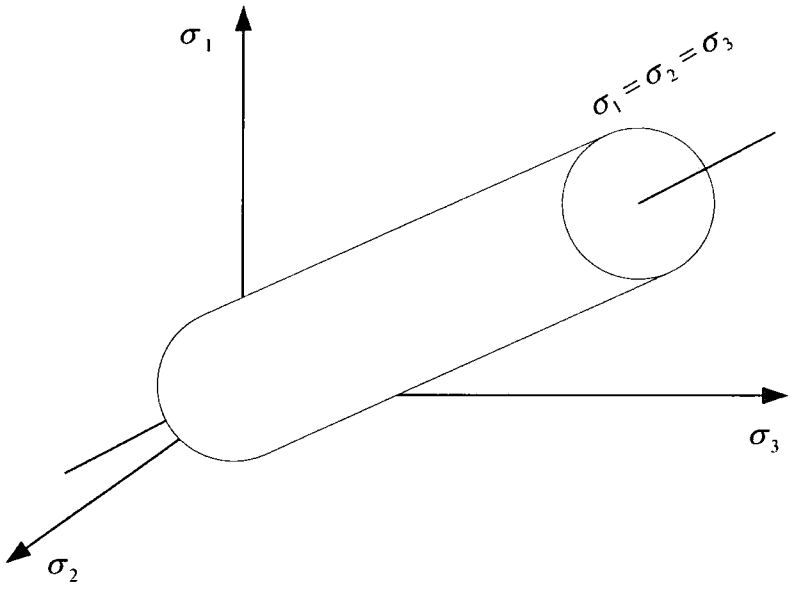

a) Von Mises yield surface.

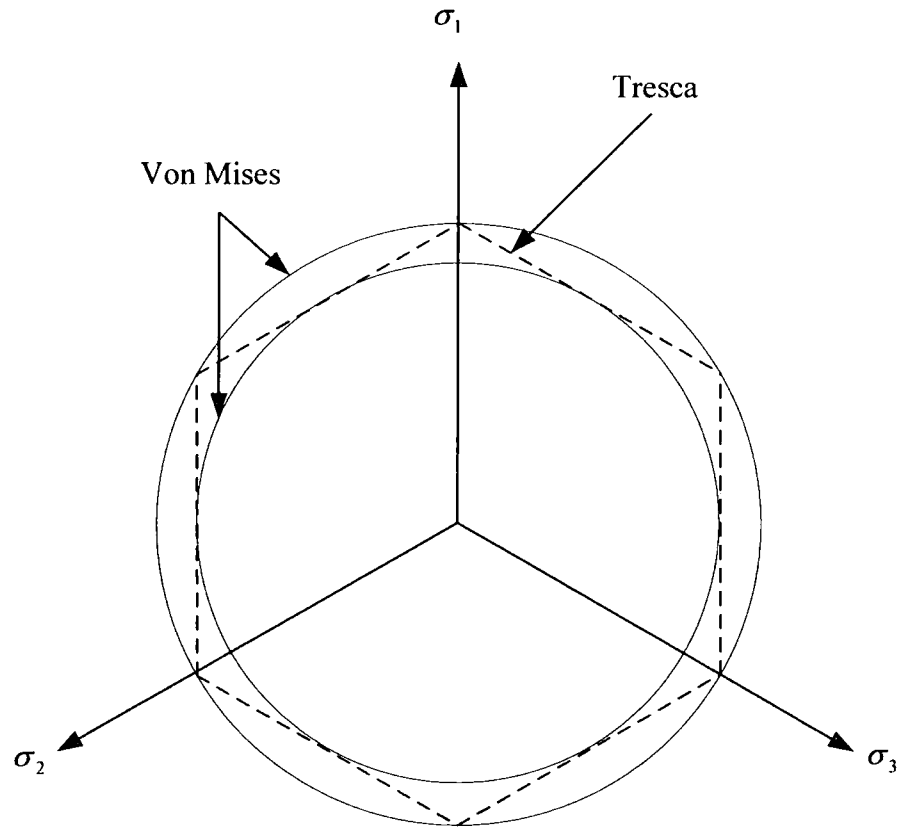

b) Comparison of Von Mises and Tresca yield surfaces plotted on the deviatoric plane.

Figure 3.7. Von Mises model and comparison with Tresca model (After Potts and Zdravkovic, 1999).

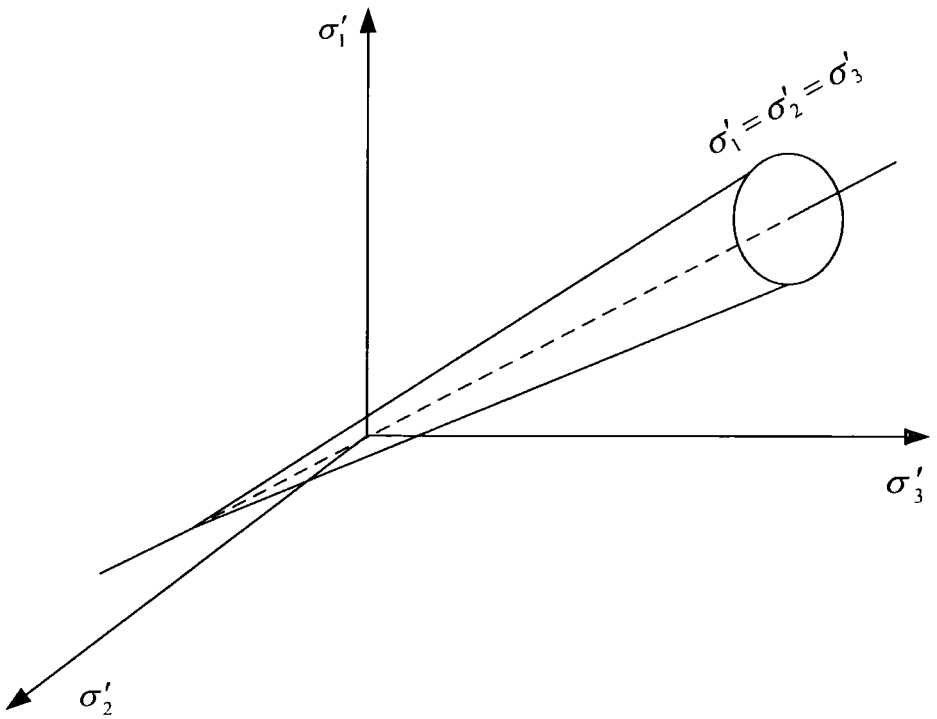

Figure 3.8. Drucker-Prager model.

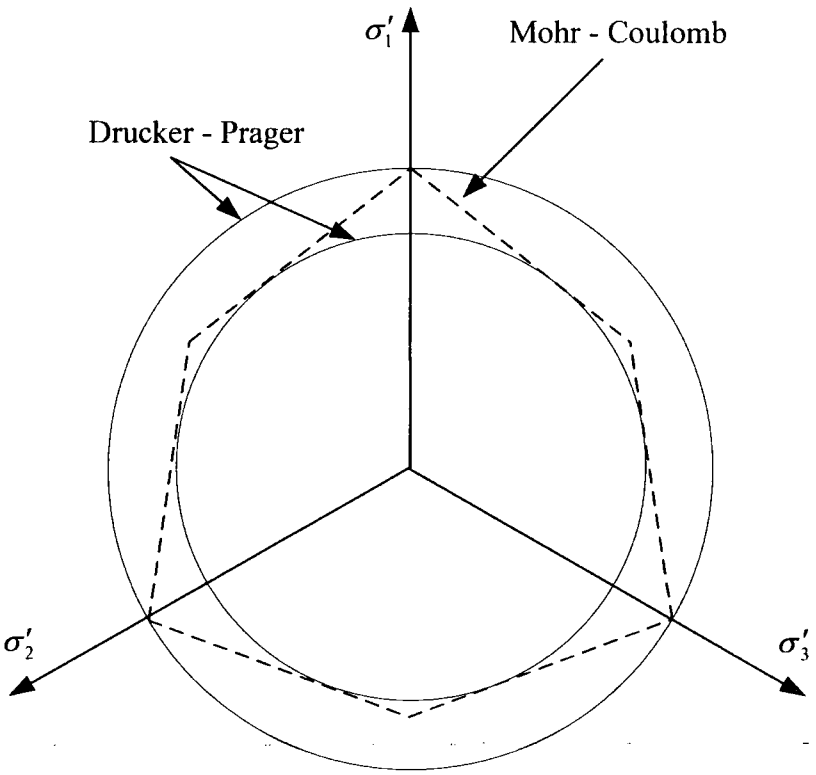

Figure 3.9. Comparison of Mohr-Coulomb and Drucker-Prager yield surfaces plotted on the deviatoric plane (After Potts and Zdravkovic, 1999).

3.7 Initial conditions

After the creation of both the geometry and the mesh of the boundary problem, the initial stress conditions of the ground have to be specified prior to any analysis stage. Similar if not identical values of stresses have to be prescribed to those acquired from field measurements so that the resulting FE predictions are realistic. Thus this part of the modelling is of great importance and unique to geotechnics.

In Chapters 6 and 7 the initial ground conditions were modelled using the "*gravity loading*" method. This is described in detail in Chapter 6. The reason for this choice was that this was the only method provided by Strand7. Hence, the same method was chosen in Plaxis for compatibility purposes. However, in Chapter 4, where tunnel excavation is modelled using just Plaxis, the "K_0 procedure" of simulating the initial ground stresses was chosen. This method can only be applied for a horizontal surface profile and is described in this section. Vertical stresses (σ'_v) are generated using the bulk unit weight of the soil. The horizontal stresses (σ'_h) are calculated using an appropriate K_0 value (dimensionless parameter described in Chapter 2) from the following equation:

$$\sigma'_h = K_0 \sigma'_v \tag{3.28}$$

In this way the initial ground stresses are generated.

3.8 Excavation

The simulation of excavation in tunnel construction problems when using the FEM, is discussed in the current section. The user has to specify the part of the domain to be excavated and remove it (i.e de-activate it). The behaviour of the remaining active part of the mesh will be the same as before the excavation if appropriate forces (traction T which refers to the internal stresses of the domain prior to the excavation) are applied instead of the de-activated part. Thus no changes of stress or displacement occur to the active part. If tractions are removed (i.e. by applying an equal and opposite force in a series of increments if non-linear analysis is employed) then the excavation boundary conditions are simulated (Brown and Booker, 1985).

In this thesis, tunnel construction and hence excavation is modelled only in 2-D (using Plaxis) and is presented in Chapter 4. In this software the user has to create the whole geometry of the boundary problem during the "Input Phase" (this is what the pre-processing stage is called in Plaxis). The parts which will not be used during the first stage of the analysis procedure ("Calculation Phase" in Plaxis) should be de-activated and then re-activated at a later stage. The properties of the de-activated parts (lining or soil elements) such as weight, stiffness, strength, stress and finally nodal displacements are not considered (i.e. they are zeroed). The resulting boundaries are hence free to deform. The previously mentioned properties of the now, re-activated, parts are fully taken into account this time.

3.9 Volume loss

Volume loss as a process and its different variations has been fully described in Chapter 2. The way Plaxis models volume loss (termed as contraction in Plaxis) for a shield driven circular tunnel with a continuous and homogeneous tunnel lining is presented in this section. Contraction is applied to the structural elements of the tunnel to simulate the decrease of its cross sectional area. Contraction is the ratio of the reduced cross sectional area over the original excavated area and is expressed as a percentage. This value is applied to the activated structural elements of the tunnel. This input value may not be fully reached during the analysis stage depending on the stiffness of the surrounding soil or other nearby structural objects.

Chapter 4

On the predicted direction of surface displacement vectors due to tunnelling

4.1 Introduction

In this chapter the problem of the direction of the surface deformation vectors (both vertical and horizontal) due to tunnelling in a greenfield site in soft ground is addressed. The author has conducted a thorough research of the literature in this area to reveal that geotechnical engineers (both in academia and in industry) seem to disagree on the direction of these vectors. Three of the most commonly accepted approaches are presented and analysed in the next section (Section 4.1.1) using plane strain FE analysis with a commercial FE package, Plaxis v.7.

Problem configuration

Throughout this chapter, the same geometry has been employed. Figure 4.1 shows the dimensions of the domain, kept constant throughout the analyses, as well as the varying parameters of this study. Four different cases were investigated in an attempt to shed light on this problem, i.e. to find which parameters influence the direction of the surface deformation vectors. The first parametric study attempts to correlate depth to the tunnel axis, z_0 with these vectors. The second parametric study refers to the case where different tunnel diameters, D are modelled. The third parametric study refers to the case where different increments of soil stiffness with depth, E_{inc} are

modelled. Finally the fourth parametric study refers to the case where volume loss, V_L varies. A total of 13 analyses were carried out.

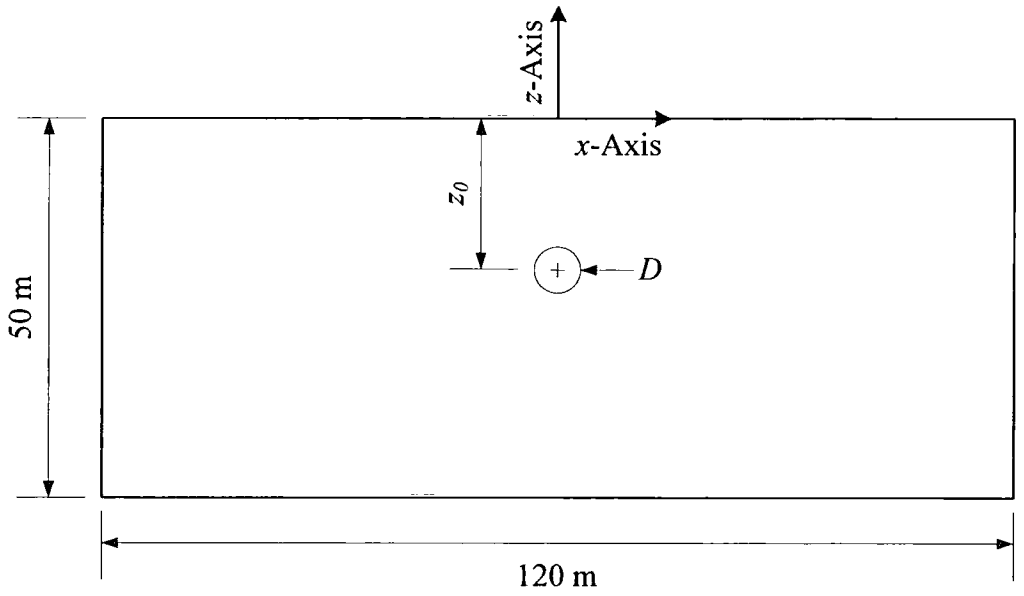

When z_0 varies:

D = 4.146m
V_L = 1.4%
E_{inc} = 1000kPa/m
z_0 = 14m, 20m, 27m and 34m

When D varies:

z_0 = 20m
V_L = 1.4%
E_{inc} = 1000kPa/m
D = 3.625m, 4,146m, 5m and 6.4m

When V_L varies:

D = 4.146m
z_0 = 20m
E_{inc} = 1000kPa/m
V_L = 1%, 1.4%, 2% and 2.5%

When E_{inc} varies:

z_0 = 20m
V_L = 1.4%
D = 4.146m
E_{inc} = 1000kPa/m, 2000kPa/m, 3000kPa/m and 4000kPa/m

Figure 4.1. Dimensions of the domain.

4.1.1 Analytical prediction methods

In the current section three well known approaches regarding the direction of the surface deformation vectors due to tunnelling in soft ground are presented. For the

first of these approaches O'Reilly and New (1982) introduced Equation 4.1 to calculate the horizontal surface movements, H_x along the transverse x-axis.

$$H_x = \frac{x}{z_0} S_x \tag{4.1}$$

where S_x is the vertical surface movements and z_0 is the depth to the tunnel axis (see Figure 2.2). To ensure the validity of this equation the following assumption was made: the net displacement vector (i.e. the resultant of the horizontal and the vertical vectors) should be aligned with the tunnel centreline (CL). Figure 4.2a shows the direction of these surface vectors at any point along the transverse direction. By taking for granted that the previous assumption is valid then the following equation can be extracted from Figure 4.2a (formed in the triangle OAB):

$$\tan\theta = \frac{H_x}{S_x} \tag{4.2}$$

The following equations can also be defined using trigonometry from Figure 4.2:

$$\begin{aligned} \tan\xi &= \frac{x}{z_0} \\ \tan\zeta &= \frac{\tan\theta}{\tan\xi} \end{aligned} \tag{4.3}$$

where ξ is the angle formed in the triangle OA'B' (see Fig. 4.2a) and ζ is the angle formed in Figure 4.2b. Since the two triangles OAB and OA'B' are similar then $\theta = \xi$.

Figure 4.2b shows a plot of Equation 4.1 where the ratio of H_x/S_x is plotted on the vertical axis, while the ratio of x/z_0 is plotted on the horizontal axis. This equation should be plotted as a straight line starting from the origin since it is of the following form: $y = mx$. At the point where $x = z_0$ the vertical and the horizontal surface movements should be equal according to Equation 4.1 (i.e $H_x = S_x$). Hence, by using Equation 4.3 $\tan\zeta = 1 \therefore \zeta = 45°$. Thus, Equation 4.1 should be inaccurate unless the

FE predictions indicate a similar angle ζ.

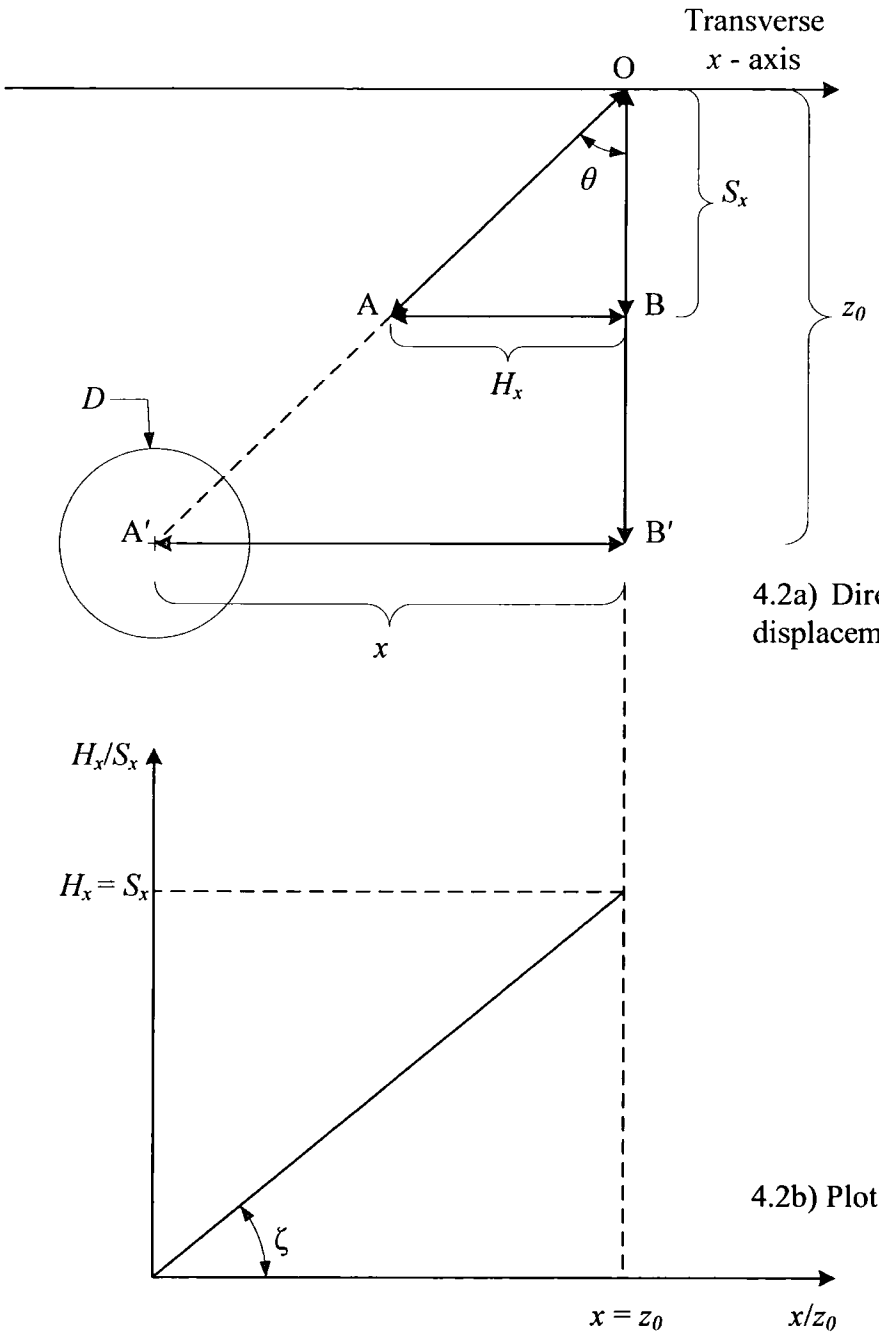

4.2a) Direction of the net displacement vector

4.2b) Plot of Equation 4.1

Figure 4.2. Direction of the net displacement vector according to Equation 4.1 introduced by O'Reilly and New (1982).

Deane and Bassett (1995) presented field data from the Heathrow Express trial tunnels driven in London clay using the NATM method of excavation. These findings indicate that the surface displacement vectors were heading somewhere between the

tunnel CL and the invert; definitely though within the tunnel. Figure 4.2a indicates that if this was the case then $\tan\theta < 1$ and therefore at the point where $x = z_0$, $\tan\zeta < 1 \therefore \zeta < 45°$.

Finally, a third approach was introduced by Taylor (1995) who suggested that the surface displacement vectors, in the case where the trough width constant K varies non-linearly with depth (see Fig. 2.16), were heading at a distance of $0.175\ z_0$ / 0.325 below the tunnel CL and definitely below tunnel invert. Thus by following the same procedure as above Taylor (1995) predicted that at $x = z_0$, $\zeta < 45°$. This time though ζ is less than the angle observed by Deane and Bassett (1995).

The aims of the analyses of this chapter therefore are to try and identify the pattern these surface vectors follow in the FE modelling of tunnelling and the parameters that affect them.

4.2 Details of the analysis

4.2.1 Introduction

Figure 4.3 shows one of the meshes used in this study. This particular domain can be characterised as a medium density mesh with two denser areas. The first is inside and around the tunnel area while the second is on the upper boundary (i.e. surface). In this way more nodes are placed at these two areas of interest; hence, greater accuracy is achieved. The mesh consists of 21,027 nodes (i.e. 42,054 d.o.f) and 2,537 fifteen-noded triangles representing the soil. Curved beam elements are used to model the structural components of the tunnel (i.e. lining). There is obviously a plane of symmetry through the vertical tunnel axis. Consequently, half of the domain only could be modelled in order to reduce the number of d.o.f and therefore save computational time. However, for this size of a problem the difference in computational time is minor. Thus it was decided that the whole domain should be modelled instead.

Initially the tunnel diameter was chosen to be D = 4.146m (commonly used diameter

when excavating for the London Underground) and the depth to the tunnel axis at z_0 = 20m (Attewell, 1978). Soil stiffness incrementally increased with depth, having a reference value on the surface ($z_{ref} = 0$) of E_{ref} = 6207 kPa with an increment of E_{inc} = 1000 kPa/m. Soil stiffness at any point within the domain was given by the following equation:

$$E_Z = E_{ref} + (z_{ref} - z_{inc})E_{inc} \tag{4.4}$$

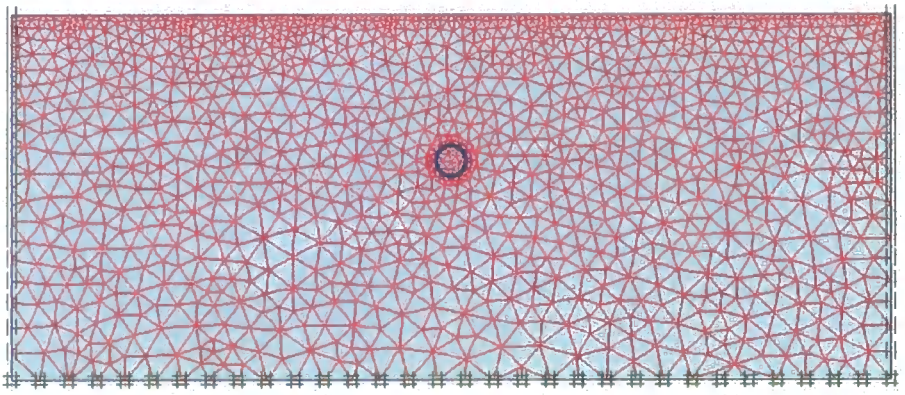

Figure 4.3. One of the generated meshes in this chapter using Plaxis v.7.

The input value for volume loss was set at V_L = 1.4% which is common when tunnelling in soft ground (Addenbrooke and Potts, 2001). Then a parametric study was carried out varying the excavation depth from its initial value (i.e. z_0 = 20m) to three other values (i.e. z_0 = 14m, 27m and 34m). This was done in order to confirm findings from the literature indicating that z_0 affects the settlement trough and the displacement vectors. Then tunnel diameter was varied from its initial value (i.e. D = 4.146m) to three other values (3.625m, 5m and finally 6.4m) so that any possible correlation between D and the surface displacement vectors would be highlighted, since no correlation was found by other researchers (e.g. O'Reilly and New, 1982, a surprising result). Finally, volume loss and soil stiffness varied in an attempt to try and identify whether other parameters apart from z_0 affect the displacement profile. The input values for volume loss were V_L =1%, 2% and 2.5% while those for the increments of soil stiffness were E_{inc} = 2000kPa/m, 3000kPa/m and 4000kPa/m.

The dimensions of the boundary problem were chosen to be 120m along the horizontal x-axis and 50m along the vertical z-axis. These values lie within the limits proposed by Potts *et al.* (2002) regarding the size of a domain.

4.2.2 Initial conditions

In this chapter, drained analysis is performed to calculate the initial conditions. These are then modelled using the "K_0 method" (which was described in detail in Chapter 3). The vertical stresses are generated using the soil's unit weight γ ($\sigma'_v = \gamma z$). The horizontal stresses are then calculated using an appropriate K_0 value ($\sigma'_h = K_0 \sigma'_v$). Plaxis uses the value of the angle of friction φ' to calculate K_0 ($K_0 = 1 - \sin\varphi'$). This method is commonly used among geotechnical engineers even though it has some restrictions in its use; i.e. it can only be applied for a greenfield site with a horizontal surface line (which is the case in this study). Prior to any excavation, the tunnel lining elements are de-activated while the finite elements representing the soil in and around the tunnel liner are activated. In this way the vertical and horizontal initial effective stresses in the soil are generated.

The whole domain consists of a single clay layer, the properties of which are presented in Table 4.1. In all calculations drained analysis is performed meaning that there are no pore water pressures changes. Soil properties are expressed in terms of effective strength parameters. Water is not present in this soil profile throughout the analyses.

Boundary conditions are imposed in such a way that no movements are permitted along the bottom boundary. Vertical movements are only permitted along the two vertical boundaries. Finally, the top boundary is free to deform in every direction.

4.2.3 Constitutive models

The structural components of the domain (i.e. the lining) are assumed to behave in a linear elastic way. The parameters required to fully describe their behaviour are presented in the Table 4.2.

Parameter	Name	Value	Units
Type of Behaviour	Elastic region	Linear Elastic	-
Type of Behaviour	Yield Surface	Mohr Coulomb	-
Young's Modulus	E_{ref}	6.207×10^3	kPa
Poisson's Ratio	ν'	0.3	-
Unit Weight	γ	20	kN/m^3
Cohesion	c'	5	kPa
Angle of Friction	φ'	25^o	-
Dilatancy Angle	ψ'	12.5^o	-

Table 4.1. Material properties of the soil.

Parameter	Name	Value	Units
Type of Behaviour	Material Type	Elastic	-
Young's Modulus	E	10^8	kPa
Cross Sectional Area	A	0.168	m^2
Second Moment of Area	I	3.95136×10^{-4}	m^4
Poisson's Ratio	ν	0.15	-
density	γ_L	24	kN/m^3

Table 4.2. Material properties of the tunnel lining.

A simple elasto-plastic model is incorporated to model soil behaviour. The plastic region is described by using the Mohr-Coulomb failure criterion. This in general is a rather simplistic way to model real soil behaviour. However, this was done mainly for two reasons. Firstly, Plaxis v.7 does not offer a pre-defined list of non-linear soil models and secondly, this type of behaviour is widely used and accepted by geotechnical engineers since it only requires a few input parameters to be specified.

4.2.4 Modelling sequence

In all calculations, the analysis procedure began with the definition of initial effective

stresses prior to tunnel construction, using a value of the ratio of effective horizontal to vertical stress, $K_0 = 0.6$. Subsequently, two load stages are defined. The first refers to the construction of the tunnel, simulated by re-activating the tunnel lining and de-activating the soil elements inside the tunnel. The second load stage refers to the imposition of volume loss for the tunnel. Each load stage was solved using standard non-linear solution techniques (modified Newton Raphson) available in Plaxis v.7.

4.2.5 Analysis results

In the current section predictions of plane strain FE analyses of tunnel excavation in soft ground are presented, focusing on the direction of the surface displacement vectors. Parametric studies are then carried out in an attempt to try and identify which parameters (if any) affect the direction of these surface vectors.

Figure 4.4 shows plots of the 2-D FE predictions when using Plaxis of the vertical surface settlements (S_x) and the horizontal surface movements (H_x) along the vertical axis, against the transverse distance plotted on the x-axis, for three different i (i.e. trough width parameter) values. This parameter is used in Equation 2.19 introduced by O'Reilly and New (1982), according to whom i is proportional to the trough width constant K and the tunnel axis depth z_0. K should lie within a range of 0.4 to 0.7 for the type of soil modelled in this analysis. However, for simplicity it is accepted that a value of $K = 0.5$ should suit most clay profiles. Hence, the first of the three vertical lines plotted in Figure 4.4 refers to the case where i is calculated for a given tunnel axis depth (z_0 = 20m) and $K = 0.5$ (this case for the rest of the chapter will be referred as K_1). The second line refers to the case where i is calculated for the same tunnel axis depth (z_0 = 20m) and $K = 0.6$ (referred to as K_2). Finally, the third line is created by drawing a parallel to the vertical axis line which intersects with the FE predictions regarding the horizontal surface movement curve (i.e. H_x) at its maximum point (referred to as K_3. Therefore K_3 is not calculated using Eq. 2.19 like K_1 and K_2 but by using the FE predictions). As a result this vertical line should coincide with the point of inflection i at the FE predictions' plot regarding the vertical surface settlement curve (i.e. S_x, Attewell and Farmer, 1974a).

The tunnel axis was driven at z_0 = 20m while the tunnel diameter was D = 4.146m. The increment of soil stiffness was E_{inc} = 1000kPa/m and volume loss was V_L = 1.4%. This particular case was regarded as the reference case for every subsequent parametric study described in the current chapter.

Three different trough width parameters i were calculated for this graph (Fig. 4.4). This indicates different shapes of the trough depending on the choice of the trough width constant K. The maximum i value was calculated at K_2, and the minimum at K_1. Finally, in the case where K is calculated from the FE predictions (K_3), the equivalent trough width parameter i was closer to the K_2 case. These findings are presented in Table 4.3.

z_0 = 20m	D = 4.146m	E_{inc} = 1000kPa/m	V_L =1.4%
	i	2.5i	
K_1	10m	25m	
K_2	12m	30m	
K_3	11.24m	28.1m	
S_{max}	-0.004m		
H_{max}	0.002m		
Angle ζ	43.5°		

Table 4.3. Calculations of the trough width constants K_1, K_2 and the angle ζ along with FE predictions regarding K_3, S_{max} and H_{max} for the reference case.

Figure 4.5 shows plots of the horizontal surface movements (H_x) along the vertical axis normalised by the maximum surface horizontal movement ($H_{x,\max}$). The latter value corresponds to H_x at the point of inflection i (i.e. $H_{x,\max} = H_{x,i}$). These transverse values are plotted against the distance x normalised by the trough width parameter i. Both of the axes are therefore expressed in dimensionless form. The three different curves of this plot correspond to the three different K values described earlier (i.e. K_1, K_2 and K_3). It is observed that the maximum of these three plots occur when $x = i$ as expected. This is the case especially for K_2 and K_3. A slight off-set can be identified in the case of K_1. These three plots seem to be almost identical within the sagging zone (i.e. $-1 \le x/i \le 1$ see Fig. 2.1). However, it seems that they differ

slightly within the hogging zone (i.e. $x/i < -1$ and $x/i > 1$ see Fig. 2.1). The trough is considered to extend until a distance of $x/i = 2.5$. Beyond this point, movements are negligible (Mair *et al.*, 1993). Thus, within the previously mentioned limits of the trough it seems that K_2 and K_3 produce slightly different predictions regarding the surface deformations from the K_1 case proposed by O'Reilly and New (1982).

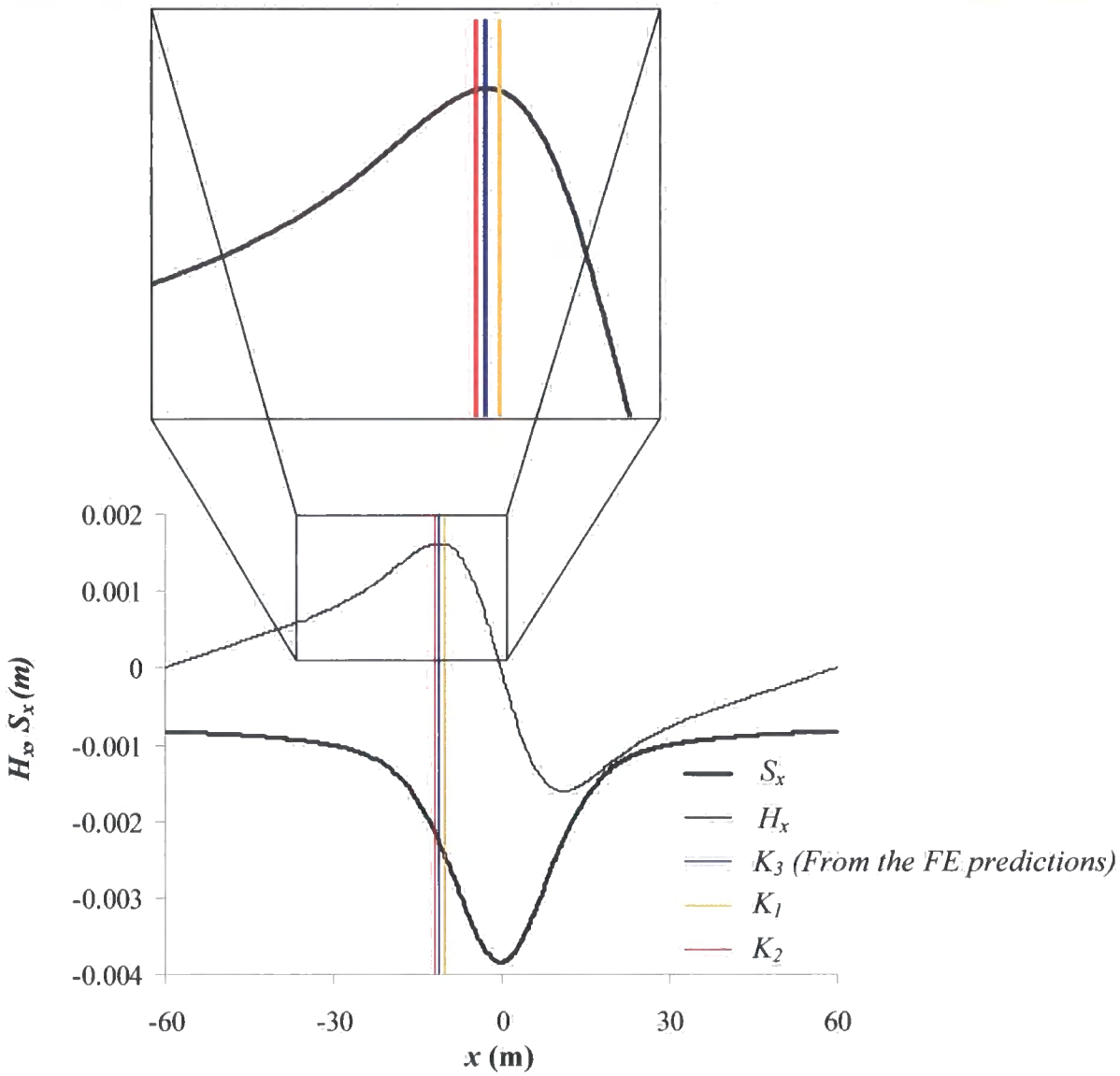

Figure 4.4. Plot of the vertical and horizontal surface movements along the transverse axis for the reference case.

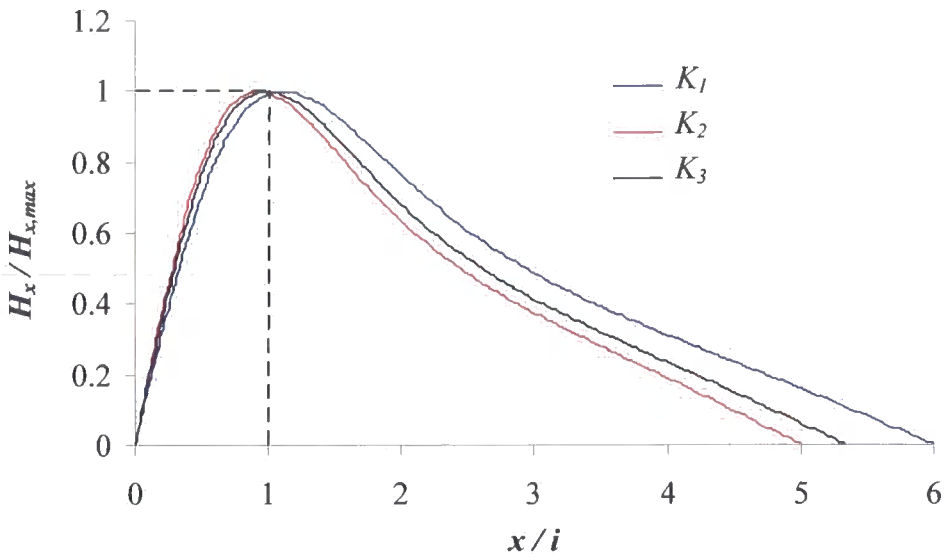

Figure 4.5. Normalised plot of the horizontal surface movements against the transverse distance x for the reference case.

Figure 4.6 shows plots of the ratio of the horizontal surface movements over the vertical surface movements (H_x / S_x) along the vertical axis, against the ratio of the transverse distance x over the depth to the tunnel axis (x/z_0) along the horizontal axis. Figure 4.6 shows a result that may be compared with Equation 4.1. The shape of this plot was expected to be a straight line (see Figure 4.2). This is the case when $0 \le x/z_0 \le 1$. Furthest from this point the gradient of a plot changes rapidly. However, as mentioned above the trough was extended to a distance of $x/i = 2.5$ or $x/z_0 = 2.5K_3$ which in this case was equal to $x/z_0 \approx 1.4$. Thus, the part of the graph where $x/z_0 > 1.4$ will not be taken into consideration. The reason for choosing K_3 rather than K_1 or K_2 (for the above calculation of x/z_0) was that this is a more accurate way to calculate K (i.e. from the FE predictions) than choosing a mean value such as $K = 0.5$. The angle ζ (see Fig. 4.2) was measured at $x/z_0 = 1$ and was found to be 43.5° (slightly less than 45°). This is a first indication in these new analyses that the surface displacement vectors are heading slightly lower than the tunnel CL (between CL and invert). The exact point can be calculated using trigonometry in Figure 4.2. That point was found to be at 21m from the surface, or just 1m below tunnel CL. This was in agreement with the findings of Deane and Bassett (1995).

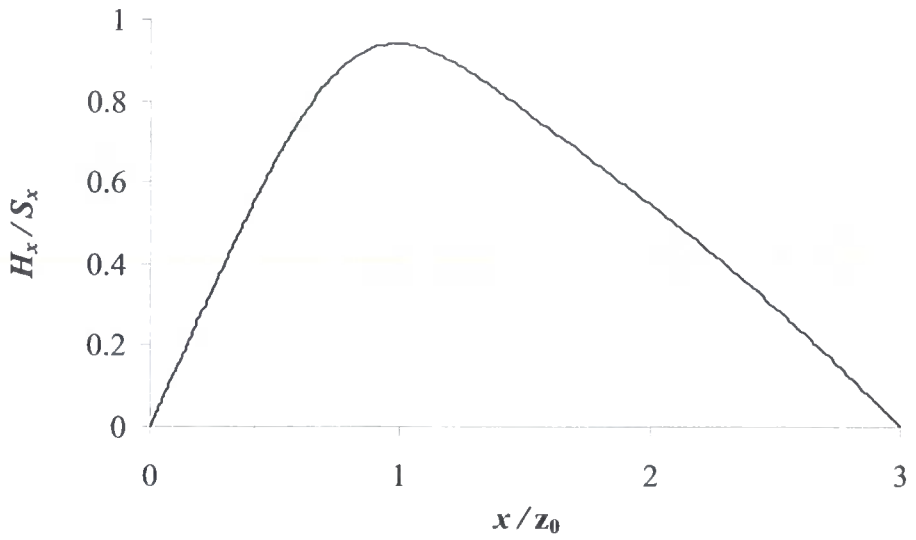

Figure 4.6. Plot of the total surface vectors against the transverse distance x for the reference case.

Parametric study varying the excavation depth

According to O'Reilly and New (1982) the trough width parameter i is directly proportional to the depth of the tunnel axis z_0 (see Equation 2.19). A parametric study is employed in this section for two reasons. The first is to confirm the previously mentioned finding and the second to identify the direction of the net surface displacement vector. For this purpose three different excavation depths are modelled (z_0 = 14m, 27m and 34m) along with the reference case where z_0 = 20m, which was presented previously in this section. Soil properties, lining properties and the dimensions of the domain are identical to the reference case and constant throughout this parametric study.

The FE predictions indicate that in every case K_3 (i.e. that obtained through the FE predictions) is always closer to the K_2 than K_1 (see Table 4.4). However, the difference would only have a marginal effect in the FE predictions. Another point which is highlighted is that the deeper the excavation the bigger the trough width parameter i and the maximum vertical surface settlement vector S_{max}. The maximum

horizontal surface displacement vector $H_{x,max}$ however seems to be less affected with an increasing depth of excavation. For the two shallow cases (z_0 = 14m and 20m) the latter vector increases. For the two deeper cases however (z_0 = 27m and 34m), it seems to stabilise (Table 4.4).

D = 4.146m			E_{inc} = 1000kPa/m				V_L =1.4%	
	z_0 = 14m		z_0 = 20m		z_0 = 27m		z_0 = 34m	
	i(m)	2.5i(m)	i(m)	2.5i(m)	i(m)	2.5i(m)	i(m)	2.5i(m)
K_1	7	17.5	10	25	13.5	33.7	17	42.5
K_2	8.4	21	12	30	16.2	40.5	20.4	51
K_3	8	20	11.2	28.1	15.5	38.7	18.9	47.2
S_{max}	-0.0043m		-0.0038m		-0.0035m		-0.0034m	
H_{max}	0.0019m		0.0016m		0.0015m		0.0015m	
Angle ζ	51°		43.5°		44.2°		48.5°	

Table 4.4. Calculations of the trough width constants K_1, K_2 and the angle ζ along with FE predictions regarding K_3, S_{max} and H_{max} for a parametric study varying z_0.

In Figure 4.7 the horizontal surface movements H_x normalised by the maximum horizontal surface movement $H_{x,max}$ along the vertical axis are plotted against the transverse distance x normalised by the trough width parameter i along the horizontal axis for the four different excavation depths. These plots show that at the point of inflection (i.e. $x = i$) the maximum surface horizontal movements occur (i.e. $H_{x,max} = H_x$) regardless of the depth to the tunnel CL. These four plots behave in an identical way within the region of the trough ($x/i \leq 2.5$). Beyond this region however, the plots seems to diverge. This difference however, should not be considered since, as mention previously in this section, the displacement vectors outside the trough's region are negligible.

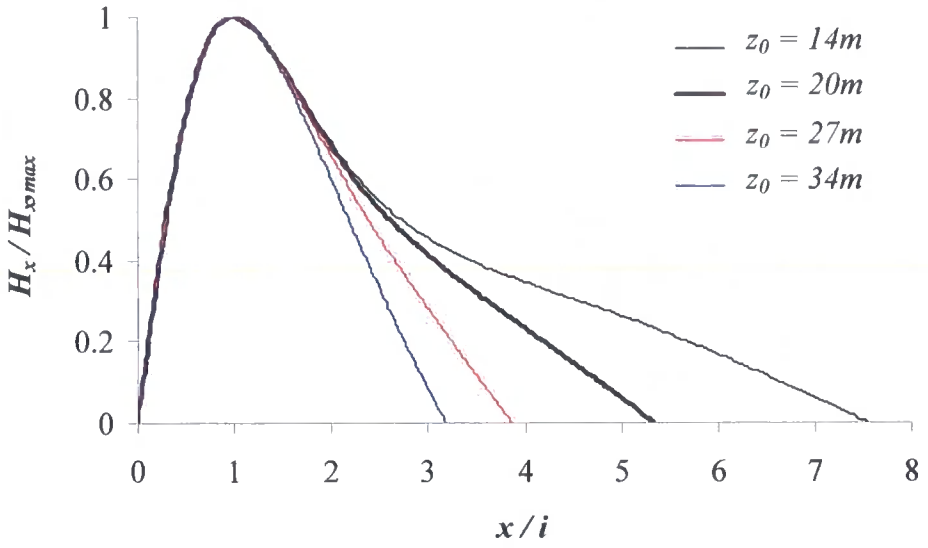

Figure 4.7. Normalised plot of the horizontal surface movements against the transverse distance x when z_0 varies.

Figure 4.8 plots the ratio of the horizontal surface movement over the vertical surface movement (H_x / S_x) along the y-axis against the ratio of the transverse distance x over the excavation depth (x/z_0) along the horizontal axis for the four different excavation depths. From this figure it is evident that these four cases do not behave in the same way within the region of the trough (i.e. $x/z_0 = 2.5K_3$). This means that the total surface displacement vectors are affected by the excavation depth z_0. Consequently, the trough, and hence i, is thought to be related to z_0. This is a confirmation of what has been found in the literature (O'Reilly and New, 1982). Another interesting outcome from this figure (Fig. 4.8) is that at $x/z_0 = 1$, the horizontal surface movements are not equal to the vertical surface movements for all of the four different excavation depths. For the two extreme cases (i.e. z_0 = 14m and 34m) $H_x / S_x \neq 1$, while for the other two cases (i.e. z_0 = 20m and 27m) $H_x / S_x \approx 1$. This is a clear indication that different total displacement directions (Angle ζ) should be predicted. Indeed, it was found that in the case where z_0 = 14m (i.e. C/D = 2.9) the total vectors form an angle of $\zeta = 51^\circ$ at $x/z_0 = 1$, meaning that the total vectors are heading somewhere above the tunnel CL. By using trigonometry it is

found that this point lies at 11.27m from the surface or 0.65m above the tunnel crown. For deeper tunnels though, angle ζ reduces; i.e. when z_0 = 20m (i.e. the soil cover over the tunnel diameter ratio is C/D = 4.3), ζ = 43.5° while when z_0 = 27m (i.e. C/D = 6), ζ = 44.2°. In both of these cases the vectors are heading slightly lower than the tunnel CL; i.e in the first at 21m from the surface or 1m below tunnel CL and in the second at 27.7m from the surface or 0.7 below tunnel CL. In both of these cases though, the point lies within the tunnel outline. Finally, in the case where z_0 = 34m (i.e. C/D = 7.7) ζ increases again having a value of ζ = 48.5°. Hence, the total vectors head towards a point 30m from the surface or 4m above the tunnel CL.

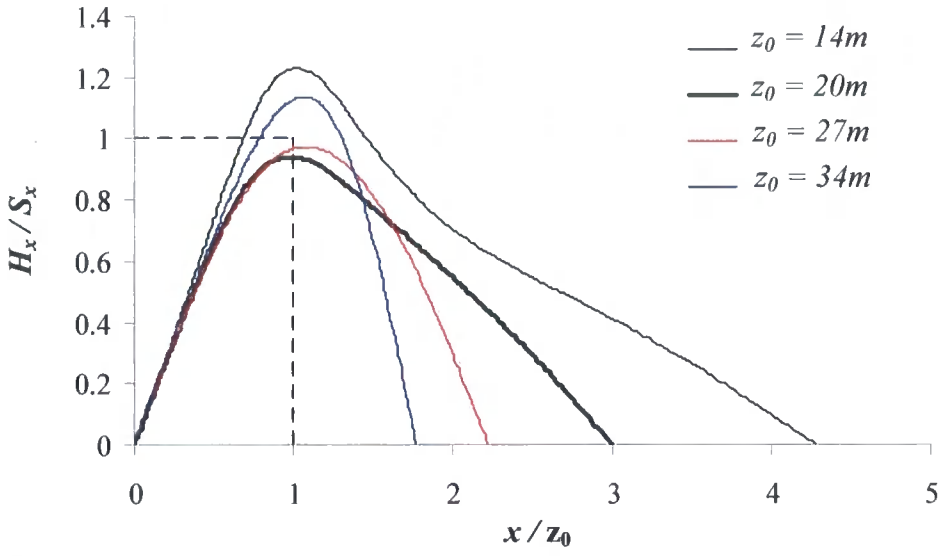

Figure 4.8. Plot of the total surface vectors against the transverse distance x when z_0 varies.

Thus for tunnels driven at a depth of $C/D \leq 2.9$ and $C/D \geq 7.7$ the net displacement vector is heading at a point different than the tunnel CL. Hence, the FE predictions do not seem to confirm the O'Reilly and New (1982) assumption regarding the validity of Equation 4.1. For tunnels driven within the range of $6 < C/D < 7.7$ though the FE predictions indicate that Equation 4.1 is valid.

Parametric study varying the tunnel diameter

According to O'Reilly and New (1982) the trough width parameter i should be proportional to both z_0 and D. Even though they manage to correlate i with z_0, their attempts to do the same with the tunnel diameter were unsuccessful. Peck (1969) on the other hand suggested that the D is directly proportional to the maximum surface settlement S_{max}. In other words the outcome of these two papers implies that if two single tunnels, of different diameters, are driven at the same depth at two different sites with identical soil properties, then two different S_{max} values will be produced (the tunnel with the bigger diameter will produce the larger S_{max}) with the two individual troughs having the same trough width parameter i (see Figure 4.9). This assumption seems however, to be incorrect.

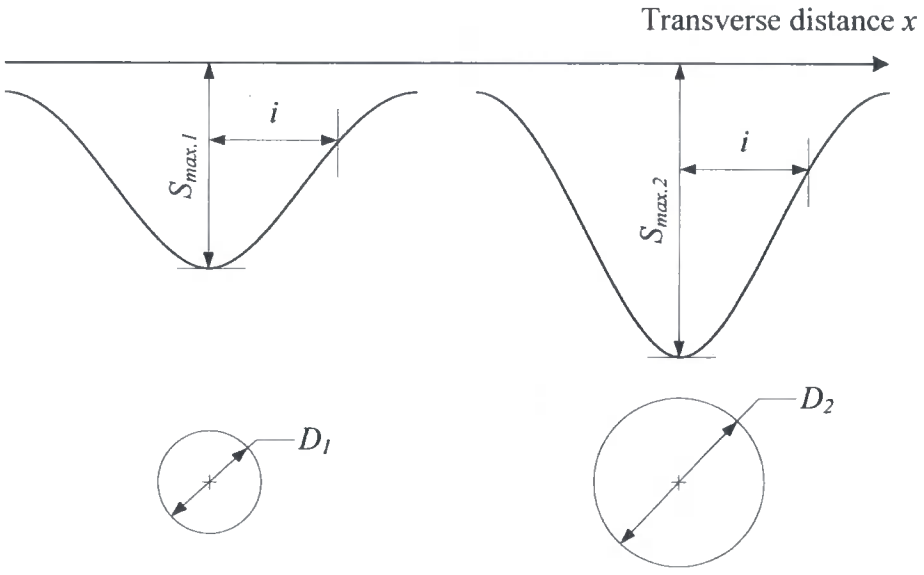

Figure 4.9. Schematic plot of two single tunnels, of different diameters, when driven at the same depth at two different sites with identical soil properties having different S_{max} values but the same i.

To investigate this point a parametric study was undertaken varying the tunnel diameter D in an attempt to try and clarify the previously mentioned *paradox*. Soil properties, lining properties and the dimensions of the domain were constant throughout this parametric study. Three different tunnel diameters are modelled (D =

3.625m, 5m and 6.4m) along with the reference case presented at the beginning of the current section where D = 4.164m. The excavation depth is constant at z_0 = 20m.

Table 4.5 summarises the most important features from the FE predictions of this parametric study. It is evident that K_3 slightly reduces as the tunnel diameter increases. Once more its value was closer to K_2. On the other hand the magnitudes of both horizontal and vertical surface deformation vectors increase as the tunnel diameter increases.

z_0 = 20m			E_{inc} = 1000kPa/m				V_L =1.4%	
	D = 3.625m		D = 4.164m		D = 5m		D = 6.4m	
	i(m)	2.5i(m)	i(m)	2.5i(m)	i(m)	2.5i(m)	i(m)	2.5i(m)
K_1	10	25	10	25	10	25	10	25
K_2	12	30	12	30	12	30	12	30
K_3	11.4	28.5	11.2	28	10.9	27.2	10.9	27.2
S_{max}	-0.0028m		-0.0038m		-0.0059m		-0.010m	
H_{max}	0.0011m		0.0016m		0.0024m		0.004m	
Angle ζ	42.6°		43.5°		43.8°		44.4°	

Table 4.5. Calculations of the trough width constants K_1, K_2 and the angle ζ along with FE predictions regarding K_3, S_{max} and H_{max} from a parametric study varying D.

In Figure 4.10 the horizontal surface movement H_x is plotted on the vertical axis and is normalised by its maximum value ($H_{x,\max}$) against the normalised ratio of the transverse distance over the trough width parameter (x/i) along the horizontal axis, for the four different tunnel diameters. These four plots are identical within the trough region ($x/i \le 2.5$). In addition they confirm that at the point of inflection ($x/i = 1$) the maximum surface horizontal displacement occurs (i.e. $H_{x,\max} = H_x$).

Figure 4.11 shows the ratio of H_x / S_x plotted against the ratio of x/z_0 for the four different tunnel diameters. The area of interest lies within the following limit: $x/z_0 = 2.5K_3$. These four plots again seem almost identical, indicating the total vectors have a similar if not the same, angle ζ. Figure 4.11 shows that at the point

where $x/z_0 = 1$ the ratio of the horizontal surface movement over the vertical surface settlement equals unity, contrary to the previous parametric study. Thus, angle ζ should be approximately 45°. The FE predictions show that at the smaller tunnel diameter (i.e. D = 3.625m) the angle ζ = 42.6°. Once more this is a clear indication that the total deformation vectors are heading below the tunnel CL. This point lies at 21.7m from the surface or just 1.7m below the tunnel CL and very close to the invert. As the tunnel diameter increases, angle ζ increases as well but it never exceeds 45°. When the tunnel diameter takes its maximum value (i.e. D = 6.4m) ζ = 44.5°. This shows that the total displacement vectors are heading at 20.4m below surface or just 0.4m below tunnel CL.

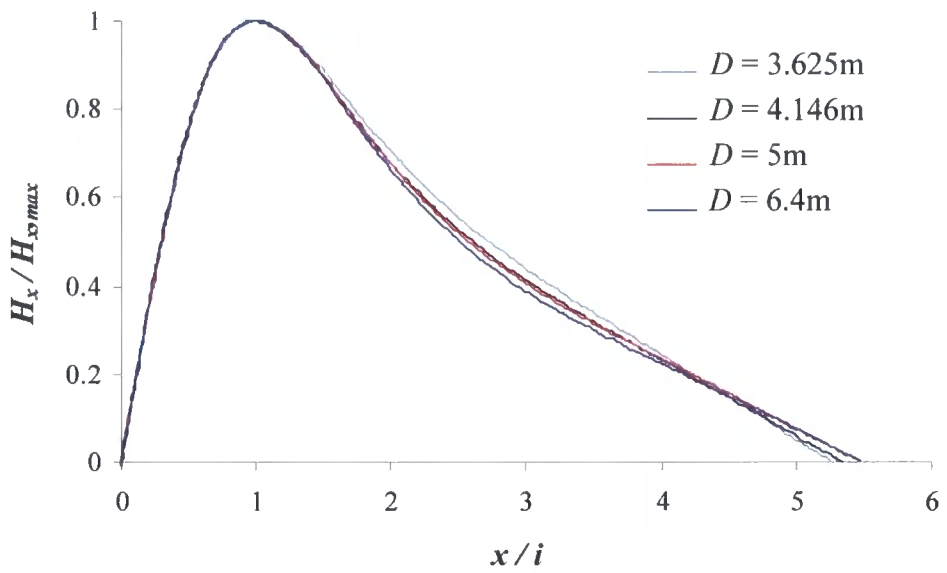

Figure 4.10. Normalised plot of the horizontal surface movements against the transverse distance x when D varies.

Hence, through the FE predictions it is clear that the trough width parameter i is only marginally affected by the tunnel diameter even if its size is almost doubled (i.e. from 3.624m to 6.4m). The assumption made by O'Reilly and New (1982) regarding the direction of the total surface vectors seems to be valid for tunnel diameters $D > 6.4$m. For smaller values though (i.e. $D \leq 6.4$m), Deane and Bassett (1995) findings seem to be confirmed instead.

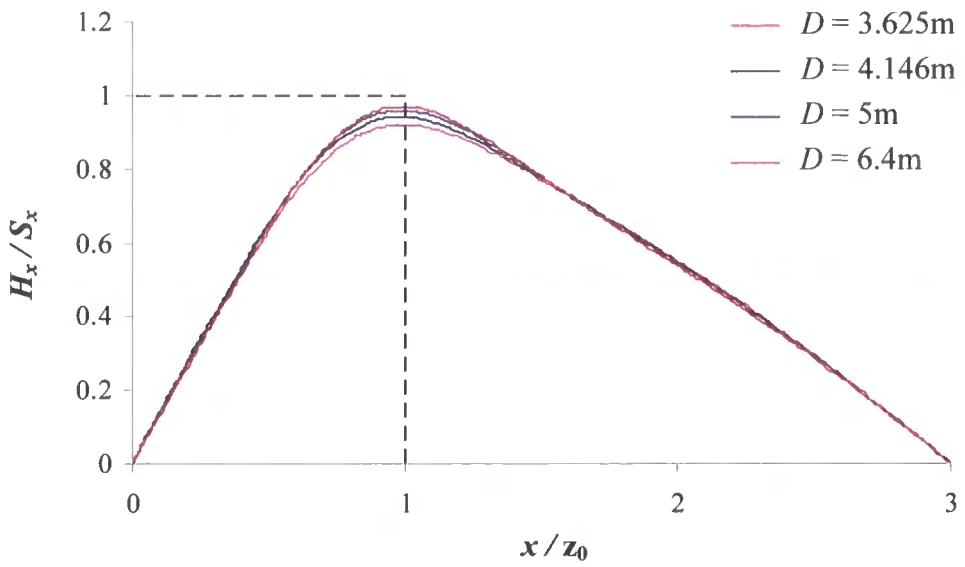

Figure 4.11. Plot of the total surface vectors against the transverse distance x when D varies.

Parametric study varying the increment of soil stiffness

By carrying out the previous two parametric studies it became apparent that the trough width parameter was proportional to the depth of the tunnel axis while only marginally affected by the tunnel diameter. The author tried to find whether there are other parameters that might influence i such as soil stiffness and volume loss. Hence, another parametric study is performed, varying the increment of soil stiffness E_{inc}. Three different increments are modelled (E_{inc} = 2000kPa/m, 3000kPa/m and 4000kPa/m) along with the reference case which was presented at the beginning of the current section where E_{inc} = 1000kPa/m. Equation 4.4 describes the increase in soil stiffness with depth. The other soil and lining properties, as well as domain dimensions, are kept constant throughout this parametric study. The depth to the tunnel axis is constant at z_0 = 20m.

The FE predictions presented in Table 4.6 show that for larger increments of soil stiffness (i.e. a stiffer soil profile) both maximum horizontal ($H_{x,max}$) and maximum vertical ($S_{x,max}$) surface movements increase. It seems that K_3 is constant throughout

these analyses but once more its values are closer to K_2. The boundaries of the trough extend until the distance of $x/z_0 = 2.5K_3$.

Figure 4.12 shows the ratio $H_x/H_{x,\max}$ plotted against the ratio x/i for the four different cases of E_{inc}. The main outcome from these four plots is that at the point of inflection (i.e. $x/i = 1$) the maximum value of the horizontal surface movements occur ($H_{x,\max} = H_{x,i}$), regardless of the values of E_{inc}. The same outcome was predicted in the previous parametric studies. These four plots behave exactly in the same way within the region of the trough.

	z_0 = 20m		D = 4.164m		V_L =1.4%			
	E_{inc}=1000kPa/m		E_{inc}=2000kPa/m		E_{inc}=3000kPa/m		E_{inc}=4000kPa/m	
	i(m)	2.5i(m)	i(m)	2.5i(m)	i(m)	2.5i(m)	i(m)	2.5i(m)
K_1	10	25	10	25	10	25	10	25
K_2	12	30	12	30	12	30	12	30
K_3	11.2	28	11.6	29	11.6	29	11.6	29
S_{max}	-0.0038m		-0.0044m		-0.0046m		-0.047m	
H_{max}	0.0016m		0.0020m		0.0023m		0.0024m	
Angle ζ	43.5°		49.2°		51.3°		52.3°	

Table 4.6. Calculations of the trough width constants K_1, K_2 and the angle ζ along with FE predictions regarding K_3, S_{max} and H_{max} from a parametric study varying E_{inc}.

Figure 4.13 shows the ratio H_x/S_x plotted against the ratio x/z_0 for the four values of E_{inc}. These four cases are identical until $x/z_0 \approx 0.5 \therefore x \approx i$. From the point of inflection until the boundaries of the trough they seem to diverge significantly. This finding suggests that the angle ζ should be different for each of the four cases. This was further supported by the fact that at the point where $x/z_0 = 1$, the horizontal surface movement was never equal to the vertical surface settlement (i.e. $H_x/S_x \neq 1$). The FE predictions presented in Table 4.6 indicate that the stiffer the soil increment the larger the angle ζ. For the less stiff increment of the four cases ζ was found to be 43.5°. This indicated that the total surface displacement vectors headed towards a point 21m from the surface, or just 1m below the tunnel CL. For

larger values of E_{inc} angle ζ becomes greater than 45° (i.e. total vectors above tunnel CL). For the stiffest soil (i.e. E_{inc} = 4000kPa/m) ζ = 52.3° indicating that the total surface vectors are heading towards a point 15.4m from the surface or 2.5m above the tunnel crown. The optimum value of E_{inc} to ensure the validity of Equation 4.1 should be within the following range: 10^3 kPa/m < E_{inc} < $2x10^3$ kPa/m. The FE predictions presented in this parametric study supported the initial assumption that soil stiffness is another factor affecting the trough width parameter hither to unconsidered.

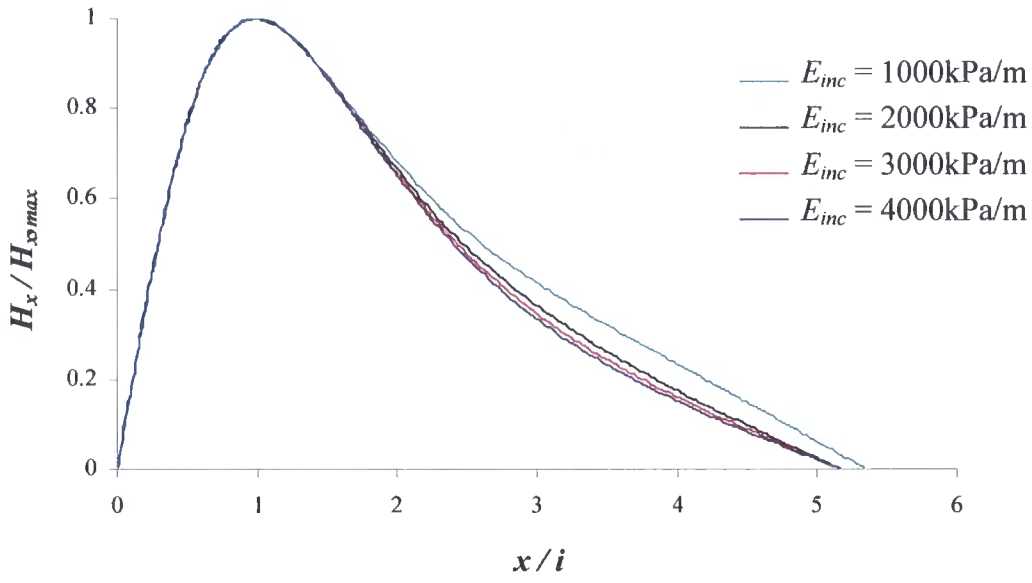

Figure 4.12. Normalised plot of the horizontal surface movements against the transverse distance x when E_{inc} varies.

Parametric study varying the volume loss

The final parametric study of this chapter is carried out to discover if volume loss V_L is related to the trough width parameter i. For this purpose three different V_L values are modelled (V_L = 1%, 2% and 2.5%) along with the reference case where V_L = 1.4%. Excavation depth is constant at z_0 = 20m in every analysis. The other soil properties, lining properties and dimensions of the domain are also constant throughout this parametric study.

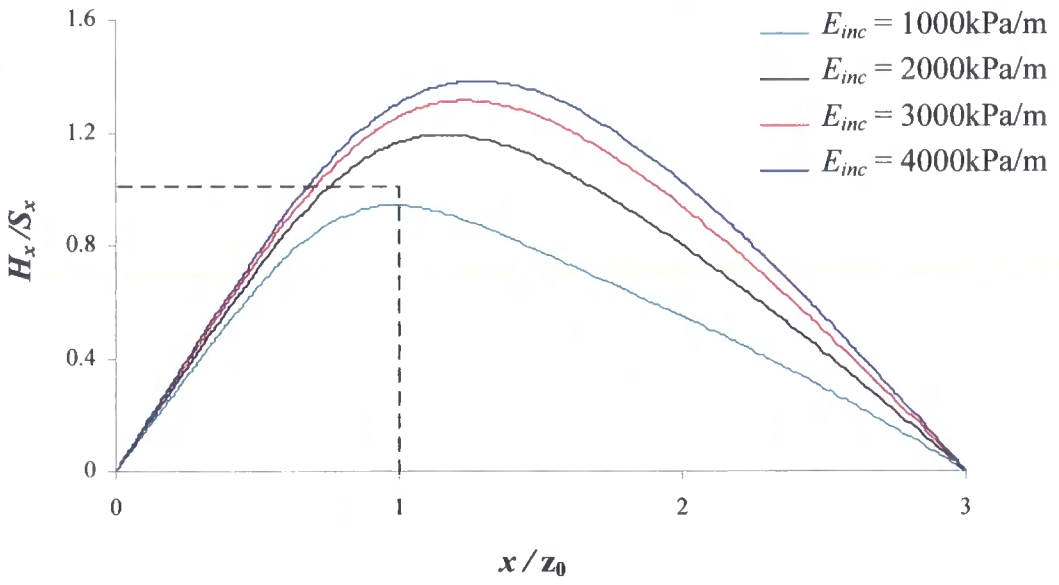

Figure 4.13. Plot of the total surface vectors against the transverse distance x when E_{inc} varies.

Table 4.7 shows the FE predictions of this parametric study regarding the maximum horizontal and maximum vertical surface vectors, the angles of these vectors, along with the values of the graphical calculation of K_3. These predictions indicate that as the value of V_L increases so do the magnitudes of $H_{x,\max}$ and $S_{\max}$. K_3 seems to gradually increase rather that being constant as in the previous parametric study. For the smallest value of V_L = 1%, K_3 is closer to K_1. However as V_L increases K_3 increases as well and in the case where V_L takes its maximum value (i.e. V_L = 2.4%) then $K_3 \approx K_2$.

Figure 4.14 shows a plot of $H_x / H_{x,\max}$ against x/i for all four cases of V_L. Once more it was evident that at the point of inflection (i.e. $x/i = 1$) the maximum horizontal surface movement occurred. Another outcome of Figure 4.14 is that the horizontal surface vectors lying within the trough region ($x/i = 2.5$) do not seem to be affected by the variation of V_L. In Figure 4.15 on the other hand, where H_x / S_x is plotted against x/z_0 it is evident that the four plots behave identically until the point of inflection (i.e. $x/i = 1 \therefore x/z_0 = K_3$, within the hogging zone). However, from that

point, and until the region of the trough (i.e. $x/z_0 = 2.5K_3$, within the sagging zone), the vectors seem to diverge. This is an indication that S_x rather than H_x is the contributory factor to this change. At the point where $x/z_0 = 1$, the ratio of $H_x/S_x \neq 1$ (except from the case where $V_L = 2\%$). This suggests that the angle $\zeta \neq 45°$. In the case where $V_L = 1\%$, angle $\zeta = 40°$. Thus the total vectors are heading at 23.8m from the surface or at 1.75m below tunnel invert (similar to Taylor, 1995 findings). As volume loss increases so does ζ. In the case where volume loss takes its maximum value (i.e. $V_L = 2.5\%$) angle $\zeta = 47°$, suggesting that the total vectors are heading at 18.6m from the surface or just 1.4m above tunnel CL but within the tunnel area. The only case where the total vectors were heading close to the CL is when $V_L = 2\%$, confirming the O'Reilly and New (1982) findings.

z_0 = 20m			D = 4.164m				E_{inc} =1000kPa/m	
	V_L = 1%		V_L = 1.4%		V_L = 2%		V_L = 2.5%	
	i(m)	2.5i(m)	i(m)	2.5i(m)	i(m)	2.5i(m)	i(m)	2.5i(m)
K_1	10	25	10	25	10	25	10	25
K_2	12	30	12	30	12	30	12	30
K_3	10.5	26.25	11.2	28	11.6	29	11.9	29.8
S_{max}	-0.0026m		-0.0036m		-0.0058m		-0.077m	
H_{max}	0.0010m		0.0016		0.0025m		0.0032m	
Angle ζ	40°		43.5°		45.6°		47.1°	

Table 4.7. Calculations of the trough width constants K_1, K_2 and the angle ζ along with FE predictions regarding K_3, S_{max} and H_{max} from a parametric study varying V_L.

4.3 Discussion

In this chapter four parametric studies were described using 2-D FEM to identify which parameters influence the trough width parameter i as well as the angle ζ of the total displacement vectors at the point where $x/z_0 = 1$.

The first study dealt with the depth of the tunnel axis. A strong relation was found between z_0, S_{max} and i. However, the total displacement vectors seemed to be

directed at an angle $\zeta \neq 45°$ in the following cases $C/D \geq 7.7$ and $C/D \leq 2.9$ where the net deformation vector is heading above the crown, in contrast to the O'Reilly and New (1982) assumption (Table 4.8). However, in between these values and especially in the case where $6 < C/D < 7.7$ the assumption made by O'Reilly and New (1982) seems to be confirmed. Consequently Equation 4.1 is applicable within the latter range of the ratio C/D.

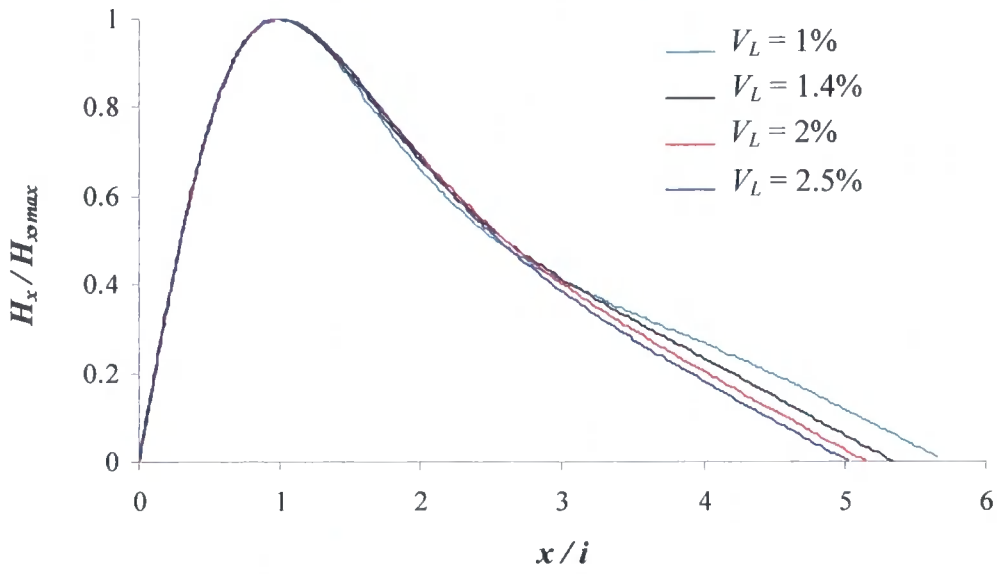

Figure 4.14. Normalised plot of the horizontal surface movements against the transverse distance x when V_L varies.

The second study dealt with the influence of the tunnel diameter D with i for a given depth of excavation. It was found that there was no strong relation between these two factors. For the validity of Equation 4.1 tunnel diameter should be D > 6.4m (Table 4.8). For smaller values the net deformation vector is heading below the tunnel CL (but within the tunnel area) confirming Deane and Bassett (1994) findings.

The third and fourth studies dealt with varying the increment of soil stiffness and the volume loss respectively for a given excavation depth. The FE predictions showed that both of these factors influence i. The vertical surface settlement rather than the horizontal surface displacement seemed to be more affected from the variation of E_{inc} and V_L. The optimum value of E_{inc} should be 10^3 kPa/m < E_{inc} < $2x10^3$ kPa/m

(Table 4.8). For larger values (i.e. stiffer soil profiles) the net deformation vector is heading above CL, while for smaller values (i.e. less stiff profiles) the deformation vector is heading below CL similar to Deane and Bassett (1994) findings. The optimum value of volume loss should be $V_L \approx 2\%$ (Table 4.8). In the case where volume loss varies within the following range $1.4\% \leq V_L \leq 2.5\%$ deformation vectors are heading below or above the tunnel CL respectively but definitely within the tunnel area. Further from that range vectors are heading outside the tunnel.

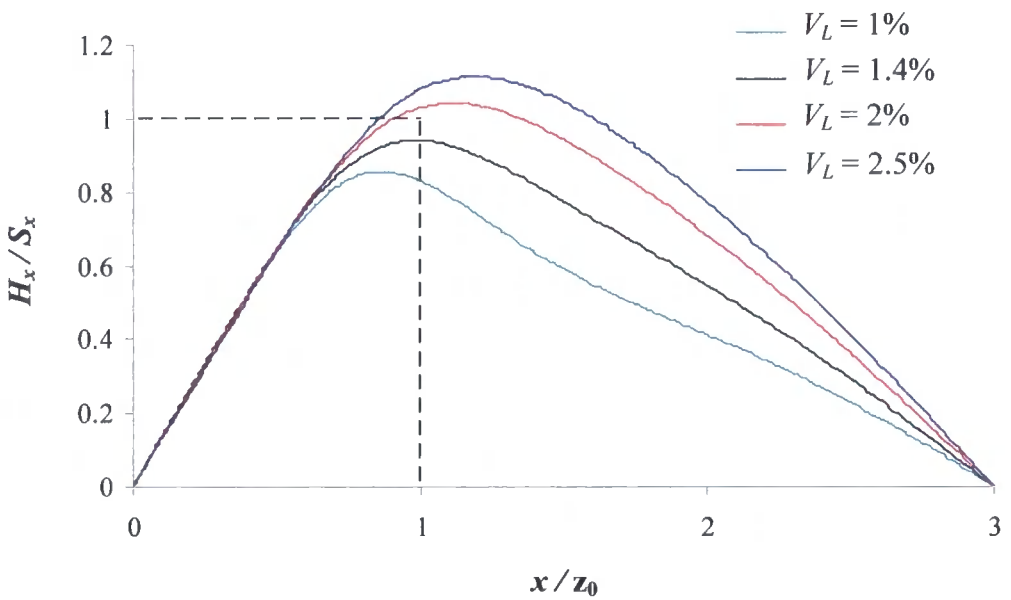

Figure 4.15. Plot of the total surface vectors against the transverse distance x when V_L varies.

Therefore a general rule relating the direction of the total displacement vectors and the four varying parameters cannot be extracted since it seemed that ζ depends on the specific soil conditions and geometry of excavation every time. Further to this it seemed that the sagging zone seemed to be more influenced than the hogging zone.

Another part of the analysis of this chapter was associated with the determination of values for the trough width constant K. Even though a value of $K = 0.5$ is suggested to satisfy most clay profiles (similar to the one modelled in this chapter), the FE predictions showed that a more accurate way to calculate K was through the FE predictions (i.e. K_3). For the soil profile used in this chapter K_3 was found to be closer

to a value of $K = 0.6$ rather than $K = 0.5$. Consequently when greater accuracy is required for the measurement of the trough width parameter i, the value of K_3 should be used instead.

	O'Reilly and New (1982) (optimum value)	Deane and Bassett (1994)	Taylor (1995)	No correlation
z_0	$6 < C/D < 7.7$	$4.3 < C/D \leq 6$	Never	$C/D \geq 7.7$ $C/D \leq 2.9$
D (m)	$D > 6.4$	$3.6 \leq D \leq 6.4$	$D < 3.6$	$D >> 6.4$
E_{inc} (kPa/m)	$10^3 < E_{inc} < 2\text{x}10^3$	$E_{inc} \approx 10^3$	$E_{inc} < 10^3$	$2\text{x}10^3 < E_{inc}$
V_L (%)	$V_L \approx 2$	$1 \leq V_L < 2$	$V_L < 1$	$2 < V_L$

Table 4.8. Summary of the FE predictions regarding the direction of the deformation vectors.

Chapter 5

Finite element mesh generation using Gmsh

5.1 Introduction

The use of three-dimensional (3-D) finite element (FE) models for geotechnics is increasing, in particular for the analysis of tunnelling projects, to simulate the progressive excavation and lining of a tunnel (or tunnels), and to include features such as underground services or surface structures and loading. A major overhead in the use of 3-D FE models is meshing and this is particularly so for tunnelling schemes. Tunnelling is still a very complex construction operation to undertake and considerable effort is required to predict the effects of tunnel construction, interaction with other structures and to ensure stability throughout. Prior to a tunnelling scheme, geotechnical surveys are carried out to learn more about the ground properties and conditions in which the tunnel is to be constructed. This process is vital in order to decide which excavation method will be used. Of prime concern in modern tunnelling in soft ground are the surface settlements and tunnel lining deformations that arise. Despite their small magnitudes their differential nature makes them potentially destructive to brittle surface structures, such as masonry buildings.

Settlement prediction is usually based on a semi-empirical approach as described in many references (e.g. Boscardin and Cording, 1989 and Boone, 1996) but the majority are however incapable of accounting for the presence of any surface structures and any 3-D effects. For this reason, engineers have turned to 3-D FE analysis to make predictions for increasingly complex schemes involving more than one tunnel, where the soil is modelled with elasto-plastic constitutive models. Until

recently 3-D modelling was the preserve of academic research, but it is increasingly being used by industry (e.g. Yeow *et al.*, 2005). Much research is being undertaken to improve modelling for this problem: some recent examples can be found in references Burghignoli *et al.* (2006), Franzius *et al.* (2006) and Jenck and Dias (2006).

To arrive at predictions of the effects of tunnelling using a FE model can be seen as a three-stage procedure: pre-processing, analysis and post-processing. Many papers report the difficulties associated with 3-D FE analysis for tunnelling (Addenbrooke and Potts, 2001; Augarde and Burd, 2001) however the majority concentrate on aspects relating to the analysis stage such as material properties and constitutive modelling. Little has been published to help those attempting to make the pre-processing stage more efficient.

Pre-processing involves the generation of a suitable FE mesh, and imposition of boundary conditions. Preparing, and checking, a mesh for a complex tunnelling simulation can be extremely time-consuming. This chapter introduces a parameterised scheme for automated, more efficient and robust 3-D mesh generation of highly complex tunnelling layouts using a freeware mesh generator (Gmsh). Comparisons are made with mesh generators found in commercial FE software.

5.2 Volume division into elements

Mesh generation is the art of dividing a volume into elements, a subject with a surprisingly long history. Plato and Aristotle were the first who dealt with this issue, almost 2,300 years ago (Senechal, 1981) although obviously not doing this for the purposes of FE analysis! A wide variety of techniques have since been developed to fill a 3-D volume with finite elements and the research literature on this topic is now vast. Thompson *et al.* (1999) and Frey and George (2000) summarise much of the recent development.

Mesh generation can be regarded as a volume-filling technique. These can be broadly divided into structured (uniform and non-uniform) and unstructured approaches. The former are based on generation from two or more groups of parallel lines which intersect (if both groups have parallel lines which intersect then uniform mesh, if only one group has parallel lines which intersect with the other non-parallel group then

non-uniform mesh). Structured meshes are straightforward to generate but can be highly inefficient for complex geometries. Unstructured techniques are more widely used and are usually based on one of the following methods: the advancing front method, the paving method or the 3-D version of Delaunay triangulation method (Topping *et al.*, 2004). Many geotechnical analyses are carried out with the assumption of near-incompressibility (to model *undrained* conditions). In this case it has been shown that tetrahedra outperform hexahedra particularly for linear elements (Bell *et al.*, 1993; Burd *et al.*, 2000). Tetrahedra are also much better for modelling curved boundaries (e.g. a tunnel outline).

5.3 Mesh generators in commercial FE software

The three stages of pre-processing, analysis and post-processing are usually incorporated into a single package in commercial software. Interestingly, the geotechnical software Plaxis installs as a single package but each stage appears as a separate program (*Input, Calculation* and *Output*). In contrast many geotechnical researchers choose to use separate software for each stage. This allows them flexibility to adapt the part in which they are most interested (usually analysis). This approach tends to be error prone due to data transfer. Some commercial packages are restricted to the creation of structured meshes and for tunnelling problems parts of the meshing have to be done by hand.

As an example of the shortcomings of using a structured mesh generator a small and simple single horizontal axis tunnel problem will be discussed. The dimensions of the domain are presented in Figure 5.1. This problem is symmetrical around the vertical tunnel axis thus, only half was modelled. At the beginning, a slice of the mesh including the tunnel was created (Figure 5.2a). The elements used for this analysis were tetrahedra (for the reasons described above), from decomposed hexahedra. This slice was then extruded in the direction of the y-axis (Figure 5.2b). Producing even this simple mesh can be time-consuming. For a series of analyses in a parametric study where, say, the tunnel depth (z_0) or diameter (D) is varied, this must be repeated almost from scratch, each time. Some time can be saved if the first mesh is carefully part-generated as shown in Figure 5.3a and re-meshing for different analyses then involves the sub-section around the tunnel, although care is needed to

ensure coincidence of nodes. This problem is straightforward mainly due to the simplicity of the geometry. Things become more complicated though when the axis is inclined (Figure 5.3b) or even curved (i.e. no symmetry). The procedure is more or less similar as the one described above. This time however, the first block of elements (the elements which form the tunnel in particular) cannot be extruded towards the *y*-axis. This is because the longitudinal axis is now inclined. The whole volume of the inclined tunnel thus, has to be re-designed element-by-element. This procedure is even more time consuming although the coarser elements close to the boundaries can be extruded as before (Figure 5.3a).

The two procedures described above refer to a single tunnel analysis. For more complicated geometries, e.g. twin tunnel construction, meshing time tends to be prohibitive for any user if an extended parametric study is required.

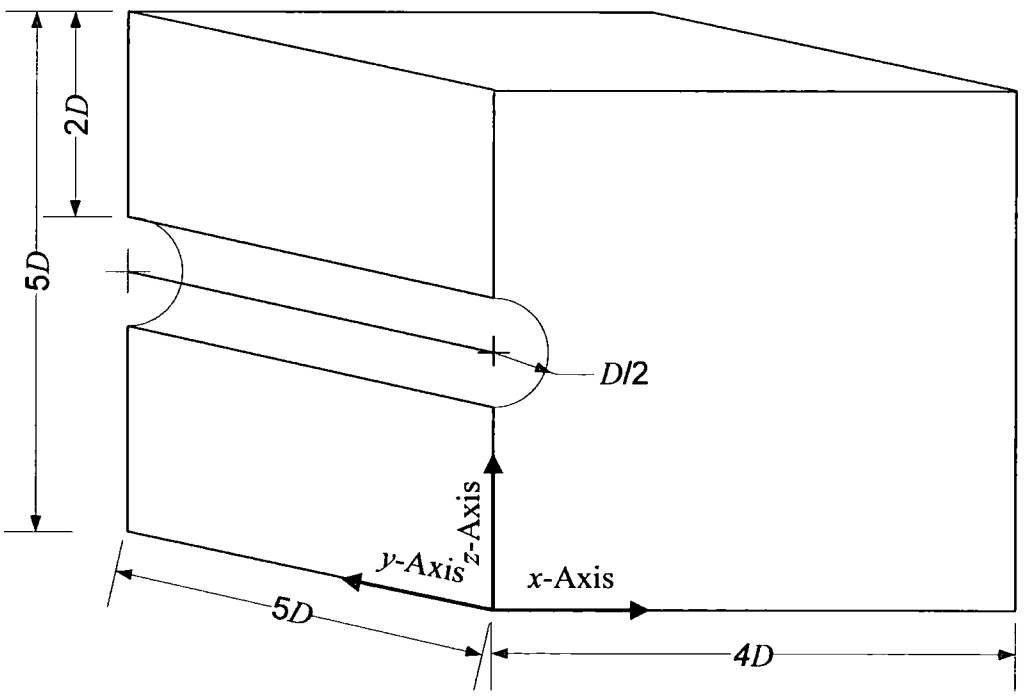

Figure 5.1. 3-D FE analysis of a single horizontal tunnel.

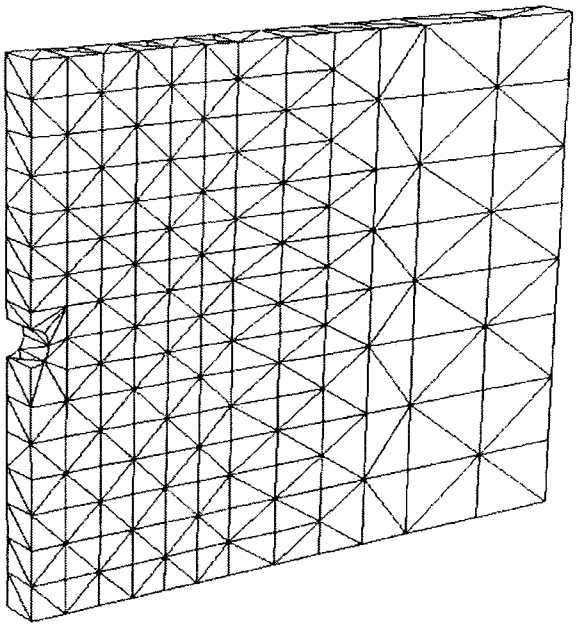

a) Slice of the domain

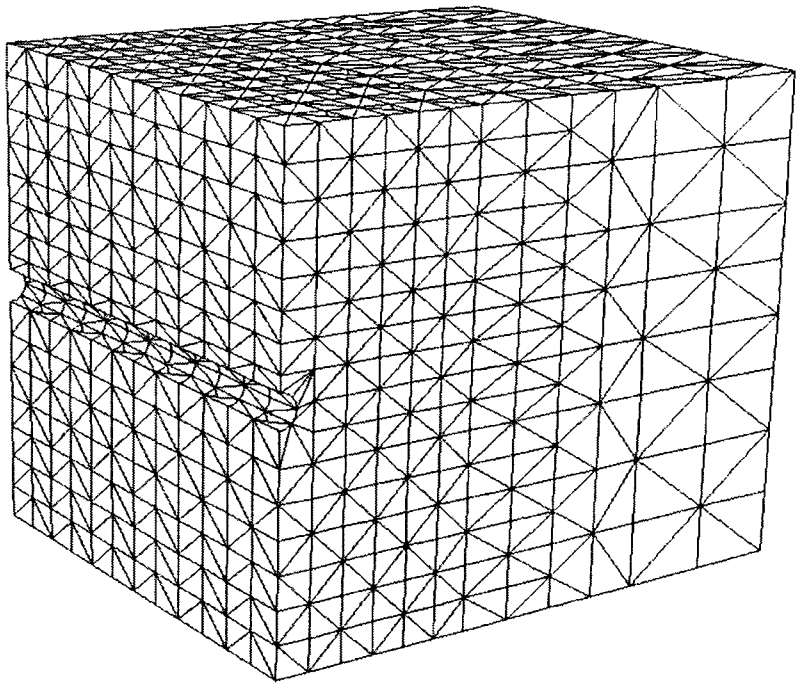

b) Whole domain

Figure 5.2. Meshing of a single horizontal tunnel axis in soft ground using a commercial FE mesh generator.

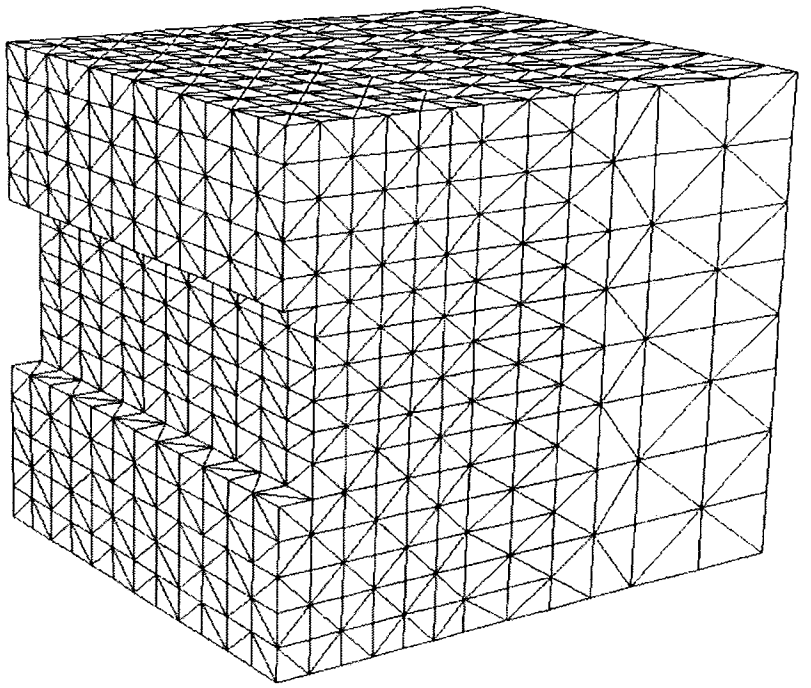

a) Partly generated mesh

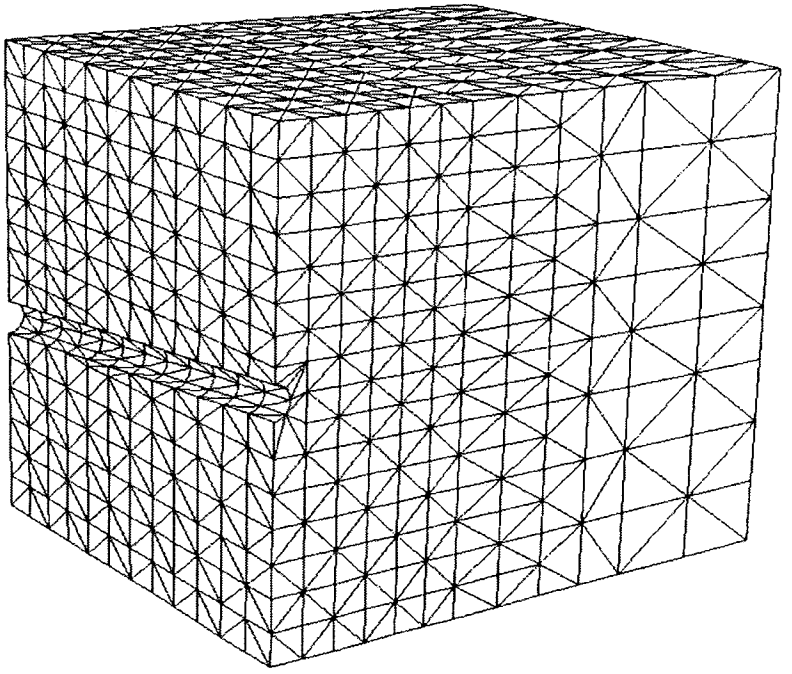

b) Meshing sub-section

Figure 5.3. Meshing of an inclined tunnel axis geometry.

5.4 Parameterized mesh generation

Motivated by the need to generate a large number of meshes for a parametric study of both single and twin-tunnelling, a scheme based on parameterizing analyses has been developed. The mesh generation software used is the versatile freeware package Gmsh (v. 1.65), developed by Geuzaine, C. and Remacle, J.F. (2005). Analysis and visualization use a commercial FE package (Strand7). This chapter focuses on the pre-processing. It has to be stressed here that all the 3-D generated meshes refer to the case of already driven tunnels with their permanent lining installed. Thus finite elements are not generated within the volume of the tunnels. The purpose of this chapter is to examine the issues associated with pre-processing, not a full analysis.

The parameters that will be used to describe a range of geometries are shown in Figures 5.4 and 5.5. Where D is the tunnel diameter, $x1$ and $z1$ are the horizontal and vertical shift of the tunnel axis respectively, and $k1$ is the tunnel inclination along the z-axis. The dimensions of the problem are identical to those described for the commercial structured mesh generator in the previous section (see Figure 5.1).

Gmsh is a fully automated 3-D unstructured tetrahedral mesh generator in which the Delaunay triangulation algorithm is implemented in 3-D. This algorithm is based on the assumption that no other points exist within the circumcircle of a triangle apart from the three points which form the triangle. This definition is adequate for a 2-D space. For a 3-D space the equivalent algorithm can be expressed as follows: no points exist within the circumsphere of a simplex other than those which form it.

Gmsh works either via a GUI or from an ASCII file containing commands. An attractive feature is the possibility of variable substitution in this input file. For instance, the outer dimensions of the mesh can be defined as X, Y, Z and their values defined at a single point prior to their first use in the file. This allows easy generation of different meshes by variation of the definitions, a major improvement from the approach using structured meshes described above, and a positive advantage for parametric studies. One of its main capabilities is the specification of a local adaptive parameter "characteristic length" (*ChL*) which can be applied to selected points in the model. In this way, the user can refine some areas within the mesh to achieve greater accuracy in the areas of interest. Such areas can be between materials of different

properties (i.e. soil-structure). However, engineering judgement and experience is required in order to decide on the level of detail within the domain.

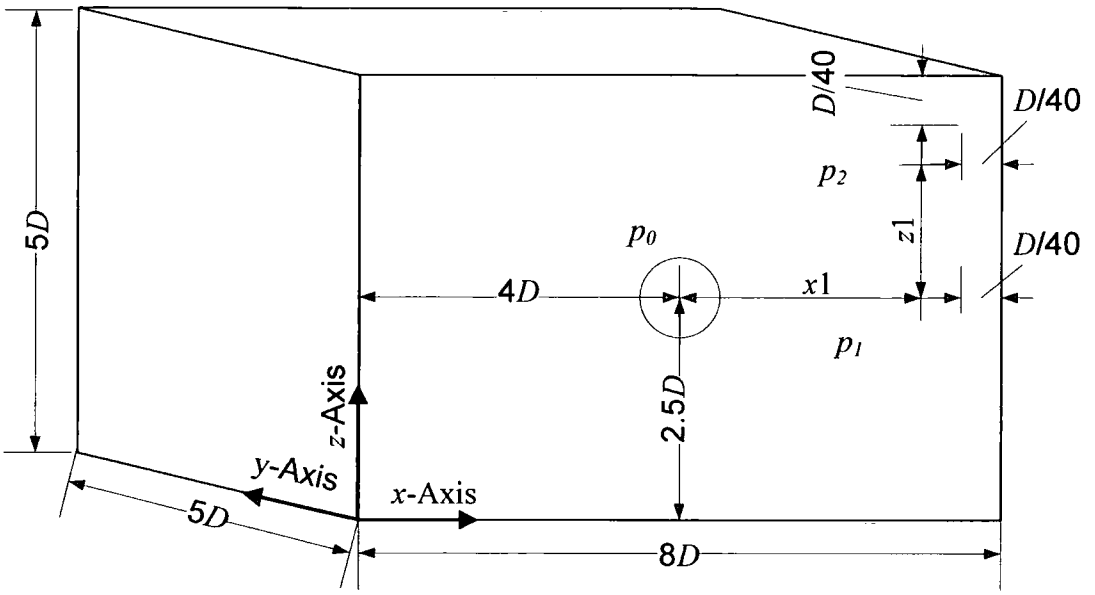

Figure 5.4. Three different tunnel positions (p_0, p_1 and p_2) of a horizontal tunnel.

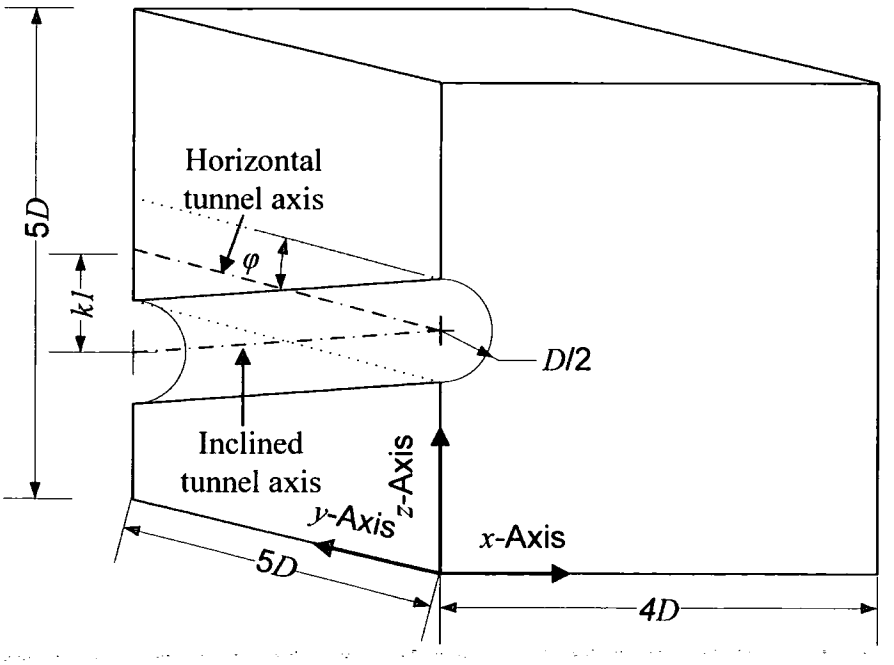

Figure 5.5. Inclined tunnel geometry.

5.5 Mesh quality

In order to measure and validate the quality of a generated mesh various shape measures are used. The most common found in literature are presented by Naylor (1999) and Field (2000). For convenience and compatibility purposes the range of these shape measures is [0, 1] with unity indicating an equilateral element. Gmsh uses the following shape measure: aspect ratio (γ) which is defined as:

$$\gamma = \frac{12}{\sqrt{6}} \frac{[3V/(\sum FA)]}{L} \tag{5.1}$$

where V is the volume of the element, L is the maximum edge length and $\sum FA$ is the sum of the face areas.

5.5.1 Description of the code

In this section mesh generation for the simplest tunnelling scheme (single tunnel with a horizontal axis) will be described. In this way the difference in philosophy to the structured approach described above will become evident. The user has to write a simple code in a text file (see Appendix A) as an input file. The main input operations executed by Gmsh in order to generate a FE mesh are presented with a flowchart in Figure 5.6. Each operation is described in detail below in this section.

The geometry of the problem should have a bottom-up orientation. At the beginning of the file, several parameters which specify the geometry of the domain (see Figures 5.4 and 5.5) and the size of the finite elements are defined with the use of numeric values or by employing other previously initialized parameters as follow:

$D = 4;$
$X = 8D;$
$Y = 5D;$
$Z = 5D;$
$ChL1 = D;$

Where D is the tunnel diameter, X, Y and Z are the dimensions of the domain in space while $ChL1$ refers to the size of the finite elements within the mesh. In this case the

domain consists of elements of the same size. In the case where the domain consists of elements of different sizes then more *ChLn* values should be initialised (where *n* refers to the number of the different *ChL* values). After the initialization of the above parameters, points, lines surfaces and volumes have to be defined. These are called "*elementary entities*" in Gmsh. An identification number is assigned to each elementary entity within parentheses (see Equations 5.2 to 5.10).

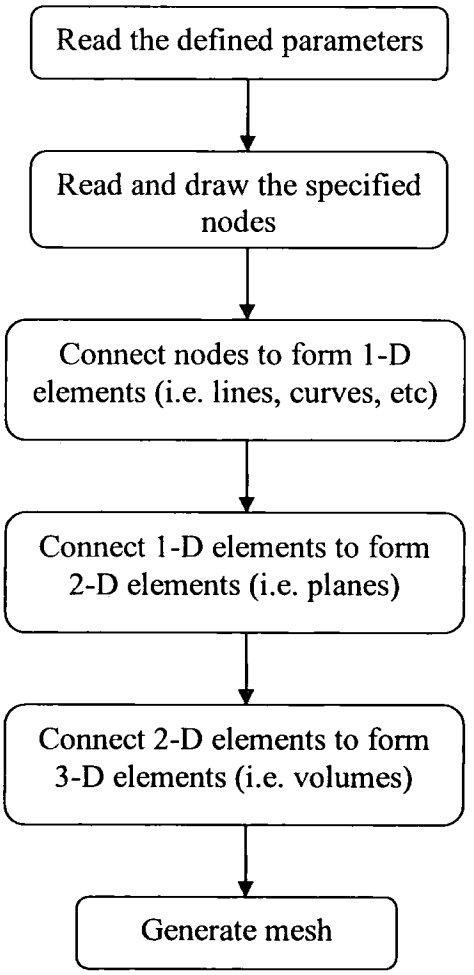

Figure 5.6. Flowchart of the main operations executed by Gmsh in order to generate a mesh.

Points at the boundaries of the domain are defined as:

$$\text{Point}(1) = \{x, y, z, ChL1\}; \tag{5.2}$$

The first three parameters within the braces refer to the coordinates of the particular point in the 3-D space (either numeric values or in respect to the global coordinates *X*,

Y and *Z*) while the fourth refers to the characteristic length (*ChL*1) of that particular point. Every point can have the same or a different characteristic length compared to the others. By this procedure one can change the values at the very beginning of the code to alter the geometry of the problem or the density of the generated mesh rather that having to re-design part of the domain manually (as in the structured commercial mesh generators). This is where most of the time is saved compared to other commercial packages.

The next step is to connect two consecutive points in order to form a line, an arc, a spline, an ellipse or any other type of curve. For the current design (Figure 5.4) lines and arcs were employed only, e.g.

Line (1) = {1, 2}; (5.3)

Circle (1) = {2, 1, 3}; (5.4)

The values within the braces of the former command ("Line") refer to the identification numbers of the points which will be connected. The middle value within the braces of the latter elementary entity ("Circle") refers to the origin point of a circle while those on either side refer to the start and end point of the circle's arc.

Then a "Line Loop" command creates a closed loop of lines, circles or ellipses which in turn, later on will form a surface. In order to create surfaces, a distinction has to be made between a "Plane Surface" (formed by straight lines) and a "Ruled Surface" (formed by curved lines), e.g.

Line Loop (1) = {1, 2, 3, 4}; (5.5)

Plane Surface (1) = {3}; (5.6)

Ruled Surface (1) = {5}; (5.7)

The numbers within the braces of the "Line Loop" command refer to the identification numbers of the elementary lines or circles. A line loop should form a closed loop in Gmsh. The values within the braces of "Plane Surface" and "Ruled Surface" refer to the identification number of the "Line loop" command. "Surface Loop" creates a closed loop of elementary surfaces which in turn, later on will form a volume.

Surface Loop (1) = {1, 2, 3, 4}; (5.8)

Volume (1) = {1}; (5.9)

The values within the braces of the "Surface Loop" command refer to the identification number of the elementary surfaces which will form this loop. The latter has to represent a closed volume. Finally the last command indicates the creation of a volume. The number in the braces of the "Volume" command denotes the identification number of a "Surface Loop". The Gmsh code is fully presented in the Appendices A to E.

In order to adjust the level of the tunnel axis to the desired position the user has to define two new parameters ($x1$ and $z1$, Fig. 5.4) at the beginning of the code and introduce them within the braces of the "Point" command as well. With this procedure the tunnel axis can be reallocated horizontally and vertically. Another parameter ($k1$) may be introduced in the code in order to create an inclined tunnel geometry. The opening of the tunnel is fixed at the same level as for the horizontal geometry. The ending will be lower this time. Therefore $k1$ will be introduced within the braces of the "Point" command when defining the coordinates of the ending hole only. When $k1 = 0$ then the axis is horizontally aligned. For non zero values though, the tunnel becomes inclined and the angle of inclination is φ (Fig. 5.5) where:

$$\varphi = \tan^{-1}\left(\frac{k1}{Y}\right) \tag{5.10}$$

Likewise more parameters can be introduced within the coordinates of the points which will alter the shape and the size of the geometry. They will only be initialised if they have non-zero values though.

5.5.1.1 Equal size finite elements

In order to validate the quality of meshes using this system, a series of generation scenarios are now described, using the code which is described above and fully presented in Appendix A. In the first case the size of the finite elements is the same all over the domain. In the second the elements within the tunnel and their projection to the surface have a different size from the rest in the domain. Thus two different characteristic length values are introduced ($ChL1$ and $ChL2$). In both cases the

dimensions of the problem and tunnel diameter are constant. The two parameters which vary are the level of the tunnel axis (i.e. $x1$, $z1$) and the size of the finite elements ($ChL1$ and $ChL2$).

In the first case a tunnel with a diameter of D = 4m is driven at a depth of $z_0 = 2.5D$ having its longitudinal axis horizontal. The dimensions of the domain are presented in Figure 5.4. ChL throughout the domain is $D/5$ (in m) and D in the first and second analyses respectively. The two different ChL values are chosen in order to observe how mesh quality is affected by the size of the elements while the position of the tunnel varies. Three different positions are chosen for this purpose (Fig. 5.4). For the first (p_0) the tunnel is driven in the middle of the domain (i.e. the most favourable position in the mesh). In the second (p_1) the distance between the right springline and the right vertical boundary is just $D/40$ (i.e. an unfavourable position and, in practice, not a mesh an analyst would actually use). Finally in the third (p_2) the distance of both the crown and the right springline from the top and right vertical boundaries respectively is $D/40$ (i.e. the worst position in the whole domain). A total of six analyses thus are performed in this section.

Figure 5.7 plots the number of the generated finite elements against their quality (γ factor) for a *very fine* mesh ($ChL1 = D/5$). From this figure it is obvious that the location of the tunnel does not affect the quality of the finite elements notably, even for the two most unfavourable tunnel positions (i.e. p_1 and p_2). This can be explained for the following reasons. The mean values of γ (the average value of the distribution) shown in Table 5.1 are almost unvarying for each of the three tunnel positions. The number of the generated tetrahedra is roughly constant regardless of the position of the tunnel. Hence, the required time for the generation of these elements is roughly the same as well. The three γ curves are smooth and almost identical having their modal value of γ (the most frequent value in a distribution) at approximately $\gamma = 0.77$. This is an indication that large areas of the domain consist of elements of good quality, since the area where most of the elements are projected is around the above mentioned γ value, which is close to unity. For the two unfavourable positions though (i.e. p_1 and p_2) there are a few tetrahedra (less than 1% of the total number of tetrahedra) with $0.25 < \gamma < 0.5$. This can be attributed to the position of the tunnel (i.e.

close to the boundaries) since there is not sufficient space between the liner and the boundaries to form equilateral tetrahedra.

Figure 5.8 shows that for a *coarse* mesh (*ChL1* = *D*) the quality is vastly affected by the position of the tunnel unlike the *very fine* mesh case described above. The three γ curves this time are not identical, having different mean values of γ for every different position (p_0, p_1 and p_2). The mean γ value decreases radically from p_0 to p_2 varying from 0.67 to 0.49 (Table 5.2). The maximum of these γ values correspond to the most favourable position of the tunnel in the domain (p_0) while the minimum value corresponds to the most unfavourable position (p_2). This is an indication of mediocre to bad mesh quality. The three modal values though are only slightly affected. The comparison of Figure 5.8a with Figure 5.7a at the same axis position (at p_0) but with distinct *ChL* produces acceptable results. At p_1 and p_2 though (Figures 5.8b and 5.8c), the projected areas are totally different compared to the cases shown in Figures 5.7b and 5.7c. This time the area where most of the elements are projected is shifted to the left, towards the zero γ value which implies irregular tetrahedra and hence poor mesh quality. Various badly shaped tetrahedra (the shape measure of these elements is between $0 < \gamma < 0.5$, see Figure 5.8a and 5.8b) which attempt to fill in the limited space between the liner and the boundaries at the two most unfavourable positions (p_1 and p_2) are generated. Hence, the number of nodes and the number of the generated tetrahedra increase as the position of the tunnel shifts from p_0 to p_2. This increases the required time for the generation of the mesh as well.

In summary, from the first case, where *ChL* is the same throughout the domain, it is evident that as the sizes of the elements increase, the quality of the mesh deteriorates, especially when the tunnel is placed closer to the boundaries (positions p_1 and p_2). The analysis performed by Gmsh for the same *ChL*, is robust when the size of the domain consists of *very fine* elements (compared with the size of the domain). This is not the case for a coarser mesh though. For this latter case roughly 57 times less nodes are produced and approximately 65 times less time is required to generate the 3-D mesh compared to the first case where *ChL* = *D*/5. The PC characteristics are presented in Table 5.1.

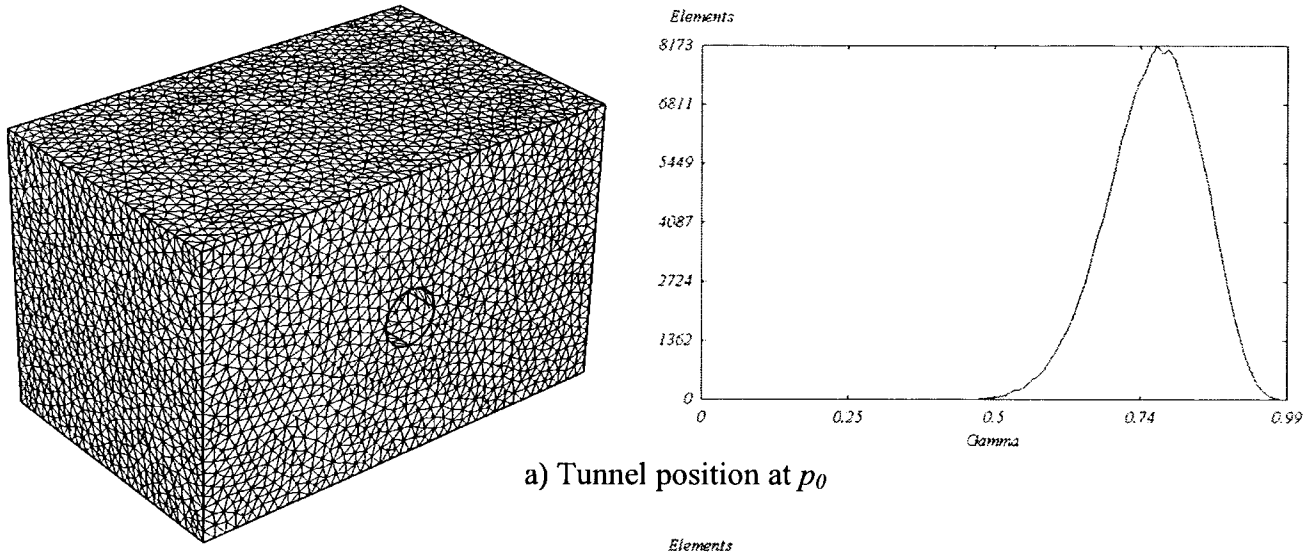

a) Tunnel position at p_0

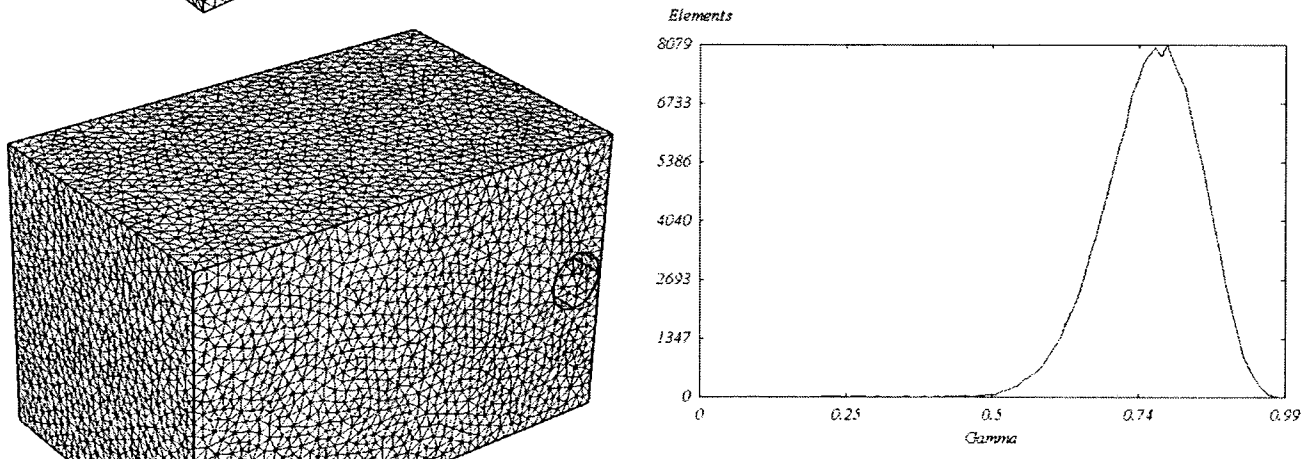

b) Tunnel position at p_1

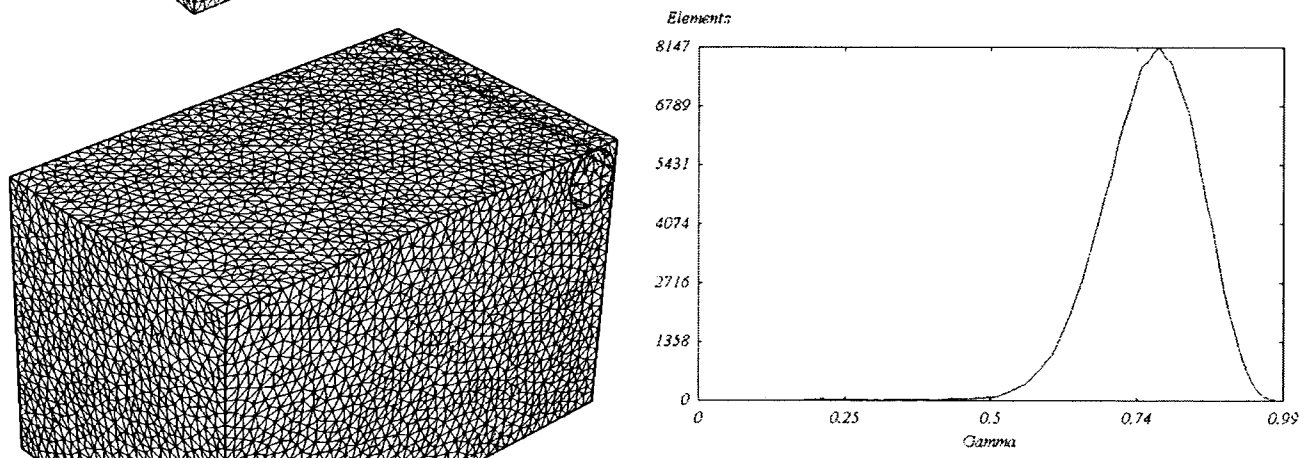

c) Tunnel position at p_2

Figure 5.7. Mesh quality measurements of a very fine mesh (when $ChL1 = D/5$) for three different tunnel positions (p_0, p_1 and p_2).

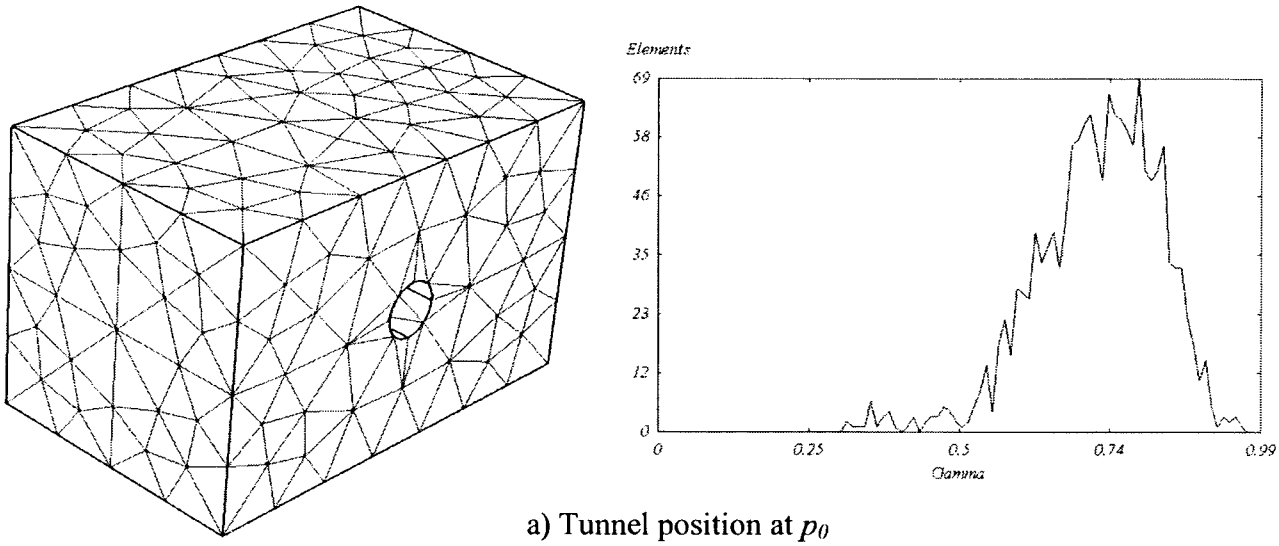

a) Tunnel position at p_0

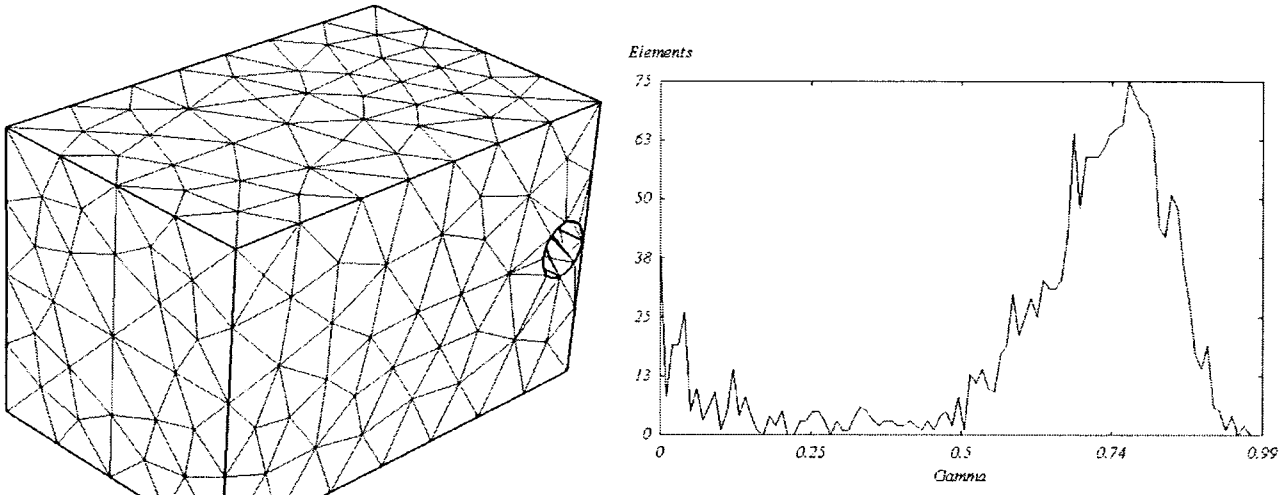

b) Tunnel position at p_1

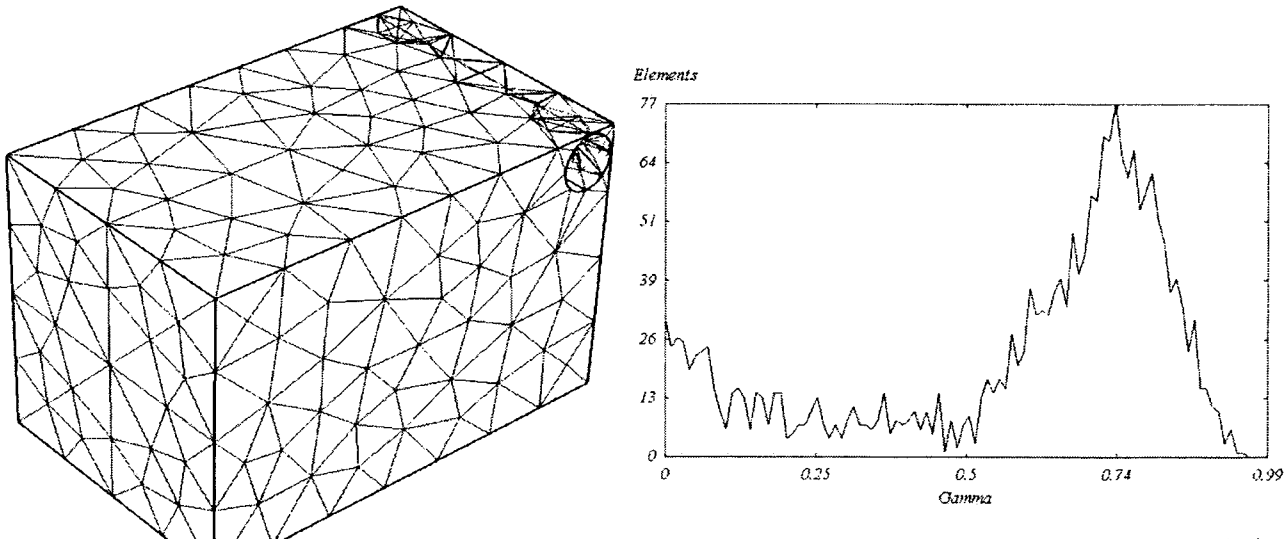

c) Tunnel position at p_2

Figure 5.8. Mesh quality measurements of a coarse mesh (when *ChL1* = *D*) for three different tunnel positions (p_0, p_1 and p_2).

PC characteristics		Processor		CPU		RAM	
		Intel (R)		2.66GHz		192MB	
D (m)	4	Position	No. of nodes	No. of 10-noded Tetrahedra	Time for 2D (s)	Time for 3D (s)	*Gamma* (γ) (mean)
X (m)	8D						
Y (m)	5D						
Z (m)	5D	p_0	229,726	163,140	< 1.0	66.3	0.769
ChL (m)	D/5	p_1	228,985	162,541	< 1.0	64.3	0.768
z_0 (m)	Z/2	p_2	230,185	163,471	< 1.0	68.8	0.767

Table 5.1. Equal size of finite elements (*ChL* = D/5).

D (m)	4	Position	No. of nodes	No. of 10-noded Tetrahedra	Time for 2D (s)	Time for 3D (s)	*Gamma* (γ) (mean)
X (m)	8D						
Y (m)	5D						
Z (m)	5D	p_0	3,123	1,546	0.04	0.65	0.670
ChL (m)	D	p_1	4,128	2,078	0.03	0.8	0.529
z_0 (m)	Z/2	p_2	4,894	2,493	0.04	1.0	0.488

Table 5.2. Equal size of finite elements (*ChL* = D).

5.5.1.2 Different size of finite elements

In order to optimise mesh quality (and hence solution accuracy) at the same time as reducing the computational time needed to perform a 3-D analysis a combination of coarse and fine finite elements is required; the former at the mesh boundaries, the latter around the tunnel. Another reason for choosing this strategy is to try and fit the mesh to the chosen geometry. Hence, refinement around the tunnel layout takes place in order to overcome the difficulties which arise in the coarse mesh described in Section 5.5.1.1 (when *ChL* = D, see Figure 5.8). Thus two different *ChL* values are now introduced (*ChL*1 for the boundaries of the domain, *ChL*2 for the tunnel liner and the area above it. This is achieved by introduced some surface nodes which have the same ChL2 value as the tunnel liner). All the other parameters vary in the same way as described in the first case. In the analyses performed in this section the following two characteristic length values are used *ChL*1 = D and *ChL*2 = D/5. These

analyses are carried out in order to assess how local mesh refinement influences the overall quality of the mesh.

The beneficial impact of refinement is vividly revealed by comparing Figures 5.8 and 5.9. The three γ curves have been improved significantly (particularly at the two less favourable positions p_1 and p_2) since the mean and modal values of these plots have shifted further towards unity. Table 5.3 shows a decrease in the number of nodes (and as a consequence the number of elements) produced and the time required for the generation of the 3-D mesh as the tunnel axis moves from p_0 to p_2. This decrease is attributed to the reduction of the refinement zone as the tunnel shifts from the centre of the domain towards the boundaries. Thus less refined elements are produced around the tunnel (since they are restricted by the boundaries) and less time is required for the generation of the 3-D mesh. By moving the tunnel axis from p_0 to p_1 and p_2 only half and a third of the nodes of the p_0 case are generated respectively. Consequently the required time for the generation of the 3-D mesh reduces by half and a third respectively compared to the p_0 case as well. However, the mean γ values only slightly differ.

In total, it can be said that mesh refinement ameliorates significantly the quality of a coarse generated mesh which then can produce finite elements of equivalent quality to a really fine generated mesh (see Figures 5.7 and 5.9). Furthermore, bigger areas of equilateral tetrahedra are formed in the domain. This is the case particularly when the tunnel lies at its most favourable position within the domain (at p_0). However even when it is placed closer to the boundaries (positions p_1 and p_2) the results are comparable and acceptable. Once more the analysis performed with Gmsh proved to be robust.

D (m)	4	Position	No. of nodes	No. of 10-noded Tetrahedra	Time for 2-D (s)	Time for 3-D (s)	*Gamma* (γ) (mean)
X (m)	8D						
Y (m)	5D						
Z (m)	5D						
ChL1 (m)	D	p_0	62,888	44,153	0.26	15.5	0.670
ChL2 (m)	D/5	p_1	36,304	24,159	0.23	8.4	0.664
z_0 (m)	Z/2	p_2	24,120	15,169	0.22	5.6	0.653

Table 5.3. Different size of finite elements (*ChL*1 = D and *ChL2* = D/5).

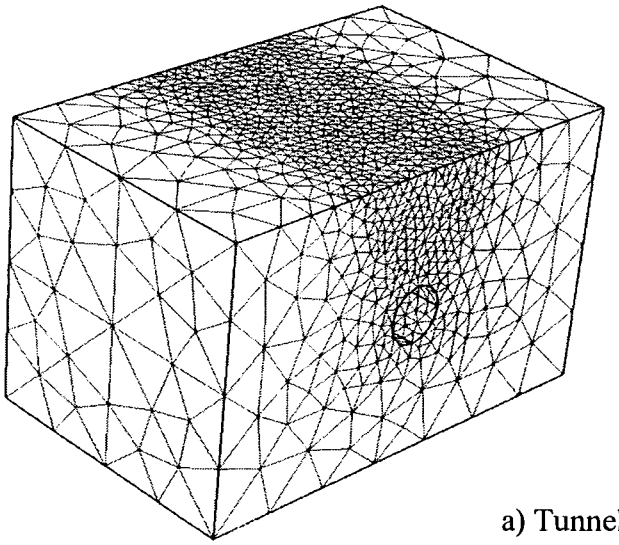

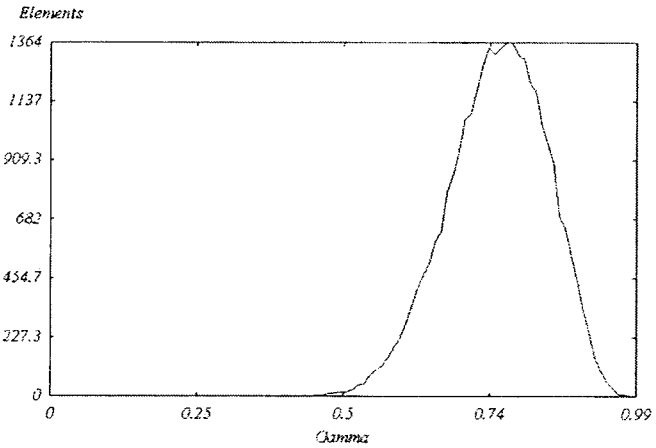

a) Tunnel position at p_0

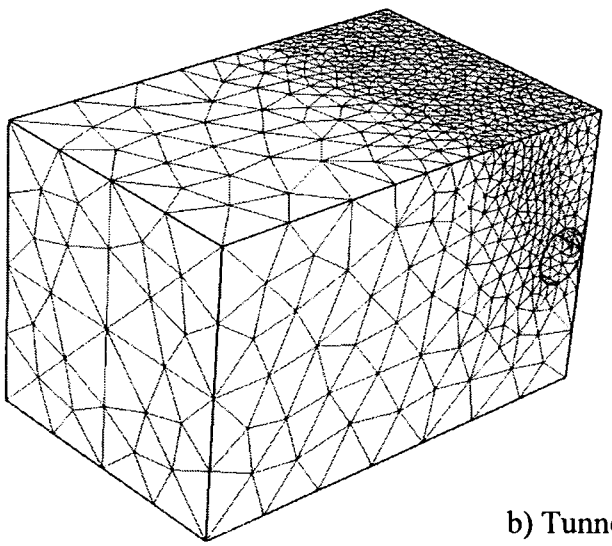

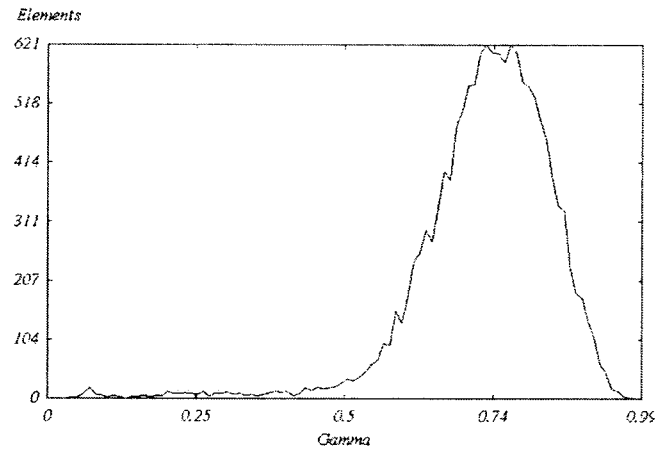

b) Tunnel position at p_1

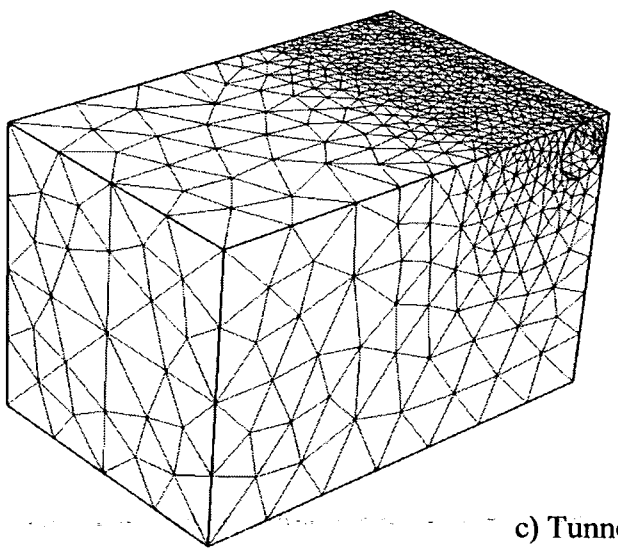

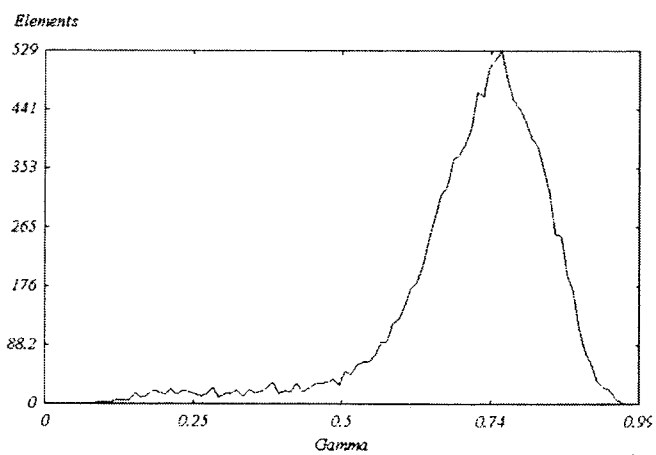

c) Tunnel position at p_2

Figure 5.9. Mesh quality measurements of a refined mesh for three different tunnel positions.

5.6 Evaluation of the meshes used for the 3-D analyses

5.6.1 Single tunnel geometry

In the current section an evaluation is made of the single tunnel geometry mesh used to run the 3-D analyses in Chapter 7. The dimensions of the domain are shown in Figure 5.10. These dimensions were chosen to fulfil the requirements presented in Chapter 7 in order to produce acceptable solutions in terms of computational time, space and convergence. These requirements deal with the twofold problem of locally varying the mesh density (e.g. around the tunnel liner) while keeping the computer resources, which are required to carry out 3-D FE analyses using commercial packages, (e.g. Strand7) low. The Gmsh code written for this case is presented in the Appendix B.

Three areas of different mesh density can be identified (Figures 5.10 and 5.11). At the eight points lying on the corners of the domain a characteristic length value of $ChL1 = 18D/4$ is used. This figure creates relatively large elements at the boundaries. At the points around the tunnel as well as those on the surface which are used to define the loaded areas a smaller value is employed ($ChL2 = 3D/4$) to attain greater accuracy around these areas. Finally a third region ($ChL3 = 9D/4$) is used to account for a smoother transition between adjacent elements which have the two previously mentioned extreme values (Figure 5.10).

Figure 5.11 shows the auto-generated meshes for the case of horizontal tunnel axis as well as the quality measurements (using the γ factor) of these finite elements. The required time for the generation of the 3-D mesh is carried out in about 1 sec while the mean γ value is approximately 0.7 (Table 5.4). From the γ plot it is evident that the vast majority of the finite elements lie above the value of 0.5. This indicates that the quality of the generated tetrahedra in total is above average. The curve is fairly smooth with its mode value close to its mode.

5.6.2 Twin tunnel geometry

In this section twin tunnelling schemes (tunnels horizontally and vertically aligned) will be presented. Thus it will become clear how the presence of a second tunnel may

influence the quality of the mesh as this was presented in Section 5.6.1 for the single tunnel case. The geometric characteristics of the domain are the same as for the single tunnel case. The new Gmsh code written for the current geometry is presented in Appendix C. Three new parameters are introduced which are used to position the second tunnel within the domain (Figure 5.12). These are $x2$, $z2$ and $k2$. The first two shift the tunnel axis horizontally and vertically respectively while the third indicates the inclination of the tunnel along the z-axis. The finite elements adjacent to the second tunnel can have the same or a different size compared to the first. In this case though, it was decided that both tunnels consist of exactly the same density. Thus, once more three different density areas (identical to those described in Section 5.6.1) are identified in the domain.

Three different geometries of multiple tunnelling are examined in this section.

- The case of twin tunnelling when both are horizontally aligned (*TH* case, Figure 5.12a).
- The case of twin tunnelling where the tunnels are vertically aligned (*TV* case, Figure 5.12b).
- The case of multiple tunnels where the first tunnel is horizontally aligned while the second is inclined (*MHI* case, the inclination angle is 4°, Figure 5.13).

Figure 5.12 shows the generated meshes and the corresponding evaluation of their quality for the above mentioned *TH* and *TV* cases. For the *TH* case the pillar width is $P = 1D$ while for the *TV* case the pillar depth is $P_D = 1D$. The number of nodes (and consequently the number of finite elements) produced are slightly higher in the *TH* case. This can be attributed to the wider zone of generated tetrahedra having a fine size ($ChL2 = 3D/4$). Consequently, it takes slightly longer to generate the mesh. In both cases the mean γ value is in excess of 0.7 while the vast majority of the finite elements are projected above 0.5 (see Table 5.5). Once more this is an indication of good quality of tetrahedral elements. In total it can be said that the position of a second tunnel marginally affects the quality of the mesh.

In the *MHI* case where the axis of the second tunnel is inclined approximately 20% more finite elements are generated (creating a large dense area around the tunnels) compared to the other two cases (*TH* and *TV*), for the same reason described above. Thus more time is required for the meshing (roughly 30%). Given that more fine

elements are generated for this particular geometry, the overall quality of the mesh slightly ameliorates. Another result which supports the latter finding is the mean γ value which in this case increases to 0.72.

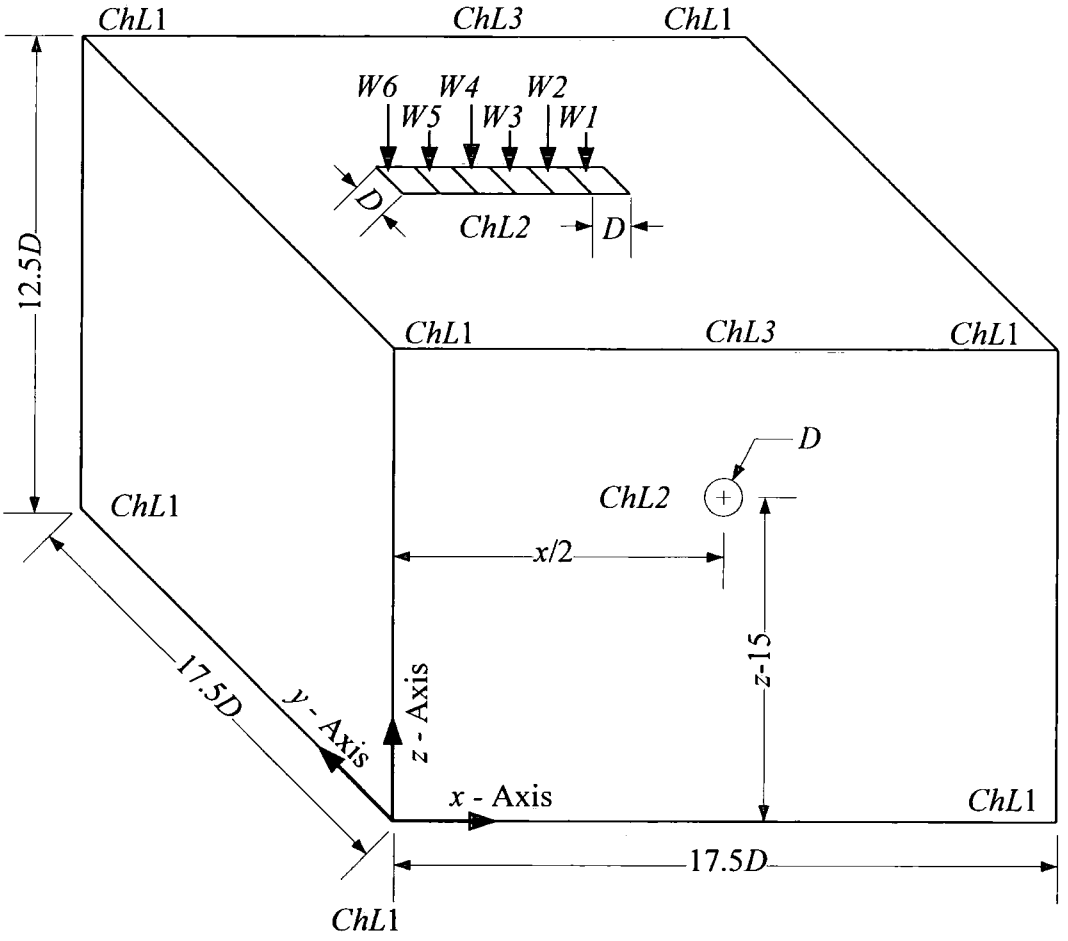

Figure 5.10. Dimensions of the domain.

By comparing both the mean and modal values as well as the shape of the γ curves for the single and twin tunnel cases, (see Figures 5.11 to 5.13 and Tables 5.4 and 5.5) the beneficial impact of the second tunnel to the quality of the mesh is identified. The explanation is that the existence of the second tunnel introduces another dense area similar to the single tunnel case. This refinement thus, improves the overall condition of the generated finite elements. However, more nodes (and hence, more tetrahedra) are generated (almost 80%) which in turn increase the amount of time required for the generation of the 3-D mesh by almost 50% for the *TH* and *TV* cases and 100% for the *MHI* case.

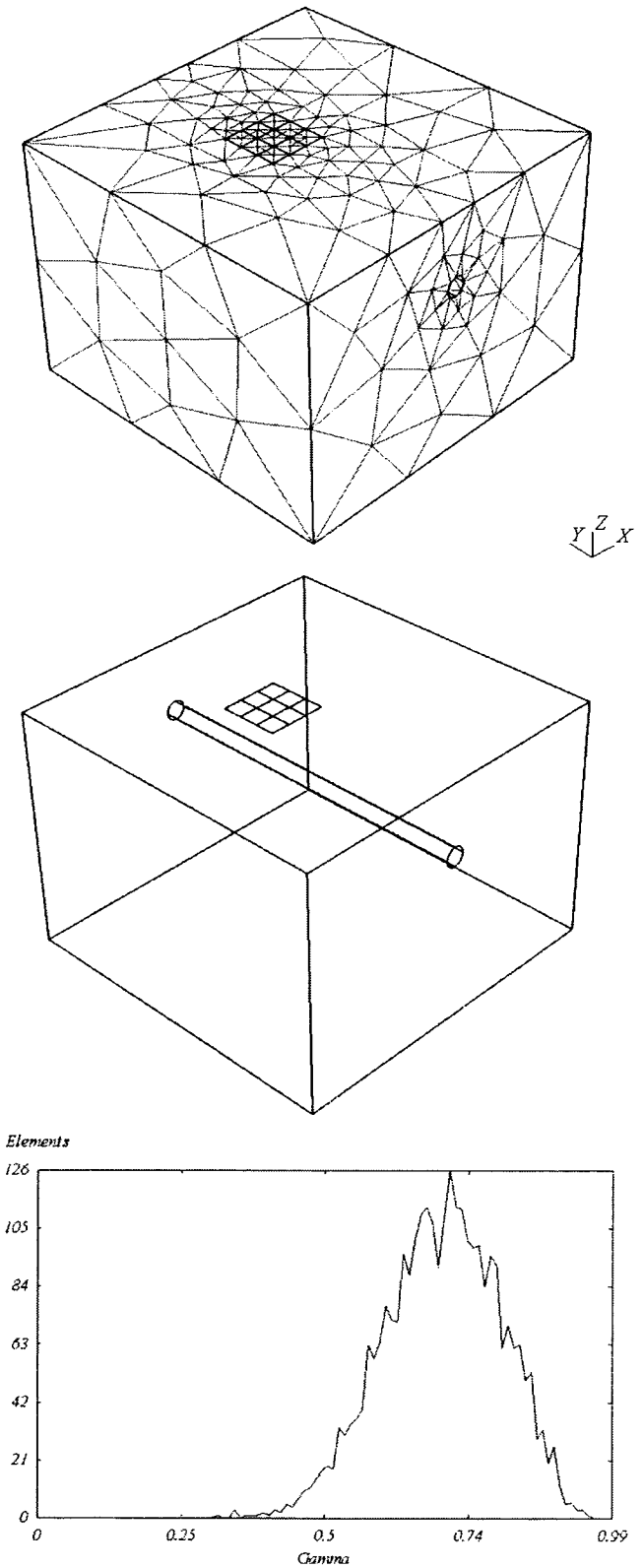

Single horizontal at z_0 = 15m

Figure 5.11. Single horizontal tunnel case.

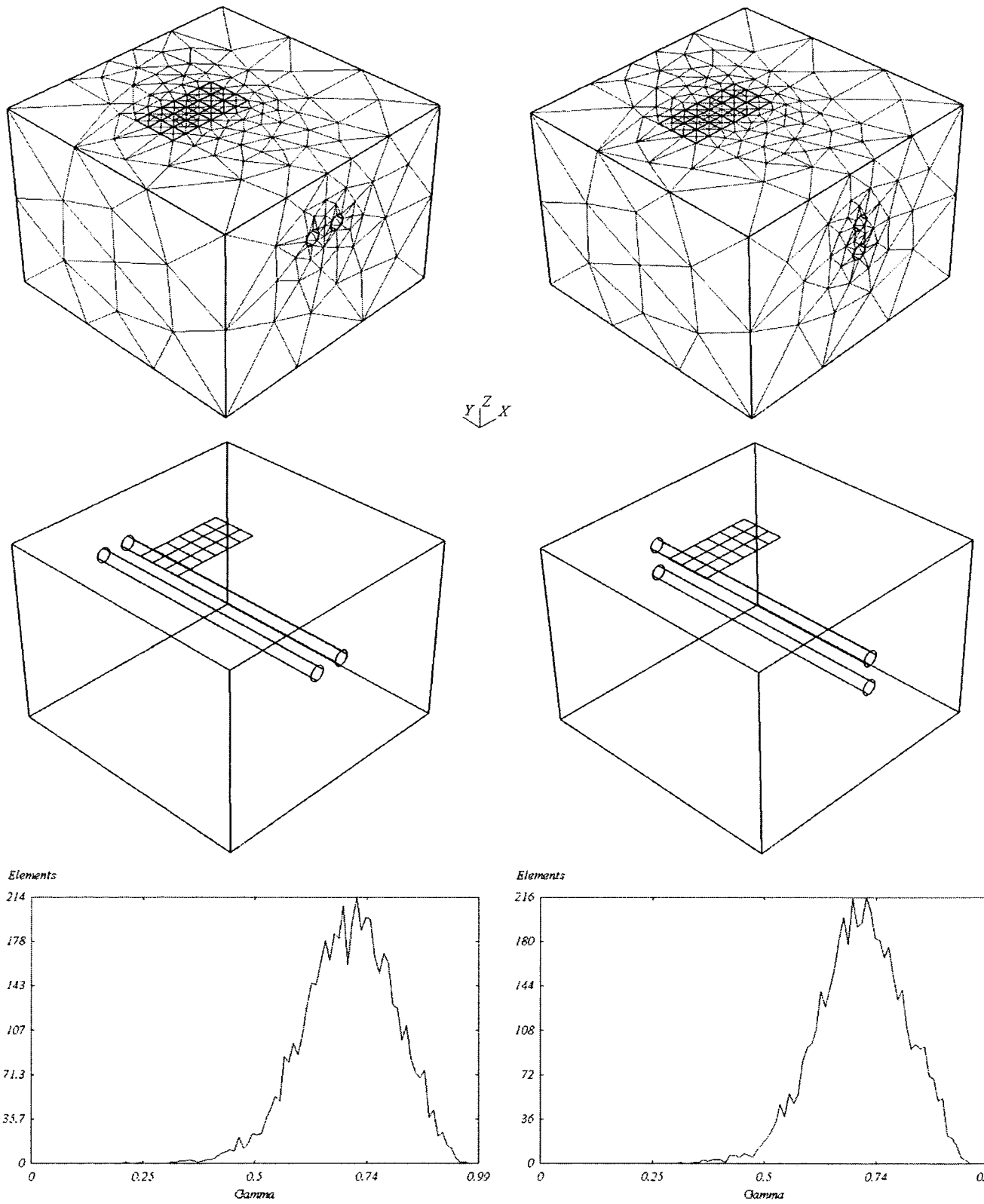

a) Twin tunnels horizontally aligned

b) Twin tunnels vertically aligned

Figure 5.12. Twin tunnel geometry for the a) *TH* and b) *TV* cases.

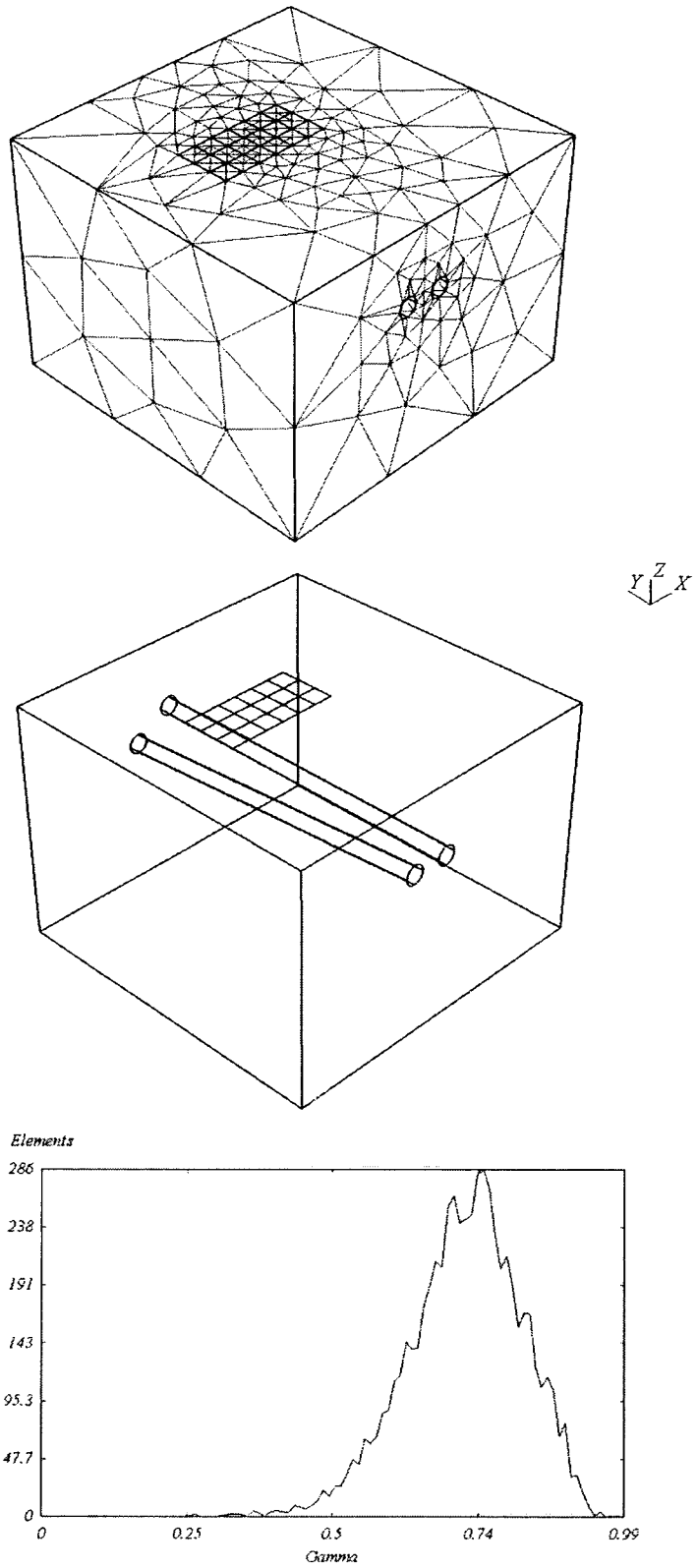

Figure 5.13. Twin tunnel geometry where the left tunnel is inclined (the inclination angle is 4°) while the right is horizontally aligned (*MHI* case).

X (m)	Y (m)	Z (m)	D (m)	z_0 (m)	*ChL1* (m)	*ChL2* (m)	*ChL3* (m)	*ChL4* (m)
17.5*D*	17.5*D*	12.5*D*	4	15	*18D*/4	*3D*/4	*9D*/4	*3D*/4
No. of nodes		No. of 10-noded Tetrahedra			Time for 2D (s)	Time for 3D (s)	*Gamma (γ)* (mean)	
4,574		2,929			< 0.1	0.9	0.701	

Table 5.4. Single horizontal tunnel case.

	X (m)	Y (m)	Z (m)	D (m)	z_0 (m)	*ChL1* (m)	*ChL2* (m)	*ChL3* (m)	*ChL4* (m)
	17.5*D*	17.5*D*	12.5*D*	4	15	*18D*/4	*3D*/4	*9D*/4	*3D*/4
	No. of nodes		No. of 10-noded Tetrahedra			Time for 2D (s)	Time for 3D (s)	*Gamma (γ)* (mean)	
TH case	7,714		5,038			< 0.1	1.484	0.707	
TV case	7,502		4,878			< 0.1	1.359	0.713	
MHI case	9,277		6,207			< 0.1	2.234	0.723	

Table 5.5. Twin tunnel cases.

5.7 Dealing with input and output files

The Gmsh output file (*.msh) consists of the results from the generated mesh in a specific format. In this file the following are presented: *i*) the unique identification number of each node as well as their coordinates and *ii*) the unique identification number of each finite element with the 2-D (six-noded triangles) and the 3-D (ten-noded tetrahedral) element topologies.

The *.msh file is further processed in order to achieve compatibility for the Strand7 input file (*.txt) to run the analyses. The main application of the compatibility process attempts to cope with node re-ordering of the ten-noded tetrahedral. Figure 5.14 shows the difference in node ordering of the latter type of 3-D finite elements between Gmsh and Strand7. Node ordering for the 2-D finite elements is the same regardless of their type (i.e. linear or quadratic variation of the displacement field of triangular or quadrilateral elements).

Some extra data have to be added in the Strand7 input file prior to the analysis stage such as: external applied loads, boundary conditions, material properties and sequence of construction or modelling. These data can either be written directly in the ASCII input file (*.txt) or added through Strand7 GUI. Special care has to be taken though to ensure that both coordinate systems are identical prior to the discretisation of the domain.

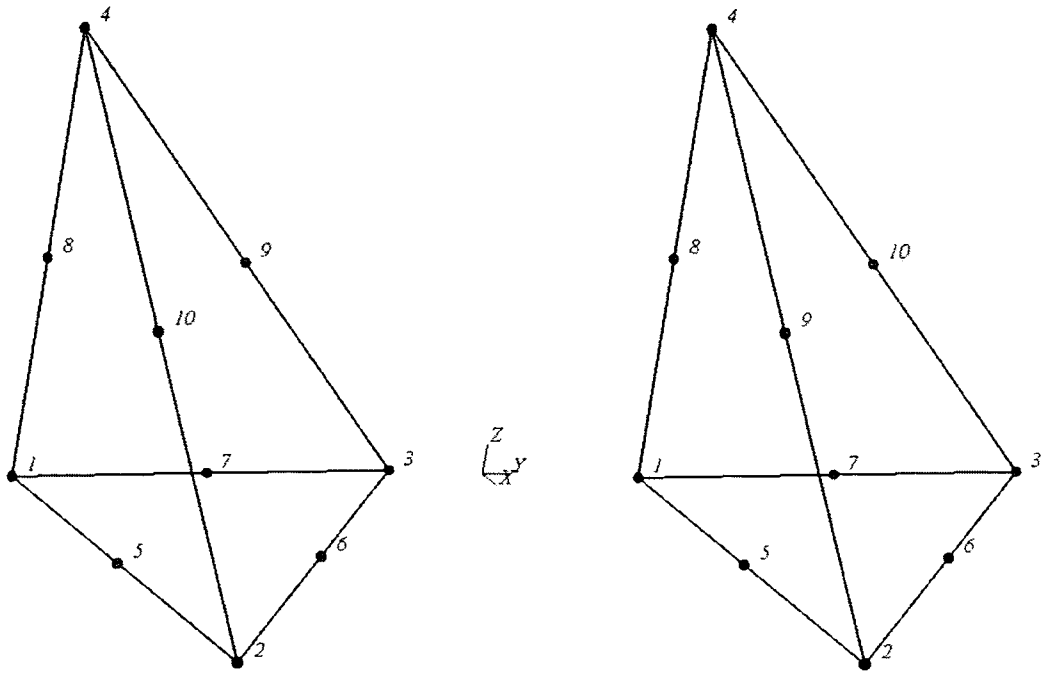

a) Gmsh node numbering b) Strand7 node numbering

Figure 5.14. Different way in node numbering between a) Gmsh and b) Strand7.

5.8 Code to model excavation

The aim of this thesis is to provide useful tools to the FE users to enable them to conduct fast, robust and efficiently 3-D FE analyses. One of the most important and popular problems amongst geotechnical engineers is the simulation of tunnel excavation and all possible variations of it. This may involve soil-tunnel interaction (various tunnel geometries) or soil- tunnel-structure interaction (where the "structure" can be a second tunnel, a building or a piled foundation). In this section therefore, a code which was specifically written to address the problem of generating appropriate meshes for single tunnel excavation and lining instalment in consecutive steps, is

presented (Appendix D). The codes which were described in the previous sections of the current chapter differ from the one presented here, since they generate meshes with pre-installed tunnels (i.e. a void within the mesh).

Figure 5.15 shows the domain (which has the same dimensions as that described in Figure 5.10) as well as the division of a single horizontal tunnel into smaller volumes of the same size. In order to define this size a new variable *Ur* is introduced at the beginning of the code. *Ur* represents the unsupported region which is created when soil elements are removed from the face of the excavation while the lining is installed at a specific distance behind the face. The importance of the length of this region was first identified by Vermeer *et al.* (2002, see Chapter 2). Three different groups of elements are used in this mesh: *i*) ten-noded tetrahedra representing the soil in the domain outside the tunnel, *ii*) ten-noded tetrahedra representing the soil to be excavated inside the tunnel and finally *iii*) six-noded triangles representing the tunnel lining.

The main task for this code was to try and create a function (which is called "CirclePlanes", see Appendix D) which would generate the first of the consecutive volumes of the single horizontal tunnel. The next step was to create a loop which would iterate the previous process until the whole length of the tunnel was formed. The number of iterations is calculated by dividing the total length of the mesh along the *y*-axis over the unsupported region *Ur*. This process is created in a separate file (`loop.txt`) from the main file (`estg.txt` see Appendix D) which contains the commands to create the domain. Special care has to be taken to ensure that both of these files are in the same working directory.

An important feature in this code is the consecutive numbering of the series of volumes into which the tunnel is partitioned. Thus, the user is not supposed to know the number of every element to be excavated in that particular volume, even though Gmsh provides this kind of information. Instead, the knowledge of the identification number of that volume is enough to remove all the elements which are contained in that region.

A major drawback of this procedure is that it is not fully automated. This means that the user has to fill in manually the unique identification number from each of the four

surfaces that each consecutive volume consists of. Furthermore, mesh quality seems to deteriorate compared to the cases described in Section 5.6.1 (see Figure 5.11). This is attributed to the discontinuities which are formed between the consecutive smaller volumes of the tunnel. Even though more finite elements (finite size) are generated compared to the single tunnel case (described in Section 5.6.1) due to the discontinuities described above the overall mesh quality deteriorates slightly. However, once more the vast majority of the generated finite elements are projected above average ($\gamma > 0.5$) with a mean value of $\gamma = 0.687$. Hence, the overall quality of the mesh is characterised as "good". The computational time needed to discretise the whole domain is almost 50% higher than that shown in Figure 5.11 since twice the number of finite elements are generated (see Table 5.6).

In order to emphasize the capabilities of Gmsh to generate even more complicated tunnelling geometries, a couple of geometries based on case studies from the Channel Tunnel Project were meshed. Figure 5.16 shows parallel, multiple tunnels which intersect with others of smaller diameter. The latter are used as escape routes in emergencies. Figure 5.17 shows some unrealistic tunnelling schemes which are presented for illustrative purposes only to highlight the fact that Gmsh can also produce tunnels having their axes not only translated (i.e. horizontal or inclined) but also rotated. The code written for the complex geometries in Figure 5.17 are presented in Appendix E.

Summary

Gmsh is a fully automated 3-D unstructured tetrahedral freeware mesh generator which works either via a GUI or from an ASCII file containing commands. Two of its main capabilities are: *i*) the possibility of variable substitution in the input file and *ii*) the specification of the "characteristic length" (*ChL*) which can be applied to selected points in the model. In this way, the user can produce areas of different density within the domain. Various tests were undertaken to examine the capabilities of Gmsh. From these it was found that this software can produce rapidly and easily 3-D meshes of good quality even for the most unfavourable positions of a tunnel in the domain and for the most complicated tunnelling schemes. Particularly when undertaking a parametric study, plenty of time can be saved during the pre-processing stage.

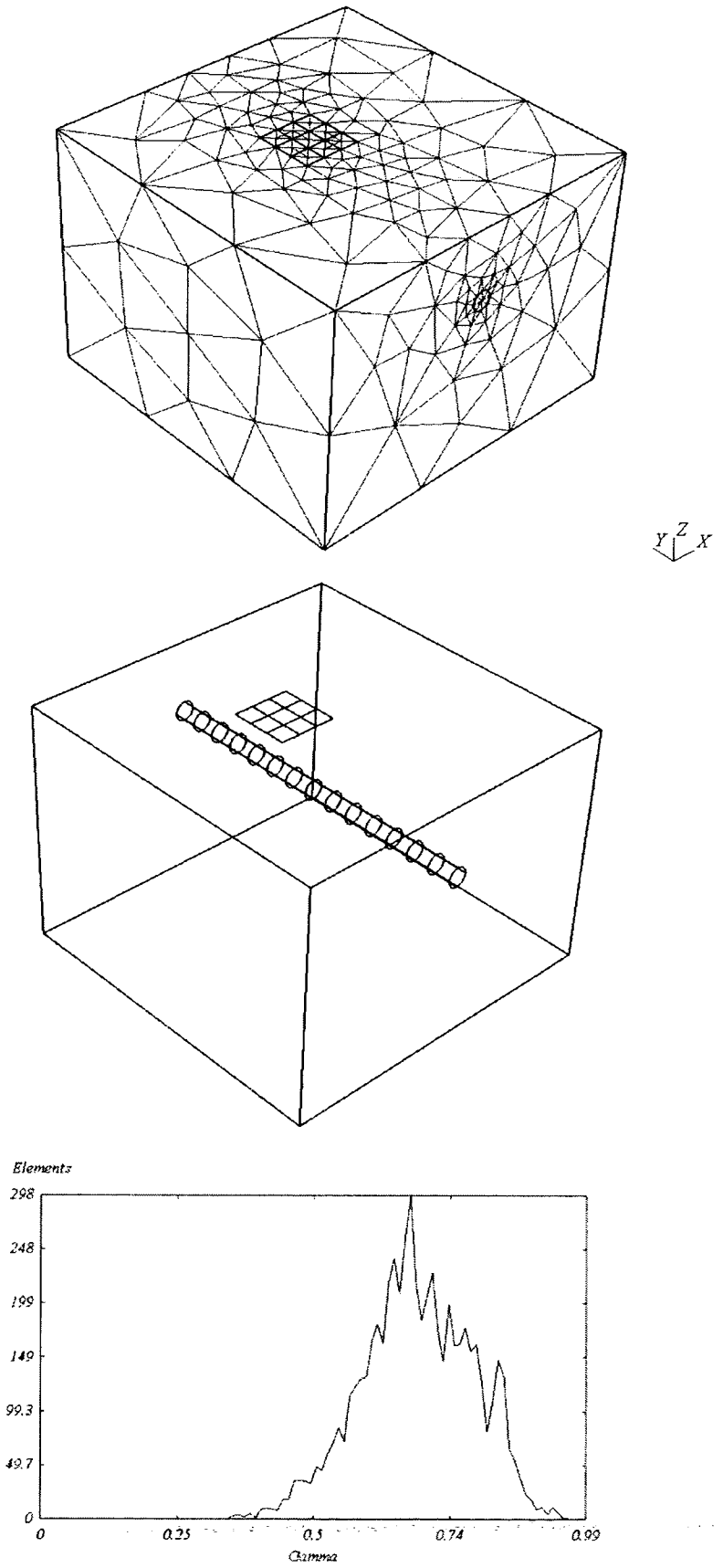

Figure 5.15. Mesh for the excavation of a single horizontal tunnel.

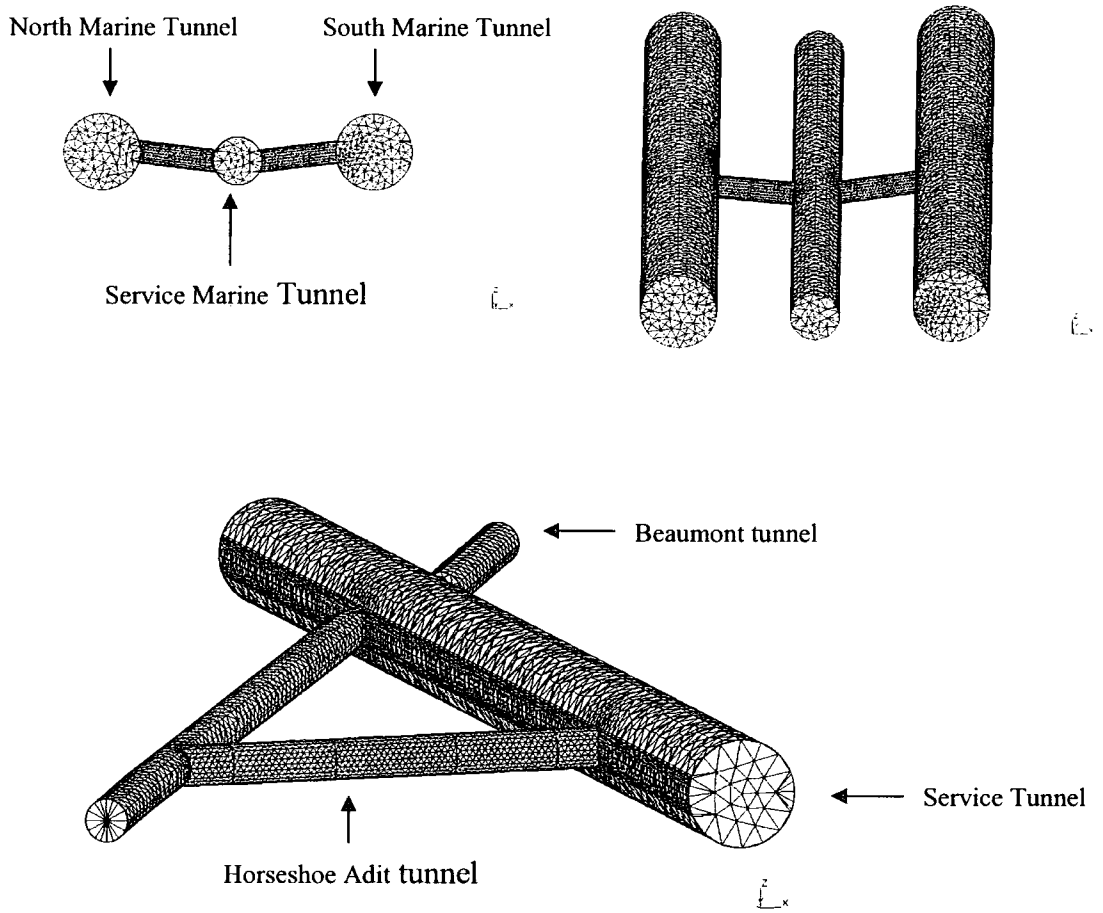

Figure 5.16. Case study from the Channel Tunnel Project.

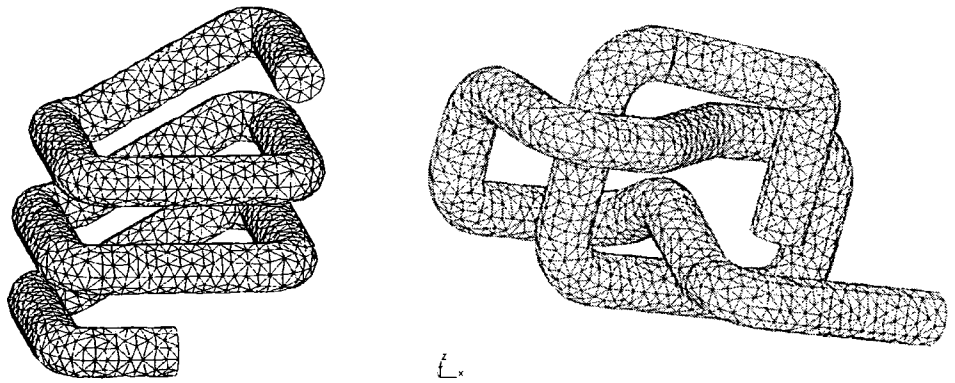

Figure 5.17. Unrealistic tunnel geometries. For illustrative purposes only.

X (m)	Y (m)	Z (m)	D (m)	z_0 (m)	*ChL1* (m)	*ChL2* (m)	*ChL3* (m)	*ChL4* (m)
17.5*D*	17.5*D*	12.5*D*	4	15	*18D/4*	*3D/4*	*9D/4*	*3D/4*
No. of nodes		No. of 10-noded Tetrahedra			Time for 2-D (s)	Time for 3-D (s)	*Gamma (γ)* (mean)	
8,793		5,824			0.25	1.64	0.687	

Table 5.6. Single horizontal tunnel excavation case.

Chapter 6

2-D FE analysis of tunnelling using Strand7 and Plaxis

6.1 Introduction

This chapter investigates the effect of surface loading on pre-existing underground structures (e.g. tunnels) in soft ground assuming plane strain conditions (2-D FE analysis). In the first part (Section 6.2) the commercial FE package Strand7 is used for this purpose. In the second part (Section 6.3) a different commercial FE software Plaxis v.8, is used to run the same analyses. The purpose of this comparison is to try and identify the differences in the FE predictions by using various codes, which might be significant to industrial users of these programs. The reasons for not using any analytical method (e.g. Boussinesq method) to estimate the tunnel deformations due to surface loading in both Chapters 6 and 7 were that these methods are only applicable to an elastic medium. They do not take into account the plastic properties of the medium or the interaction between the medium and any pre-existing structure in it. According to Moore (1987b) Boussinesq method fails to take into account the effect of shear stresses and strains developing in the overlying strata.

In the current plane strain analyses three different tunnel geometric configurations are considered. In the first case a single tunnel analysis is carried out (*ST* case). In the second a twin tunnel analysis is carried out, where both tunnels are horizontally aligned (*TH* case). Finally in the third case twin tunnels are vertically and diagonally aligned (*TVD* case). A parametric study was performed for the above three cases

varying the position of the tunnel axis (z_0), pillar width (P), pillar depth (P_D) as well as the position of the surface loaded area (W). Figure 6.1 shows the parameters varied in this study. For the single tunnel case (shown as a solid circle) z_0 varies. For the twin tunnel configuration (where the second tunnel is presented as a dotted circle) P and P_D vary. In all cases the loaded area shifts from $W1$ to $W6$. Throughout this parametric study the dimensions of the domain (x, y), tunnel diameter (D), magnitude (400kN/m) and area (W) of the applied load were constant. Surface load was applied directly to the surface of the finite elements hence modelling a flexible footing. No interface elements were used to model the existence of any type of foundations or treatment of the ground prior to its loading.

6.2 Details of analysis using Strand7

6.2.1 Single tunnel case (*ST*)

6.2.1.1 Introduction

Figure 6.2 shows one of the meshes used for the single tunnel parametric case where z_0 = 20m. Coarser elements appear close to the vertical and bottom boundaries. Finer elements exist around the tunnel liner and the surface (top boundary) since these are the two areas of interest. The latter areas could have been further refined. The reason this is not done is that these 2-D FE domains produced by Strand7 are cross sections from a 3-D mesh (analyses with which are the subject of Chapter 7). Strand7 imposes some restrictions when performing 3-D non-linear static analyses, which are discussed later (Chapter 7), for instance, the finer the mesh the longer an analysis takes to complete. Thus a compromise has to be made between the coarseness of the domain and the time to execute the 3-D FE analyses. This compromise being constrained by the requirement that the mesh must be able to capture the solution appropriately. Therefore these cross-sections presented here are composed of medium to large elements (This is further discussed in Chapter 7). The mesh in Strand7 is created and imported from Gmsh (the freeware FE mesh generator described in Chapter 5) since Strand7 can neither produce an unstructured mesh nor can it be as flexible as Gmsh in the pre-processing stage of the analyses. The mesh consists of 241 nodes (482 d.o.f) and 107 six-noded triangular elements which are used to model

the soil, and 16 two-noded beam elements used to model the tunnel lining. Even though there is a plane of symmetry (Fig. 6.2 along the vertical tunnel axis) and thus half of the domain could be modelled providing the loading was also symmetric, it was decided that the whole domain would be modelled in all analyses.

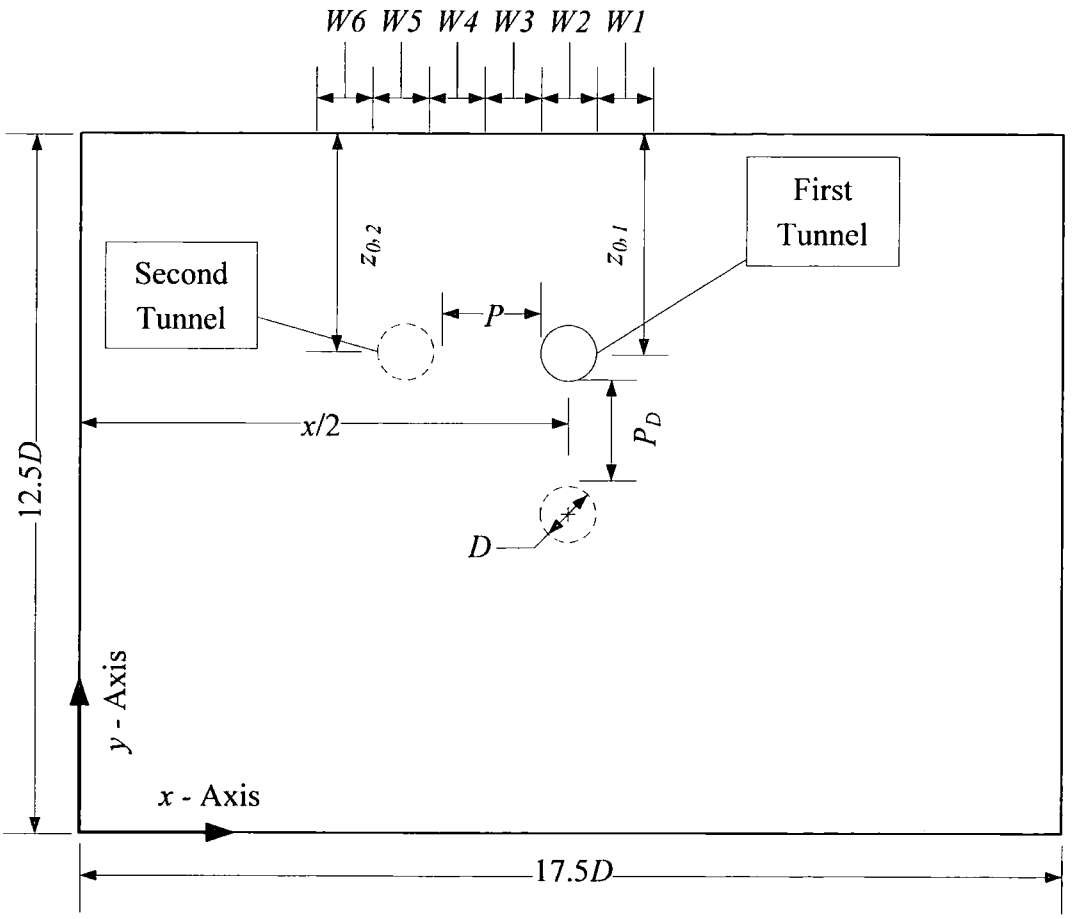

Figure 6.1. Geometric parameters of the soil, the tunnels and the loaded area.

Tunnel diameter (D) was chosen to be 4m which is comparable to the diameter of running tunnels for the Underground in London (Attewell, 1978). The dimensions of the modelled domain were chosen to be 70m long (or 17.5D) in the x direction and 50m deep (12.5D) in the y direction. For z_0 = 15m, 20m and 25m the chosen values lie within limits proposed by Potts *et al.* (2002). They suggested that for tunnels in clay the depth of the mesh should be approximately 2D to 3D below tunnel invert. As for the optimal width of the domain two factors have to be considered. The mesh has to be sufficiently wide to ensure minimal displacements along the vertical boundaries. However, the larger the domain the larger the number of the degrees of freedom

(d.o.f). This immediately affects the solution in terms of computational time. Hence a compromise has to be made between these two crucial factors. It was decided that the above dimensions were appropriate for this study.

The surface load is constant at 400kN/m. This magnitude was chosen to resemble the uniform stress of a 10-storey building, assuming a stress of $10kN/m^2$ per storey for a 4m wide loaded area. The latter value over a full building width is probably unrealistic. However, it was chosen as a worst case value (perhaps including the effect of an accidental concentrated load) to accentuate the differences in the parametric study. The value of $10kN/m^2$ per storey was chosen after BS 8002 (British Standards Institution, 1994) recommendations.

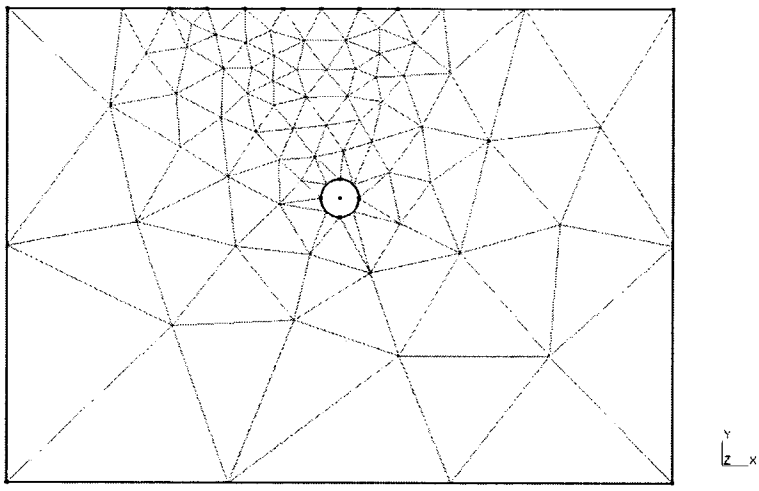

Figure 6.2. Generated mesh for the single tunnel analysis when z_0 = 20m.

Since there is a plane of symmetry (Fig 6.2 along the vertical tunnel axis) the areas *W*1 and *W*3 produce the same effect for the single tunnel scenario. For this reason only *W*3 of the two is analysed, together with loads at *W*2 and *W*4. Areas *W*5 and *W*6 are further away from the tunnel and hence thought only of marginal significance. In total 9 analyses were carried out in the current parametric study. These can be classified as follows: three different tunnel depths (z_0 = 15m, 20m and 25m) and three different surface loaded areas (*W*2, *W*3 and *W*4).

6.2.1.2 Initial conditions

The realistic determination of the initial stress conditions is of great importance in FE modelling in geotechnics. This is one of the most significant differences between FE analyses in mechanical engineering and those in geotechnics. Several approaches exist for this purpose. The most common of which is the K_0 procedure where stresses prior to any construction are initialised. This method is only applicable for horizontal ground surfaces and greenfield sites. This is not the case in this study. Consequently a different approach is adopted to simulate initial ground conditions.

Herein tunnel excavation is not modelled. Instead tunnels with their permanent lining appear in the mesh as if wished in place. Stresses prior to this stage are not generated. Gravity loading is uniformly applied to the whole domain [*gravity loading* method. In this method the gravitational acceleration ($g = 9.81$ kN/m^3) along with the soil's unit weight ($\gamma = 20$ kN/m^3) are initialised so that the self weight is generated]. The resulting displacements are then set as the zero datum for the subsequently steps of the analysis.

The stratigraphy is the same throughout the analyses presented in Chapters 6 and 7. This consists of one clay layer, the characteristics of which are presented in Table 6.2. Drained analyses are performed throughout this chapter using effective strength parameters.

As for the boundary conditions, in plane strain analysis no horizontal or vertical movements are permitted along the horizontal boundary at the base of the mesh. On the two vertical mesh boundaries, only vertical movements are allowed. Finally the top mesh boundary is free to move.

6.2.1.3 Constitutive models

The two-noded beam elements used to model the lining are assumed to behave in a simple linear elastic way. Thus two parameters (Young's modulus E and Poisson's ratio ν) are required for this model. Table 6.1 shows the full characteristics of the lining, including the geometrical properties.

Soil does not behave in a linear nor an elastic way. Thus a more realistic and advanced constitutive model should be adopted. A simple elasto-plastic constitutive model is therefore used. For the plastic region a Mohr-Coulomb yield criterion with associated flow (described in Chapter 3) is used amongst others available. For the latter model four parameters need to be specified. Those are cohesion (c'), angle of friction (φ') and the two previously mentioned parameters (E' and ν'). Table 6.2 summarises these characteristics.

Parameter	Name	Value	Units
Type of Behaviour	Material Type	Elastic	-
Young's Modulus	E	10^8	kPa
Cross Sectional Area	A	0.168	m^2
Second Moment of Area	I	3.95136×10^{-4}	m^4
Poisson's Ratio	ν	0.3	-
density	γ_L	24	kN/m^3

Table 6.1. Material properties of the tunnel lining.

Parameter	Name	Value	Units
Type of Behaviour	Elastic region	Linear Elastic	-
Type of Behaviour	Yield Surface	Mohr Coulomb	-
Young's Modulus	E'	6.207×10^3	kPa
Poisson's Ratio	ν'	0.33	-
Unit Weight	γ	20	kN/m^3
Cohesion	c'	5	kPa
Angle of Friction	φ'	25^o	-

Table 6.2. Material properties of the soil.

6.2.1.4 Modelling sequence

In all calculations carried out in Chapters 6 and 7 the analysis procedure began with the tunnels driven and the permanent lining installed. Displacements from this stage are not measured. Two load stages are then defined. During the first drained analysis

is performed and *gravity load* is applied to the mesh in five consecutive increments. In the following stage drained loading is applied (i.e. no pore water pressure changes) and the surface load (400kN/m) is vertically applied to the pre-defined surface areas (*W*1 to *W*6) in twelve successive increments (see Table 6.3). The displacements due to the first load stage are considered as the zero datum. Thus only those predicted by the FE analysis due to the second stage (surface loading) are examined.

Stage No.	Incr.	% Total Gravity	% Total load
Stage 1	1	20	-
	2	40	-
	3	60	-
	4	80	-
	5	100	-
Stage 2	6	100	20
	7	100	40
	8	100	50
	9	100	60
	10	100	65
	11	100	70
	12	100	75
	13	100	80
	14	100	85
	15	100	90
	16	100	95
	17	100	100

Table 6.3. Number of increments per stage of analysis.

6.2.1.5 Analysis results

In this section results are presented for the case of surface loading above an existing single tunnel driven in soft ground. Predictions of surface settlements, tunnel lining deformations as well as the distribution of bending moments around the liner, are presented to study the effects of various parameters with this configuration.

Figure 6.3 shows plots of the ratio of the surface settlements due to the surface loading over the tunnel diameter (S'/D, vertical axis) against the transverse distance x (horizontal axis) for three different surface loaded areas (W). The depth of the tunnel axis is at z_0 = 15m. It can be seen that the value of the maximum settlement of

the trough due to loading (S'_{max}) slightly reduces as the load changes its position from *W*2 to *W*4. The maximum value occurs when the load is applied above *W*2.

Figure 6.4 shows plots of the ratio of the maximum surface settlements due to load over the tunnel diameter (S'_{max}/D) for three different tunnel depths (z_0 = 15m, 20m and 25m. For the remaining of this chapter these depths will be referred as: the three different tunnel depths) against the relative position of the surface loaded area (*W*). An interesting point from Figure 6.4 is that S'_{max}, is marginally affected by the tunnel axis position for shallow tunnelling, since the curves are parallel. However, at z_0 = 25m and load at *W*3 an increase of S'_{max} can be observed between *W*2 and *W*3. This is followed by a rapid decrease from *W*3 to *W*4. The difference between the two curves (z_0 = 20m and 25m) at *W*3 (where the peak point occurs) is minor.

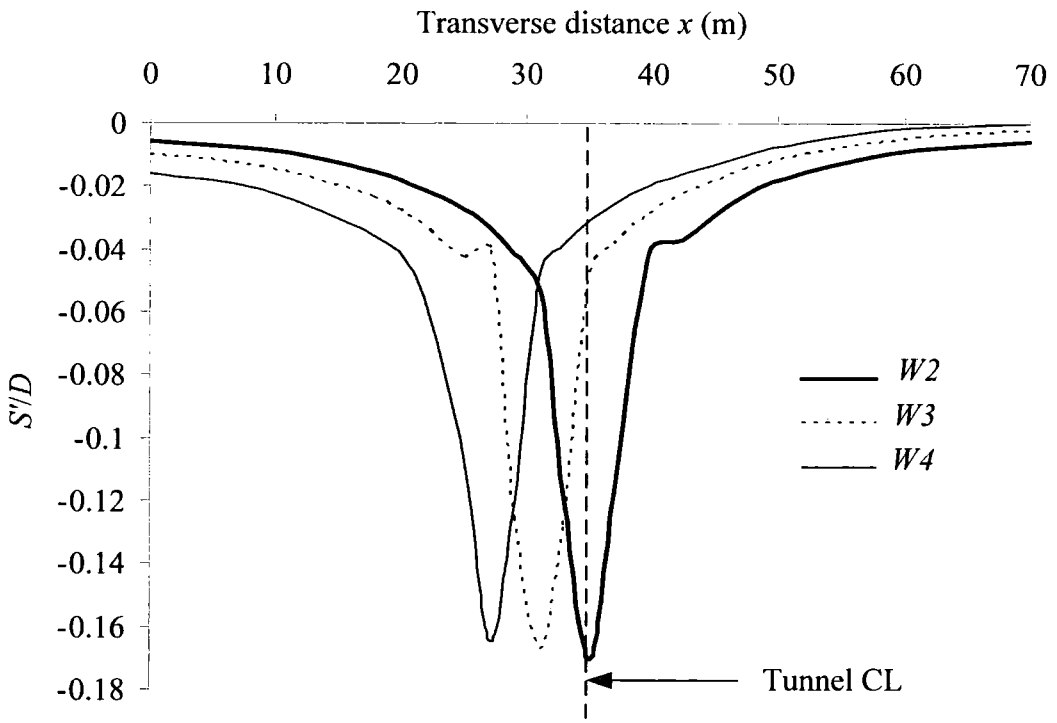

Figure 6.3. Surface settlements above an existing single tunnel (CL at 35m) due to surface loading (in dimensionless form). The position of the load varies from *W*2 to *W*4.

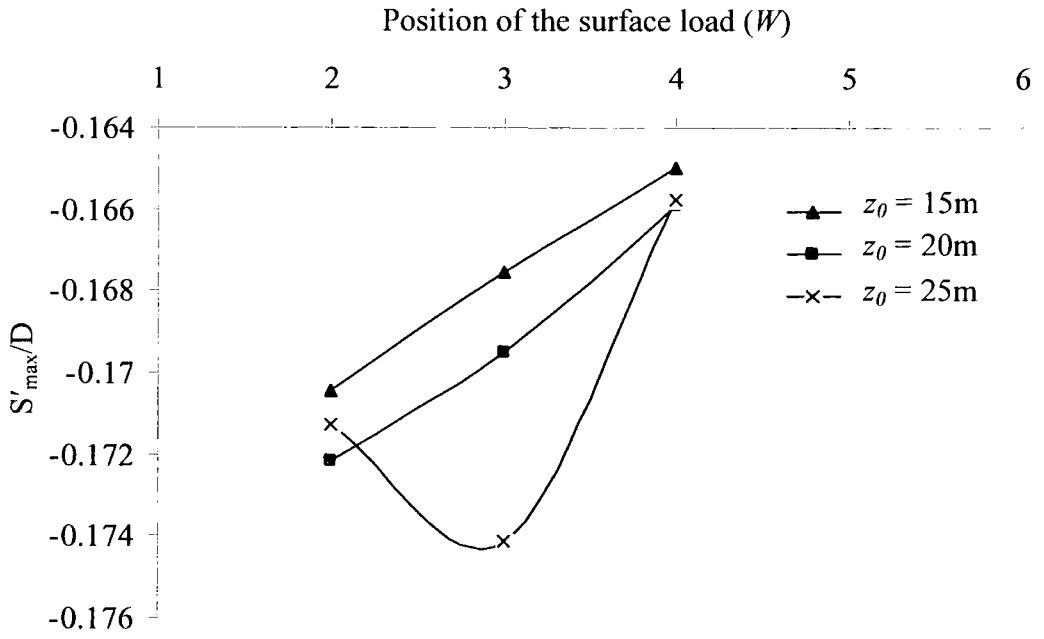

Figure 6.4. Plots of the maximum surface settlements due to surface loading (in dimensionless form) against the position of the load for various excavation depths.

In Figure 6.5 the deformed shape of the tunnel (scaled up, shown as coloured lines) for three different tunnel depths due to the effect of the surface loading only (no gravity is considered) is presented. This is then compared to the original shape (black solid line) prior to both gravity and surface loading respectively. The first obvious outcome is that the whole tunnel seems to squat. In other words there is an elongation of the horizontal diameter with a simultaneous decrease of the vertical. Further to this obvious vertical translation a secondary type of movement seems to occur coincidentally. The deformed lining seems to slightly rotate anti-clockwise opposing the position of the applied surface load as this shifts towards *W*4. The shallower the tunnel the bigger the lining deformations.

Figure 6.6 shows the magnitudes of the previously mentioned movements (squatting and anti-clockwise rotation). The changes of both horizontal (along springlines) and vertical (crown to invert) tunnel diameters are plotted on the vertical axis as a percentage of the initial tunnel diameter against the position of the applied load (horizontal axis) for three different tunnel depths. The following sign convention is adopted throughout this chapter: a positive change indicates an increase of the tunnel diameter while negative specifies a decrease. The results show that the shape of the

tunnel alters due to the surface loading. An increase in the horizontal diameter (thin lines) and a decrease in the vertical (dotted lines) is observed in all cases. The maximum increase of the horizontal diameter is approximately 1% of the tunnel diameter, when the load is applied directly above the tunnel (*W*2) while the tunnel axis is at z_0 = 15m. The maximum decrease of the vertical diameter on the other hand is roughly 1% of the tunnel diameter at the same loaded area *W*2 and the same tunnel depth. The magnitudes of these changes are seen to decrease as the loaded area moves towards *W*4. Deeper tunnels (z_0 = 20m and 25m) seem to be less affected by surface loading and therefore the corresponding changes of the tunnel diameter are significantly smaller (approximately 0.5% of the tunnel diameter), yet follow the same trend as for the shallow case.

Another crucial measurement of the tunnel lining response to the surface loading is the crown settlement. Figure 6.7 shows crown settlement predictions plotted on the vertical axis as a percentage of the initial tunnel diameter against surface loading area for three different tunnel depths. The maximum crown settlement value is 3.6% of the tunnel diameter at z_0 = 15m when the load is directly applied above the tunnel C.L. (at *W*2). A decrease of the crown settlement is observed in the following two cases: *i*) the loaded area moves from *W*2 to *W*4 and *ii*) for deeper excavations (approximately 2.5% of the tunnel diameter).

In the following bending moment distributions around the tunnel lining are presented. The following sign convention for bending moments will be used throughout this chapter. Negative bending moments correspond to straightening of the lining (tension at intrados) while positive moments indicate increase of the lining curvature (compression of intrados). Figure 6.8 shows the distribution of bending moments around the lining (in kNm/m) for different stages of the FE modelling, against the angle around the tunnel. This angle starts from the crown (0°) moving in a clockwise direction towards the invert (180°). This convention is used throughout this chapter. Positive bending moments appear around the springline (45° to 105°) while negative around both crown and invert. This is in agreement with the tunnel squatting shape which was presented in Figure 6.5. In Figure 6.8 three different curves are drawn. The first corresponds to the distribution of bending moments during the first stage of analysis (i.e. gravity loading) while the second curve during the second stage (i.e.

gravity and surface loading stages). Finally the third line depicts the change between the previous two curves. This approach is adopted from Schroeder (2002, Figures 8.23 and 8.24, pp. 351). In this way the effect of just the surface loading on the liner can be established. From the latter curve the maximum positive bending moment is 58kNm/m at around 67° while the maximum negative is -62kNm/m at crown. This figure refers to the case where z_0 = 15m and the load is applied directly above the tunnel (*W*2).

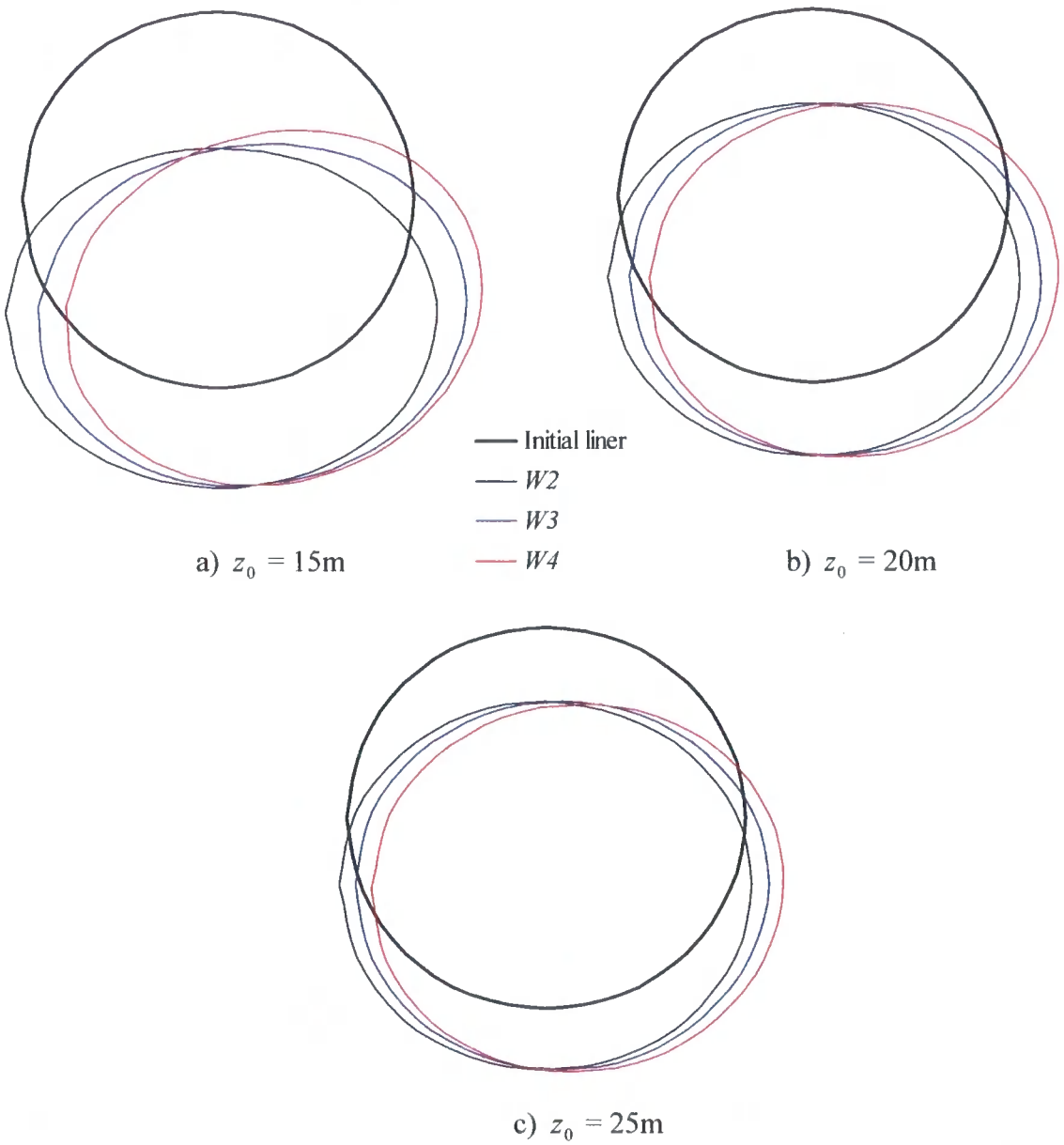

Figure 6.5. Deformed shape of the tunnel due to the surface loading for three different loaded areas (*W*2, *W*3 and *W*4) and three different tunnel depths (z_0 = 15m, 20m and 25m).

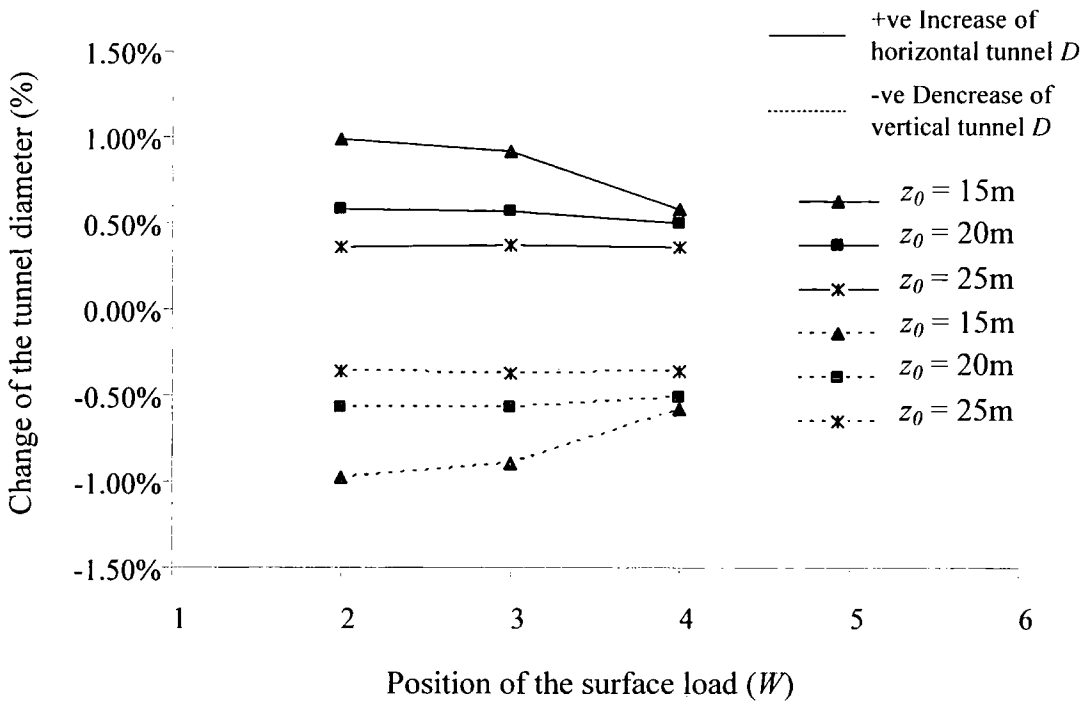

Figure 6.6. Changes of horizontal and vertical tunnel diameters as a percentage of the initial tunnel diameter due to the surface loading against the position of the applied load for various excavation depths.

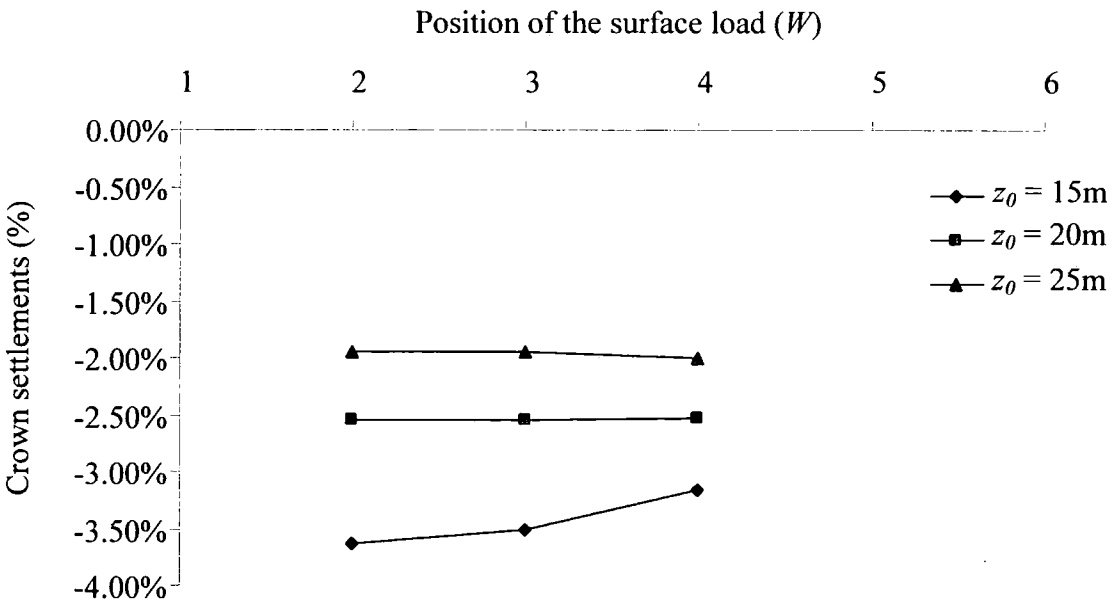

Figure 6.7. Crown settlements expressed as a percentage of the initial tunnel diameter against the position of the surface loaded area for different excavation depths.

Figure 6.9 show plots of the change of bending moments (solely due to the effect of loading as explained previously) around the liner for three different excavation depths. This time the loading area varies from *W*2 to *W*4. The maximum negative change of bending moments lies approximately at the crown (315° to 360°). The maximum positive change of bending moments always lies close to the springlines (approximately at 67° rather than 90° and at 248° rather than 270°). Bending moments due to the surface loading seem to increase for shallower tunnels.

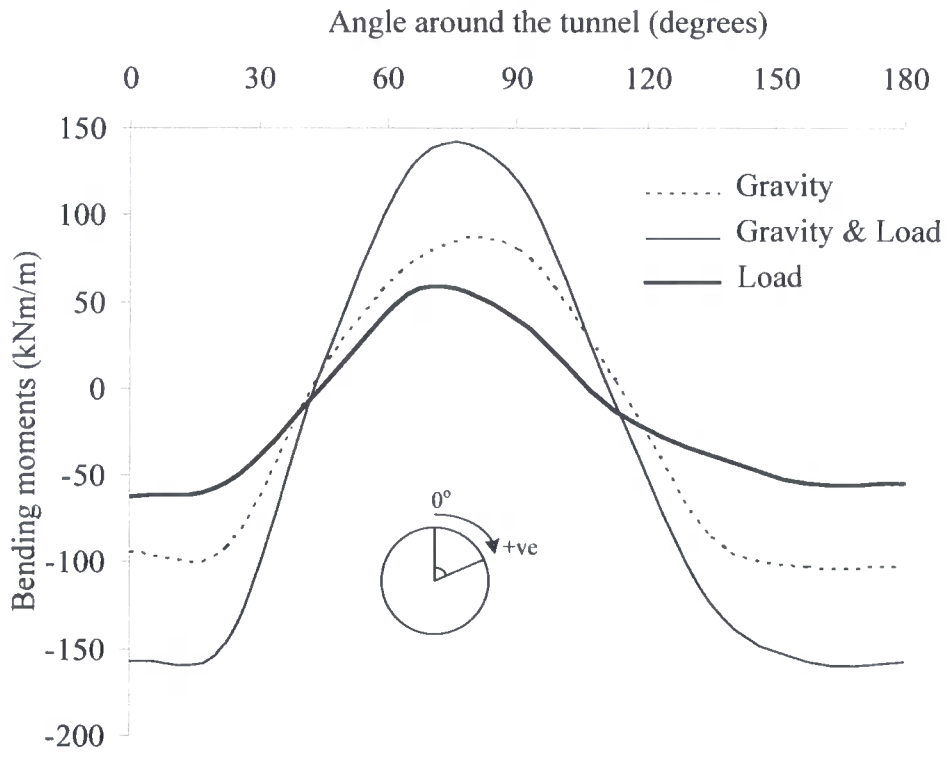

Figure 6.8. Distribution of bending moments around the tunnel liner at different stages of the FE modelling when z_0 = 15m and the load lies at *W*2.

Figure 6.10 depicts plots of the maximum change of bending moments from maximum positive (dotted lines) to maximum negative (thin lines) around the liner just due to the effect of surface loading against three different loading positions (*W*2, *W*3 and *W*4) and three different excavation depths. The deeper the tunnel the less it is affected by the load, the position of which in turn does not seem to have a serious impact (almost parallel to the horizontal axis) on the liner when z_0 = 20m and 25m. However, when excavation depth reduces to z_0 = 15m the picture alters dramatically.

The change of bending moments appears to increase from *W2* to *W3* and then rapidly decrease until *W4*. The first outcome from this observation is that shallow tunnels are mostly affected when the surface loaded area is located roughly in the region of one diameter each side from the centre line.

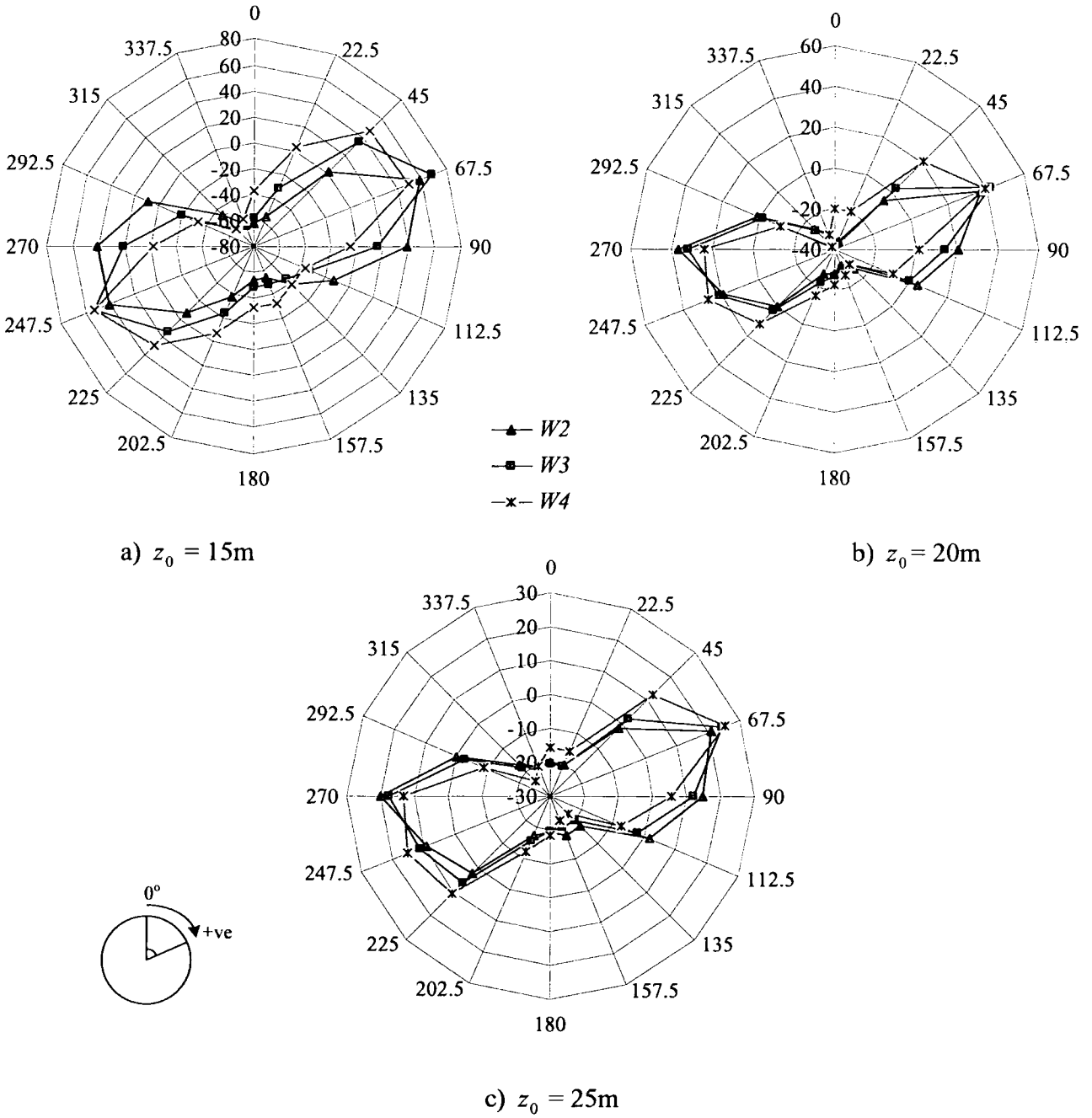

a) z_0 = 15m

b) z_0 = 20m

c) z_0 = 25m

Figure 6.9. Change of bending moments due to the effect of surface loading for different surface loaded areas when z_0 = 15m, 20m and 25m. The axial axis refers to the distribution of bending moments (kNm/m) around the tunnel, while the circumferential axis refers to the angle around the tunnel.

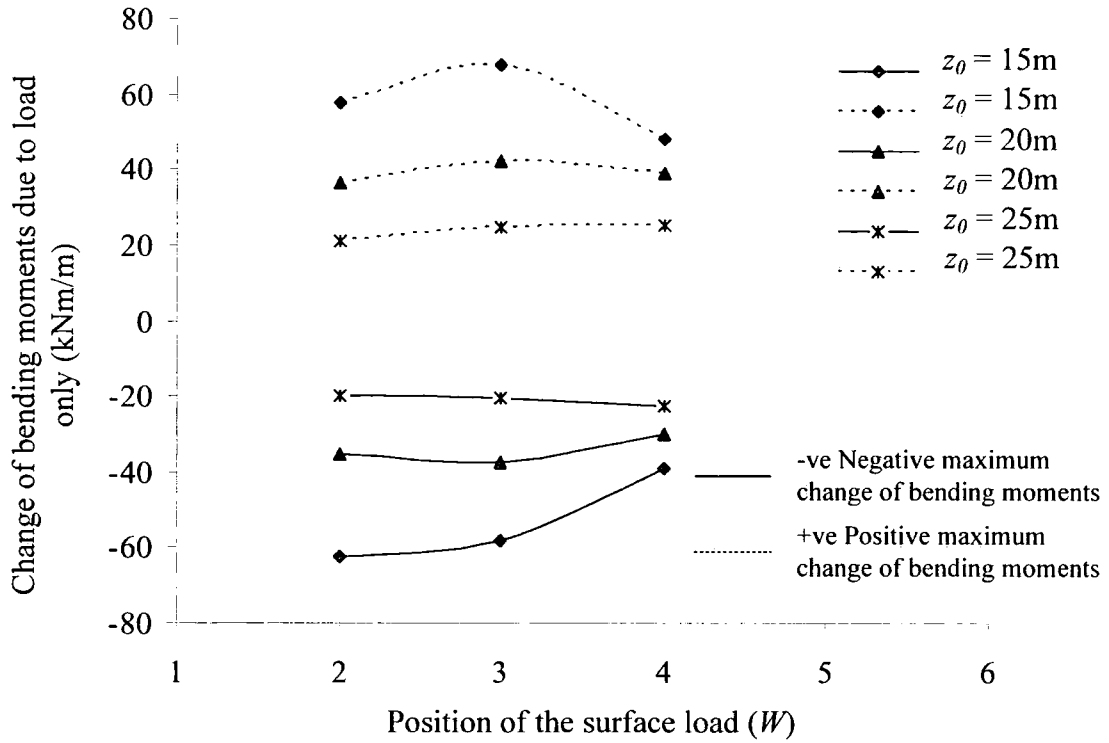

Figure 6.10. Change of bending moments due to the effect of surface loading for different surface loaded areas and different excavation depths.

6.2.2 Twin tunnels horizontally aligned (case *TH*)

6.2.2.1 Introduction

In this section results are presented for the case of twin parallel tunnels with their axes horizontally aligned. Figure 6.11 shows one of the meshes used for the current parametric study where $z_{0,1} = z_{0,2} =$ 20m (where $z_{0,1}$ refers to the excavation depth of the first tunnel and $z_{0,2}$ refers to the excavation depth of the second tunnel (Fig. 6.1) while the pillar width is $P = 1D$. The 2-D plane strain mesh consists of 371 nodes (742 d.o.f.). This is then split into 166 six-noded triangular elements to model the soil and 32 two-noded beam elements for the linings.

6.2.2.2 Details of the analysis

The details of the analysis are identical to those described in the single tunnel case (Section 6.2.1) except for the following two features:

- a second tunnel is present prior to any loading stage. This does not affect the number of increments or loading stages which are used (Table 6.3) and
- no plane symmetry exists. Hence, all six of the surface loaded areas (*W*1 to*W6*) are analysed. Additionally two different tunnel depths ($z_{0,1} = z_{0,2} =$ 15m and 20m) and three different pillar widths (P = 1D, 2D and 3D) are modelled. This gives a total of 36 analyses in this parametric study. The horizontal position of the left tunnel (for the remaining of this chapter it will be referred as second tunnel) varies while that of the right (it will be referred as first tunnel) is fixed.

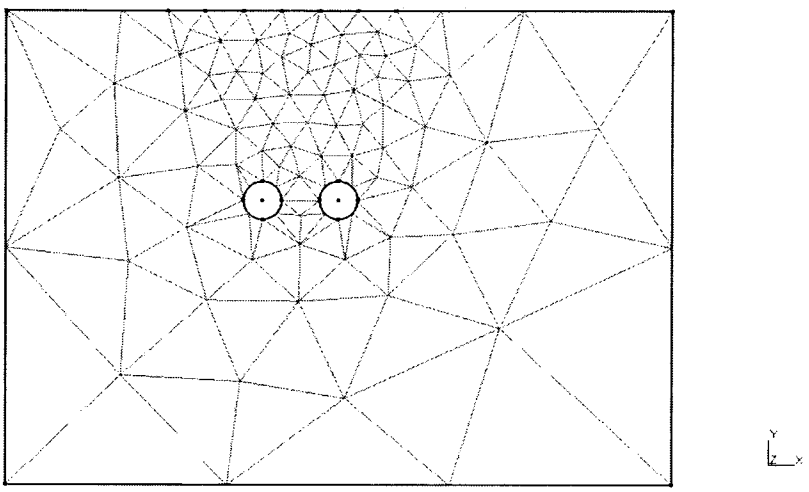

Figure 6.11. Generated mesh for the twin tunnel analysis when $z_{0,1} = z_{0,2} =$ 20m and $P = 1D$.

6.2.2.3 Analysis results

In this section findings are introduced for the case of surface loading above pre-existing twin tunnels which are horizontally aligned. Figure 6.12 shows predictions of the ratio of the maximum surface settlement due to the surface loading effect over the tunnel diameter (S'_{max}/D) against the relative position of the surface loaded area (W) for two different excavation depths ($z_{0,1} = z_{0,2} =$ 15m and 20m). Thin lines refer to the shallow case ($z_{0,1} = z_{0,2} =$ 15m) while the dotted lines refer to the $z_{0,1} = z_{0,2} =$ 20m case. It is interesting to observe that for deeper driven tunnels larger surface deformations occur. This can be attributed to the fact that soil is not restricted by the position of the two tunnels and consequently has more space to deform.

For the shallow case ($z_{0,1} = z_{0,2}$ = 15m) when P = 1D (i.e. second tunnel below the $W4$ area. See Figure 6.1), S'_{max} occurs above the first tunnel when $W2$ area is loaded as mentioned above. As the pillar width increases from P = 2D (second tunnel below $W5$) to P = 3D (second tunnel below $W6$) S'_{max} occurs at $W3$ and $W4$ respectively (Figure 6.12). This indicates that S'_{max} takes place either above the first tunnel or between the two tunnels but always at a pillar width distance of P = 2D from the axis of the second. The maximum value of S'_{max} occurs in the case where P = 3D and the load is applied at $W4$. The deformation trend described in this paragraph is not so clear for the deeper case.

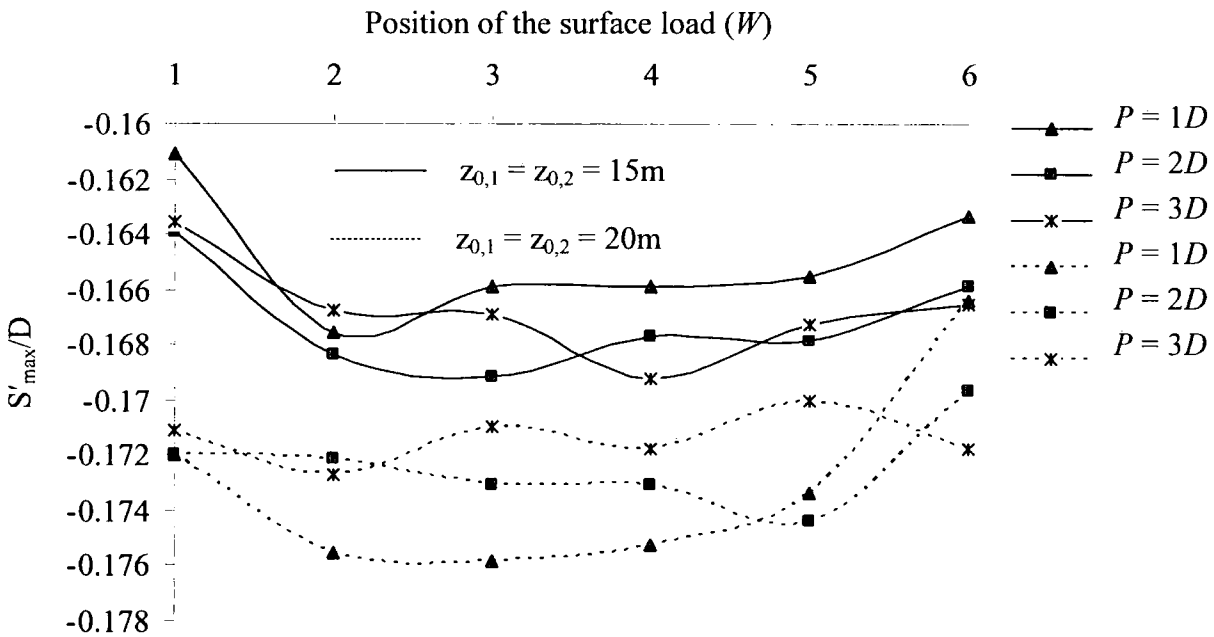

Figure 6.12. Plots of the maximum surface settlements due to surface loading (in dimensionless form) against the position of the load for various excavation depths.

Figure 6.13 presents the lining deformations (scaled up) of both tunnels when P = 1D and for two different depths ($z_{0,1} = z_{0,2}$ = 15m and 20m) due to the effect of surface loading (coloured circles). These are then compared to the original tunnel shapes prior to any loading stage (black thick circles). Similar patterns of deformation to the single tunnel case are observed for both tunnels (squatting and anti-clockwise rotating). Deeper tunnels seem to be less affected (smaller lining deformations) from surface loading.

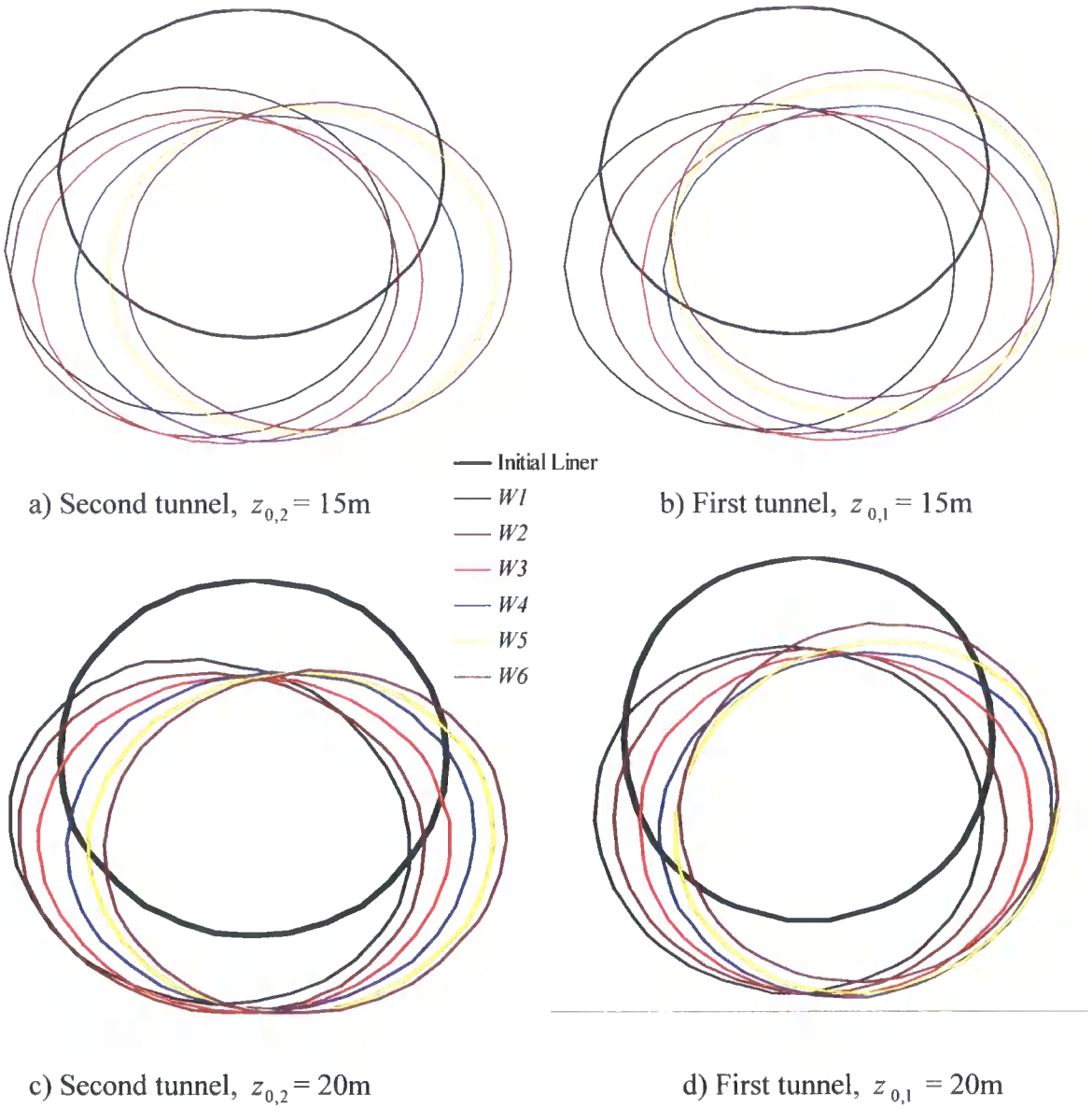

Figure 6.13. Deformed shape of the tunnels due to the surface loading for six different loaded areas. The tunnel axes are driven at $z_{0,1} = z_{0,2}$ = 15m, 20m and $P = 1D$.

Figures 6.14 and 6.15 show plots of the change of tunnel diameter (as a percentage of the initial tunnel diameter) against the relative position of the surface loaded area for both tunnels and for different depths. The thin lines refer to the horizontal tunnel diameter (along springlines). The dotted lines on the other hand refer to the vertical (crown to invert). For the vast majority of the cases an increase of the horizontal diameter with a simultaneous decrease of the vertical is observed. The only exception refers to the second tunnel case where $z_{0,2}$ = 15m, $P = 3D$ and when the surface load is applied from *W1* to *W2*. Herein the opposite effect is detected (i.e. increase of the

vertical and decrease of the horizontal diameter). As the loaded area shifts towards *W6* though the pattern of lining deformation alters to a squat shape again.

The maximum increase of the horizontal diameter as well as the maximum decrease of the vertical of each tunnel (0.8% of the tunnel diameter) always occurs when the surface load is directly applied above for $z_{0,1} = z_{0,2} =$ 15m. Thus, a clear trend for the magnitudes of these changes can be identified. These changes appear to fade as the load is applied further away from each tunnel's centre line.

For deeper excavations the above mentioned tendency for the lining deformation slightly alters. The maximum changes this time seem to occur when the load is shifted 1*D* from each tunnel's centre line towards the other tunnel (rather than directly above).

Figure 6.16 show plots of the crown settlement predictions expressed as a percentage of the initial tunnel diameter for both first (thin line) and second (dotted line) tunnels against the relative position of the surface loaded area (*W*). These plots refer to three different pillar widths (*P* = 1*D*, 2*D* and 3*D*) and two different excavation depths ($z_{0,1} = z_{0,2} =$ 15m and 20m). Similar behaviour is observed for both tunnels regardless of both *P* and z_0. The magnitudes though are bigger for the shallow case. Compared with the single tunnel case the maximum crown settlements (3.3% of the tunnel diameter) do not occur when the surface load is applied directly above each tunnel. Instead this happens when the load is shifted 1*D* from each tunnel's axis.

Figure 6.17 shows the interaction between the two parallel tunnels and the surface load compared to the single tunnel case (*ST*) in terms of crown settlements. For the twin tunnel case crown settlement predictions from the first tunnel are plotted as a percentage of the single tunnel case against the position of the surface loaded area (*W*) for two different depths ($z_{0,1}$ = 15m and 20m) and for three different pillar widths (*P* = 1*D*, 2*D* and 3*D*). Thin lines refer to the shallow case while dotted to the deeper. It can be seen that greater interaction occurs for the shallow tunnel case since there is a difference of 5% to 15% compared to the single case. For the deeper case results are almost identical to the single. This implies less or even no interaction between the two parallel driven tunnels.

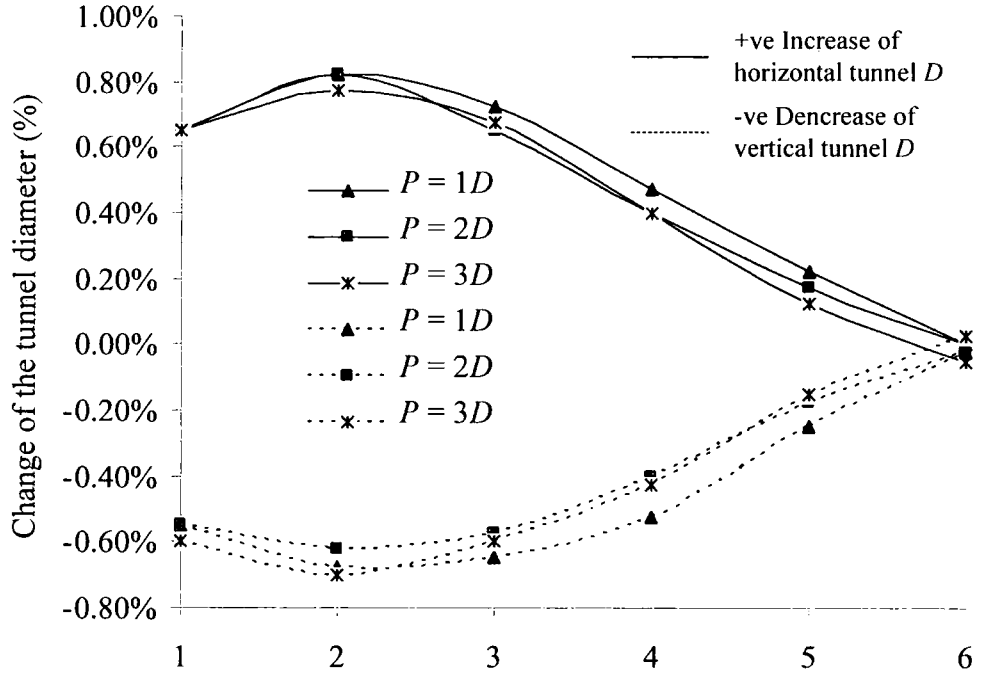

a) Regarding the first tunnel

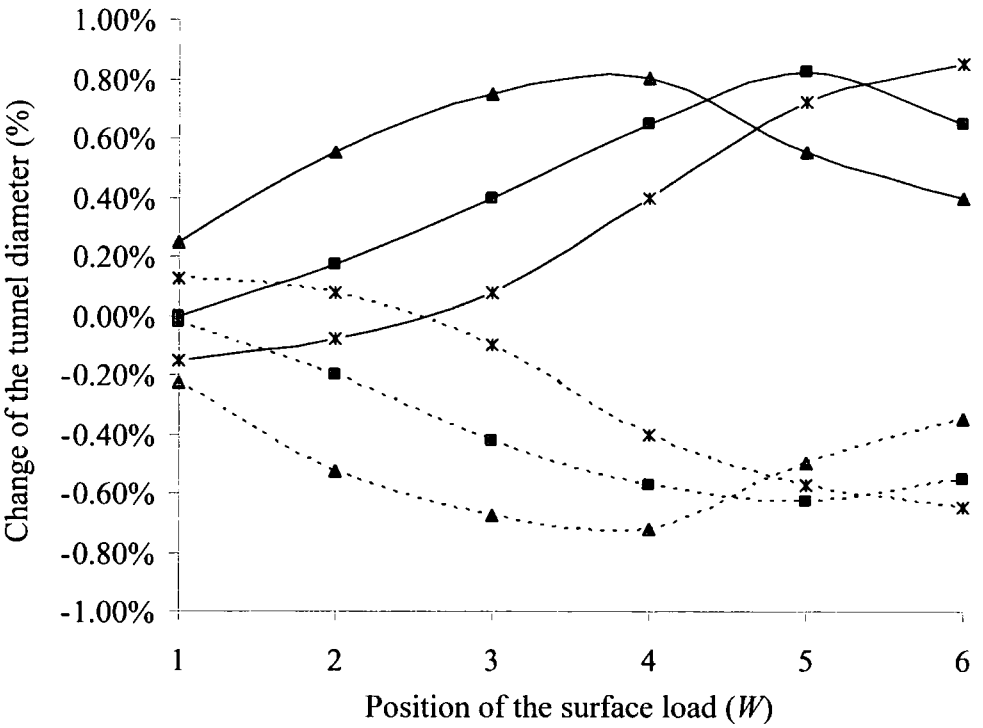

b) Regarding the second tunnel

Figure 6.14. Changes of horizontal and vertical tunnel diameters expressed as a percentage of the initial tunnel diameter due to the surface loading against the position of the applied load for $z_{0.1} = z_{0.2} = 15$m.

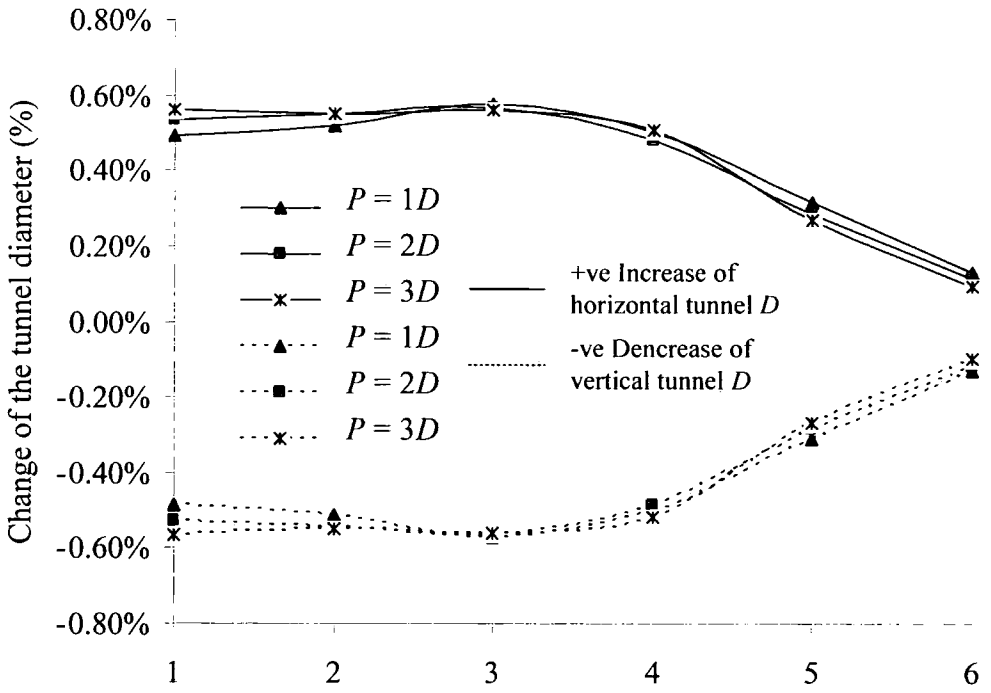

a) Regarding the first tunnel

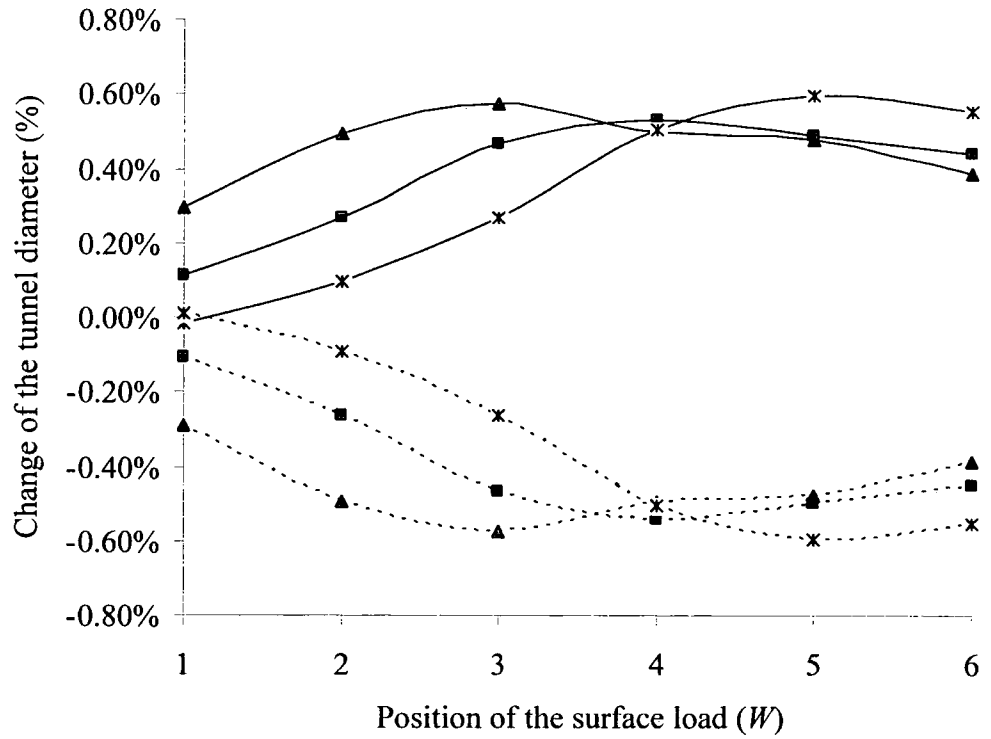

b) Regarding the second tunnel

Figure 6.15. Changes of horizontal and vertical tunnel diameters expressed as a percentage of the initial tunnel diameter due to the surface loading against the position of the applied load for $z_{0,1} = z_{0,2} = 20$m.

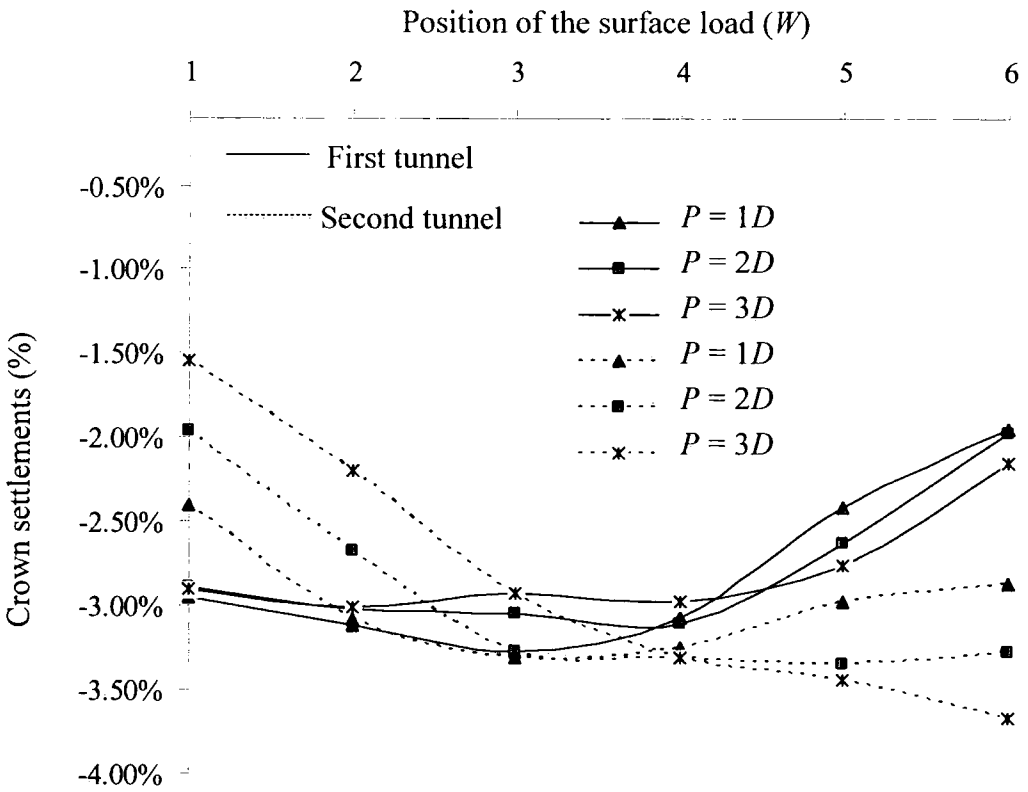

a) $z_{0,1} = z_{0,2} = 15$m

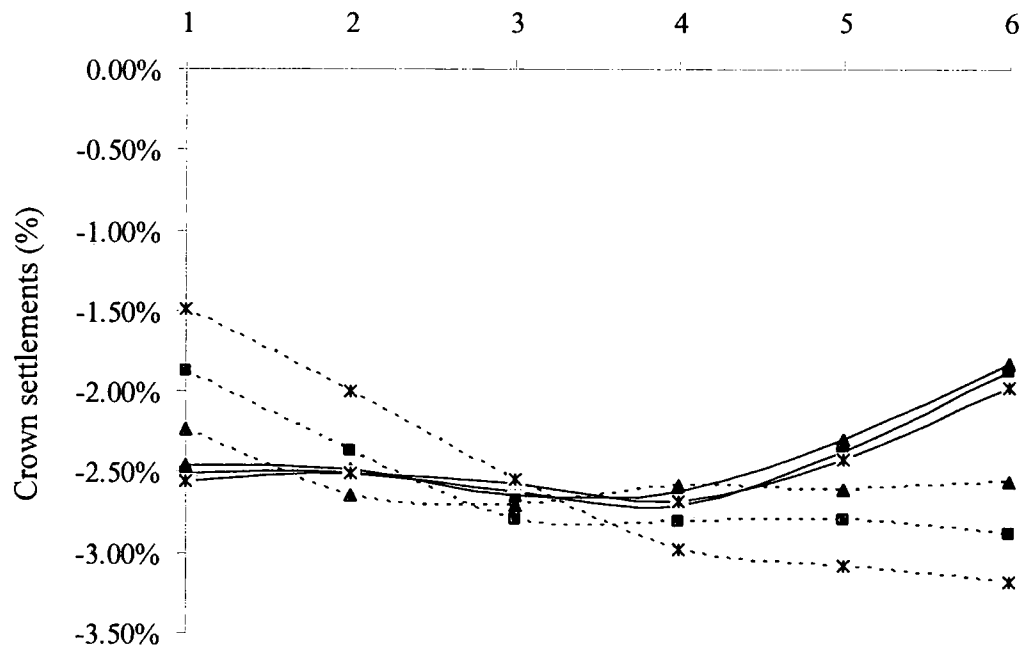

b) $z_{0,1} = z_{0,2} = 20$m

Figure 6.16. Crown settlements due to loading expressed as a percentage of the initial tunnel diameter against the position of the surface loaded area for different excavation depths.

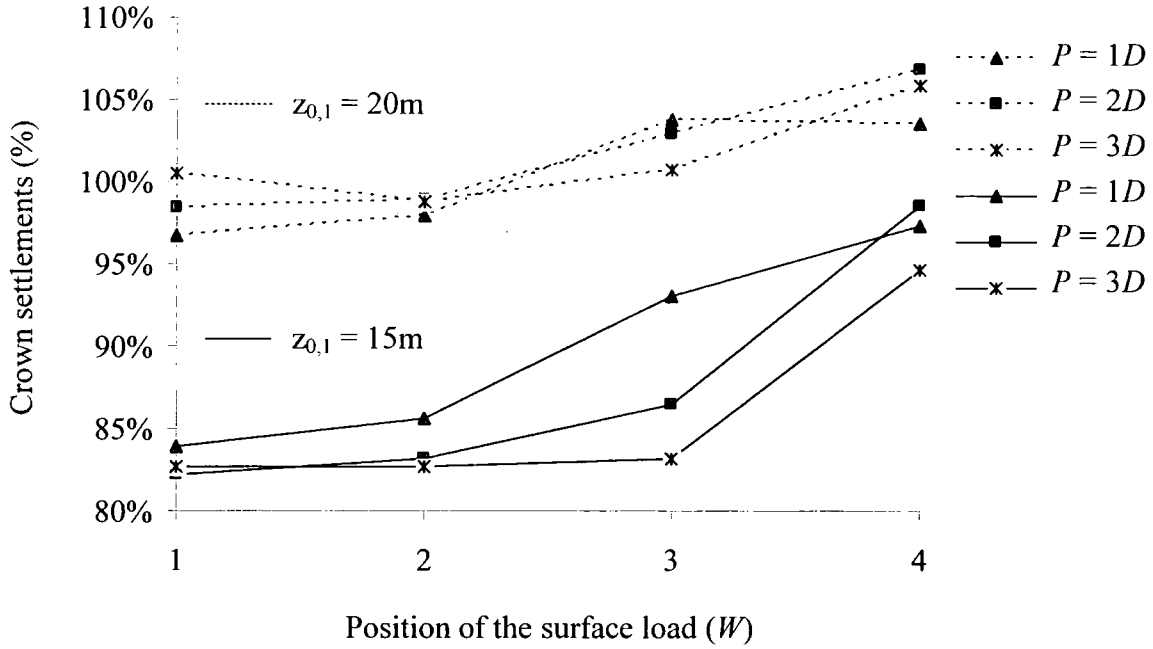

Figure 6.17. Plots of the crown settlements due to loading of the first tunnel in the twin tunnel case as a percentage of the single tunnel results for various surface loading areas and two different tunnel depths.

Figure 6.18 shows the change of bending moments due to the effect of the surface load for both tunnels and for different excavation depths ($z_{0,1} = z_{0,2}$ = 15m and 20m) when $P = 1D$. The same sign convention for the bending moment distributions is used as for the single tunnel case. Positive maximum changes of bending moments appear around the springlines (68° to 90° and 248° to 293°) for both tunnels. Negative maximum changes of bending moments on the contrary appear most commonly around the crown (338° to 0) and invert (158° to 180°). This is the case regardless of the excavation depth.

Figures 6.19 and 6.20 depict plots of the change of bending moments from maximum positive (dotted line) to maximum negative (thin line) around the liner just due to the effect of surface loading against six different loading positions ($W1$ to $W6$). The excavation depth varies from $z_{0,1} = z_{0,2}$ = 15m to 20m. The magnitudes of these changes seem to be greater for shallow excavation. The first tunnel appears to behave in the same way as for the single tunnel case. The peak of these changes of bending moments for the latter tunnel appears when the load is directly applied above at $W2$ and then gradually decreases until $W6$, when $z_{0,1} = z_{0,2}$ = 15m. For the deeper case

the peak is shifted towards *W*3, regarding the same tunnel. Similar but not so obvious trend characterises the second tunnel's behaviour.

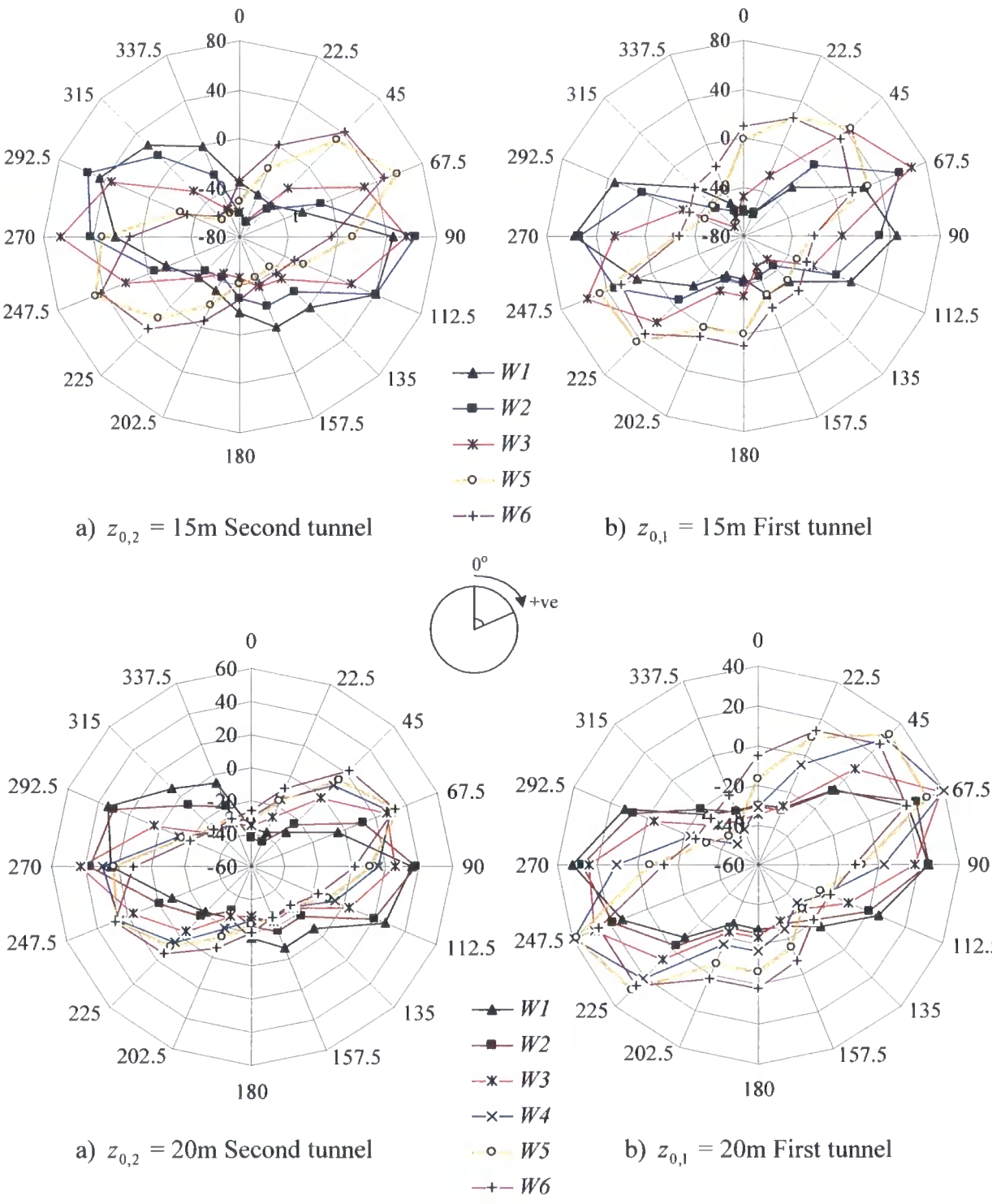

a) $z_{0,2}$ = 15m Second tunnel

b) $z_{0,1}$ = 15m First tunnel

a) $z_{0,2}$ = 20m Second tunnel

b) $z_{0,1}$ = 20m First tunnel

Figure 6.18. Change of bending moments due to the effect of surface loading for different surface loaded areas when $z_{0,1} = z_{0,2}$ = 15m and 20m. The axial axis refers to the distribution of bending moments (kNm/m) around the tunnel, while the circumferential axis refers to the angle around the tunnel.

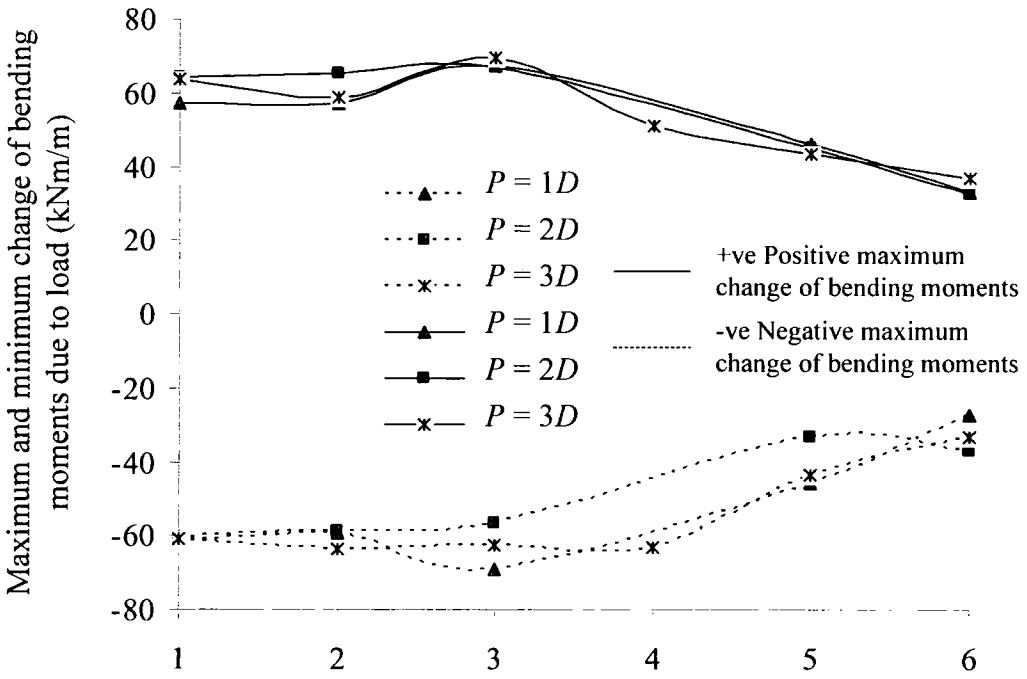

a) Regarding the first tunnel

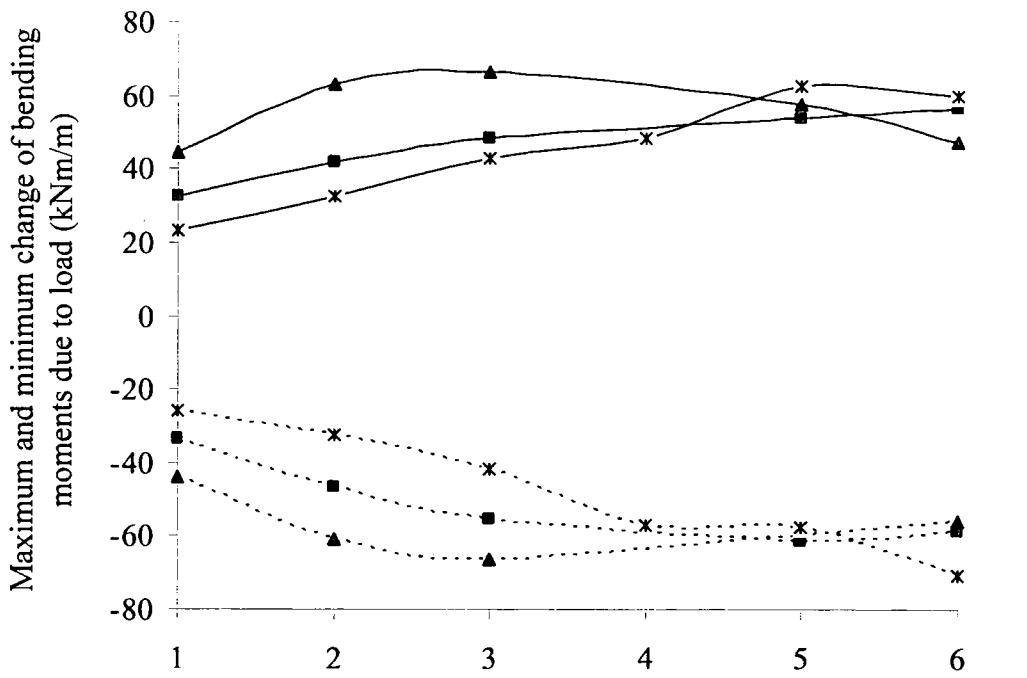

b) Regarding the second tunnel

Figure 6.19. Maximum and minimum change of bending moments due to the effect of surface loading for different surface loaded areas when $z_{0,1} = z_{0,2} = 15$m.

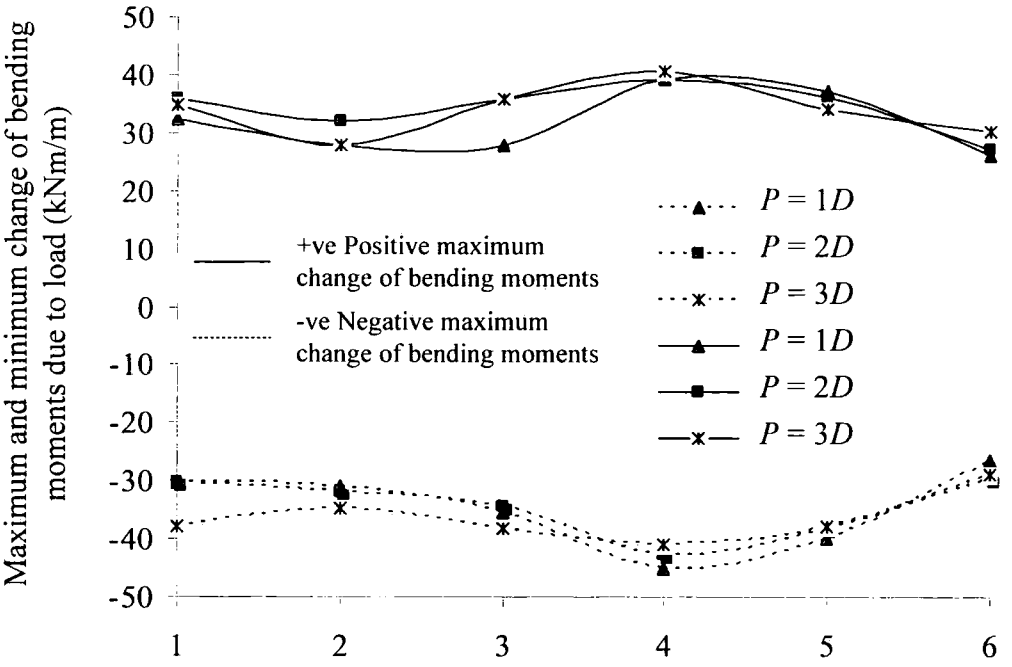

a) Regarding the right tunnel

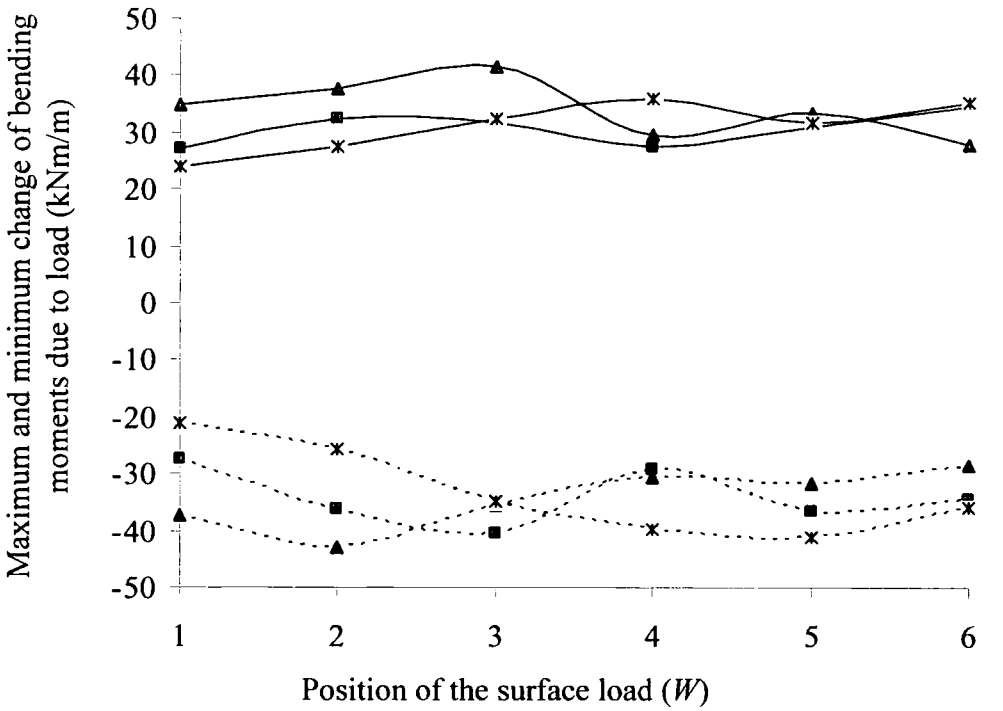

b) Regarding the left tunnel

Figure 6.20. Maximum and minimum change of bending moments due to the effect of surface loading for different surface loaded areas when $z_{0,1} = z_{0,2} = 20$m.

6.2.3 Twin tunnels vertically aligned (case *TVD*)

6.2.3.1 Introduction

In this section results are presented for the twin tunnel case where the axes are vertically and diagonally aligned (case *TVD*). Figure 6.21 shows one of the meshes used in this study where $z_{0,1}$ = 15m and $z_{0,2}$ = 20m for the upper and lower tunnels respectively. The pillar width distance in this case is P = 1D. The mesh consists of 331 nodes (662 d.o.f.). Soil is modelled with 146 six-noded triangular elements while tunnel liner with 32 two-noded beam elements.

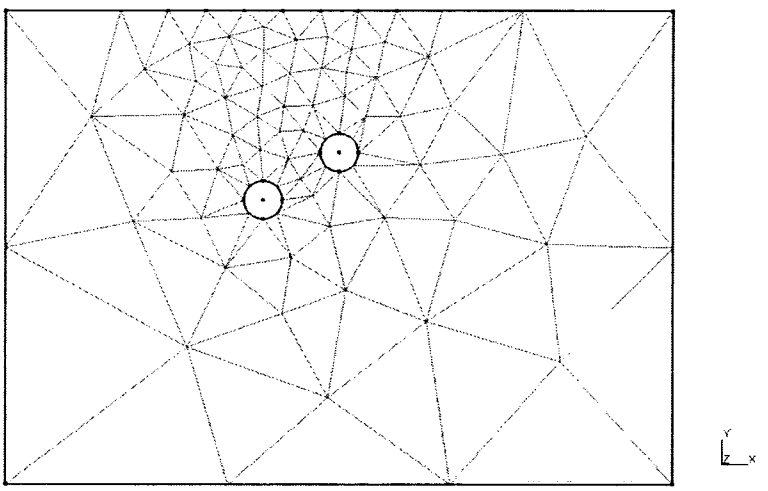

Figure 6.21. Generated mesh for the *TVD* case when $z_{0,1}$ =15m for the upper tunnel, $z_{0,2}$ = 20m for the lower tunnel and P = 1D.

6.2.3.2 Details of the analysis

The analysis details are identical to those described in Sections 6.2.1 and 6.2.2. The upper tunnel's axis is always fixed at $z_{0,1}$ = 15m. The position of the lower tunnel varies though ($z_{0,2}$ = 20m and 23m). Three different pillar widths are modelled (P = piggy-back, where the lower lies exactly beneath the upper tunnel, P = 0 and P = 1D) with six different surface loading areas ($W1$ to $W6$). Consequently, a total of 36 analyses were performed in the current parametric study.

6.2.3.3 Analysis results

Figure 6.22 shows the ratio of the maximum surface settlement distribution due to the surface load only over the tunnel diameter (S'_{max}/D) against the position of the loaded area (W) for the above mentioned two different excavation depths of the lower tunnel. Both shape and magnitudes of these plots are similar regardless of the second tunnel's depth. Consequently soil deformations due to loading seem to be restricted and formed by the position of the upper tunnel. The trend in both cases (Figure 6.22a and 6.22b) indicates that when P = piggy-back and P = 0 the maximum surface settlement (S'_{max}) occurs above the upper tunnel when $W2$ area is loaded. However when the lower tunnel is driven further away (P = 1D) the maximum surface settlement occurs above the lower tunnel when $W4$ area is loaded.

In Figure 6.23 both tunnels' deformed shape (coloured circles) due to the effect of the surface loading is presented (scaled up) for the case where the lower tunnel lies at two different depths ($z_{0.2}$ = 20m and 23m) and P = piggy-back. Black thick circles indicate the initial shape of the liner prior to any loading stage. Similar lining behaviour is observed as that described in Sections 6.2.1 and 6.2.2 (i.e. squatting and rotating anti-clockwise as the load shifts from $W1$ to $W6$). The deformations of the lower tunnel though seem to be smaller compared to the upper.

Figures 6.24 and 6.25 show plots of the change of both horizontal (along the springlines) and vertical (crown to invert) tunnel diameters expressed as a percentage of the initial tunnel diameter against the relative position of the surface loaded area (W). Thin lines refer to the horizontal changes of the tunnel diameter. Dotted lines on the other hand correspond to the vertical changes. The upper tunnel behaves in the same way as the right tunnel does in the twin tunnel case described in Section 6.2.2. The maximum increase and decrease of the upper tunnel's diameter always occurs when the surface load is directly applied above at $W2$ (approximately 1% of the tunnel diameter). The shape of these changes for the lower tunnel does not alter significantly regardless of the depth or the surface loaded area. However as the load shifts further away (towards $W6$) the changes for the lower tunnel smoothly reduce towards zero (i.e. no change of D compared to initial shape). For the upper tunnel though the changes rapidly decrease until finally they reach zero.

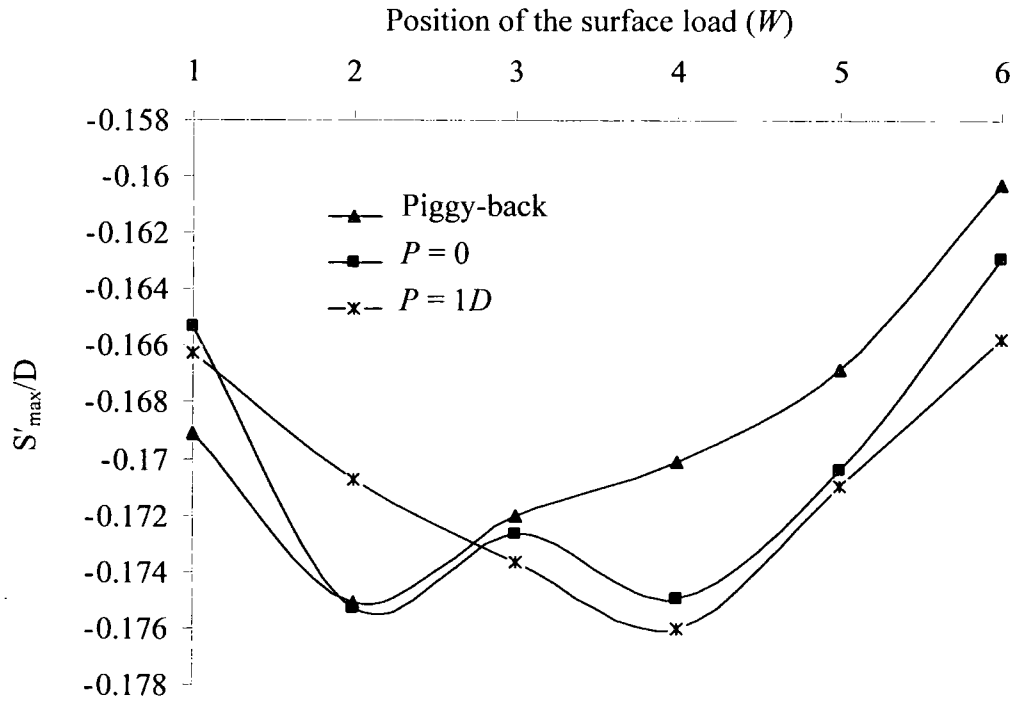

a) When the lower tunnel is at $z_{0.2}$ = 20m

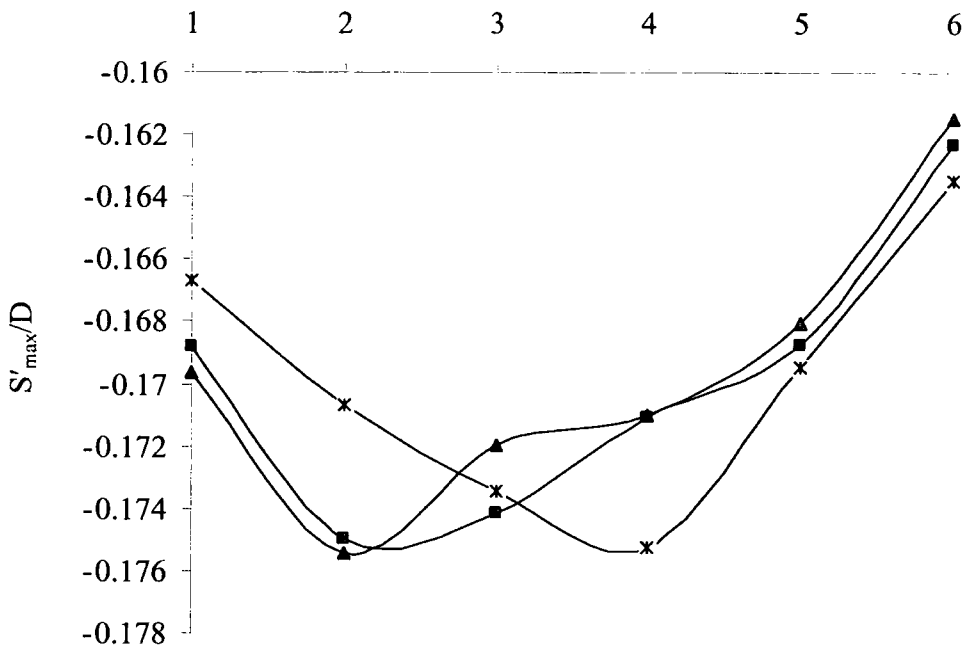

b) When the lower tunnel is at $z_{0.2}$ = 23m

Figure 6.22. Plots of the maximum surface settlements due to surface loading against the position of the loaded area for two different excavation depths and three different pillar widths.

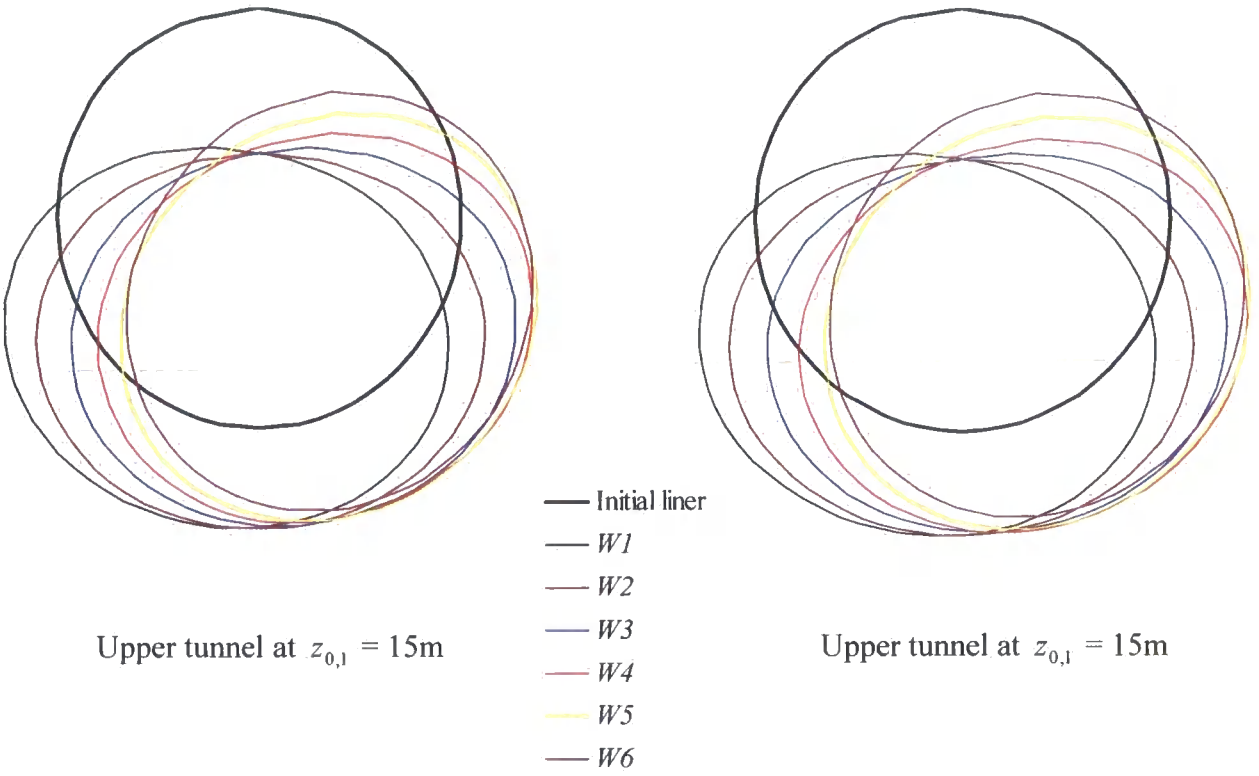

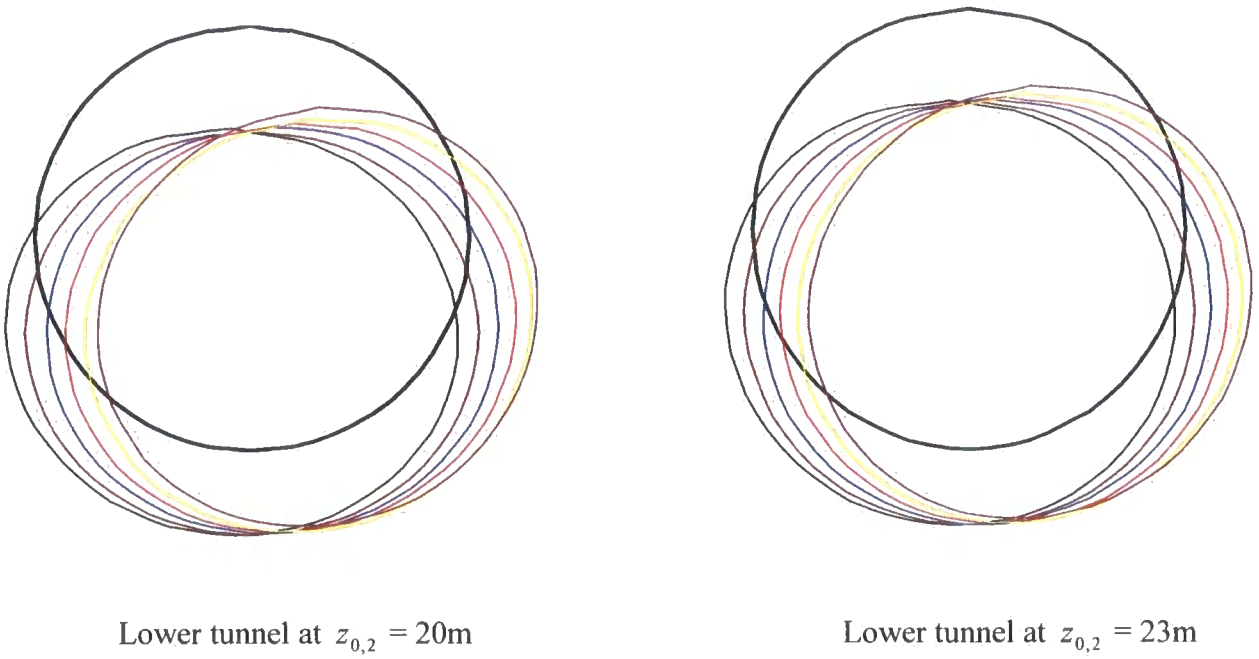

Figure 6.23. Deformed shape of the tunnels due to the surface loading when the second tunnel is driven at $z_{0,2}$ = 20m and 23m while P = piggy-back.

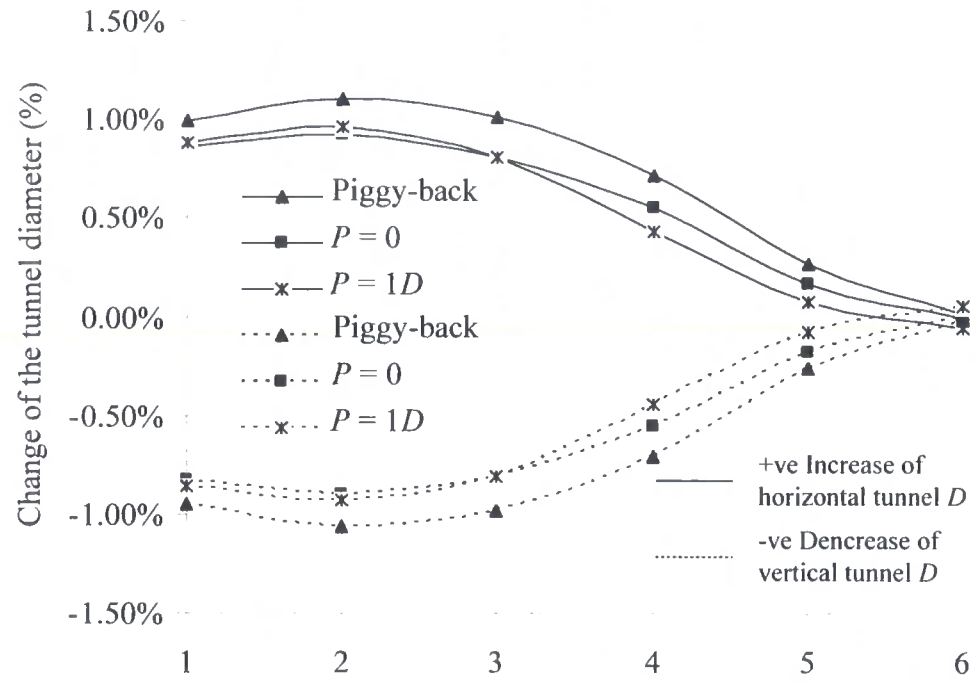

a) Regarding the upper tunnel

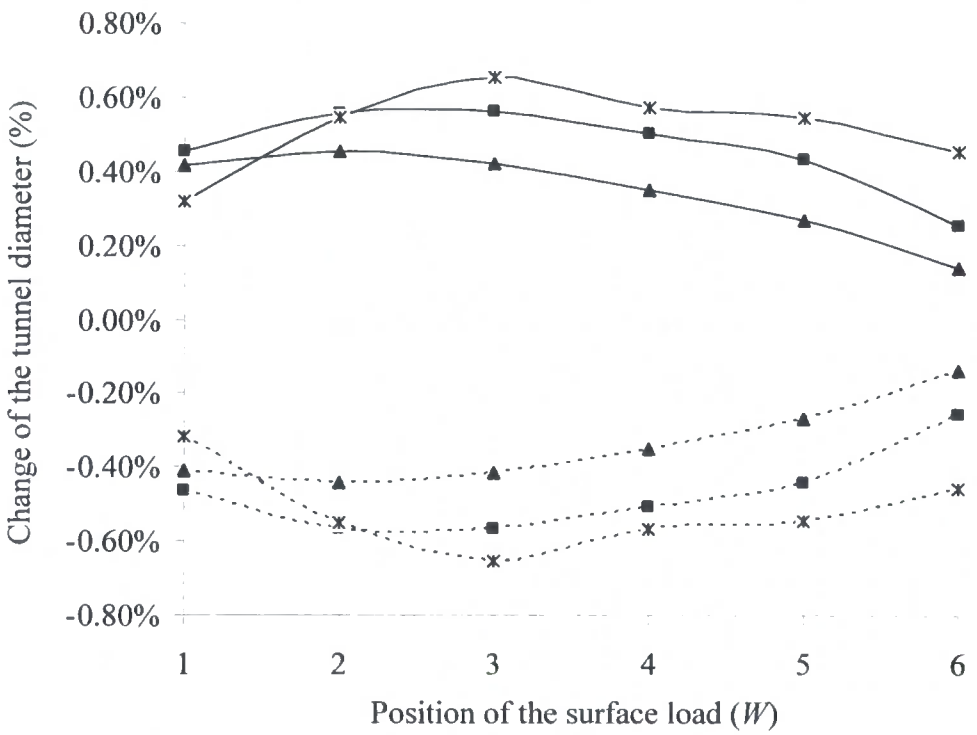

b) Regarding the lower tunnel

Figure 6.24. Changes of horizontal and vertical tunnel diameters due to the surface loading expressed as a percentage of the initial tunnel diameter against the position of the applied load when the lower tunnel lies at $z_{0,2}$ = 20m.

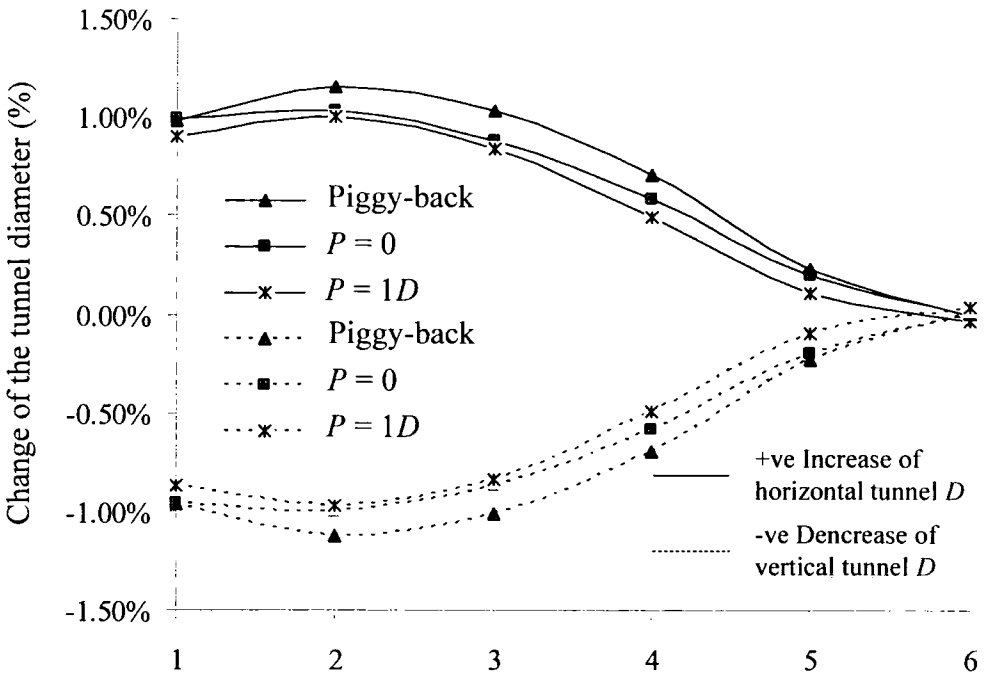

a) Regarding the upper tunnel

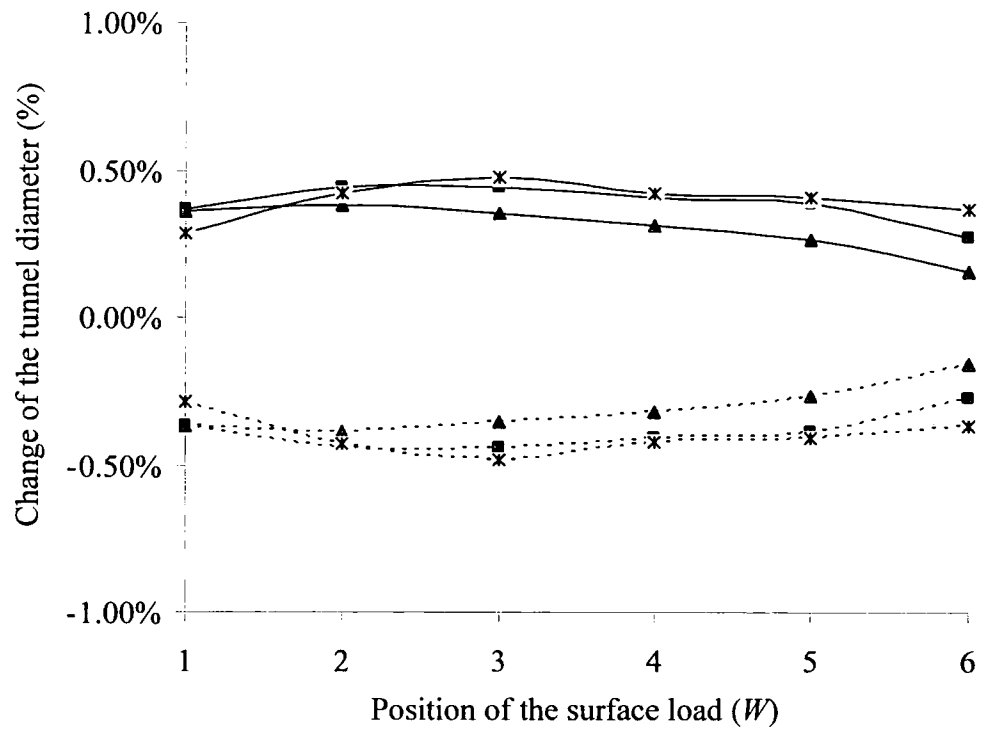

b) Regarding the lower tunnel

Figure 6.25. Changes of horizontal and vertical tunnel diameters due to the surface loading expressed as a percentage of the initial tunnel diameters against the position of the applied load when the lower tunnel lies at $z_{0,2}$ = 23m.

In Figure 6.26 both tunnels' crown deformations expressed as a percentage of the initial tunnel diameters are plotted against the relative position of the surface loaded area (*W*). Thin lines refer to the upper tunnel while dotted lines to the lower. The crown deformation predictions for each tunnel seem to be unaffected from both pillar width (*P*) and tunnel depth (z_0). The maximum crown deformation for the upper tunnel (approximately 3.5%) takes place when the load is applied directly above it similar to the single tunnel case. As for the lower tunnel slightly bigger values correspond to shallower excavation. The trend though remains the same.

Figure 6.27 shows the interaction between the two tunnels in the *TVD* case and the surface load compared to the single tunnel case (*ST*) in terms of crown settlements. For the *TVD* case crown settlement predictions from the upper tunnel are plotted as percentage of the single tunnel case against the position of the surface loaded area (*W*) for different pillar widths (*P* = piggy-back, 0 and 1*D*) when $z_{0,2}$ = 15m. It can be observed that a small amount (less than the twin tunnel shallow case) of interaction exists (none to 6%) compared to the single case results. Greater interaction appears between the tunnels when they are closely spaced (*P* = piggy-back and 0) of approximately 5%. When the lower tunnel is driven further away (*P* = 1*D*) less interaction between the two vertically aligned tunnels occurs (none to 3%). In every case Strand7 predicts bigger interaction for closely spaced shallow parallel tunnels.

Figure 6.28 depicts the distribution of the bending moments (kNm/m) around the liners due to the effect of the surface loading for different depths of the lower tunnel ($z_{0,2}$ = 20m and $z_{0,2}$ = 23m). This figure refers to the case where *P* = piggy-back. The sign convention for bending is the same as the one described for the single tunnel case (Section 6.2.2). The magnitudes always appear to be greater for the upper tunnel. Positive maximum changes of bending moments approximately develop around the springlines from 45° to 90° and from 225° to 270°. Negative maximum changes of bending moments occur around the crown from 293° to 23° and around the invert from 113° to 203°. These values are constant regardless of the position of the lower tunnel. Positive maximum changes of bending moments for the lower tunnel approximately develop around the springlines from 45° to 90° and from 248° to 270°. Negative maximum changes of bending moments approximately develop around the crown at 315° to 23° and around the invert at 135° to 203°. The range is the same

regardless of the depth. However the absolute values of bending moments (for the lower tunnel) slightly reduce for deeper excavations. The rotation of both liners due to the surface loading which was identified in Figure 6.23 is evident.

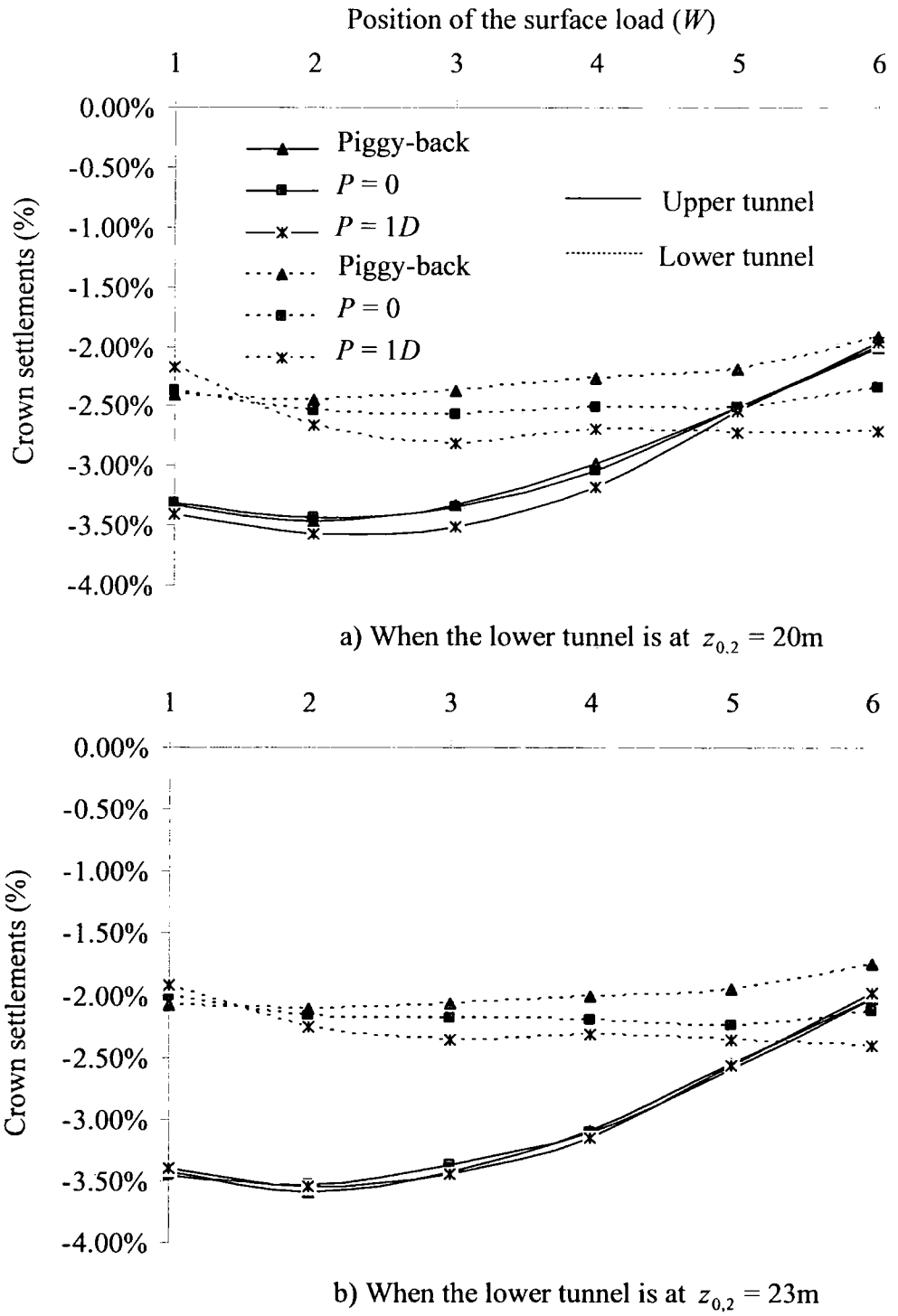

Figure 6.26. Crown settlements expressed as a percentage of the initial tunnel diameter against the position of the surface loaded area for different excavation depths.

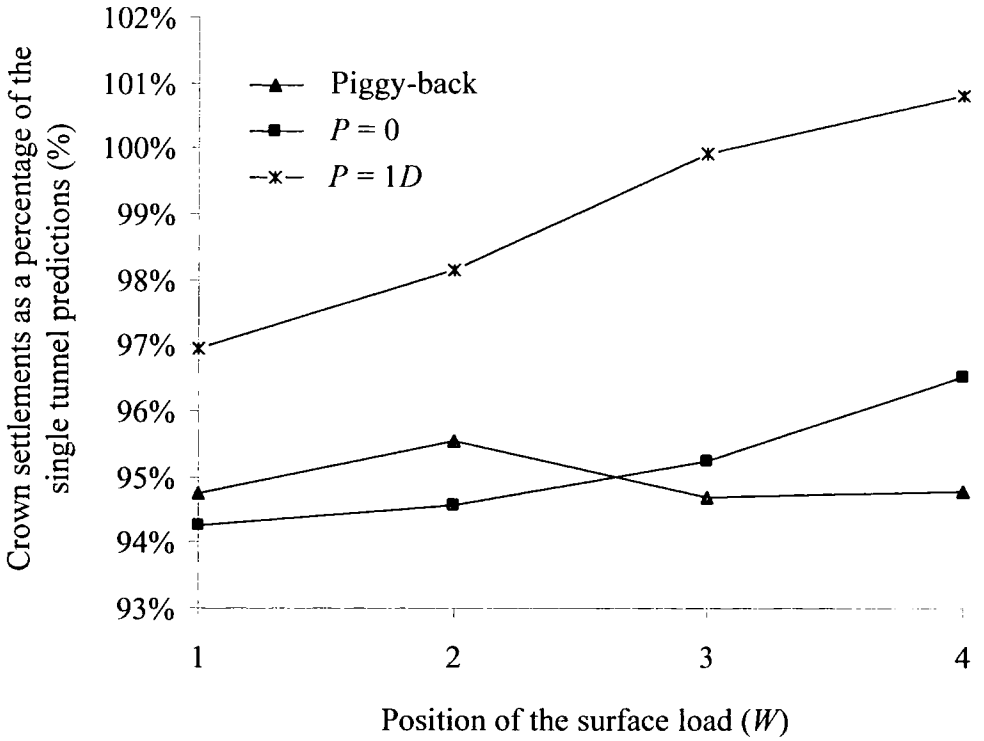

Figure 6.27. Plots of the crown settlements due to loading of the upper tunnel case as a percentage of the single tunnel predictions for various surface loading areas when $z_{0.2} = 20$m.

Figures 6.29 and 6.30 show plots of the change of bending moment distribution around the liners from maximum positive (thin lines) to maximum negative (dotted lines) solely due to the effect of surface loading against the position of the surface loading area (W). These maxima do not have their peak directly above the upper tunnel (at $W2$) as in the twin tunnel case in Section 6.2.2. Instead these are shifted towards $W3$. As the load moves further away (towards $W6$) these values rapidly decrease towards zero (i.e. no deformation). The magnitudes of these changes for the lower tunnel seem to be smaller compared to the upper. Additionally the trend of these curves is similar regardless of the depth.

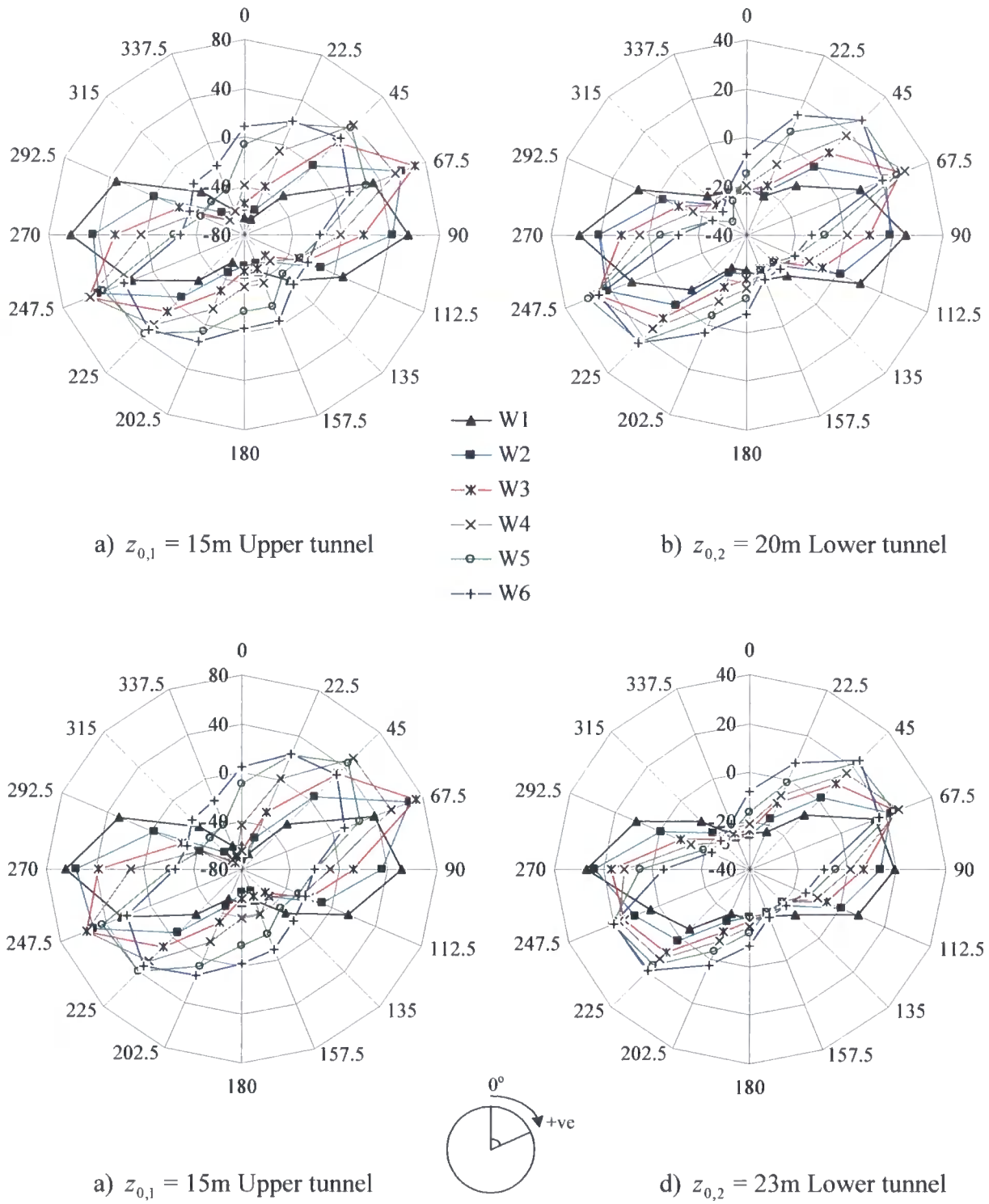

a) $z_{0,1}$ = 15m Upper tunnel

b) $z_{0,2}$ = 20m Lower tunnel

a) $z_{0,1}$ = 15m Upper tunnel

d) $z_{0,2}$ = 23m Lower tunnel

Figure 6.28. Change of bending moments due to the effect of surface loading for different surface loaded areas and different tunnel depths ($z_{0,2}$ = 20m and 23m). The axial axis refers to the distribution of bending moments (kNm/m) around the tunnel, while the circumferential axis refers to the angle around the tunnel.

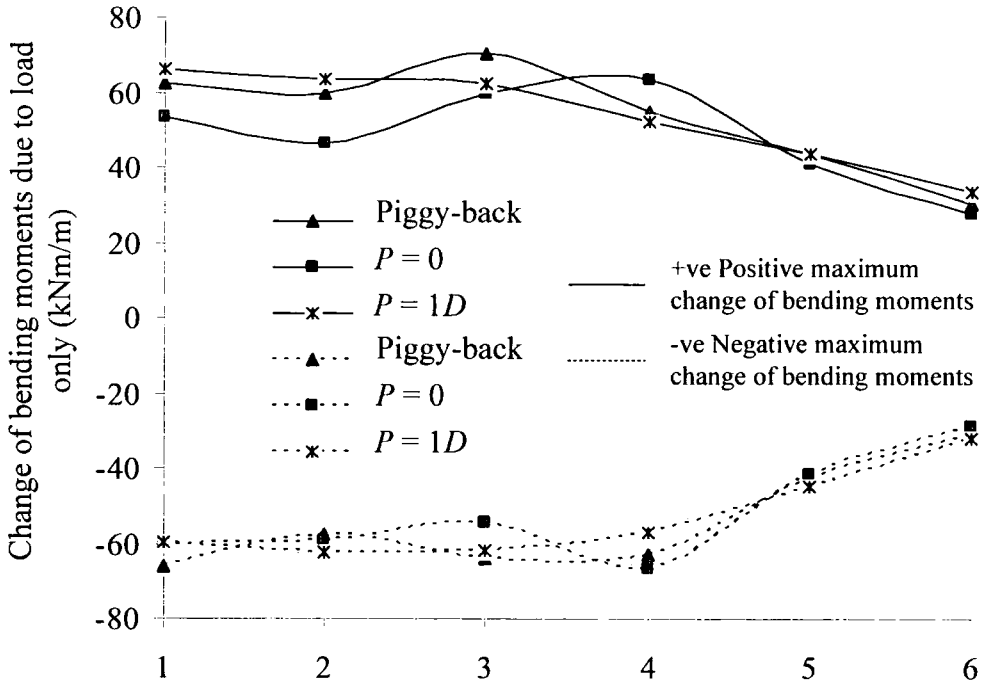

a) Regarding the upper tunnel

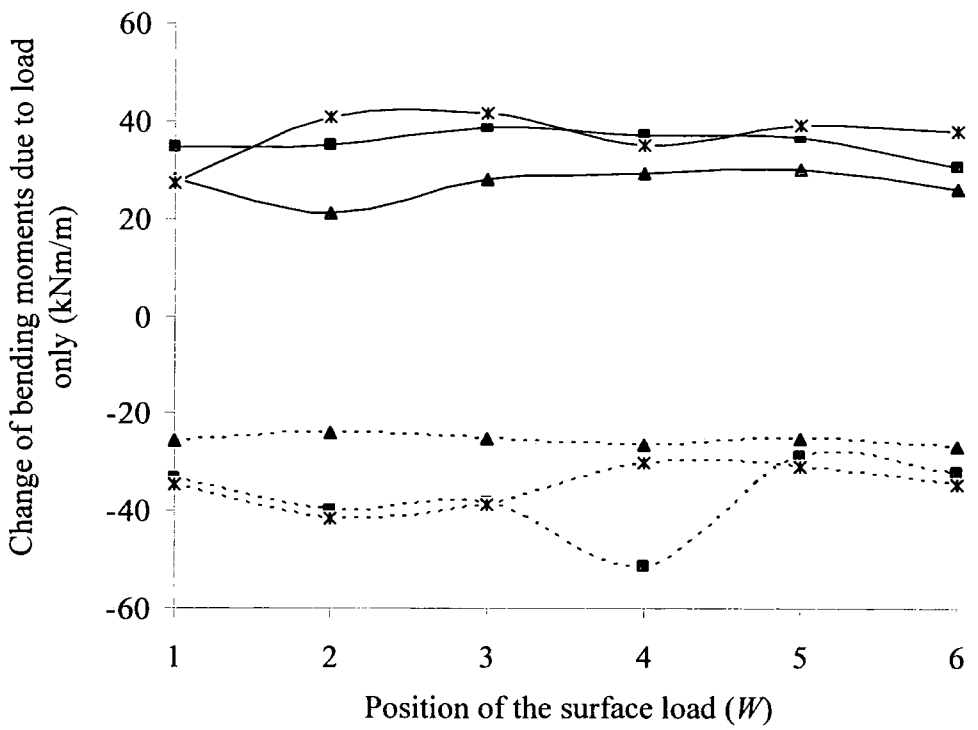

b) Regarding the lower tunnel

Figure 6.29. Maximum and minimum change of bending moments due to the effect of surface loading for different surface loaded areas when the lower tunnel is at $z_{0,2}$ = 20m.

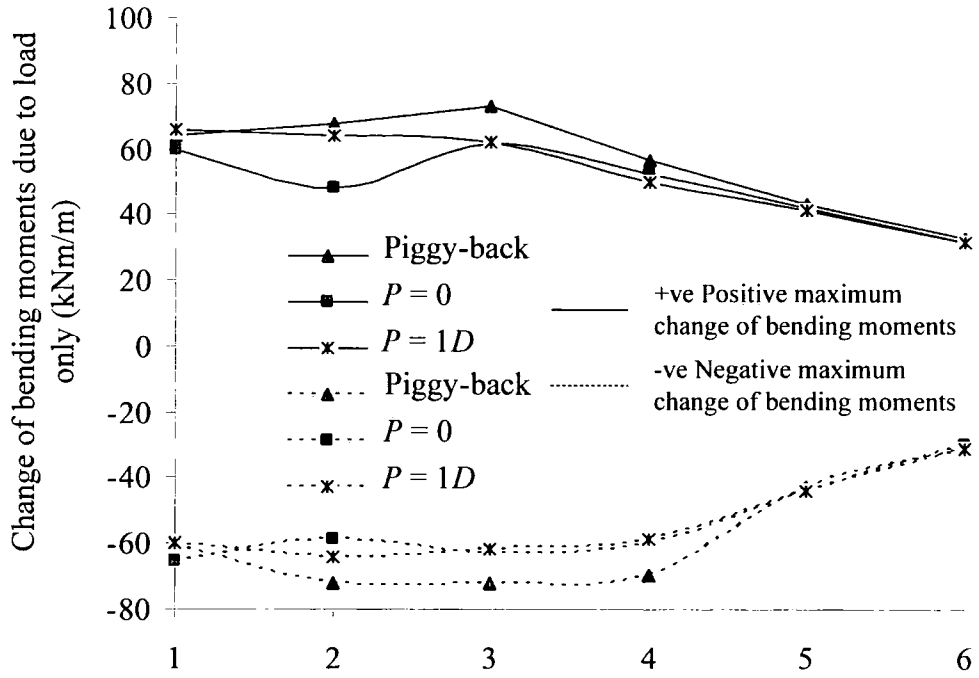

a) Regarding the upper tunnel

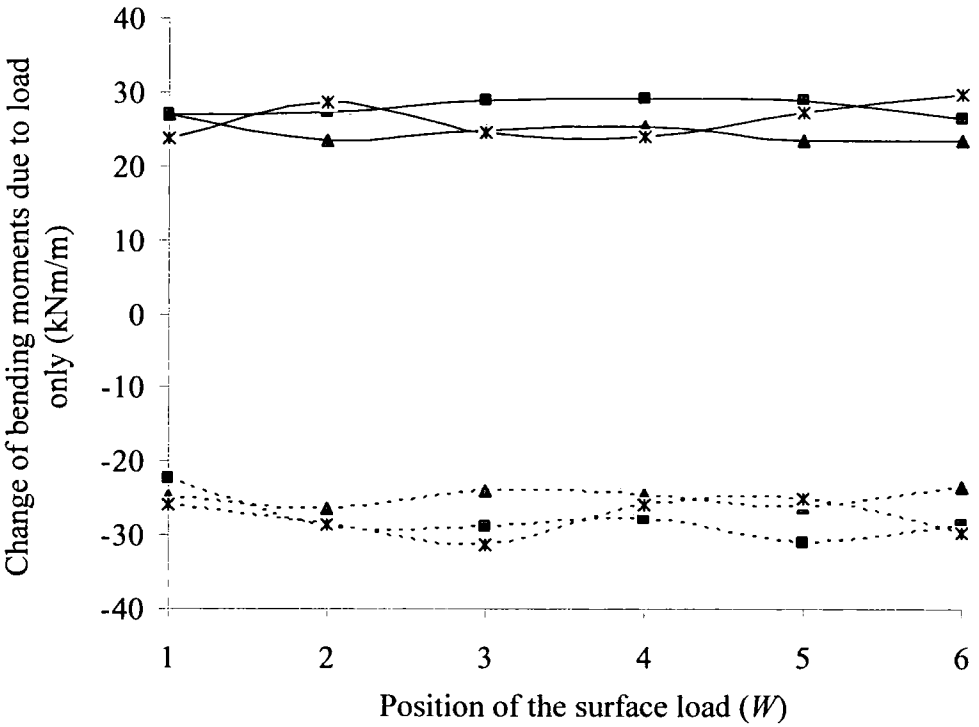

b) Regarding the lower tunnel

Figure 6.30. Maximum and minimum change of bending moments due to the effect of surface loading for different surface loaded areas when the lower tunnel is at $z_{0,2}$ = 23m.

6.2.4 Comparison of the *ST* case with the *TH* and *TVD* cases

In this section the FE predictions regarding the first tunnel (in the *TH* case) and the upper tunnel (in the *TVD* case) are compared with the predictions regarding the single tunnel (*ST* case) in order to investigate the interaction mechanism of soil-tunnel-structure in 2-D. The above mentioned comparison is made in terms of maximum surface settlements due to loading, lining deformations and bending moment distribution.

The FE predictions presented in Sections 6.2.2.3 regarding the first tunnel (*TH* case) and in Section 6.2.3.3 regarding the upper tunnel (*TVD* case) are smaller than those regarding the *ST* case. This is a first indication of the existence of interaction. In both of the compared cases the shape of the tunnels seems to squat while the reduction of the vertical tunnel diameter coincides with the increase of the horizontal. The maximum lining deformation occurs when the surface load is applied at *W*2. No lining deformation is predicted when the load is applied at *W*6 which indicates that at that distance the interaction ceases. Crown settlements are roughly constant when the load is applied between *W*1 and *W*4 [within the region of 2*D* from the first tunnel (*TH* case) and the upper tunnel (*TVD* case)]. Further from that region the crown settlements seem to reduce. Similar behaviour is observed with the distribution of the bending moments around the liners.

In total it seems that interaction occurs within the region of *W*1 to *W*4 ($P \leq 2D$) and then ($P \geq 3D$) it starts to reduce. The contributory factors to this complex mechanism are the surface load and the excavation depth rather than pillar width since when the pillar width varied the FE predictions were constant. Greater interaction is predicted in the *TH* case compared to the *TVD* case. This implies that the existence of the lower tunnel (*TVD* case) does not contribute to the complex interaction mechanism in the same way as it does the second tunnel in the *TH* case.

6.3 Details of analysis using Plaxis

6.3.1 Single tunnel case (*ST*)

6.3.1.1 Introduction

In this section the results of an identical program of analyses to the previous section are described using Plaxis v.8. The latter is a commercial 2-D FE software. In Figure 6.31 one of the generated meshes for the single tunnel parametric analysis is presented for z_0 = 20m. The dimensions of the domain as well as the tunnel diameter and the magnitude of the surface load are the same as those described in Section 6.2.1. The auto-generated mesh consists of 2,817 nodes and is divided into 330 fifteen-noded triangular elements. The reason for using different type of elements (fifteen-noded triangles rather than six-noded triangles) compared to Strand7 is for achieving greater accuracy. Curved beam elements are used to model the tunnel lining. The number of nodes is considerably higher than that used in Strand7 even though the number of the elements is similar. In Plaxis v.8 the user cannot import a mesh from another software. Thus it was entirely created in Plaxis v.8 pre-processing stage. Differences in the refinement as a result are evident.

Three different tunnel depths (z_0 = 15m, 20m an 25m) are modelled as well as three different surface loaded areas (*W*2, *W*3 and *W*4). This gives a total of 9 analyses for this study.

6.3.1.2 Initial conditions

The gravity loading method which is described in Section 6.2.1 is used to determine the stress conditions prior to surface loading. The tunnel with its permanent lining appears in the mesh as if wished in place. Thus excavation is not modelled. Stratigraphy and boundary conditions are identical to those presented in Section 6.2.1.

6.3.1.3 Constitutive models

Beam elements which are used to model the liner are assumed to behave in a linear elastic way similar to Strand7. Their properties are presented in Table 6.1. A simple

elasto-plastic model is used to model soil behaviour. The plastic region of the soil is described by Mohr-Coulomb failure criterion with non-associated flow (In Strand7 the same failure criterion is used with associated flow though). Soil properties are presented in Table 6.2.

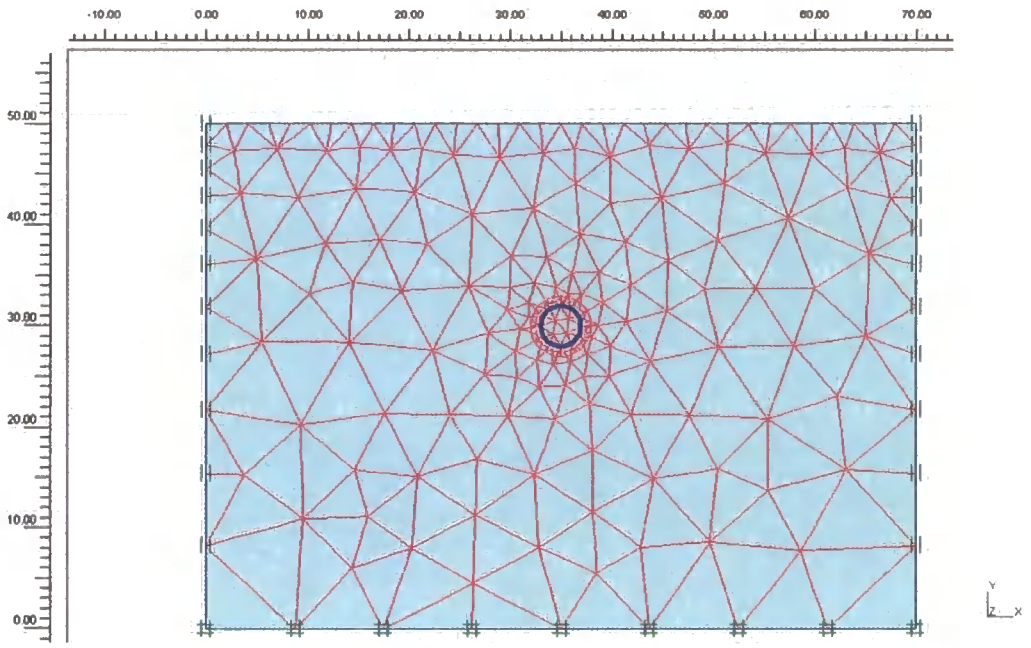

Figure 6.31. Generated mesh for the single tunnel analysis when $z_0 = 20$m.

6.3.1.4 Modelling sequence

The calculations performed using Plaxis v.8 in the current chapter assume the tunnel and its permanent lining as if wished in place. This is achieved by activating the lining and de-activating the cluster inside the tunnel. Stresses are not generated for this part of the analysis. Two load stages are consequently defined. During the first gravity loading is applied throughout the mesh. In the subsequent stage surface load is activated. The generated displacements from the first loading stage are considered to be the zero datum. Thus only those predicted by the FE analysis due to the second load stage are measured.

6.3.1.5 Analysis results

In this section the results of 2-D FE analyses of surface loading above a single tunnel driven in soft ground are presented comprising of surface settlements, lining deformations and bending moments. Figure 6.32 shows plots of the ratio of the

maximum surface settlements due to the surface loading (S'_{max}/D) over the tunnel diameter against the position of the loaded area on the surface (W). Each of these three curves refer to a different tunnel depth (z_0 = 15m, 20m an 25m. These will be referred as the three different tunnel depths for the remaining of this chapter). The maxima of these curves every time appear above the tunnel axis (i.e. when $W2$ area is loaded). As the load shifts towards $W4$ they gradually decrease. The latter trend is the same regardless of excavation depth z_0. These values seem to be relatively higher (approx. 8%) than those predicted by Strand7 when undertaking an equivalent 2-D FE analysis.

Figure 6.33 depicts the lining deformations (scaled up) due to the surface load for three different tunnel depths. The shapes of the deformed liners are then compared to the original (thick circles) prior to any loading stage. This figure verifies previous predictions made from Strand7. These are: anti-clockwise rotating and squatting (increase of the horizontal diameter and decrease of the vertical) of the liners as the load transfers from $W2$ to $W4$. These variations for different values of D are presented in Figure 6.34. In this, changes of the horizontal (thin lines) and vertical (dotted lines) tunnel diameter expressed as a percentage of the initial tunnel diameter are plotted against the relative position of the surface loaded area (W) for three different tunnel depths. The results indicate an increase of the horizontal diameter (along springlines) followed by a decrease of the vertical (crown to invert) in all cases regardless of the depth. Shallow tunnels experience greater deformations (approximately 1% of the tunnel diameter) which reduce as the load shifts towards $W4$. The maximum increase of the horizontal diameter and the maximum decrease are roughly 0.9%. In both cases the load is applied above the tunnel (at $W2$) which in turn lies at z_0 = 15m. As the load shifts towards $W4$ these changes reduce. These predictions are in good agreement with Strand7 since they measure changes of D rather than absolute values, where discrepancies may occur.

In Figure 6.35 crown deformations are expressed as a percentage of the initial tunnel diameter against the position of the loaded area (W) are plotted for three different tunnel depths. The maximum crown deformation was approximately 2% of the tunnel diameter and occurred at z_0 = 15m when the load was applied at $W2$. This value is almost half that compared to the prediction of Strand7. Nevertheless the general trend

is similar. As the load moves further away from the tunnel's centre line the crown deformations reduce.

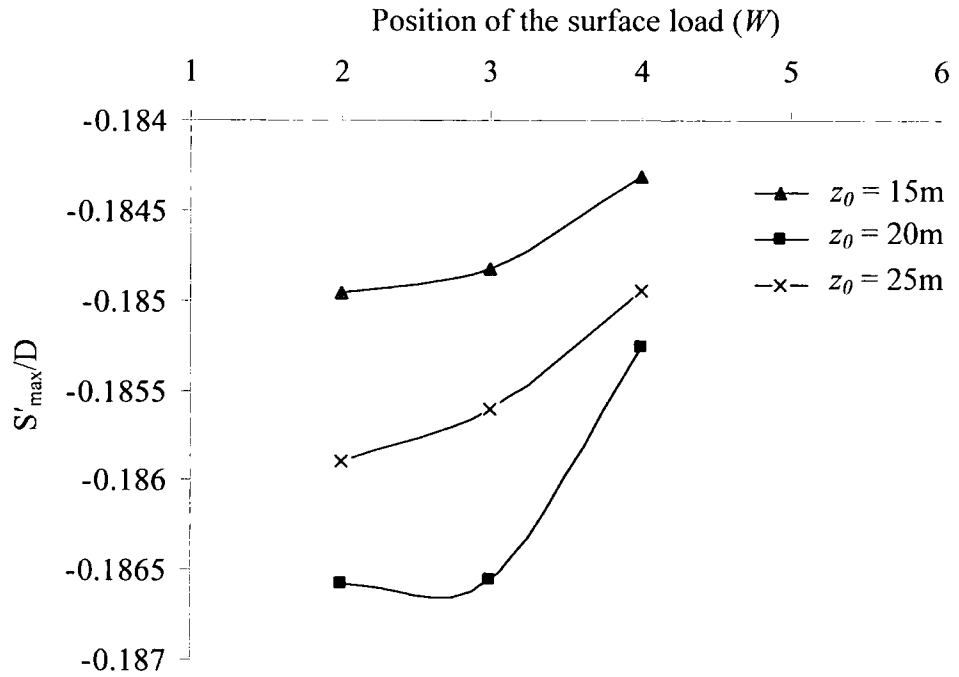

Figure 6.32. Plots of the ratio of the maximum surface settlements due to surface loading over the tunnel diameter against the position of the load for various excavation depths.

The bending moment distribution around the liner solely due to the effect of surface loading is presented in Figure 6.36. The sign convention for the bending moments is the same as that described in Section 6.2.1. This figure covers the cases of three different tunnel depths and the loaded area varies from *W*2 to *W*4. The maximum positive change of bending moments for the three loaded areas lies around the springlines from 56° to 78° and from 244° to 277°. The maximum negative changes on the other hand are situated around the crown from 330° to 360° and the invert from 180° to 146°.

Figure 6.37 shows plots of the positive and negative maximum changes of bending moments (kNm/m) around the liner due to the surface loading against the position of the loaded area (*W*) for three different tunnel depths. Thin lines indicate the maximum positive changes while dotted lines indicate maximum negative changes. Shallower tunnels seem to be mostly affected by surface loading particularly when the latter is

applied directly above the tunnel's centre line. As the load shifts further away these values reduce rapidly. For deeper tunnels though this reduction is smoother. Similar trends were identified in Strand7. However the current predictions seem to be smaller by between 16% to 40%.

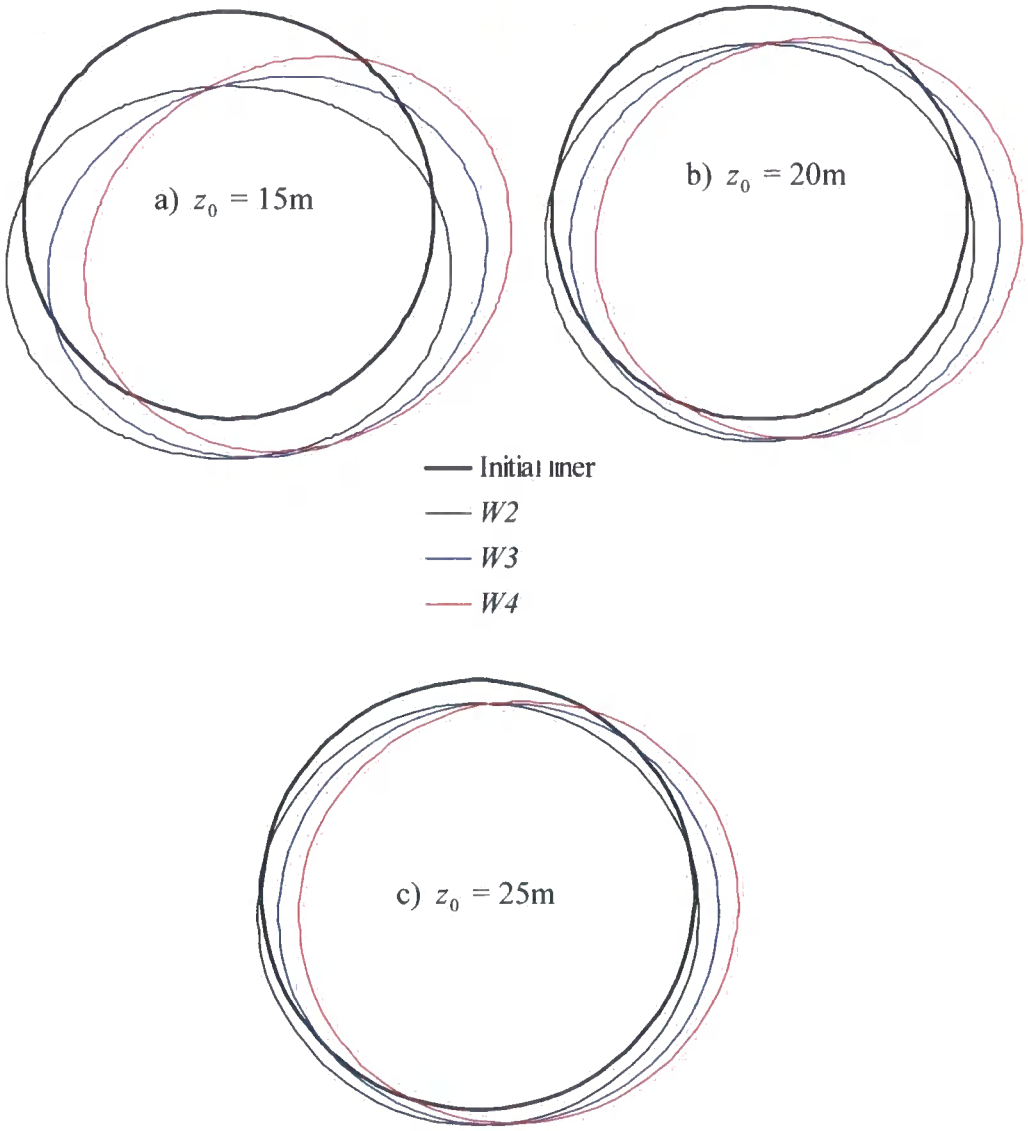

Figure 6.33. Deformed shape of the tunnel due to the surface loading for three different loaded areas (*W*2, *W*3 and *W*4) and three different tunnel depths (z_0 = 15m, 20m and 25).

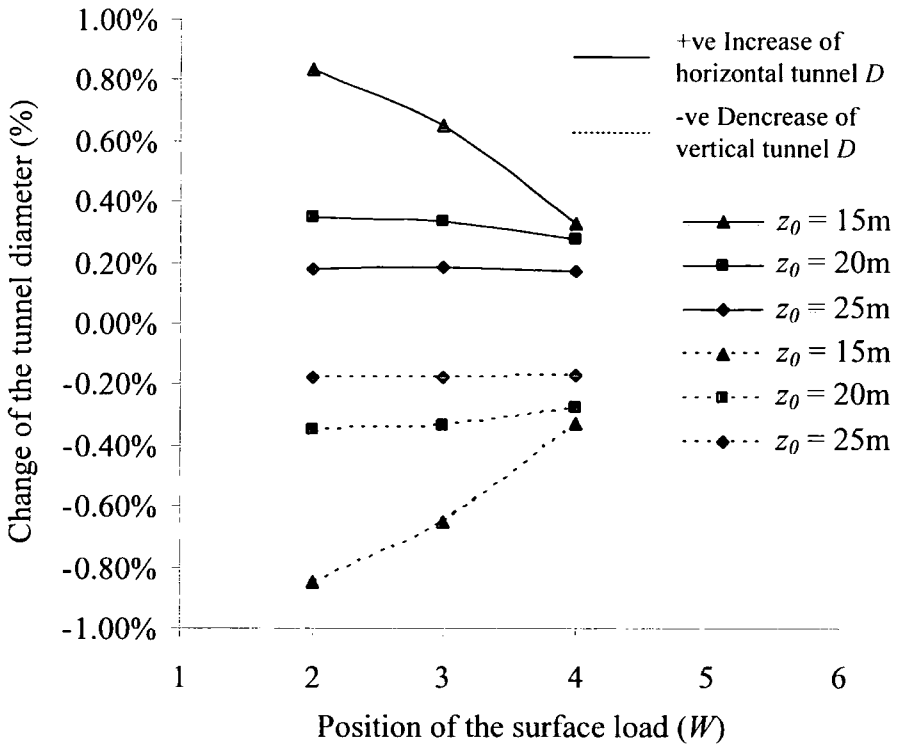

Figure 6.34. Changes of horizontal and vertical tunnel diameters due to the surface loading against the position of the applied load for various excavation depths.

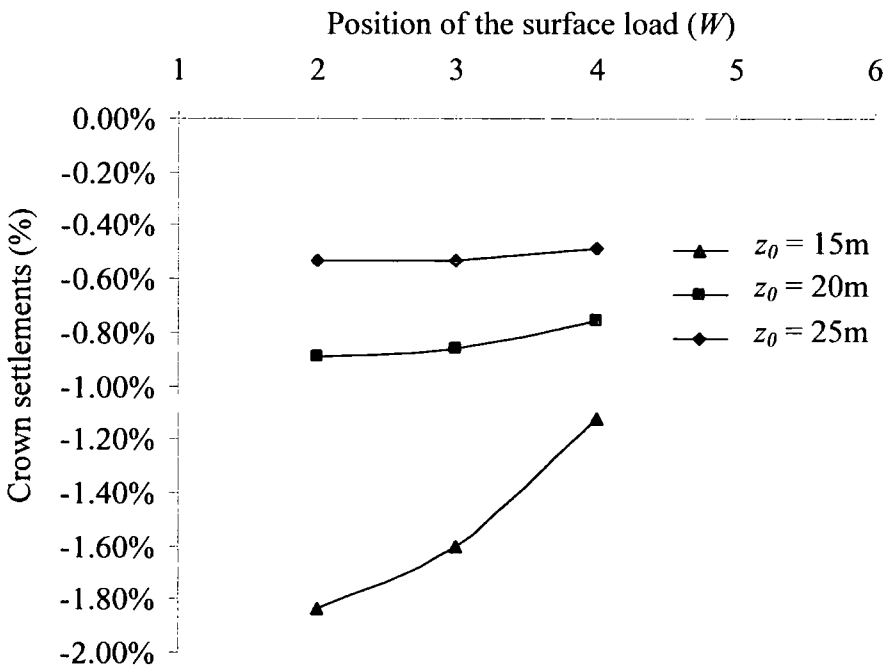

Figure 6.35. Plot of the crown settlements as a percentage of the initial tunnel diameter against the position of the surface loaded area for different excavation depths.

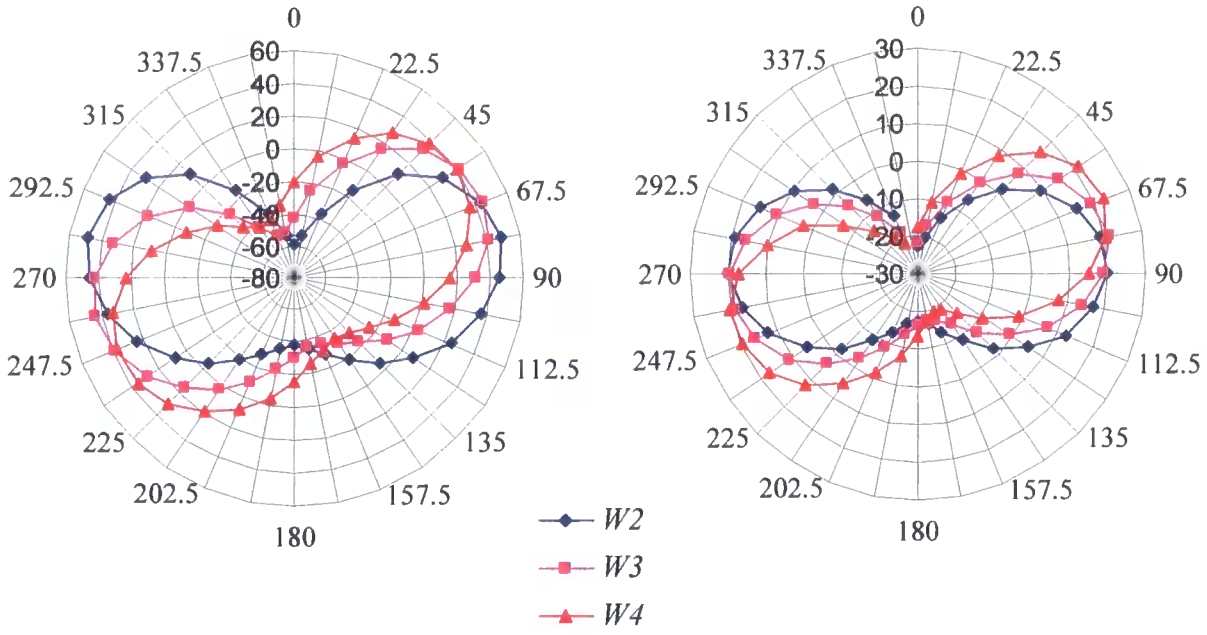

a) z_0 = 15m

b) z_0 = 20m

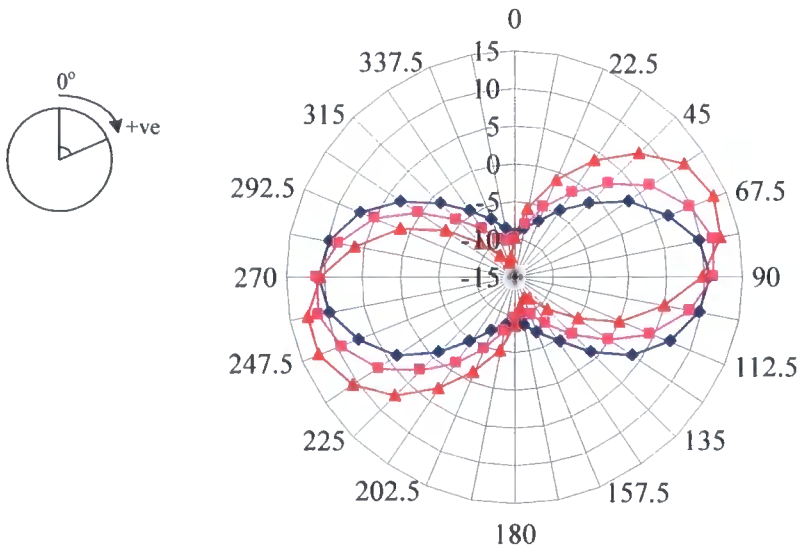

c) z_0 = 25m

Figure 6.36. Change of bending moments due to the effect of surface loading for different surface loaded areas and three different tunnel depths z_0 = 15m, 20m and 25m. The axial axis refers to the distribution of bending moments (kNm/m) around the tunnel, while the circumferential axis refers to the angle around the tunnel.

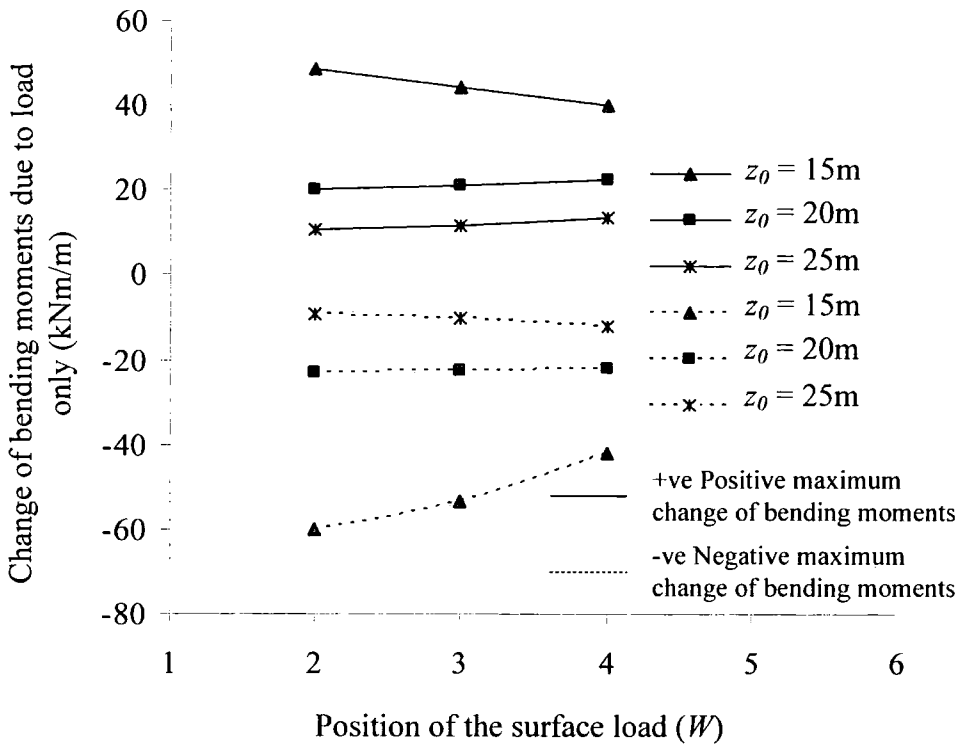

Figure 6.37. Change of bending moments due to the effect of surface loading for different surface loaded areas and different excavation depths.

6.3.2 Twin tunnels horizontally aligned (case *TH*)

6.3.2.1 Introduction

In this section analyses for the case of twin tunnels with their axes horizontally aligned are carried out using Plaxis v.8. Figure 6.38 presents one of the meshes employed for the current parametric study where z_0 = 20m and P = 1D. The latter mesh consists of 3,121 nodes and 364 fifteen-noded triangular elements. Curved beams are used to model the lining. A coarser mesh is employed inside the left tunnel's cluster compared to the right since results from the latter tunnel will be used for comparison purposes to the single tunnel geometry.

6.3.2.2 Details of the analysis

The details of the analysis are similar to those described in Section 6.3.1. The difference in this study is that a second tunnel is introduced prior to gravity loading.

This does not, however, influence the number of load stages which still remain two. Two different tunnel depths (z_0 = 15m and 20m), three distinct pillar widths (P = 1D, 2D and 3D) and all six of the surface loaded areas ($W1$ to $W6$) are modelled. This gives a total of 36 analyses in the particular study. The right tunnel's position is set while that of the left varies.

6.3.2.3 Analysis results

Figure 6.39 shows plots of the ratio of the maximum surface settlements due to the surface loading (S'_{max}/D) over the tunnel diameter against its position (W). The thin lines refer to the shallow case (when both tunnels are at z_0 = 15m) while the dotted lines to the deeper case (z_0 = 20m). For the latter tunnels bigger settlements occur since soil has more space to deform. The maxima of these curves occur when the load is applied in between the tunnels rather than above them (as in the single tunnel case). Plaxis v.8 predictions are higher by almost 10% than those from Strand7.

Figure 6.40 depicts tunnel liner deformation due to loading (scaled up, coloured circles) when pillar width is P = 1D for two different depths (z_0 = 15m and 20m). Thick circles indicate the initial shape of the lining prior to gravity loading. Both tunnels deform in a similar two-fold way. Squatting and anti-clockwise rotating. These findings are in agreement with previous results.

Figures 6.41 and 6.42 show plots of the change of the tunnel diameter due to the surface load expressed as a percentage of the initial tunnel diameter against the position of the loaded area (W) for each tunnel. Thin lines refer to the change of the horizontal diameter (along springlines) whereas dotted lines stand for the change of vertical diameter (crown to invert). These two graphs persuasively support the findings from Figure 6.40 regarding the rotating and squatting shape of the liners. Additionally, deeper tunnels seem to be less affected from the surface load although the trend indicates similar kinds of lining deformations. In every case, for each tunnel the maximum change of D (roughly 0.8% of the tunnel diameter) occurs when the load is applied directly above. As the load shifts further away these changes reduce towards zero (no change of D). However when the surface load is applied at its furthest possible distance, the vertical diameter is seen to increase while the

horizontal reduces. This is more evident for shallower tunnels. These predictions are in agreement with Strand7.

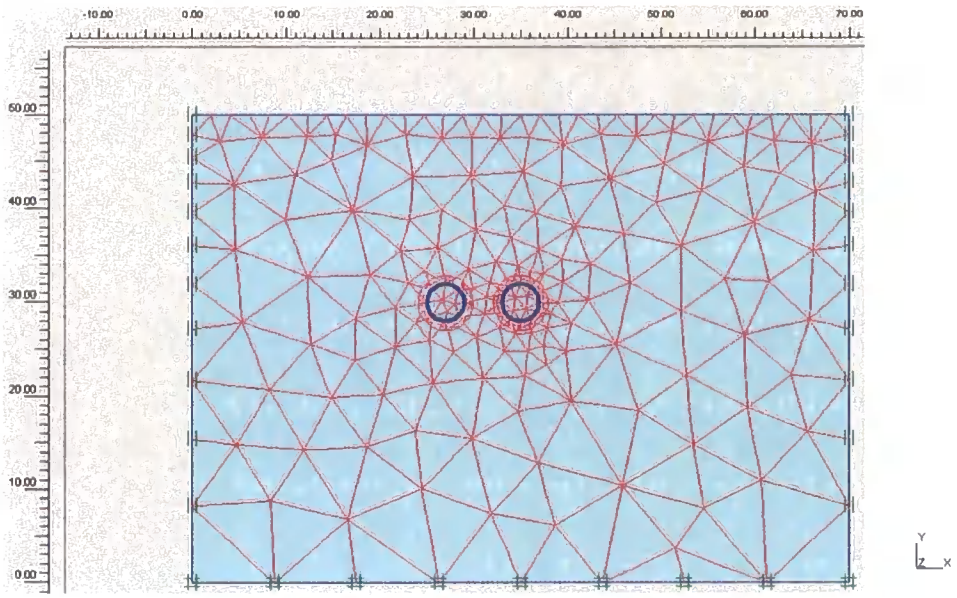

Figure 6.38. Generated mesh for the twin tunnel analysis when z_0 = 20m and P = 1D.

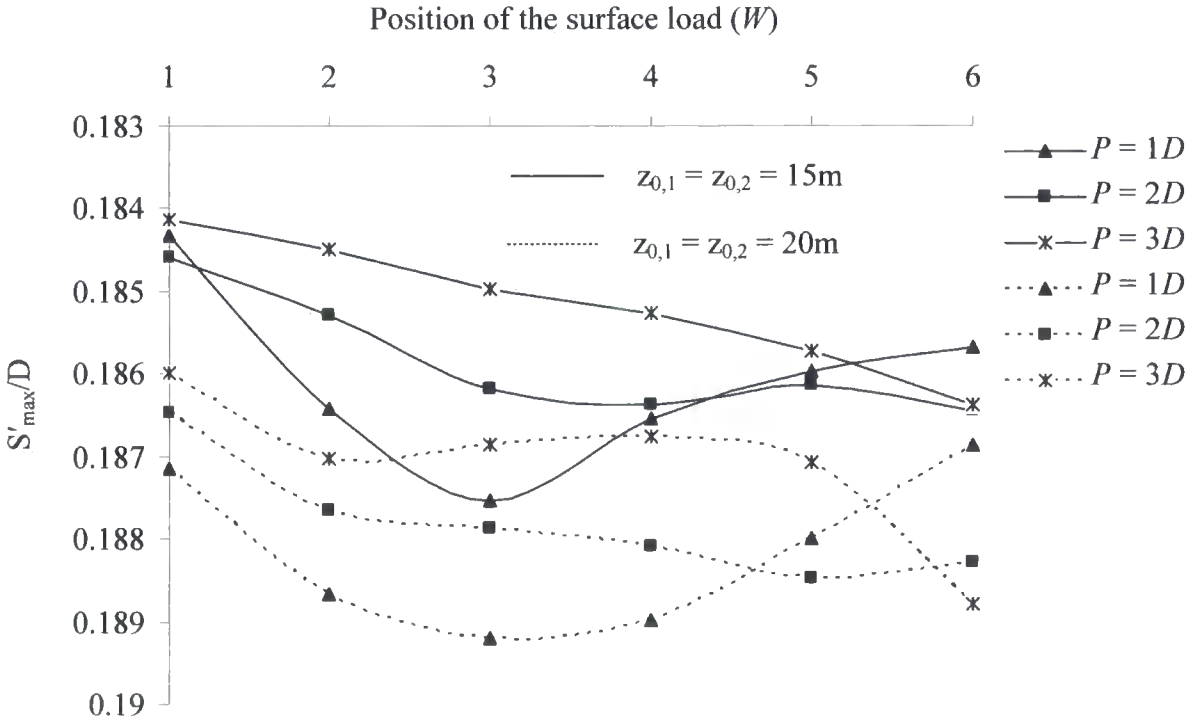

Figure 6.39. Plots of the ratio of the maximum surface settlements due to surface loading over the tunnel diameter against the position of the load for various tunnel depths.

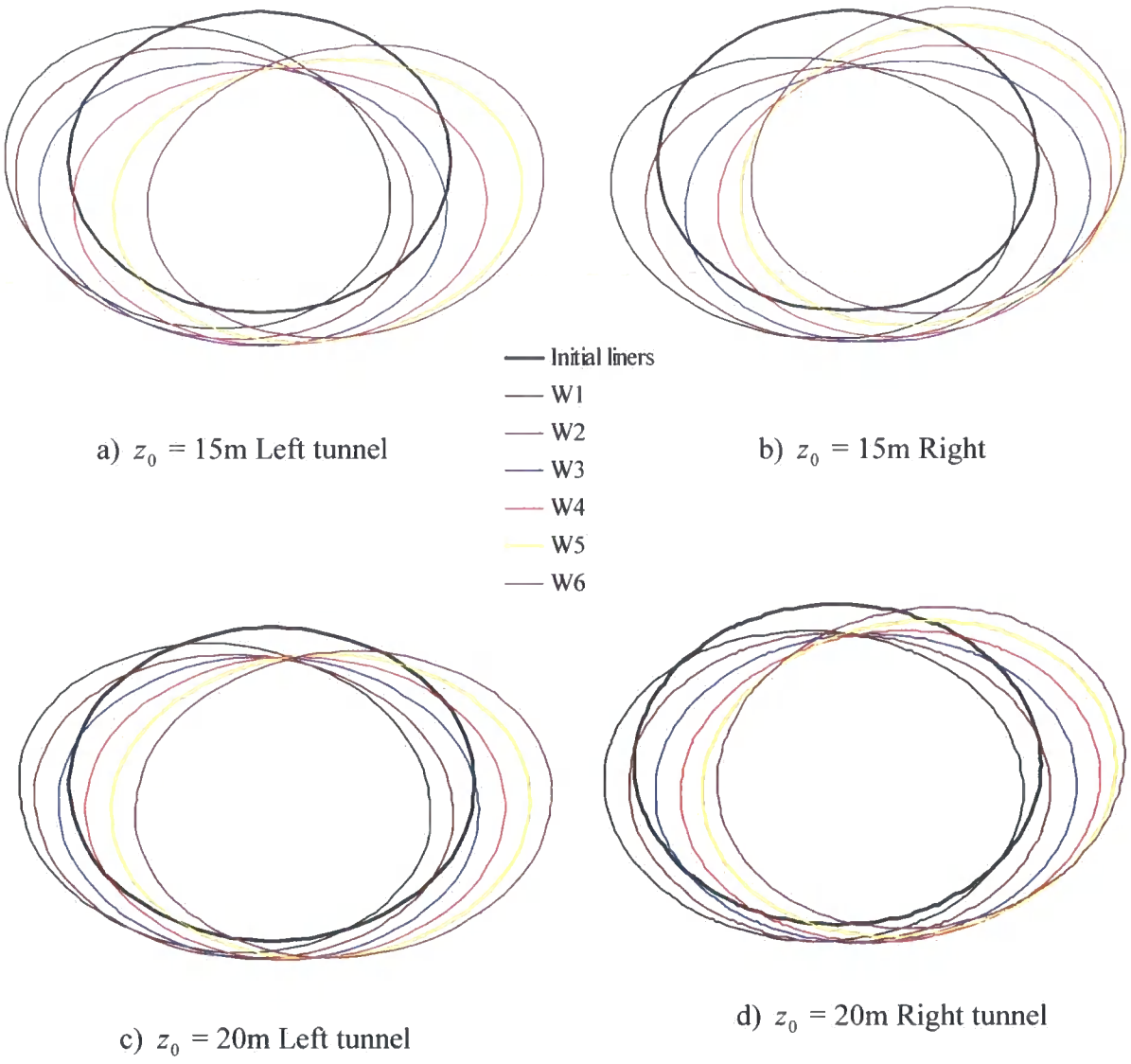

Figure 6.40. Deformed shape of the tunnels due to the surface loading for six different loaded areas. The tunnel axes are driven at z_0 = 15m and 20m while $P = 1D$.

Plots of both tunnels' crown deformations expressed as a percentage of the tunnel diameter against the relative position of the loaded area (W) are presented in Figure 6.43. Thin curves refer to the right hand side tunnel whereas dotted to the left. Once more deeper tunnels seem to be less affected from the surface load. The trend of crown deformations is similar to Strand7. Plaxis v.8 predictions though are up to 50% smaller.

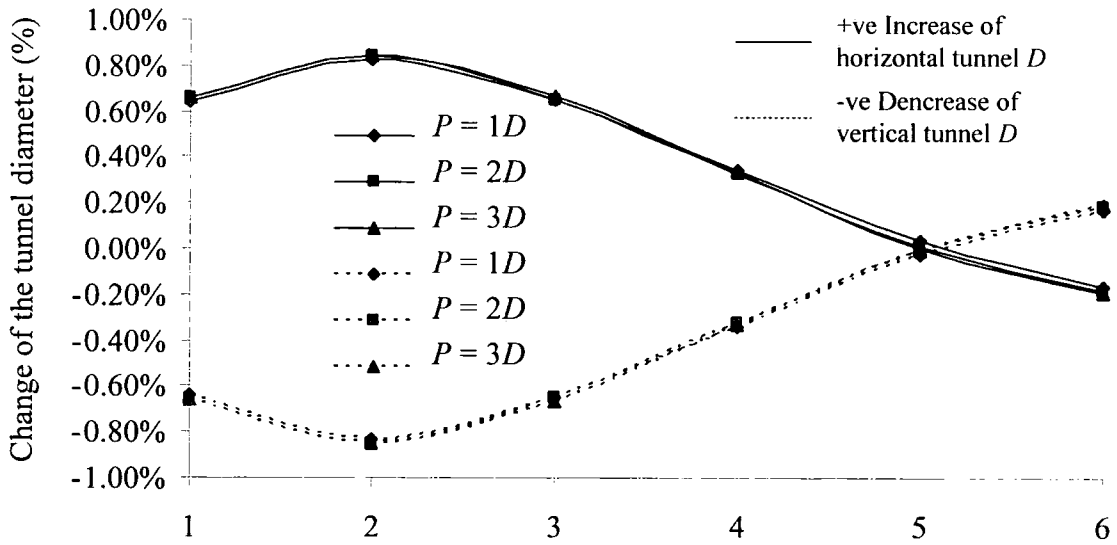

a) Regarding the right tunnel

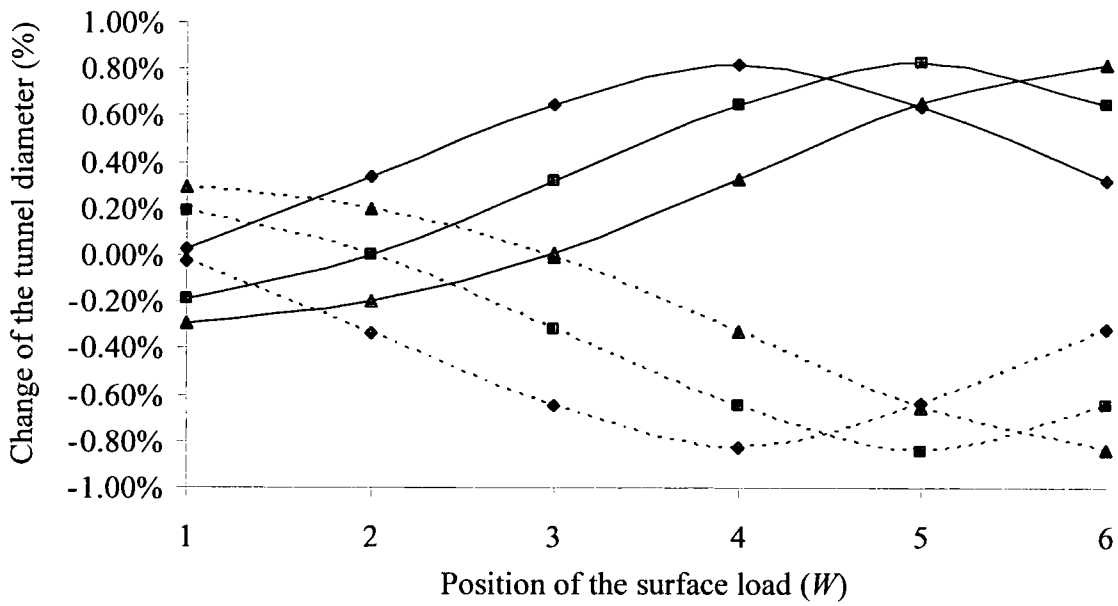

b) Regarding the left tunnel

Figure 6.41. Changes of horizontal and vertical tunnel diameters due to the surface loading expressed as a percentage of the tunnel diameter against the position of the applied load when z_0 = 15m.

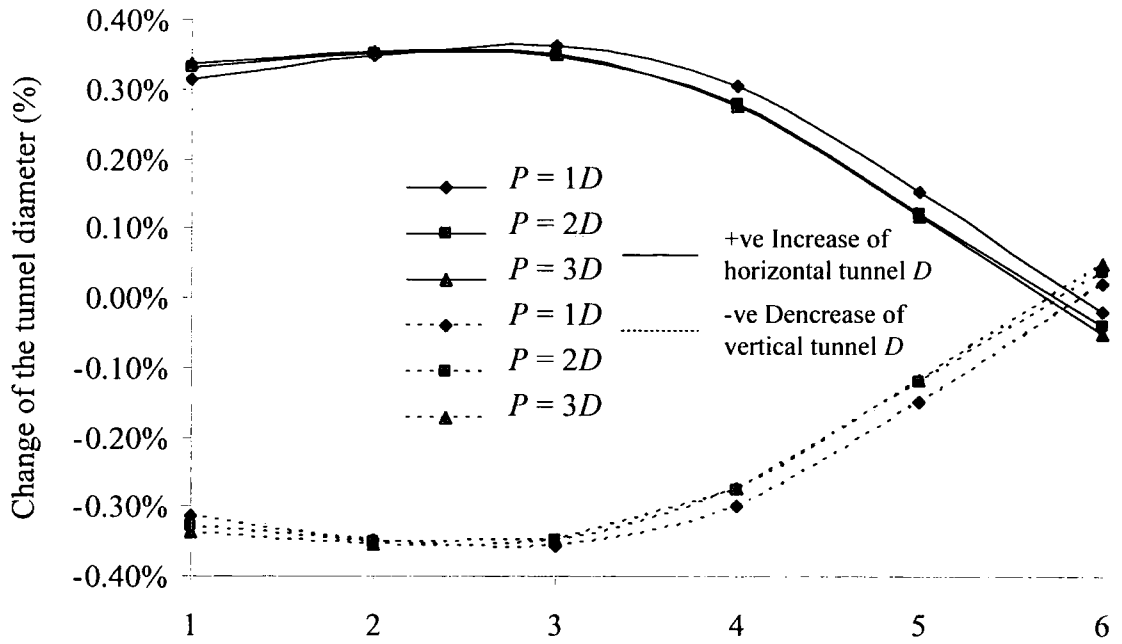

a) Regarding the right tunnel

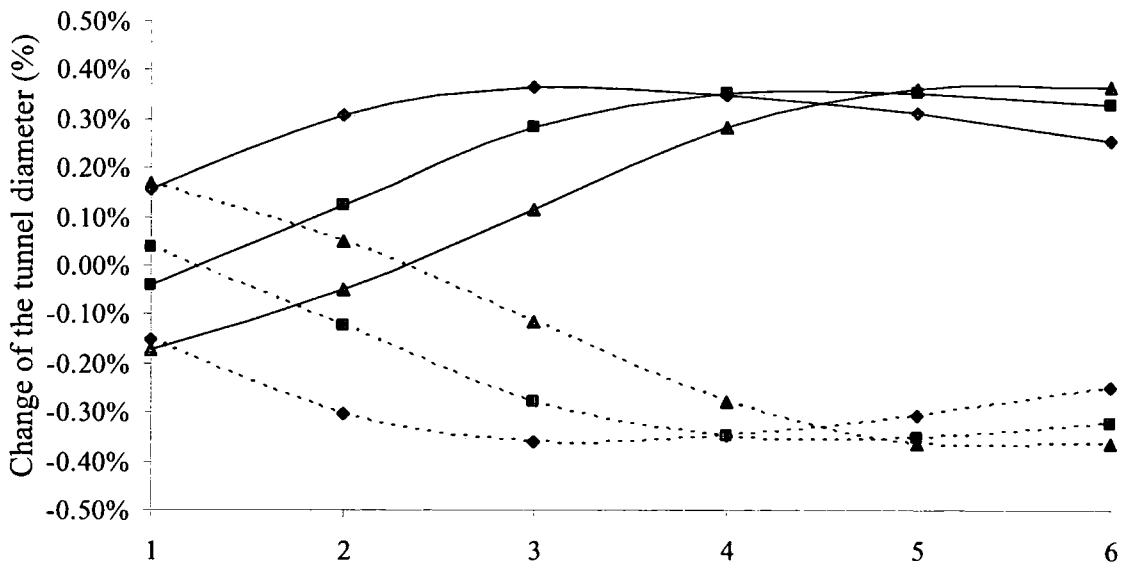

b) Regarding the left tunnel

Figure 6.42. Changes of horizontal and vertical tunnel diameters due to the surface loading expressed as a percentage of the tunnel diameter against the position of the applied load when z_0 = 20m.

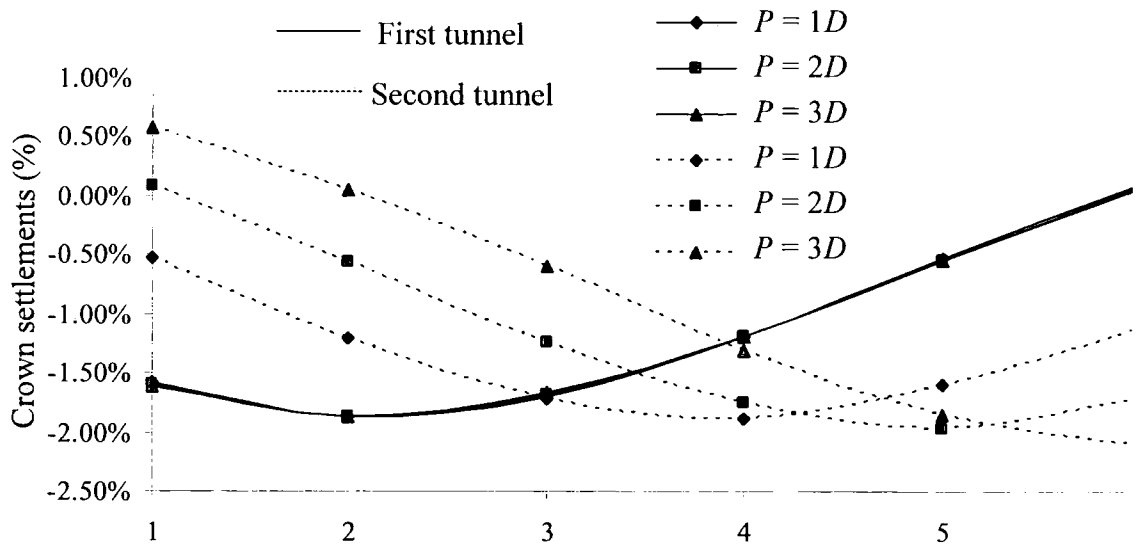

a) When z_0 = 15m

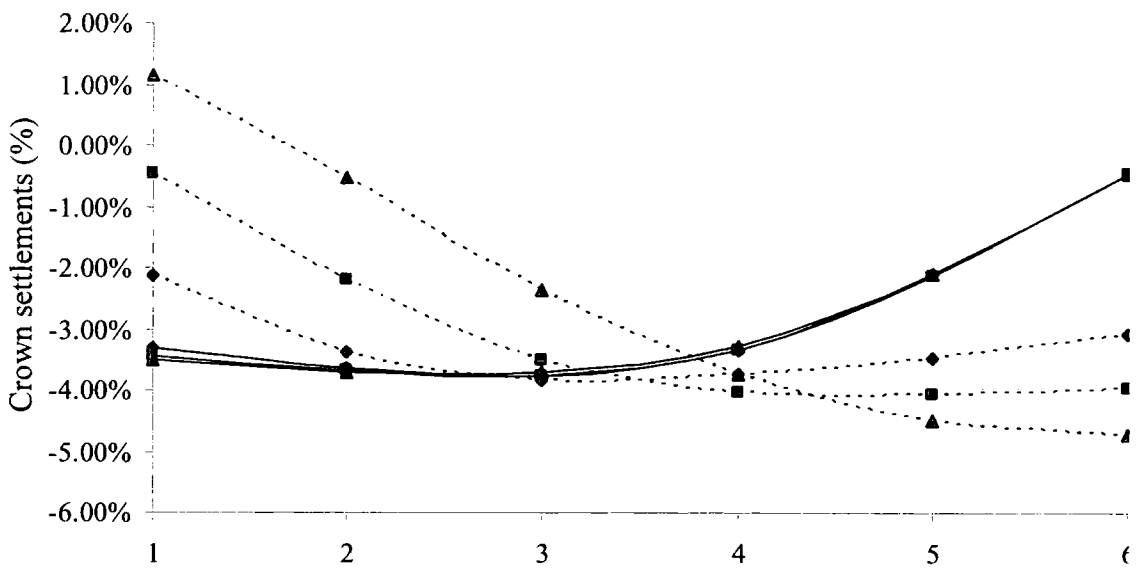

b) When z_0 = 20m

Figure 6.43. Crown settlements expressed as a percentage of the tunnel diameter against the position of the surface loaded area for different excavation depths.

Figure 6.44 shows the interaction between the two parallel tunnels and the surface load compared to the single tunnel case (*ST*) in terms of crown settlements. For the twin tunnel case crown settlements predictions from the right hand side tunnel are plotted as a percentage of the single tunnel case against the position of the surface loaded area (*W*) for two different depths (z_0 = 15m and 20m) and three different pillar widths (*P* = 1*D*, 2*D* and 3*D*). Black thin lines refer to the shallow case while colours refer to the deeper case. It can be seen that Plaxis v.8 predictions for the twin tunnel case are almost identical to the single tunnel case results (i.e. almost no interaction between the two parallel tunnels). This picture is different to the Strand7 results especially for the shallow case.

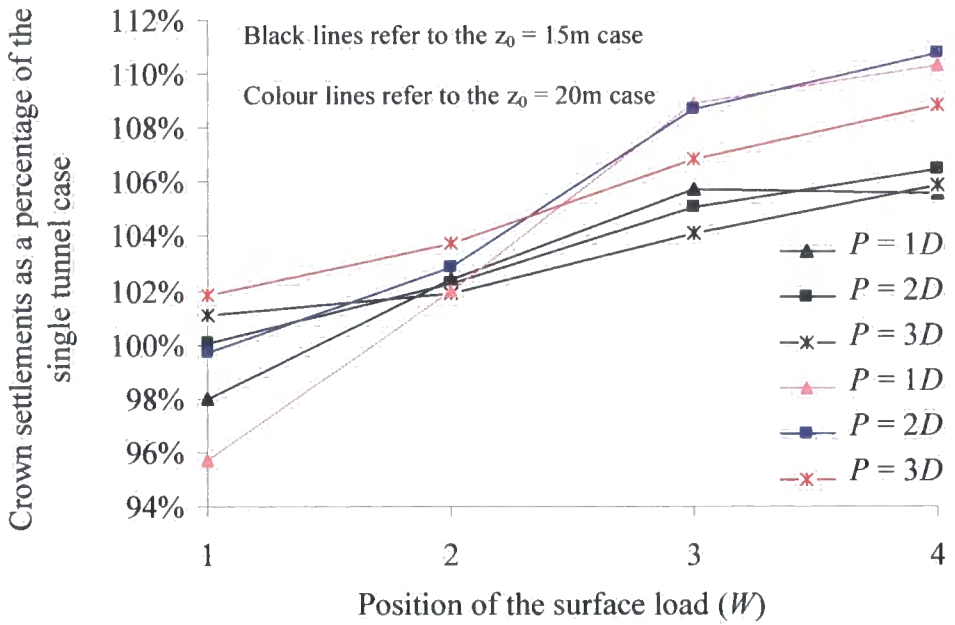

Figure 6.44. Plots of the crown settlements due to loading of the right tunnel in the twin tunnel case as a percentage of the single tunnel results for various surface loading areas and two different tunnel depths.

The change of bending moments around each liner solely due to the effect of surface loading is plotted in Figure 6.45 when pillar width distance is *P* = 1*D*. The sign convention for bending moments is the same as described in previous Sections. For the right hand tunnel the maximum positive changes of bending moments appear around the springlines from 34° to 101° and from 225° to 293°. The maximum negative changes on the other hand appear around the crown from 304° to 23° and around the invert from 124° to 191°. The left hand tunnel on the other hand has its

maximum positive changes around the springlines from 56° to 123° and from 236° to 315°. The maximum negative changes appear around the crown from 349° to 34° and around the invert from 146° to 225°. It seems that these maxima between the two tunnels do not coincide. Instead they have rotated by approximately 11° to 45°.

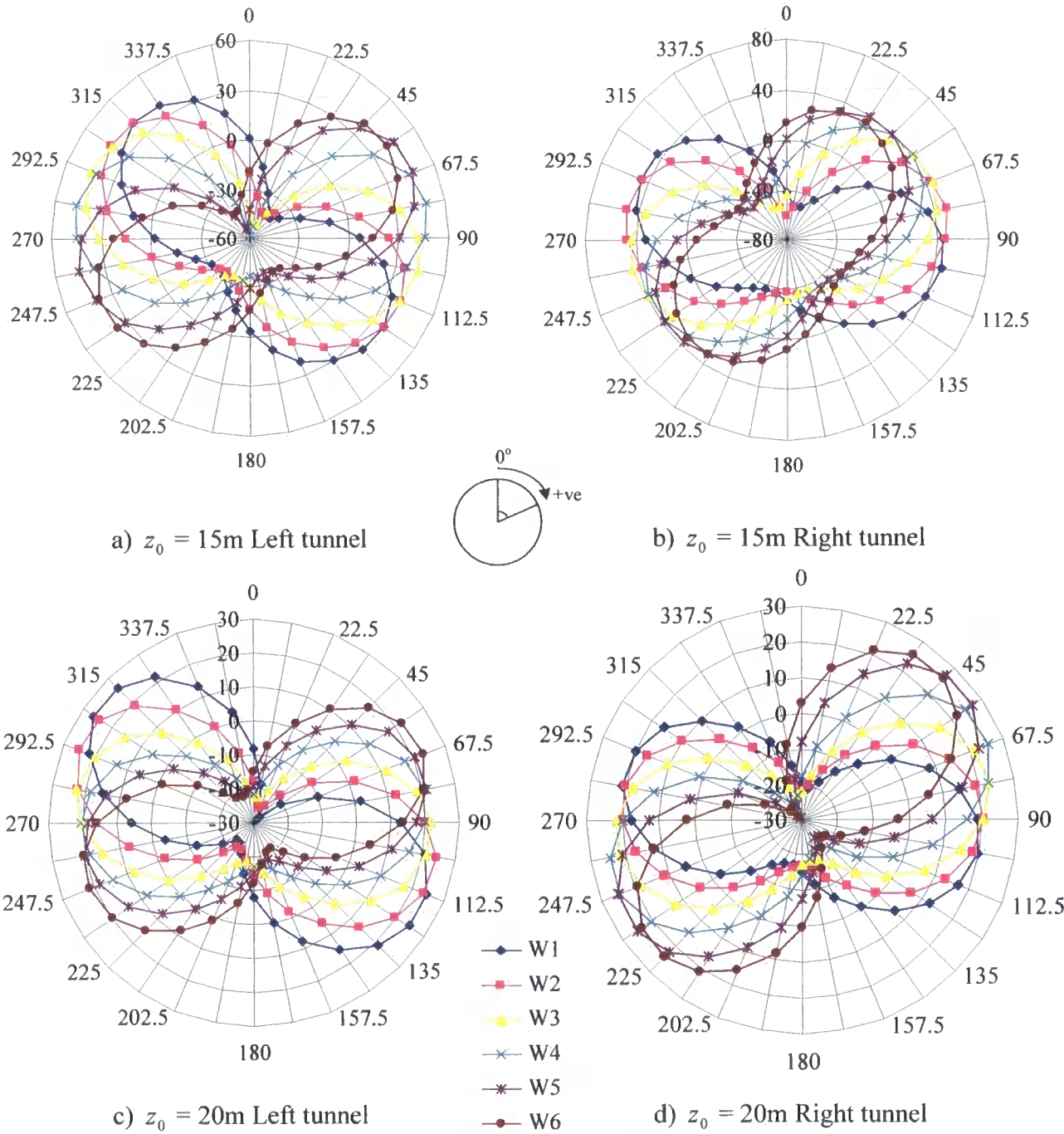

a) z_0 = 15m Left tunnel

b) z_0 = 15m Right tunnel

c) z_0 = 20m Left tunnel

d) z_0 = 20m Right tunnel

Figure 6.45. Change of bending moments due to the effect of surface loading for different surface loaded areas when z_0 = 15m and 20m. The axial axis refers to the distribution of bending moments (kNm/m) around the tunnel, while the circumferential axis refers to the angle around the tunnel.

Figures 6.46 and 6.47 show plots of the maximum and minimum changes of bending moments around the liners due to the effect of surface loading against the position of the loaded area (*W*). Thin curves indicate the maximum positive changes whereas dotted curves the maximum negative. For the shallow tunnelling case (z_0 = 15m) it appears that the maxima of these curves for both tunnels lie above their centre lines each time. For deeper tunnels though the previously mentioned trend alters significantly. The same discrepancy is captured by both FE codes (Strand7 and Plaxis v.8). Furthermore Plaxis v.8 predictions are smaller than Strand7 by almost 10% to 30%.

6.3.3 Twin tunnels vertically aligned (case *TVD*)

6.3.3.1 Introduction

In this section Plaxis v.8 analyses for the case of twin tunnels which are vertically aligned are presented. Figure 6.48 shows one of the meshes used for the *TVD* case where $z_{0,1}$ = 15m and $z_{0,2}$ = 20m for the upper and lower tunnels respectively. The pillar width for this case is $P = 1D$. The domain consists of 3,985 nodes. 471 fifteen-noded triangular elements are used to model soil. Curved beam elements are used to represent tunnel liners.

6.3.3.2 Details of the analysis

Analysis details are identical to those described in Section 6.3.2. The C.L. of the upper tunnel is always fixed at $z_{0,1}$ = 15m while that of the lower varies ($z_{0,2}$ = 20m and 23m). Six different surface loaded areas (*W*1 to *W*6) are modelled as well as three different pillar widths (P = piggy-back when the lower tunnel is exactly below the upper, $P = 0$ and $P = 1D$). Thus a total of 36 analyses were carried out in this parametric study.

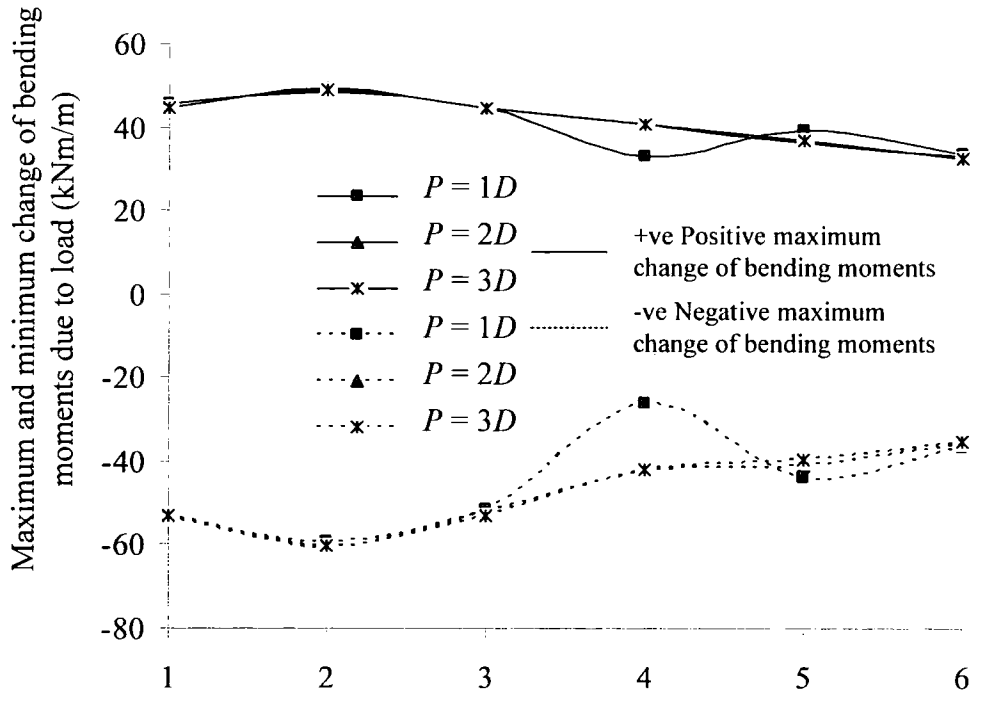

a) Regarding right tunnel

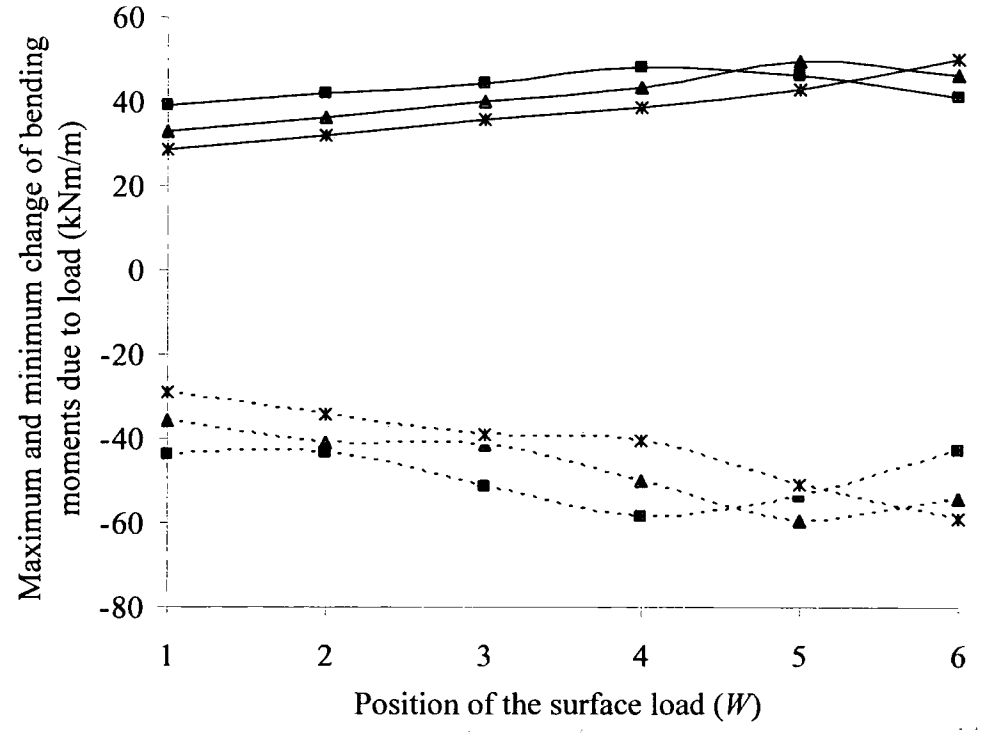

b) Regarding left tunnel

Figure 6.46. Maximum and minimum change of bending moments due to the effect of surface loading for different surface loaded areas when z_0 = 15m.

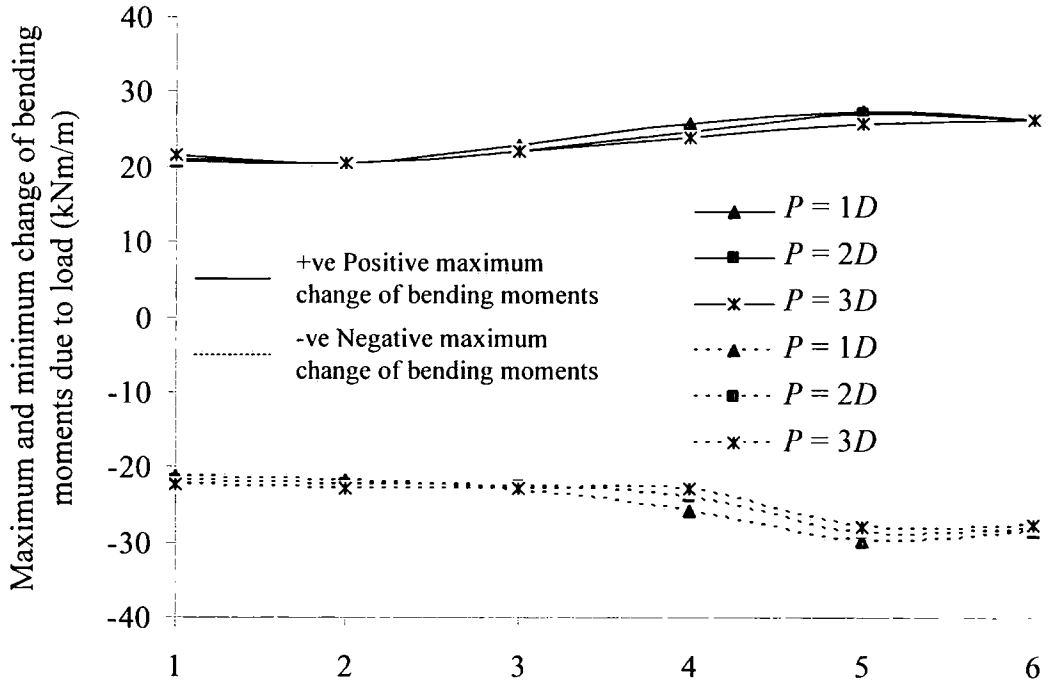

a) Regarding right tunnel

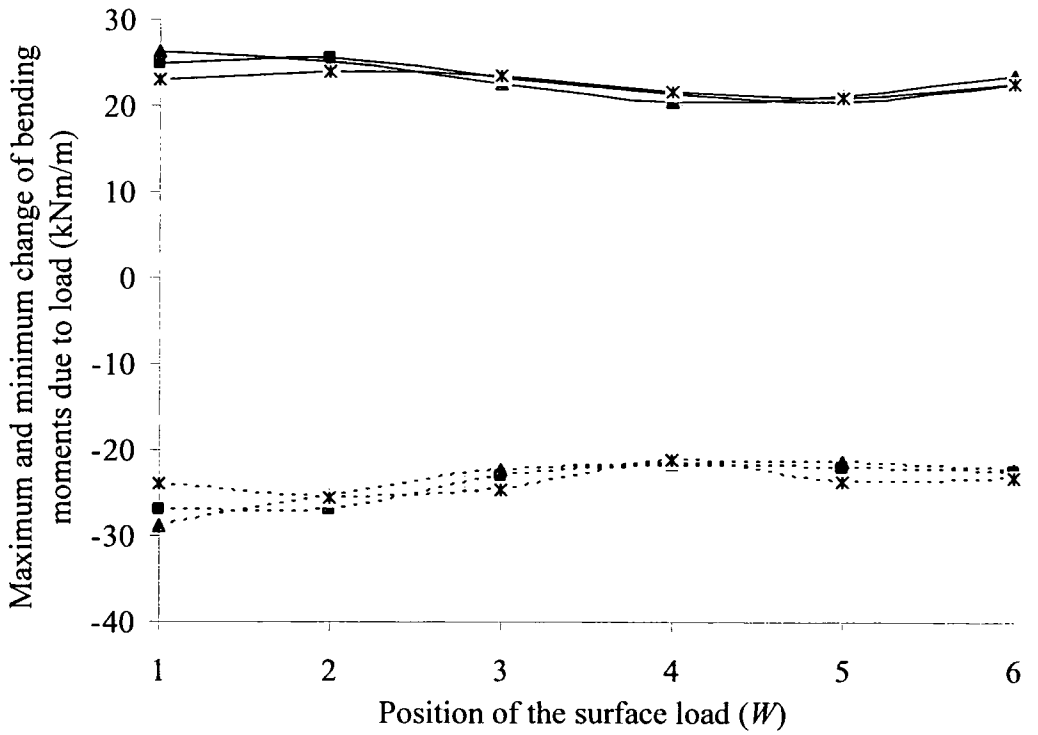

b) Regarding left tunnel

Figure 6.47. Maximum and minimum change of bending moments due to the effect of surface loading for different surface loaded areas when z_0 = 20m.

6.3.3.3 Analysis results

Figure 6.49 shows plots of the ratio of the maximum surface settlement due to the surface loading over the tunnel diameter (S'_{max}/D) against the relative position of the load (W). Similar shapes and magnitudes are observed in this figure for different excavation depths of the lower tunnel. The trend in both cases (Figures 6.49a and 6.49b) indicates that for every pillar width modelled the maximum settlement always appears above the C.L. of the lower tunnel (e.g. when P = piggy-back above $W2$, when $P = 0$ above $W3$ and finally when $P = 1D$ above $W4$). This finding slightly differs from the Strand7 predictions regarding the same study for the $P = 0$ case. Plaxis v.8 results are about 10% higher than Strand7.

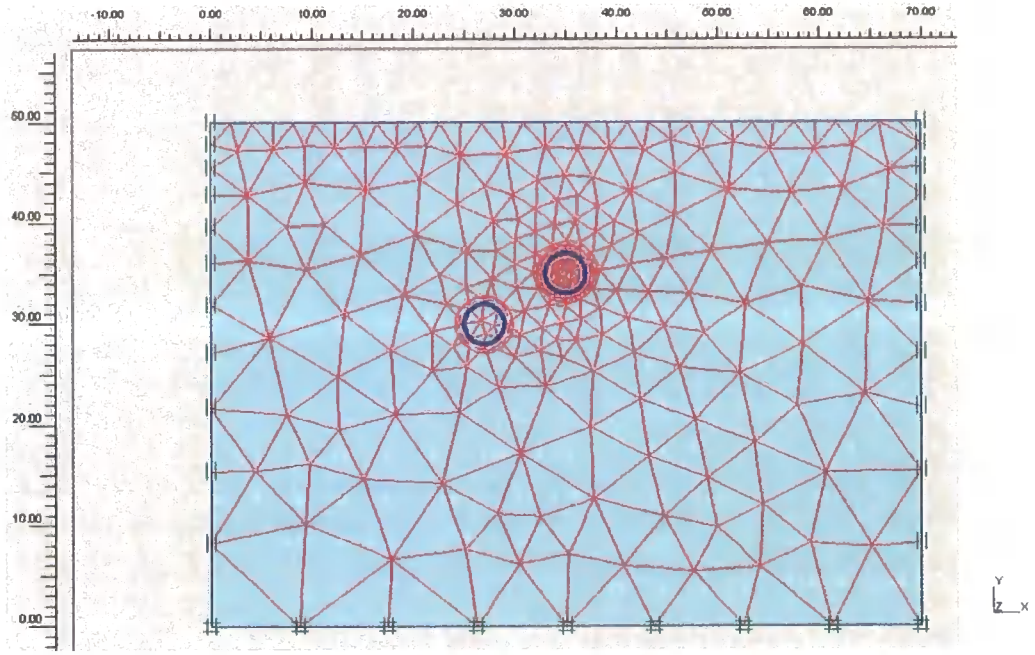

Figure 6.48. Generated mesh for the *TVD* case when $z_{0,1}$ = 15m and $z_{0,2}$ = 20m for the upper and lower tunnel respectively while $P = 1D$.

Figure 6.50 depicts both tunnels' deformed shape (coloured circles) due to the surface loading for different excavation depths of the lower tunnel when P = piggy-back. These shapes (scaled up) can be compared with the original liners prior to any loading stage (black thick circles). Lining behaviour is once again similar to that described in Sections 6.2 and 6.3 (i.e. squatting and anti-clockwise rotating). Another interesting point which is highlighted is that the lower tunnel deforms less than the upper.

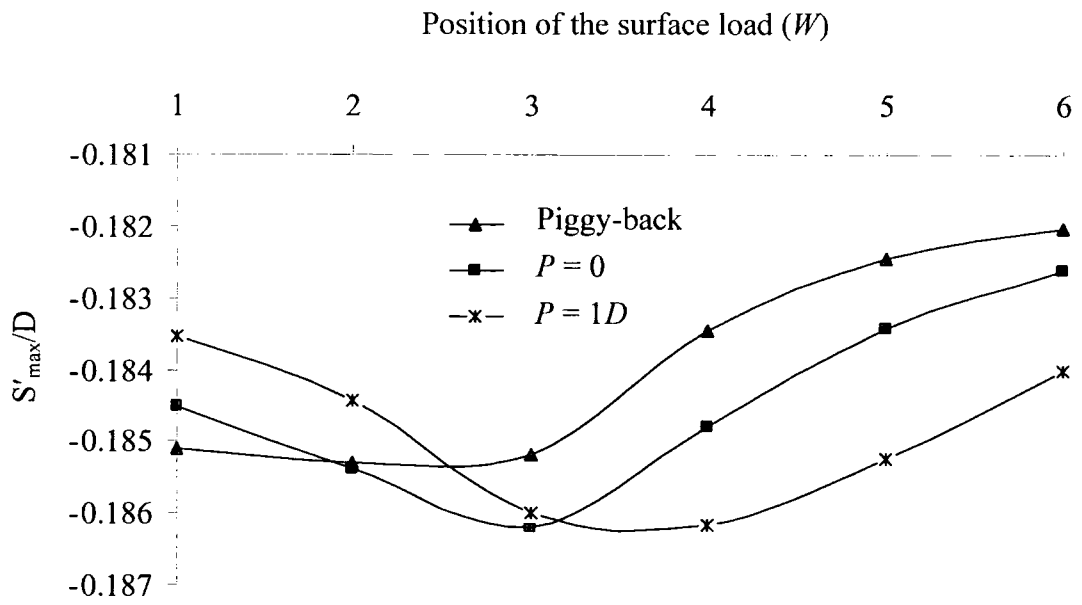

a) When the lower tunnel is at $z_{0,2}$ = 20m

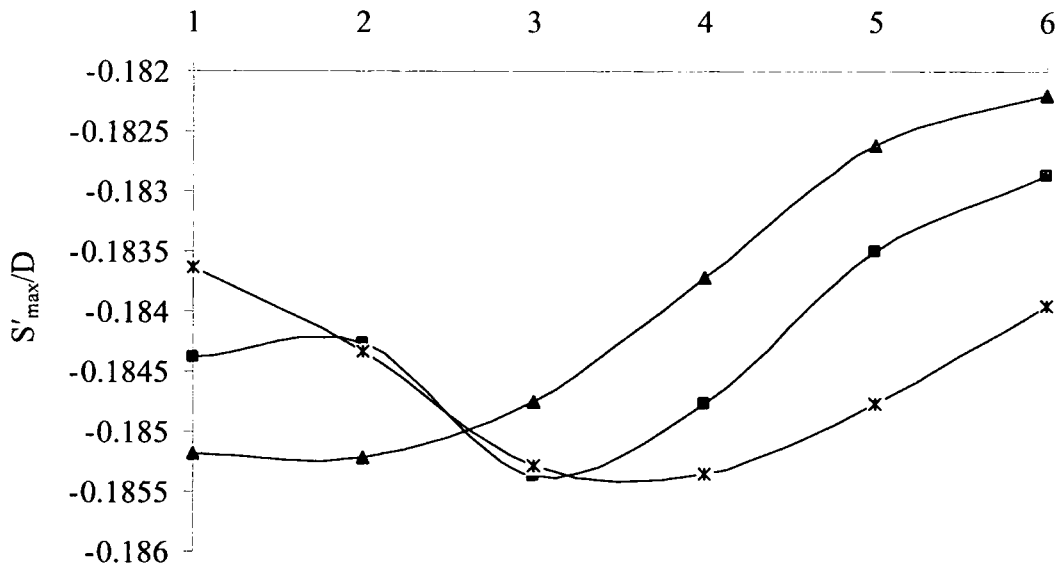

b) When the lower tunnel is at $z_{0,2}$ = 23m

Figure 6.49. Plots of the ratio of the maximum surface settlements due to surface loading over the tunnel diameter against the position of the loaded area for two different excavation depths and three different pillar widths.

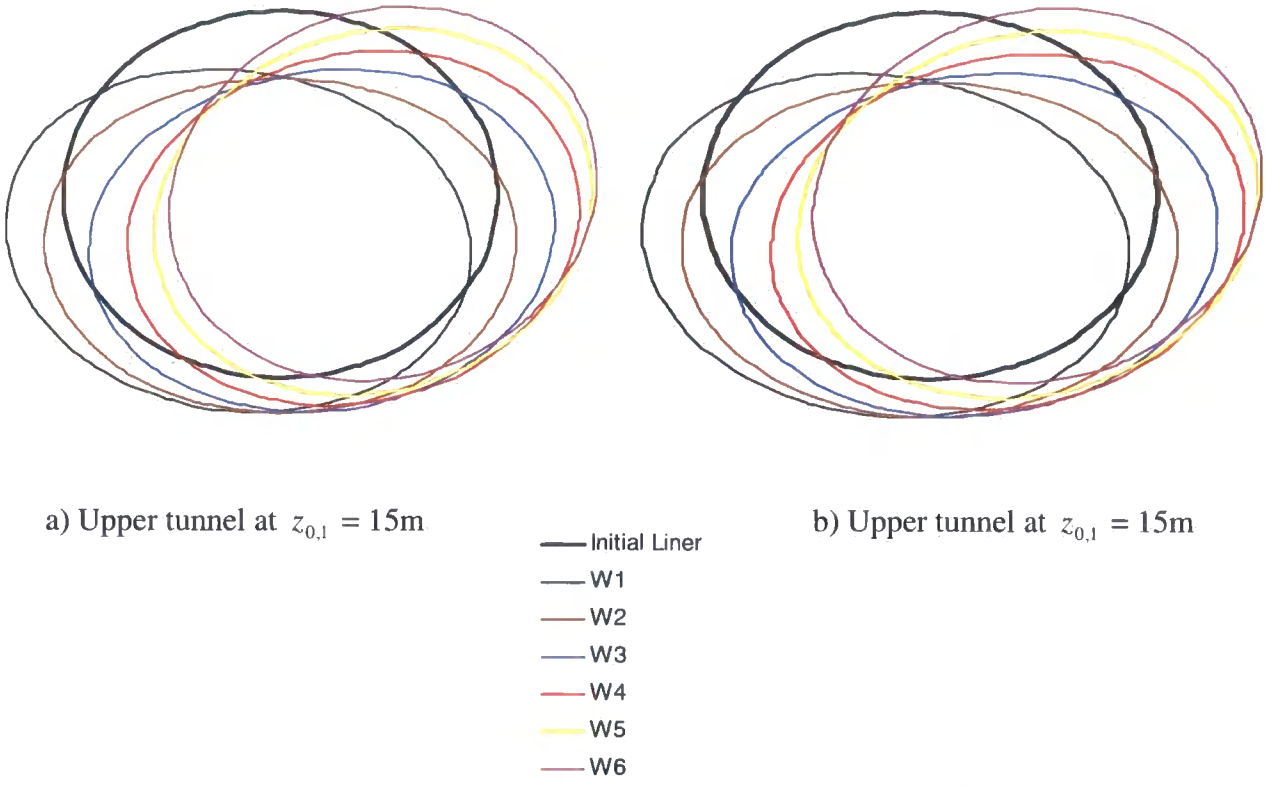

a) Upper tunnel at $z_{0,1}$ = 15m

b) Upper tunnel at $z_{0,1}$ = 15m

c) Lower tunnel at $z_{0,2}$ = 20m

d) Lower tunnel at $z_{0,2}$ = 23m

Figure 6.50. Deformed shape of the tunnels due to the surface loading when the second tunnel is at $z_{0,2}$ = 20m and 23m while P = piggy-back.

Figures 6.51 and 6.52 show plots of the change of horizontal (thin lines) and vertical (dotted lines) tunnel diameter expressed as a percentage of the initial tunnel diameter against the position of the surface load (*W*). These findings are in agreement with Figure 6.50. The maxima of these curves regarding the upper tunnel (roughly 1% of *D*) always occur when the surface load is directly applied above its C.L. (i.e. at *W*2). As the load shifts towards *W*5 the changes of the tunnel diameter reduce to zero (no deformations). When the load is applied at *W*6 the shape of the tunnel changes to oval with the larger deformed axis being the vertical diameter. This may attributed to the proximity of the load at *W*6 to the left hand side boundary. The upper tunnel does not seem to be influenced by the position of the lower. The latter tunnel's behaviour is similar to the other (the maximum occurs above the C.L. for each different value of *P*). The magnitudes between them are however significantly lower. The general shape is in agreement with predictions made by Strand7, however the magnitudes predicted by the two FE codes seem to differ by 25% to 50%.

Figure 6.53 shows crown deformations expressed as a percentage of the tunnel diameter against the relative position of the surface loaded areas (*W*). Thin lines refer to the upper tunnel while dotted to the lower. Crown deformations for the upper tunnel seem to be unaffected of both P and z_0. As for the lower tunnel smaller magnitudes appear for deeper excavation depths. The maxima of these curves for each tunnel occurs when the surface load directly applies above its C.L.

Figure 6.54 shows the interaction between the two tunnels and the surface load in the *TVD* case compared to the single tunnel case (*ST*) in terms of crown settlements. For the *TVD* case crown settlements predictions from the upper tunnel are plotted as percentage of the single tunnel case against the position of the surface loaded area (*W*) for different pillar widths (*P* = piggy-back, 0 and 1*D*) when $z_{0,1}$ = 15m. It can be observed that a small amount of interaction exists (none to 5%) compared to the single case predictions. Results are similar compared to the twin tunnel shallow case from *W*1 to *W*3. As the surface load shifts towards *W*4 though a difference in the prediction of interaction is identified.

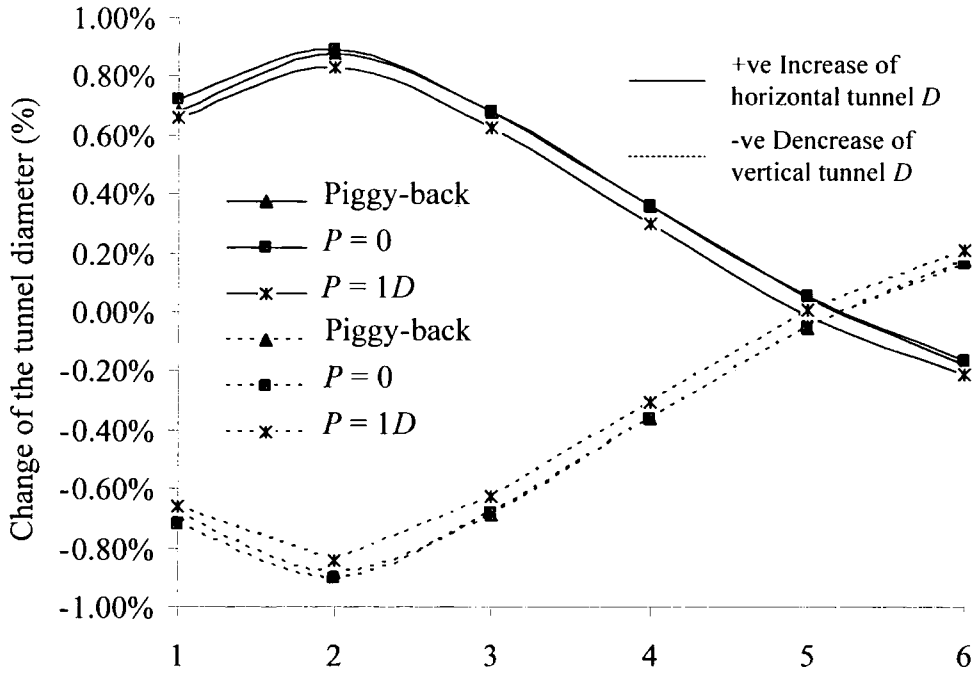

a) Regarding the upper tunnel

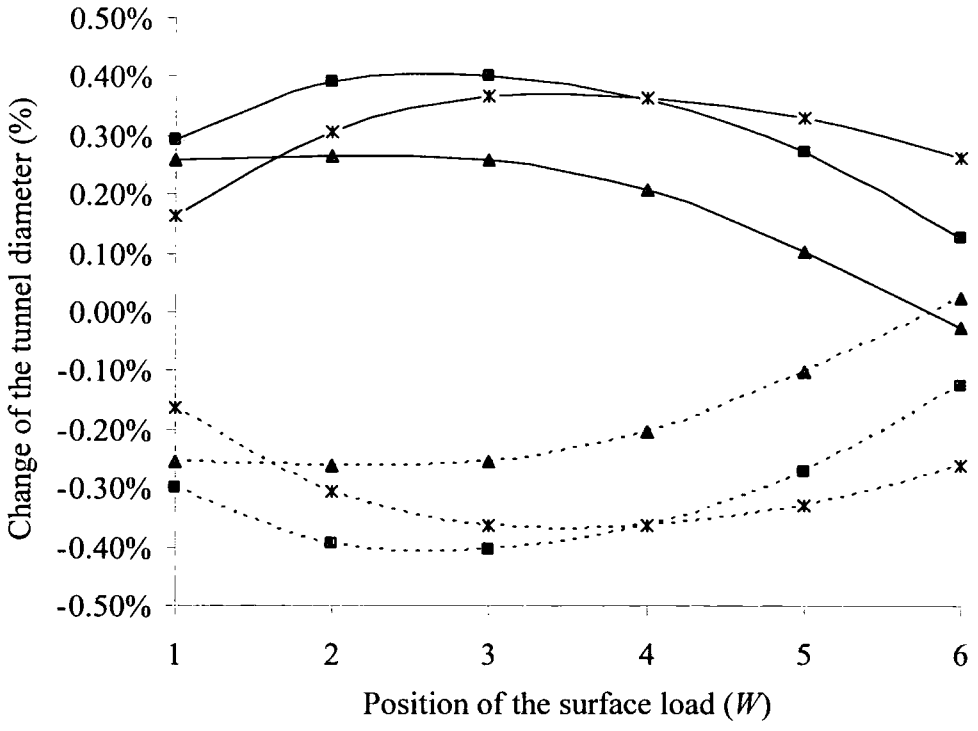

b) Regarding the lower tunnel

Figure 6.51. Change of horizontal and vertical tunnel diameter due to the surface loading expressed as a percentage of the initial tunnel diameter against the position of the applied load when the lower tunnel lies at $z_{0,2} = 20$m.

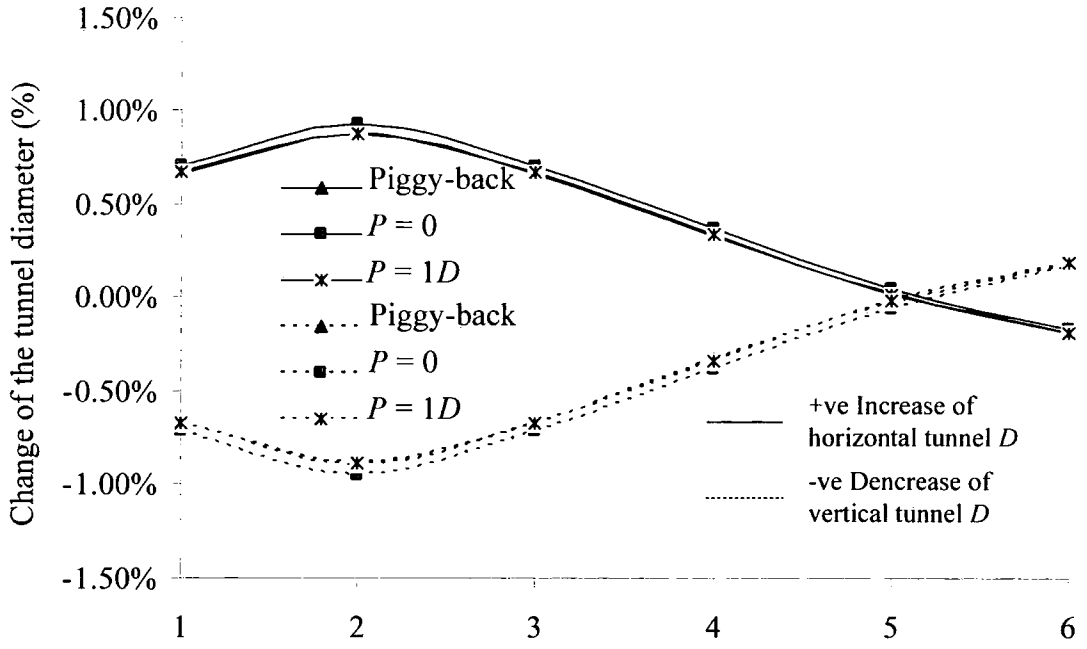

a) Regarding the upper tunnel

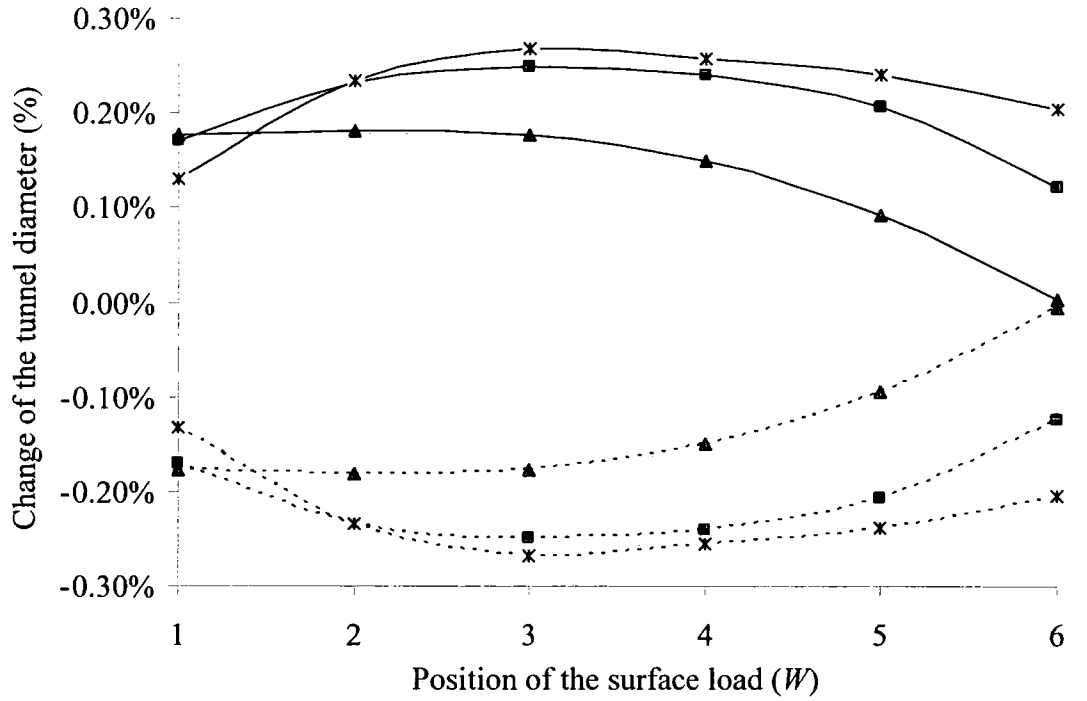

b) Regarding the lower tunnel

Figure 6.52. Change of horizontal and vertical tunnel diameter due to the surface loading expressed as a percentage of the initial tunnel diameter against the position of the applied load when the lower tunnel lies at $z_{0,2}$ = 23m.

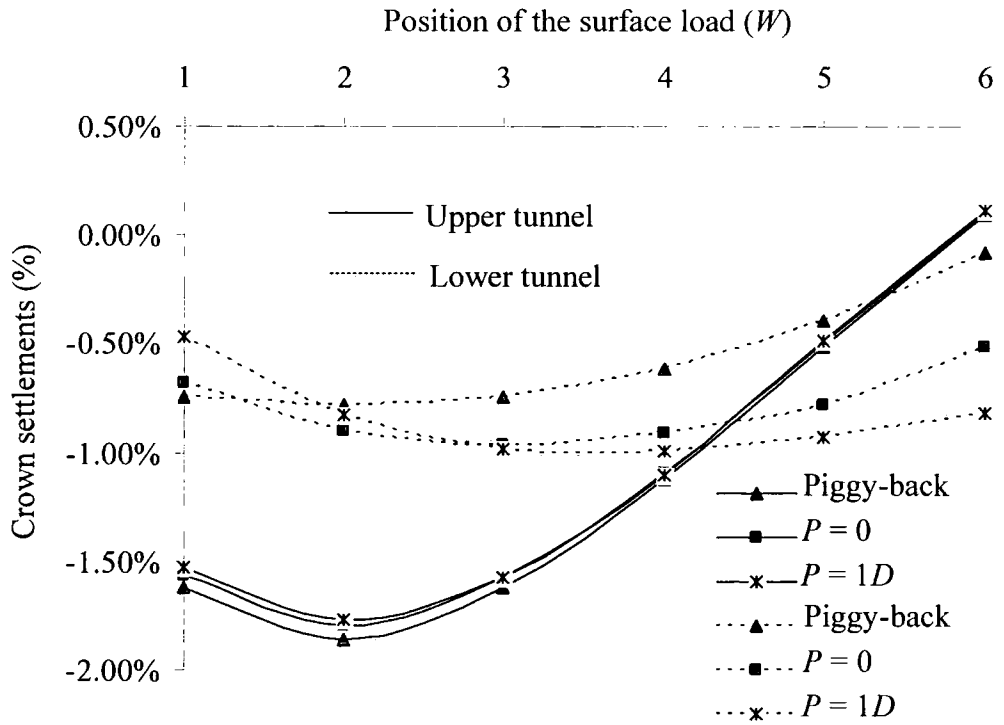

a) When the lower tunnel is at $z_{0.2}$ = 20m

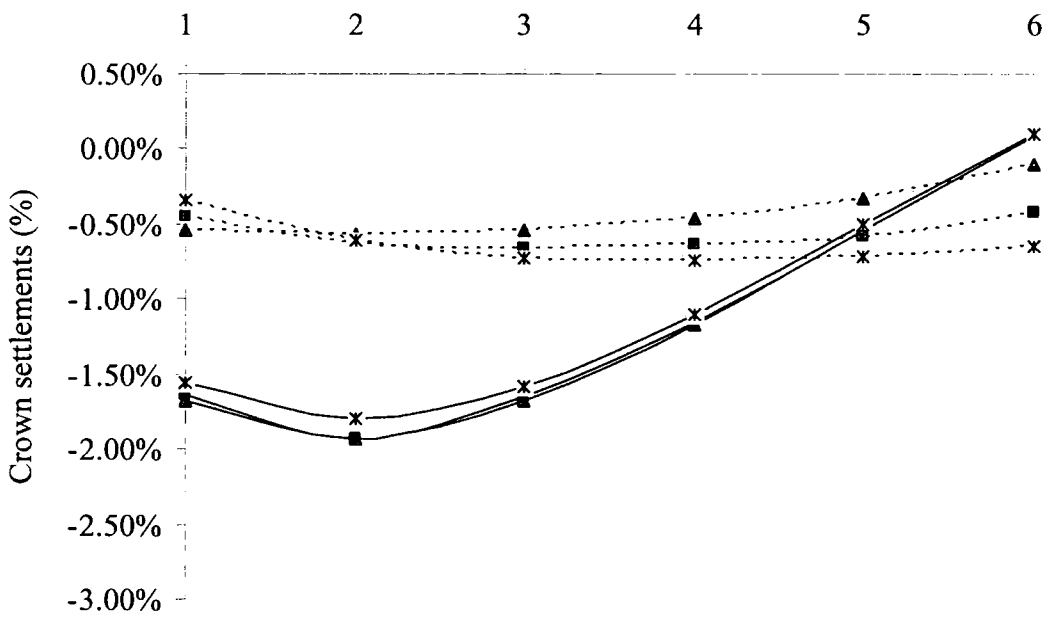

b) When the lower tunnel is at $z_{0.2}$ = 23m

Figure 6.53. Crown settlements expressed as a percentage of the tunnel diameter against the position of the surface loaded area for different excavation depths.

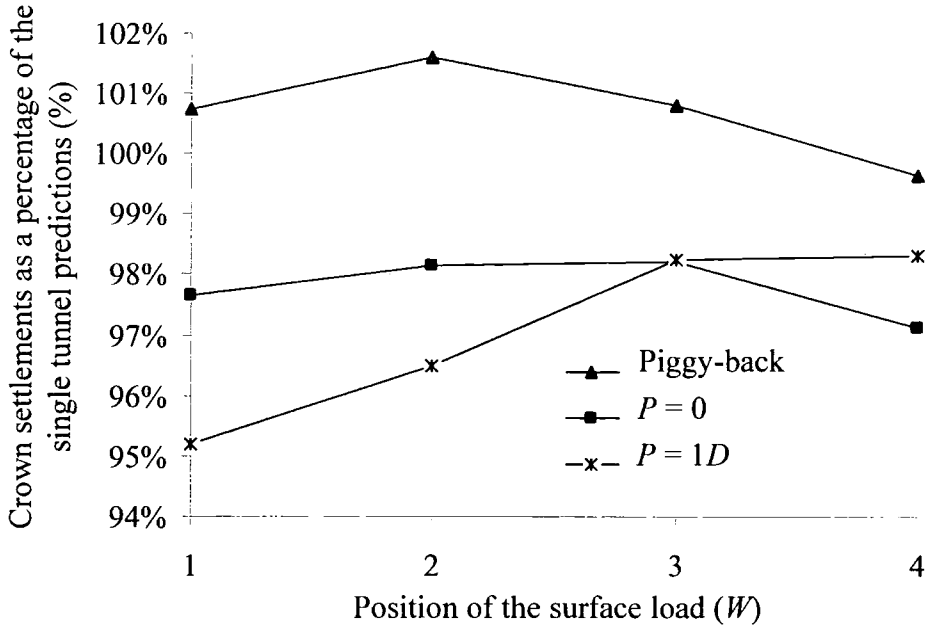

Figure 6.54. Plots of the crown settlements due to loading of the upper tunnel in the Piggy-back case as a percentage of the single tunnel results for various surface loading areas when $z_{0.1}$ = 15m.

In the next figure (Figure 6.55) the distribution of the change of bending moments due to the effect of the surface loading is plotted for different depths of the lower tunnel ($z_{0.2}$ = 20m and 23m). Both of these figures refer to the case where P = piggy-back. The sign convention for the bending moments has already been set in Section 6.2.1. The magnitudes are greater for the upper tunnel in every case as expected from the lining deformation predictions in Figure 6.50. Positive maximum changes of bending moments regarding the upper tunnel approximately develop from 34° to 101° and from 219° to 298° around the springlines. The negative maximum changes of bending moments develop from 300° to 23° around the crown and from 130° to 195° around the invert. In the case where the lower tunnel is driven at $z_{0.2}$ = 20m positive maximum changes of bending moments develop from 23° to 100° and from 225° to 280° around springlines. Negative maximum changes on the other hand develop from 315° to 11° around the crown and from 135° to 190° around the invert. The range of these maxima is similar for the case where the lower tunnel is driven at $z_{0.2}$ = 23m. However the absolute values of bending moments for the deeper case are smaller. These two figures clearly indicate that the upper tunnel is unaffected by the position of the lower. The range of these values is slightly bigger than that predicted by Strand7.

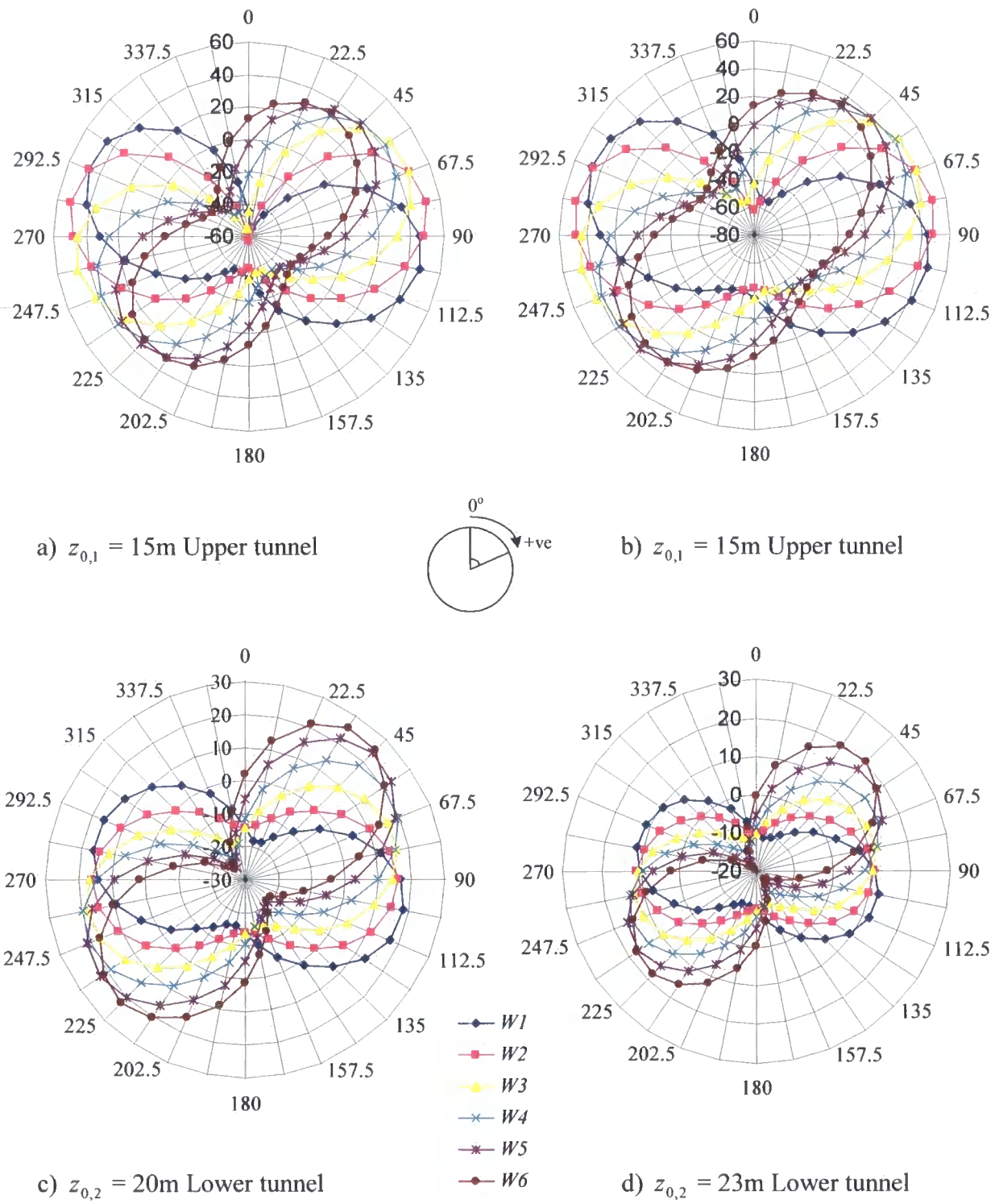

a) $z_{0,1}$ = 15m Upper tunnel

b) $z_{0,1}$ = 15m Upper tunnel

c) $z_{0,2}$ = 20m Lower tunnel

d) $z_{0,2}$ = 23m Lower tunnel

Figure 6.55. Change of bending moments due to the effect of surface loading for different surface loaded areas when the lower tunnel is driven at $z_{0,2}$ = 20m and 23m. The axial axis refers to the distribution of bending moments (kNm/m) around the tunnel, while the circumferential axis refers to the angle around the tunnel.

Finally Figures 6.56 and 6.57 show plots of the maximum and minimum change of bending moments (kNm/m) around both liners due to the surface loaded area against the relative position of the loaded area (*W*). Thin lines refer to positive changes while dotted to negative. The maxima of these curves lie directly above the upper tunnel's C.L (at *W*2). A similar trend is evident for the other loaded areas and the lower tunnel. For both tunnels however, regardless of the excavation depth Plaxis v.8 produces smaller results compared to Strand7 by about 25% to 40%.

6.3.4 Comparison of the *ST* case with the *TH* and *TVD* cases

FE predictions regarding the first tunnel (in the *TH* case) and the upper tunnel (in the *TVD* case) are compared with those in the *ST* case in terms of maximum surface settlements, tunnel lining deformations and bending moment distribution around the lining. The outcome from this comparison is presented in this section.

Plaxis FE predictions in regarding crown settlements are constant within a region of *W*1 to *W*3 (rather than *W*4 as is predicted in Strand7) and then gradually reduce. This indicates that interaction occurs within the previously mentioned region. This is further supported from the outcome of the distribution of bending moments. The maximum deformation of the tunnel lining occurs when the load is applied at *W*2 forcing the tunnel to squat. These deformations reduce as the load shifts towards *W*5. At *W*6 though the load seems to produce an ovalisation of the lining with the vertical tunnel diameter greater than the horizontal (in contrast to the previous load cases).

In general Plaxis predicts similar amount of interaction between the two different tunnel geometric configurations (*TH* and *TVD*). This implies that the contributory factors for the complex interaction mechanism are the surface load and the excavation depth. Pillar width only marginally seems to affect the Plaxis predictions.

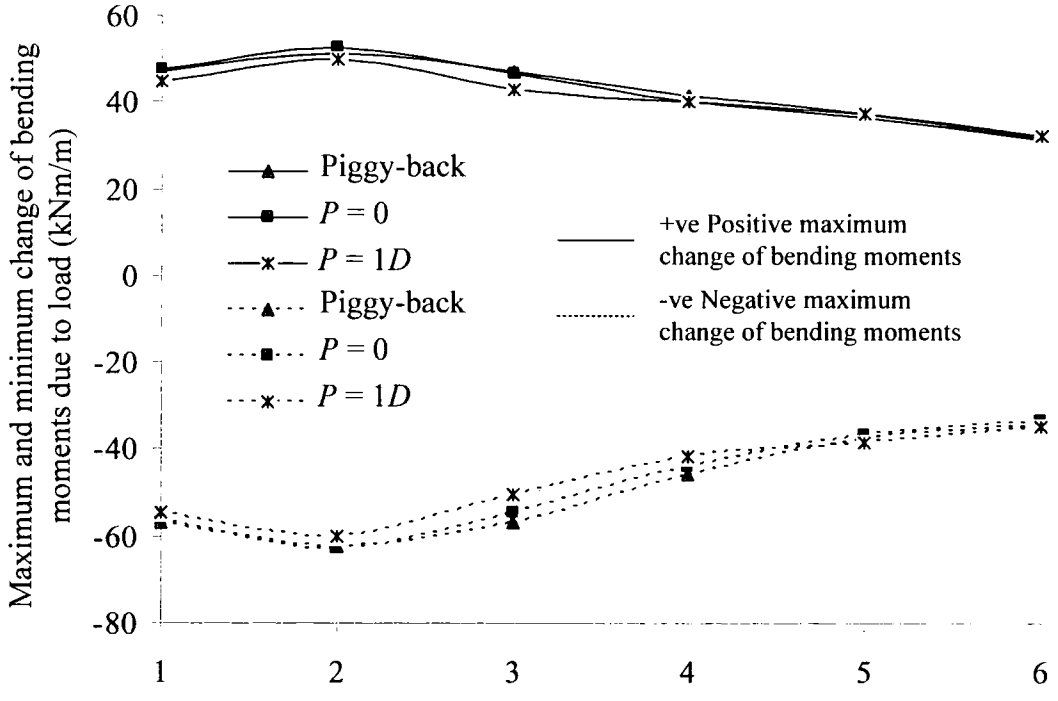

a) Regarding the upper tunnel

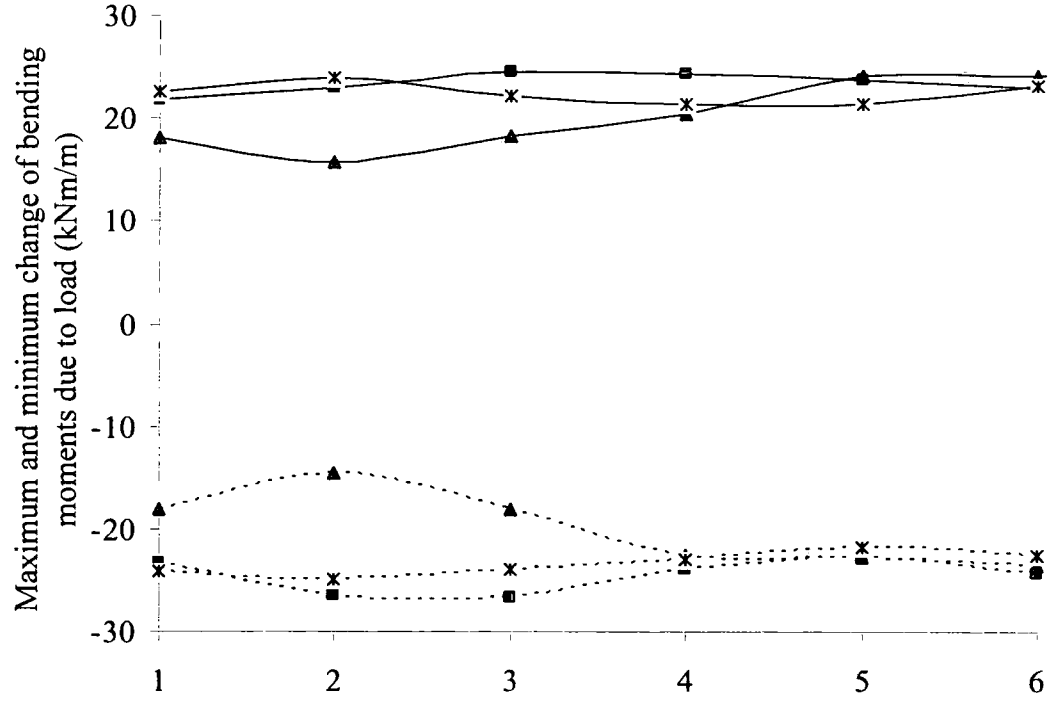

b) Regarding the lower tunnel

Figure 6.56. Maximum and minimum change of bending moments due to the effect of surface loading for different surface loaded areas when the lower tunnel is at $z_{0,2}$ = 20m.

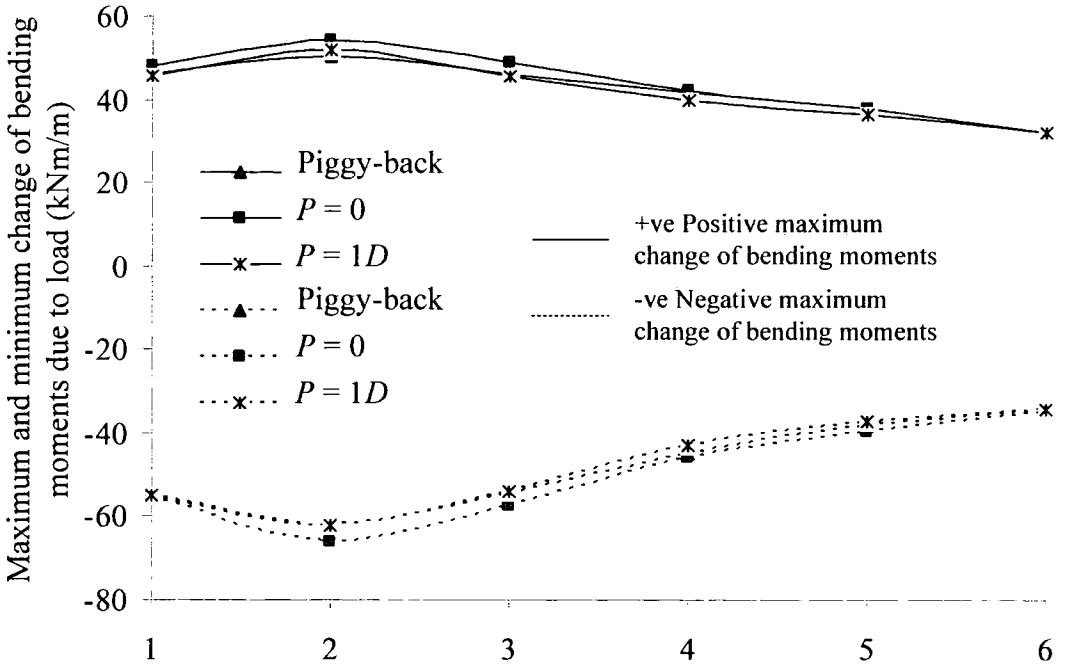

a) Regarding the upper tunnel

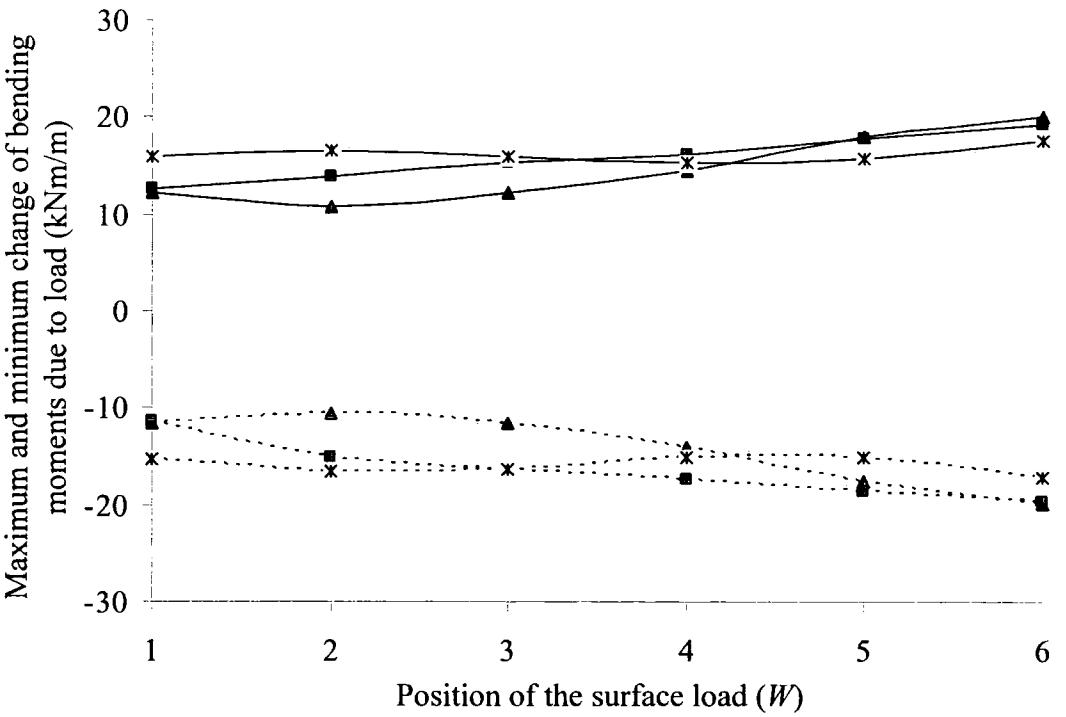

b) Regarding the lower tunnel

Figure 6.57. Maximum and minimum change of bending moments due to the effect of surface loading for different surface loaded areas when the lower tunnel is at $z_{0,2}$ = 23m.

6.4 Comparison between the Strand7 and Plaxis predictions

In the current chapter 2-D FE predictions were presented investigating the effect of surface loading above pre-existing tunnels driven in soft ground. Two different FE packages were used for this purpose to compare and validate the produced results. In total 162 analyses were carried out varying the excavation depth, the pillar width, the pillar depth and the position of the surface loaded area. The general trend between the two FE packages regarding the lining distortions, the crown settlements and the bending moment distribution around the tunnel liners was similar. Both packages predict that when the surface load is applied within the region of $W1$ to $W4$ [i.e. a horizontal distance of $P \leq 2D$ from the first (*TH* case) or upper tunnel (*TVD* case)] the existence of the interaction mechanism was evident regardless of the tunnel geometric configuration. Further from that distance no interaction occurred. Both FE packages gave evidence that the contributory factors to the interaction mechanism were the surface load, the excavation depth and to a lesser extent pillar width.

Small differences in the predictions between Strand7 and Plaxis occurred. Strand7 in particular predicted the existence of stronger interaction mechanism for the *TH* case compared to the *TVD* case. Plaxis on the other predicted similar amount of interaction between the two different tunnel geometric configurations and smaller compared to Strand7 predictions. These differences are attributed to the following three factors:

- Different types of finite elements were used to model soil in the domain. Six-noded triangles were used in Strand7. Even though this type of finite element was available in Plaxis as well, it was decided that the fifteen-noded triangle should be used instead for greater accuracy.
- Different meshes were generated between the two FE packages. The reason was that in Plaxis the user cannot import a mesh as in Strand7.
- Finally, even though the same elasto-plastic soil model with the Mohr-Coulomb failure criterion was used between the two FE packages, the plastic potential function was different. Associated flow was used in Strand7 while Plaxis used non-associated flow. According to Potts and Zdravkovic (1999) the latter way of modelling real soil behaviour is more realistic than the first.

From the previously mentioned differences in modelling it seems that Plaxis predictions were more accurate and realistic given that a denser mesh was used to discretise the domain which consisted of finite elements with more nodes while non-associated flow was adopted for the plastic potential function.

Chapter 7

3-D FE analysis of tunnelling using Strand7

7.1 Introduction

In this chapter 3-D FE analyses are carried out using the commercial FE package Strand7. The purpose of this study is to investigate the 3-D interaction effects of a surface load, acting above tunnels driven in soft ground and compare them with the equivalent 2-D presented in Chapter 6. The position of the load varies while its magnitude is constant. The following tunnel geometric configurations are analysed:

- Single tunnel horizontally aligned (case *ST*)
- Twin tunnels horizontally aligned (case *TH*)
- Twin tunnels vertically and diagonally aligned (case *TVD*)
- Multiple tunnels where one axis is horizontally aligned and the other axis is inclined (case *MHI*)

A parametric study was undertaken for the above mentioned tunnel geometric configurations varying the depth to the tunnel axis (z_0), the pillar width (P) and pillar depth (P_D), as well as the position of the surface loaded area (W). Figure 7.1 shows how these parameters vary for each of the above mentioned tunnel geometric configurations. The dimensions of the domain (x, y, z), the tunnel diameter (D), the magnitude of the surface load (400kN) and the dimensions of the area of load application (W) are considered to be constants throughout the analyses of this chapter. For compatibility purposes, the surface load is directly applied on the top boundary of the domain without the use of any type of interface elements, similar to the way it is

modelled when performing 2-D plane strain analysis (Chapter 6). The following convention is used in this chapter: the right hand side tunnel (see Fig. 7.1) is called "the first", while the left hand side tunnel is called "the second". Consequently, $z_{0,1}$ and $z_{0,2}$ are the depths to the tunnel axes of the first and the second tunnels respectively. The solid circle in Figure 7.1 represents the single tunnel scenario whereas the dotted circles correspond to the twin tunnel configuration.

7.2 Single tunnel case (*ST*)

7.2.1 Introduction

The meshes throughout this chapter are generated in Gmsh and then imported to Strand7. The reasons for this choice, as well as the exact procedure, are presented in detail in Chapter 5. One of the meshes used in this study is depicted in Figure 7.2. This particular mesh consists of 2,769 ten-noded tetrahedra representing the soil, 192 six-noded triangles representing the structural components of the domain (i.e. tunnel liner), or 7,266 in terms of nodes. Soil and lining elements shared the same nodes at the tunnel boundary. The interface between these two different materials was not modelled (similar to Wongsaroj *et al.*, 2007). Tunnel boundary was modelled in the same way throughout this chapter. The depth to the tunnel axis is z_0 = 15m. Three different areas of mesh density can be identified in this figure (Fig. 7.2). The first area consists of medium size finite elements which lie around the tunnel liner and on the loaded area on the top boundary. The second area consists of very coarse finite elements which are generated close to the four vertical and the bottom boundaries. Finally, the third area consists of elements the size of which is a transition between the previously mentioned two cases. The reason for not creating a higher density mesh (consisting of finer finite elements) is that Strand7 imposes restrictions regarding the size of the problem when performing a 3-D non-linear static FE analysis. Table 7.1 shows the correlation of the size of the problem (in terms of number of nodes, number of equations and size of the stiffness matrix $[K_G]$) and the time required for the solution (t), for a series of analyses performed in this study. It is evident that solution time increases rapidly and non-linearly with increasing size of a

problem. Larger size problems were prohibitive to perform in these parametric studies due to the large amount of time required for the solution.

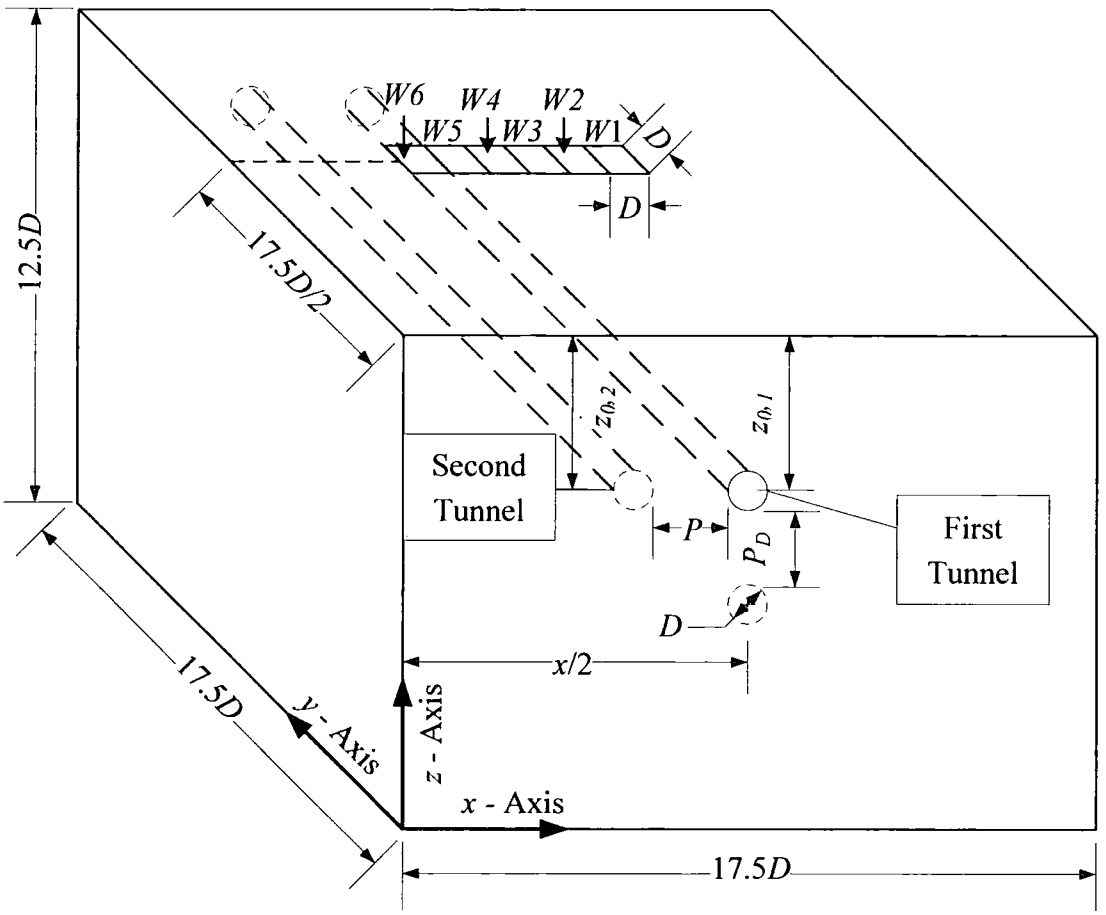

ST case
z_0 = 15m, 20m
Varying load surfaces:
W2, *W3*, *W4*

TH case
$z_{0,1} = z_{0,2}$ = 15m, 20m
P = 1*D*, 2*D*
Varying load surfaces:
W1, *W2*, *W3*, *W4*, *W5*, *W6*

TVD case
$z_{0,1}$ = 15m
$z_{0,2}$ = 20m, 23m
P_D = *D*/4, 1*D*
P = piggy-back, 0, 1*D*
Varying load surfaces:
W1, *W2*, *W3*, *W4*, *W5*, *W6*

MHI case
$z_{0,1} = z_{0,2}$ = 15m
P = 1*D*, 2*D*
Varying load surfaces:
W1, *W2*, *W3*, *W4*, *W5*, *W6*

Figure 7.1. Geometric parameters regarding the soil, the tunnels and the surface loaded area.

For compatibility purposes with the 2-D FE analyses presented in Chapter 6 the tunnel diameter D = 4m. The grid dimensions are chosen to be 17.5D long across the x-axis, 17.5D long across the y-axis and 12.5D deep along the z-axis. In Figure 7.2 there is a plane of symmetry along the vertical tunnel diameter. Hence, the surface loaded areas $W1$ and $W3$ produce the same effects for the single tunnel case. Therefore, only one of these two is modelled ($W3$) along with $W2$ and $W4$. In total 6 analyses are performed in this study which are classified as follows: three different surface loaded areas ($W2$, $W3$, $W4$) and two different excavation depths (z_0 = 15m, 20m).

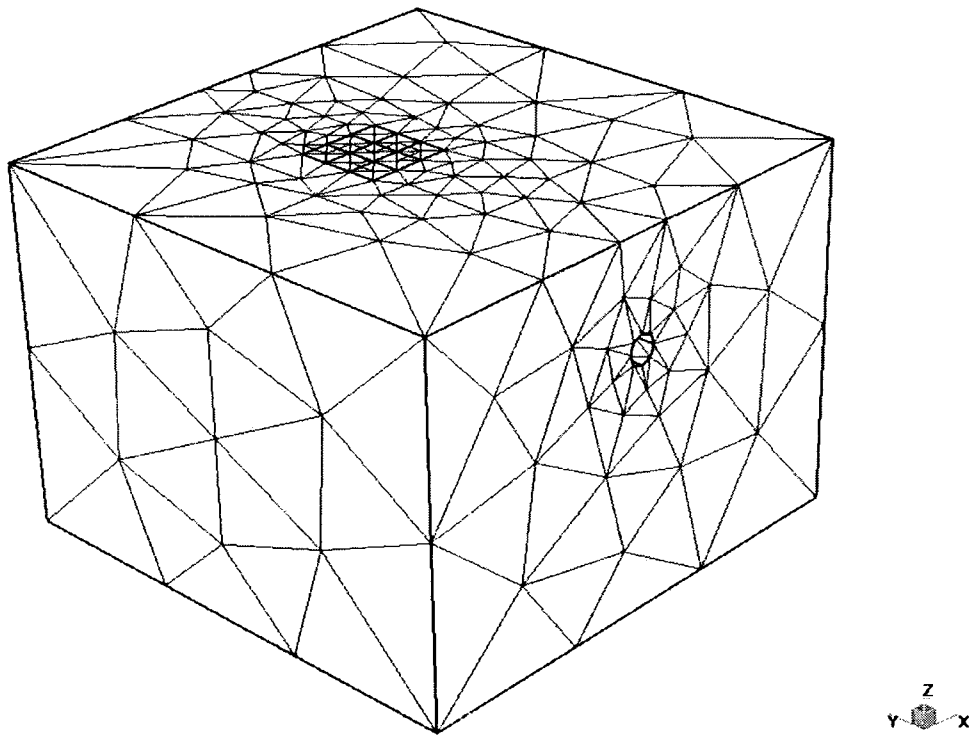

Figure 7.2. Generated mesh for the single tunnel analysis when z_0 = 15m.

7.2.2 Details of the analysis

7.2.2.1 Initial conditions

The tunnels along with their permanent lining, in the analyses presented in the current chapter, appear in the mesh as if wished in place; i.e. no tunnel excavation is modelled. The site of interest is a non-greenfield since other structures (single or twin tunnels) are present. Consequently the "*gravity loading*" method is used rather than the "K_0 procedure" to determine the stress field prior to the surface loading (as

explained in Chapter 3). The resulting displacements are considered as the zero datum for the subsequent stages of the analysis. The soil profile used in this study is identical to the one modelled for the plane strain analyses presented in Chapter 6. Soil properties are presented in Table 6.2.

The boundary conditions are set so that horizontal normal movements were not permitted along the four vertical boundaries of the domain. On the bottom horizontal boundary no movements are permitted at all, while on the top horizontal boundary nodes away from the edges are free. The above settings regarding the calculation of the initial stresses, the stratigraphy and the boundary conditions are the same throughout the analyses of this chapter.

PC characteristics		Processor Intel (R)	CPU 2.80GHz	RAM 3GB
No. of Nodes	No. of Tetrahedra	Matrix size $[K_G]$ (MB)	No. of Equations	Solution time t
7,266	2,769	77	12,255	20m
7,153	4,085	150	17,277	58m
20,168	5,124	230	22,426	2h 9m
22,335	6,454	340	27,768	3h 56m
23,314	6,941	423	29,750	10h 6m

Table 7.1. Correlation of the size of a problem and the time required for solution.

7.2.2.2 Constitutive models

The structural components of the domain (i.e. tunnel lining) are assumed to behave in an isotropic linear elastic way. Their properties are presented in Table 6.1. Soil behaviour is described by a simple elastic perfectly plastic constitutive model where the plastic region is described using the Mohr-Coulomb failure criterion along with an associated flow. Undrained conditions are assumed throughout these analyses.

7.2.2.3 Modelling sequence

Two load stages are used for the analyses performed in this chapter. In the first stage drained analysis is performed (using effective stiffness parameters) and gravity is uniformly applied in the domain in five successive increments by initialising the soil's unit weight (γ = 20 kN/m^3) and the gravitational acceleration (g = 9.81 kN/m^3).

During this stage the tunnel is already installed and the corresponding displacements are considered as the zero datum. During the second stage, drained loading is applied (i.e. no pore water pressure changes) while the surface load is applied in twelve increments (see Table 6.3). The procedure is described in detail in Section 6.2.1.4.

7.2.3 Analysis results

In this section results are presented for the case of a surface load applied above a single tunnel whose axis is horizontally aligned. 3-D FE predictions regarding the surface settlements due to the load (S'), the tunnel lining deformations along both the transverse and the longitudinal axes, and finally the bending moment distribution of the lining are presented.

Figure 7.3 depicts the ratio of the surface settlements produced due to the effect of the surface load over the tunnel diameter (S'/D) plotted along the vertical axis against the transverse distance x (horizontal axis) for three different surface loading positions (W). The tunnel CL is driven at z_0 = 15m. The maximum value of S' occurs when the load is applied directly above the tunnel CL at *W2*. As the load shifts further away towards *W4* the value of S'_{max} reduces.

In Figure 7.4 the ratio of S'_{max}/D is plotted against the relative position of the surface loaded area W (horizontal axis) for two different excavations depths (z_0 = 15m and 20m). The findings indicate that only minor changes occur to S'_{max} as z_0 varies. The maximum difference between the two plots occurs when the load is applied at *W3*. Smaller values of S'_{max} are predicted for shallow tunnels. This may be attributed to the fact that soil is not allowed to deform freely since it is stiffened by the existence of the tunnels close to the surface.

Figure 7.5 presents the crown settlements due to the effect of the surface loading expressed as a percentage of the tunnel diameter against the longitudinal direction y for three different loading positions (*W2*, *W3* and *W4*). The depth to the tunnel axis is at z_0 = 15m. These three plots indicate that as the surface load shifts from *W2* towards *W4* the crown settlements tend to increase. The difference between the value of crown settlements at the tunnel entrance (i.e. at y = 0) and that below the applied

surface load (i.e. at y = 17.5D/2, see Fig. 7.1) is approximately 0.1% of the tunnel diameter regardless of the position of the load. The maximum values of the crown settlement (roughly 0.2% of the tunnel diameter) are then plotted in Figure 7.6 against the relative position of the surface loaded area (W) for two different excavation depths. It is found that the deeper the excavation the less the effect of the applied load. Hence, smaller crown settlements are produced in the case where z_0 = 20m.

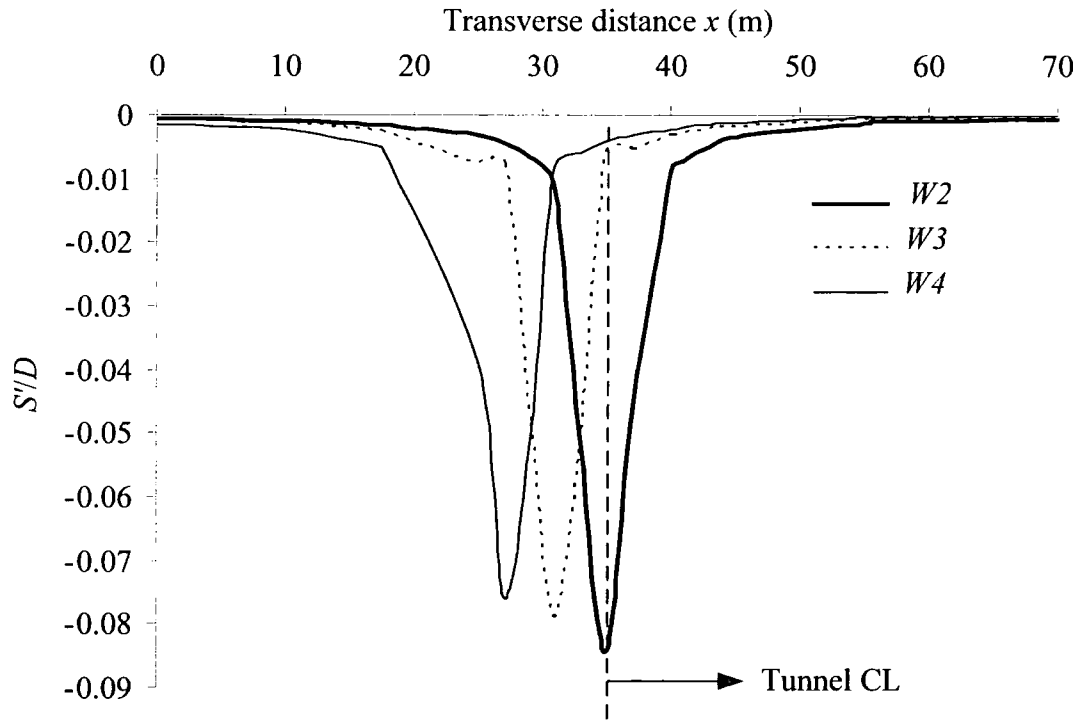

Figure 7.3. Plot of the ratio of the surface settlements above an existing single tunnel due to the surface load over the tunnel diameter against the transverse distance x. The position of the load varies from $W2$ to $W4$.

Figure 7.7 shows the deformed shape of the tunnel liner (scaled up) due to the effect of the surface load (shown as coloured lines) at a plane normal to the longitudinal y-axis at a distance of y = 17.5D/2, for two different excavation depths. The deformed shape can then be compared to the initial undisturbed lining prior to any loading stage (shown as a solid line). The whole tunnel seems to translate vertically. A secondary minor horizontal translation takes place opposing the position of the applied surface load as this shifts from $W2$ towards $W4$. Smaller movements occur for deeper excavated tunnels.

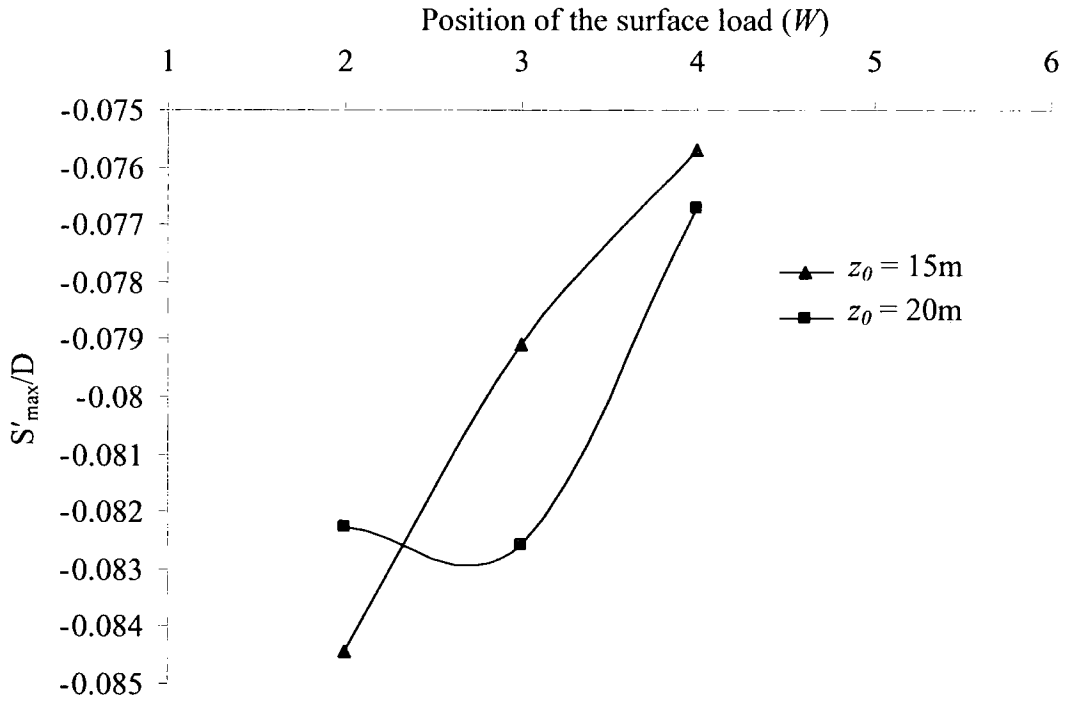

Figure 7.4. Plots of the maximum surface settlement due to surface loading against the position of the surface loaded area for two different excavation depths.

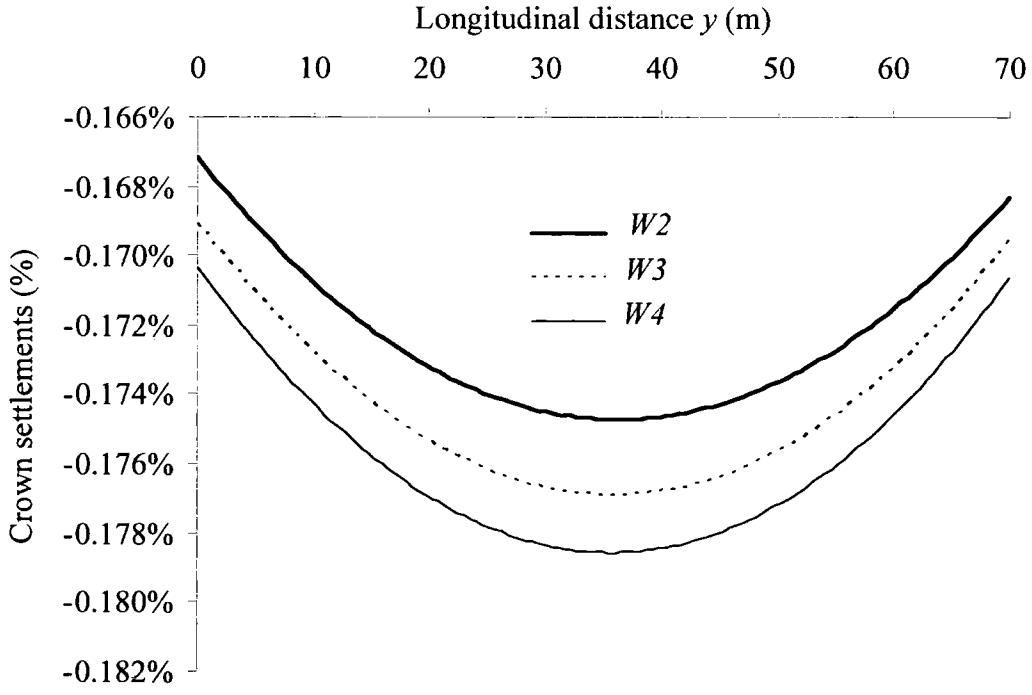

Figure 7.5. Crown settlements due to loading along the longitudinal y-axis for three different surface loading positions. The depth to the tunnel axis is at z_0 = 15m.

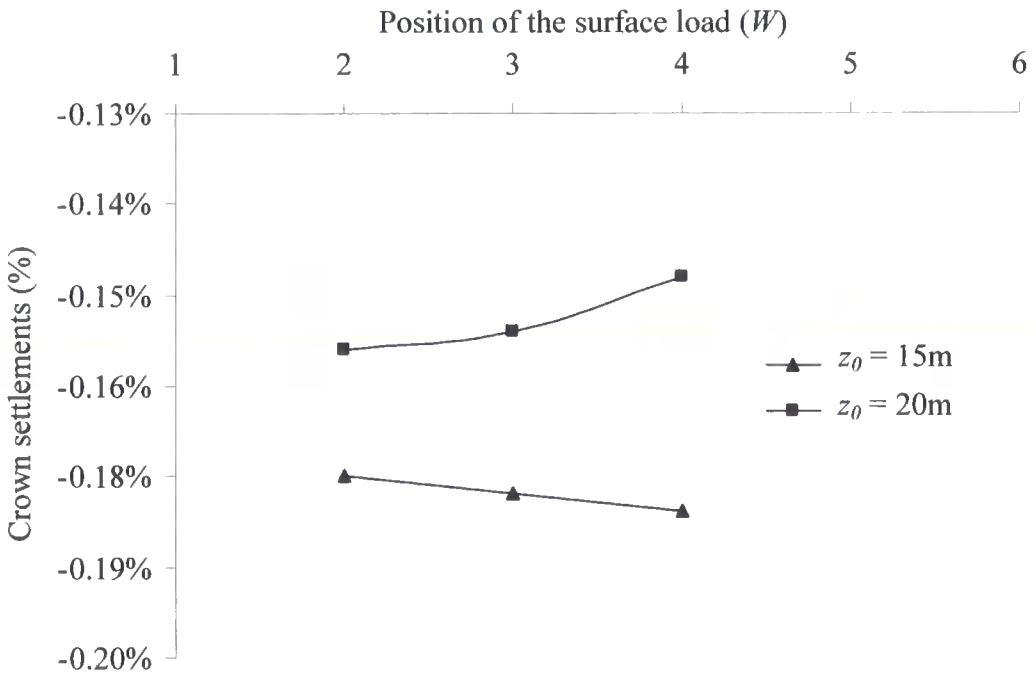

Figure 7.6. Maximum crown settlements against the position of the surface loaded area for two different excavation depths.

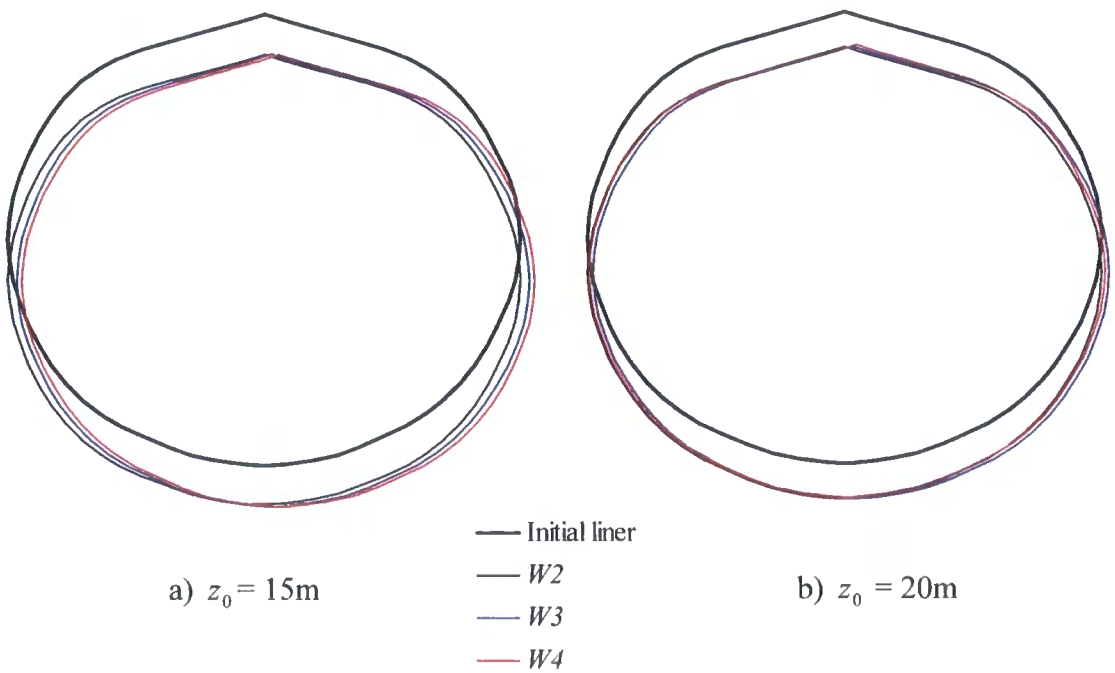

Figure 7.7. Deformed shape of the tunnel due to the surface loading for three different loaded areas (*W*2, *W*3 and *W*4) and two different tunnel depths (z_0 = 15m, 20m).

Figure 7.8 shows the change of bending moment distribution (in kNm/m) around the tunnel liner solely due to the effect of the surface load (akin to Fig. 6.9) for two different excavation depths, at a transverse plane at y = 17.5D/2. The same sign convention as used in Chapter 6 is adopted throughout; i.e. negative bending moments correspond to straightening of the lining (tension at intrados) while positive bending moments indicate increase of the lining curvature (compression of intrados). Tunnel crown lies at an angle of 0° while the tunnel invert is at 180°, moving in a clockwise direction. Deeper tunnels seem to produce smaller values of bending moments. The maximum positive value of bending moment seems to occur at around 225° (rather than 270°), while the maximum negative occur at 135° instead of 180°. Had more nodes been generated around the tunnel, more accurate predictions could have been obtained. However, as explained in Section 7.2.1 restrictions are imposed by the FE software used.

In Figure 7.9 the maximum positive and negative values of the change of bending moments (kNm/mm) solely due to the surface load around the tunnel at y = 17.5D/2 are plotted (horizontal axis) against the relative position of the surface load (W) for two different excavation depths. These plots indicate that shallower tunnels lead to larger values of bending moments and therefore these tunnels are more affected from the surface load which appears intuitively curved. The position of the load does not seem to vastly affect the liner since these plots are almost parallel to the horizontal axis.

7.3 Twin tunnels horizontally aligned (case *TH*)

7.3.1 Introduction

In this section the case of twin tunnels which are horizontally aligned is examined. Figure 7.10 shows one of the meshes used for this geometric configuration, where the depth to the tunnel axes is $z_{0,1} = z_{0,2}$ = 15m while the pillar width is P = 1D. The 3-D mesh consists of 20,168 nodes. In terms of elements, these are 5,124 ten-noded tetrahedra and 384 six-noded triangles.

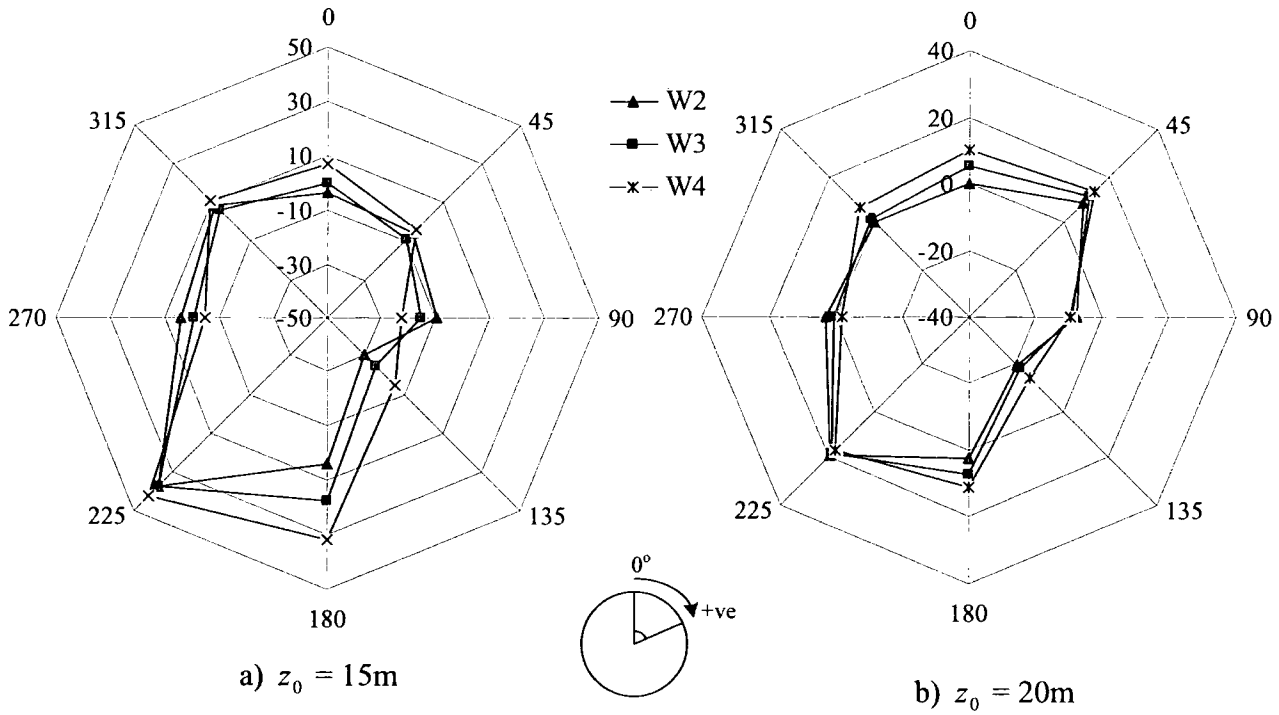

a) z_0 = 15m

b) z_0 = 20m

Figure 7.8. Change of bending moments due to the effect of surface loading for different surface loaded areas when z_0 = 15m and 20m. The axial axis refers to the distribution of bending moments (kNm/m) around the tunnel, while the circumferential axis refers to the angle around the tunnel.

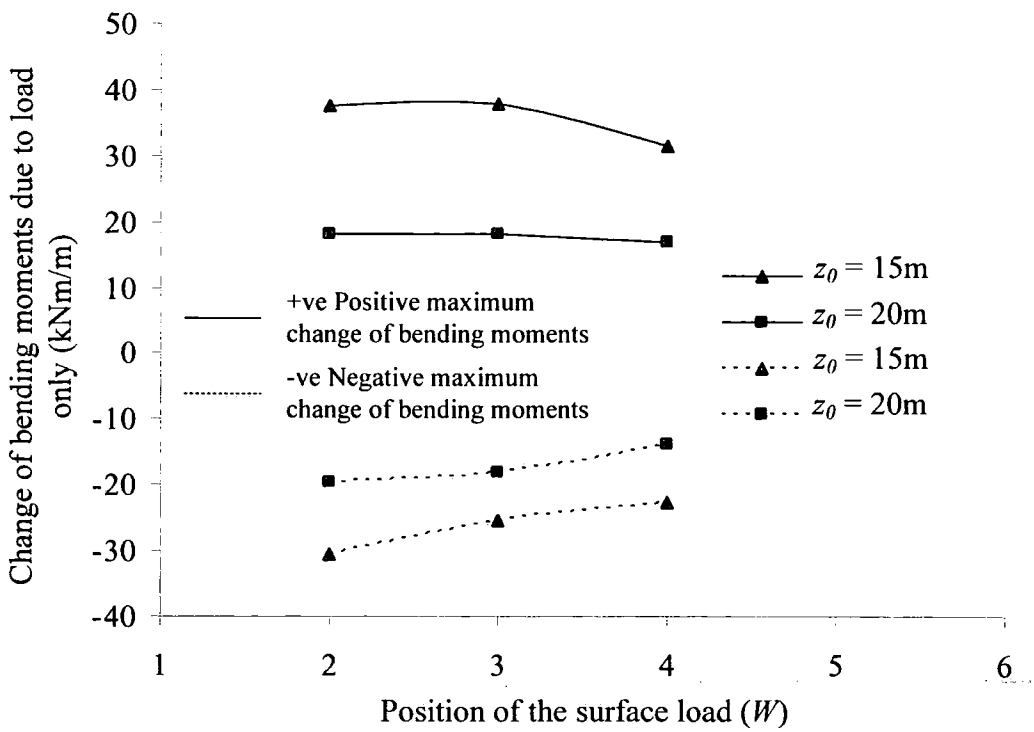

Figure 7.9. Change of bending moments due to the effect of surface loading for different surface loaded areas and different excavation depths.

The details of the analysis are identical to those presented in Section 7.2.2. The only difference is that during the calculation of the initial conditions a second tunnel is present in the domain. This however does not affect the number of the loading stages. Six surface loading positions are modelled (*W1* to *W6*), along with two different excavation depths ($z_{0,1} = z_{0,2} =$ 15m and 20m) and two different pillar widths ($P =$ $1D$ and $2D$). Consequently 24 analyses were performed in this study.

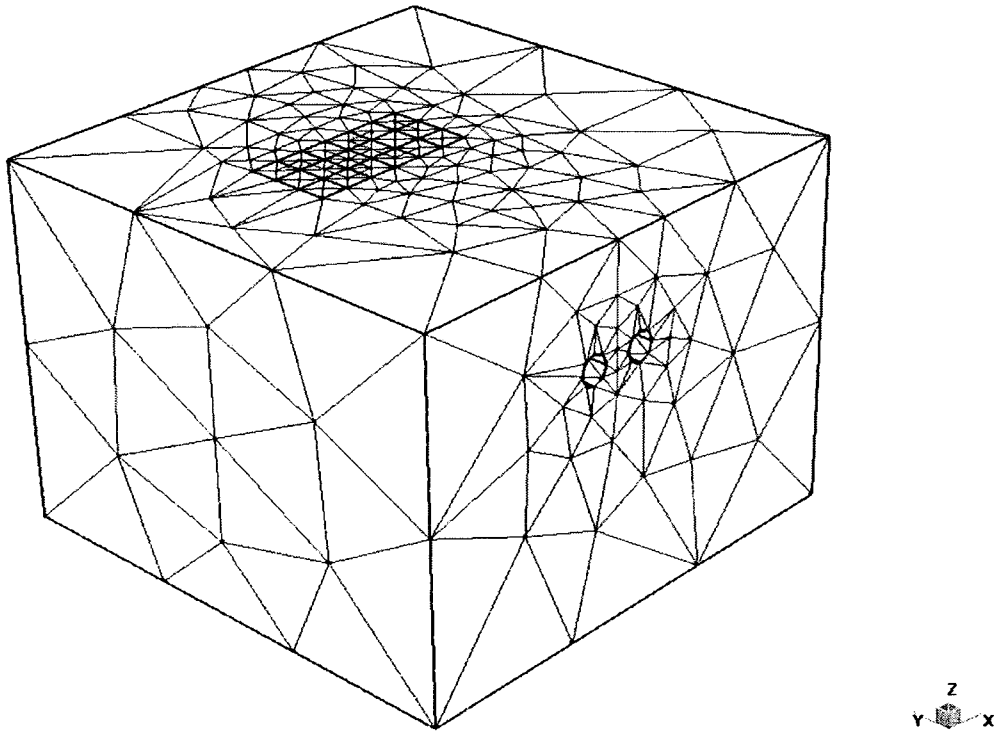

Figure 7.10. Generated mesh for the *TH* case when $z_{0,1} = z_{0,2} =$ 15m and $P = 1D$.

7.3.2 Analysis results

The dimensionless ratio of S'_{max}/D plotted on the vertical axis against the relative position of the surface load (*W*) along the horizontal axis is presented in Figure 7.11. Two different excavation depths and two different pillar widths are modelled. Thin lines refer to the $z_{0,1} = z_{0,2} =$ 15m case whereas dotted lines refer to the $z_{0,1} = z_{0,2} =$ 20m case. In the case where $P = 1D$ the maximum value of S'_{max} roughly occurs at *W3* (i.e. the mid-distance between the two tunnels) regardless of the excavation depth. In the case where the tunnels are further separated ($P = 2D$) the trend is not so clear to identify.

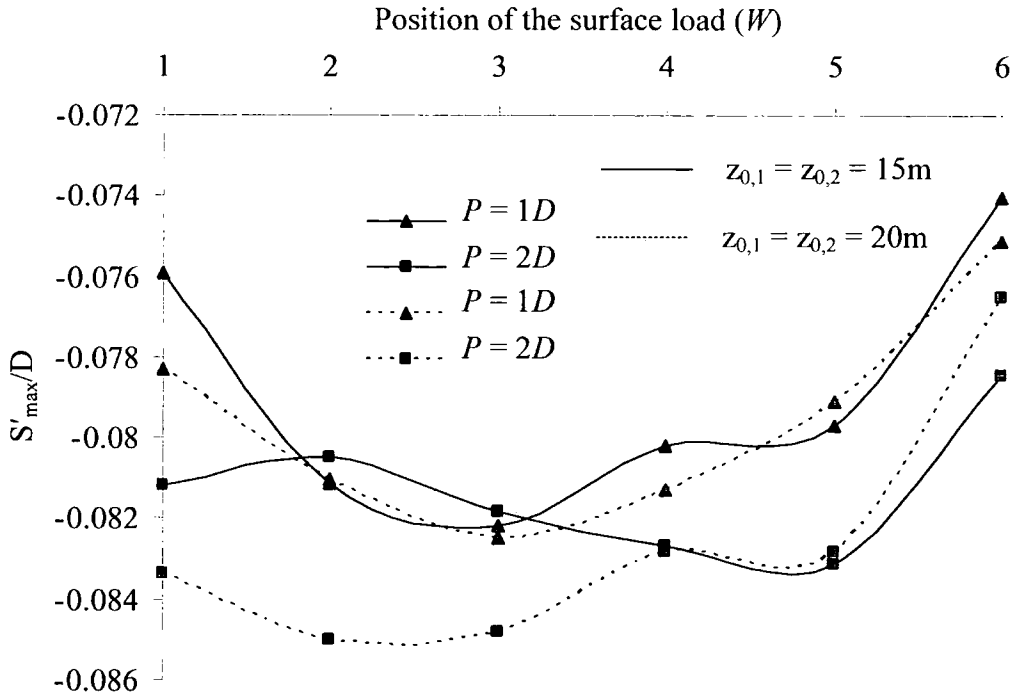

Figure 7.11. Plots of the ratio of S'_{max}/D against the position of the load for various excavation depths.

Figure 7.12 shows the crown settlements due to the load expressed as a percentage of the tunnel diameter of the first tunnel against the longitudinal direction y for six different loaded areas. Two different tunnel depths are modelled ($z_{0,1}$ = 15m and 20m) when the pillar width is $P = 1D$. The FE predictions indicate that the maximum crown settlements regarding the shallow case occur when the load is applied in the vicinity of *W2* (directly above the first tunnel's CL) and *W3*. As the load shifts further away the resulting settlements decrease. Another interesting outcome from this figure is that when the load is applied at *W1* (1*D* to the right of the first tunnel) the predicted settlements are similar to those produced at *W5* (1*D* to the left of the second tunnel). This can be attributed to the interaction between the twin tunnels and the applied load. The maximum crown settlements regarding the deeper case occur when the surface load is applied between *W1* and *W3* (roughly above the first tunnel). As the load shifts away from that tunnel towards *W6*, these deformations seem to reduce. The interaction mechanism which was identified for the shallow case seems to no longer exist for the deeper case.

The maximum crown settlements due to the load expressed as a percentage of the tunnel diameter against the relative position of the surface loaded area (*W*) are plotted

in Figure 7.13, for two different excavation depths and two different pillar widths. The thin lines correspond to crown settlements of first tunnel while the dotted lines to the second tunnel. Similar behaviour is observed for each of the two tunnels regardless of both P and z_0. However, slightly larger values of crown settlements are predicted for the shallow case (approximately 0.02% of the tunnel diameter). When the load is applied within the region of *W1* to *W4* the predicted values of the maximum crown settlements appear to be constant. Further from this area (at *W5* and *W6*) these values reduce rapidly. This is an indication that the interaction mechanism due to the load is strong when the load is applied within *W1* to *W4* (i.e. 2D to 3D from the first tunnel's CL). For the deeper case a similar trend to the shallow case is evident with a much smoother transition though from *W1* to *W6*. This indicates a smaller interaction compared to the shallow case.

Figure 7.14 shows the deformed shape of both tunnels (scaled up) due to the effect of the surface load (shown as coloured lines) for two different excavation depths and six different surface loaded areas (*W*). The pillar width distance is P = 1*D*. These deformed shapes are then compared to the initial tunnel lining (solid lines) prior to any loading stage. The tunnel seems to behave like a rigid body. Hence, no change of its vertical or horizontal diameter occurs so as to alter its shape. Vertical and (smaller) horizontal translations are the two distinct movements caused by the surface load. These shapes are not circular as they should. Instead a peak is formed at the crown. This is attributed to the small amount of points used at the tunnel boundary.

Figure 7.15 shows the interaction between the two horizontally aligned tunnels and the surface load compared to the single tunnel case (*ST*). The FE predictions regarding the crown settlements of the first tunnel (for the *TH* case) are plotted on the vertical axis as a percentage of the single tunnel case against the relative position of the surface loaded area (*W*). Two different pillar widths (P = 1*D*, 2*D*) and two different excavation depths ($z_{0,1}$ = 15m and 20m) are modelled. Thin lines refer to the shallow case, and dotted lines to the deepest. These plots indicate that for the deeper of the two analysed cases ($z_{0,1}$ = 20m) less or no interaction is identified compared to the shallower case ($z_{0,1}$ = 15m) where interaction is more evident. The difference though is small (between 2% to 5%). As the surface load shifts away from the first tunnel the interaction decreases regardless of the excavation depth. This outcome is

further supported by the data plotted on Figure 7.13.

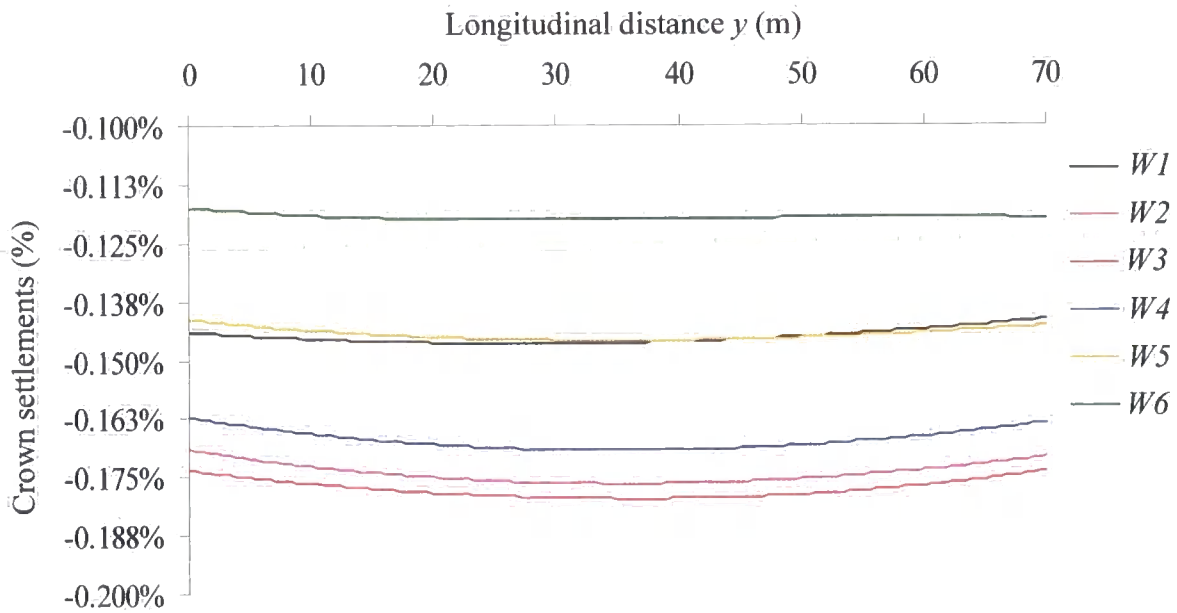

a) First tunnel at $z_{0,1}$ = 15m

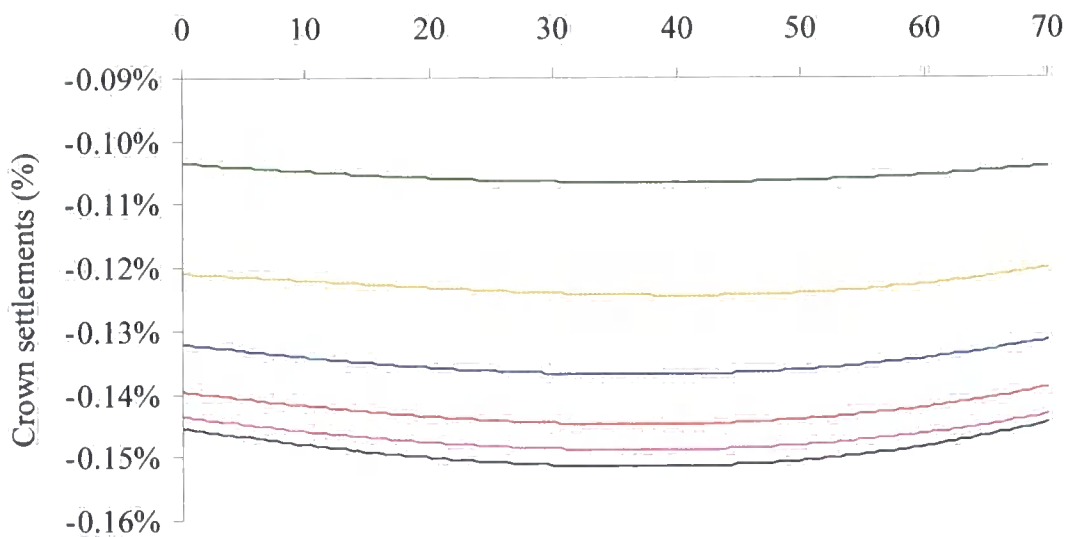

b) First tunnel at $z_{0,1}$ = 20m

Figure 7.12. Crown settlements expressed as a percentage of the tunnel diameter along the longitudinal *y*-axis regarding the first tunnel (for the *TH* case) for two different excavation depths and six different surface loaded areas. The pillar width is $P = 1D$.

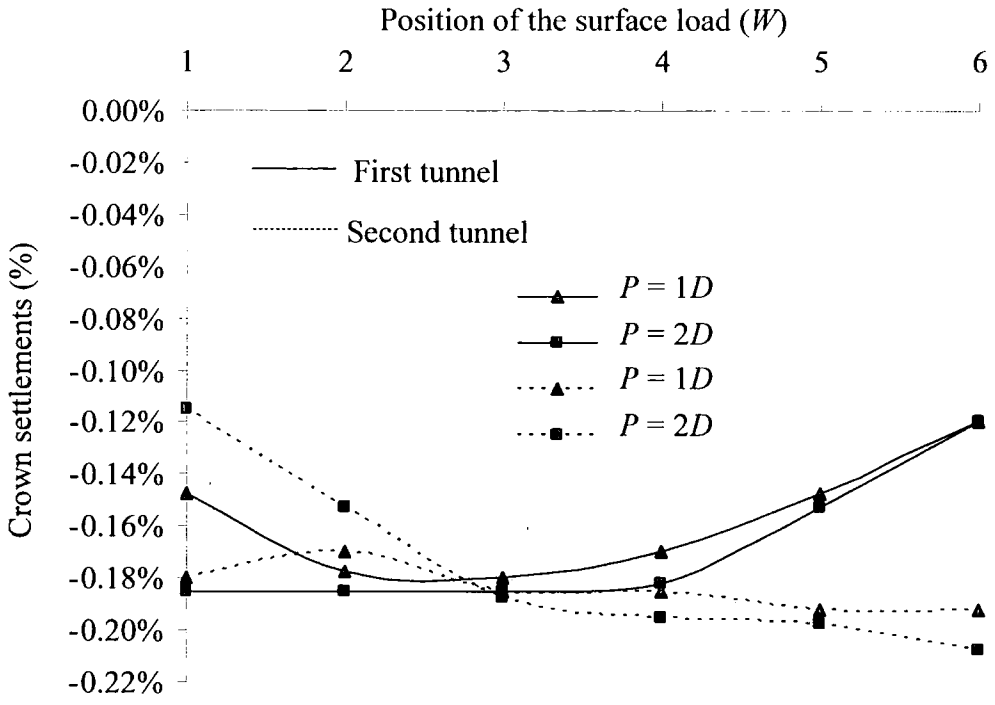

a) $z_{0,1} = z_{0,2} = 15$m

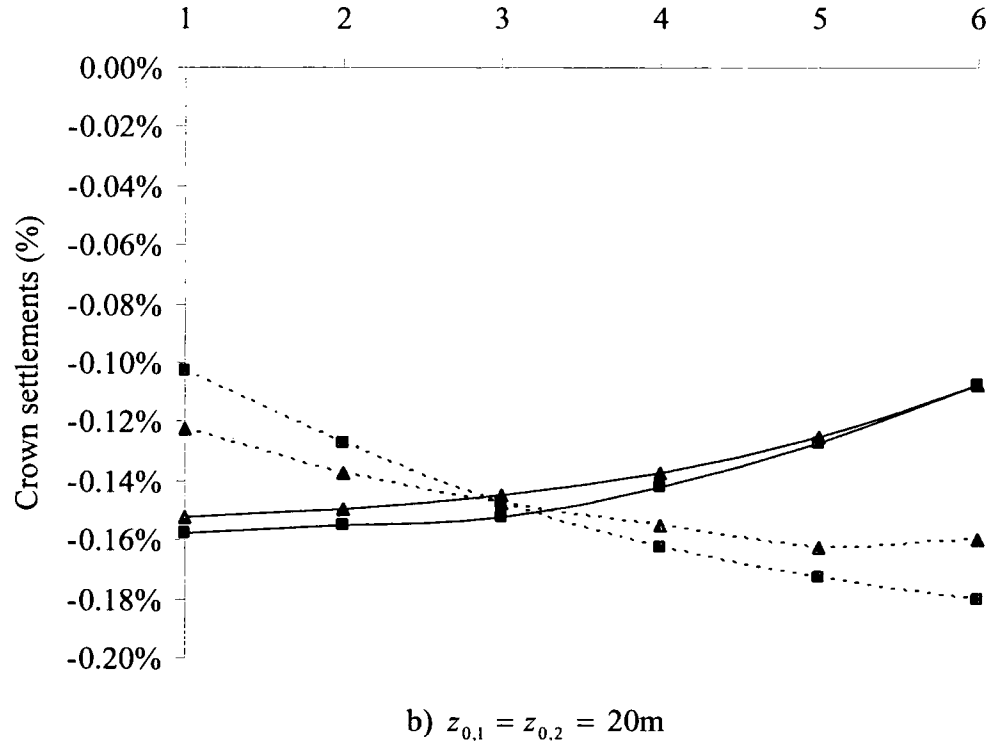

b) $z_{0,1} = z_{0,2} = 20$m

Figure 7.13. Maximum crown settlements expressed as a percentage of the tunnel diameter against the position of the surface loaded area for different excavation depths.

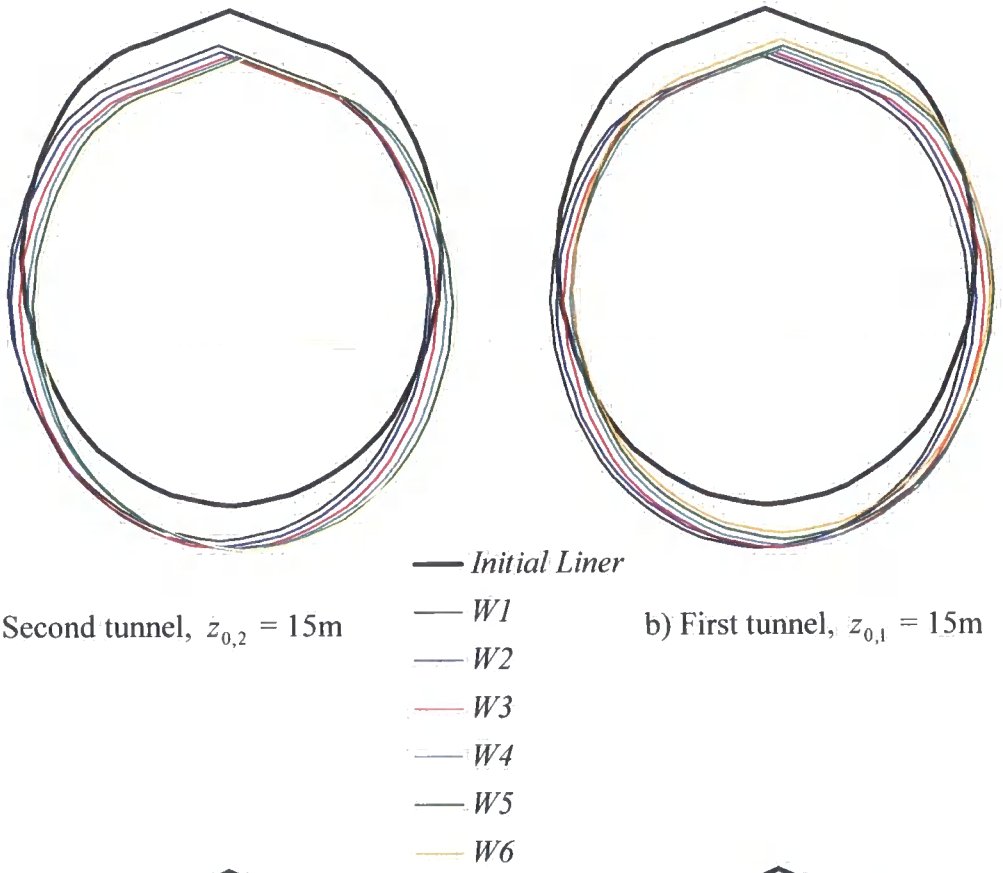

a) Second tunnel, $z_{0,2}$ = 15m

b) First tunnel, $z_{0,1}$ = 15m

c) Second tunnel, $z_{0,2}$ = 20m

d) First tunnel, $z_{0,1}$ = 20m

Figure 7.14. Deformed shape of the tunnels due to the surface loading for six different loaded areas. The tunnel axes are driven at $z_{0,1} = z_{0,2}$ = 15m and 20m while $P = 1D$.

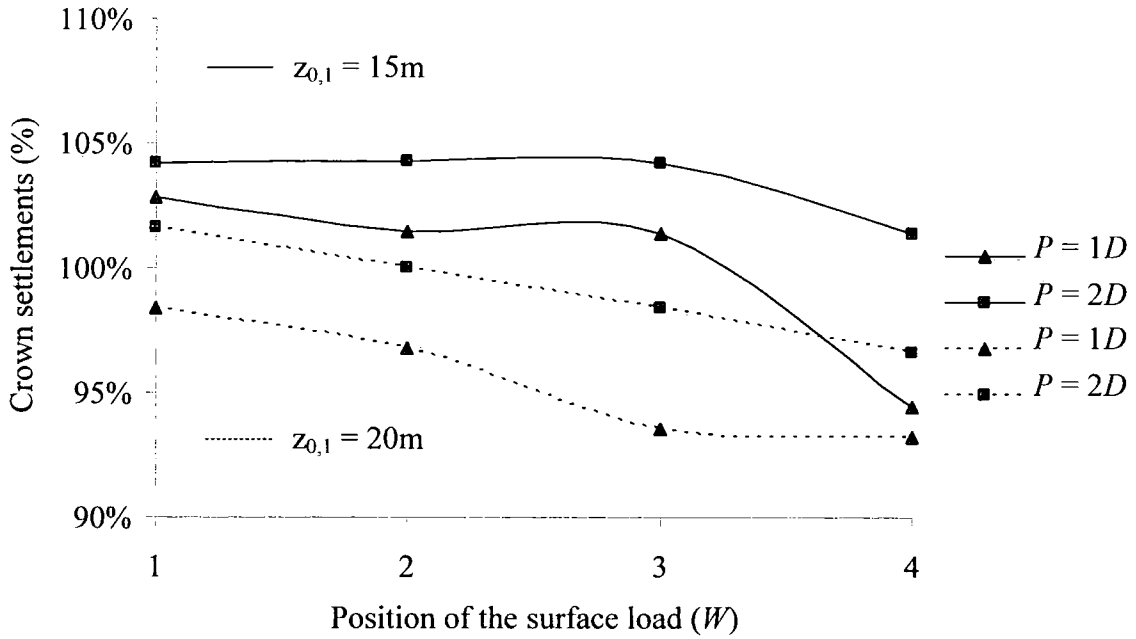

Figure 7.15. Plots of the crown settlements due to loading of the first tunnel in the *TH* case as a percentage of the single tunnel predictions for various surface loading areas and two different tunnel depths.

Figure 7.16 depicts the distribution of the change of bending moments (in kNm/m) around each tunnel for various surface loading positions (W) and for two different excavation depths. The pillar width is $P = 1D$. Positive maximum values of bending moments due to the surface loading occur around 180° and 225° while negative maximum occur at 135° for both tunnels, regardless of the tunnel depth. In Figure 7.17 the maximum positive and negative values of the change of bending moments regarding the first tunnel are then plotted on the vertical axis against the relative position of the surface loaded area (W, horizontal axis) for two different pillar widths ($P = 1D$ and $2D$). It appears that deeper tunnels are less affected by the surface load since smaller values of bending moments are predicted. These plots are almost parallel to the horizontal axis (no peak). This indicates that the load acting normal to the surface only marginally affects the maximum values of the bending moments.

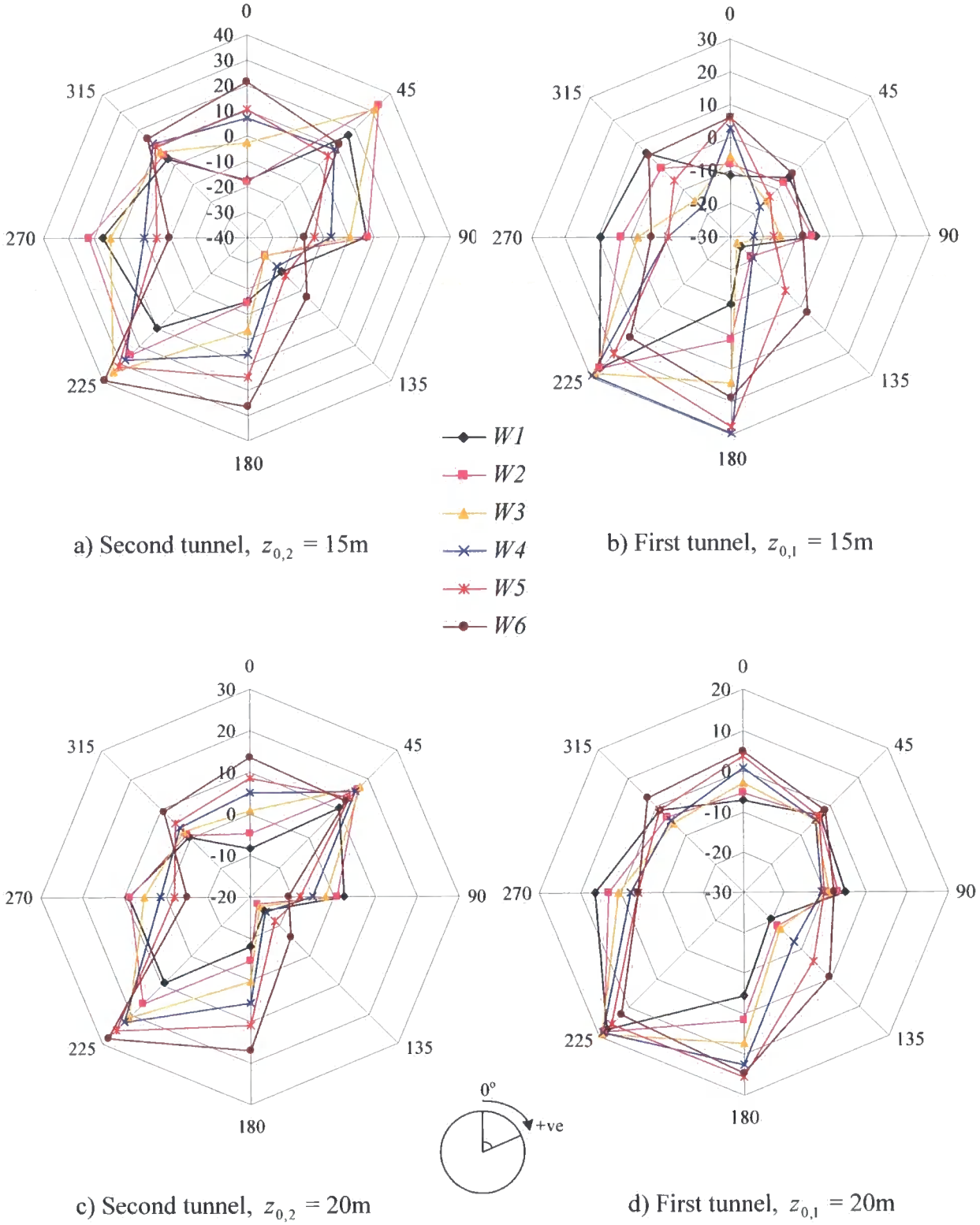

a) Second tunnel, $z_{0,2}$ = 15m

b) First tunnel, $z_{0,1}$ = 15m

c) Second tunnel, $z_{0,2}$ = 20m

d) First tunnel, $z_{0,1}$ = 20m

Figure 7.16. Change of bending moments due to the effect of surface loading for different surface loaded areas and different tunnel depths when $P = 1D$. The axial axis refers to the distribution of bending moments (kNm/m) around the tunnel, while the circumferential axis refers to the angle around the tunnel.

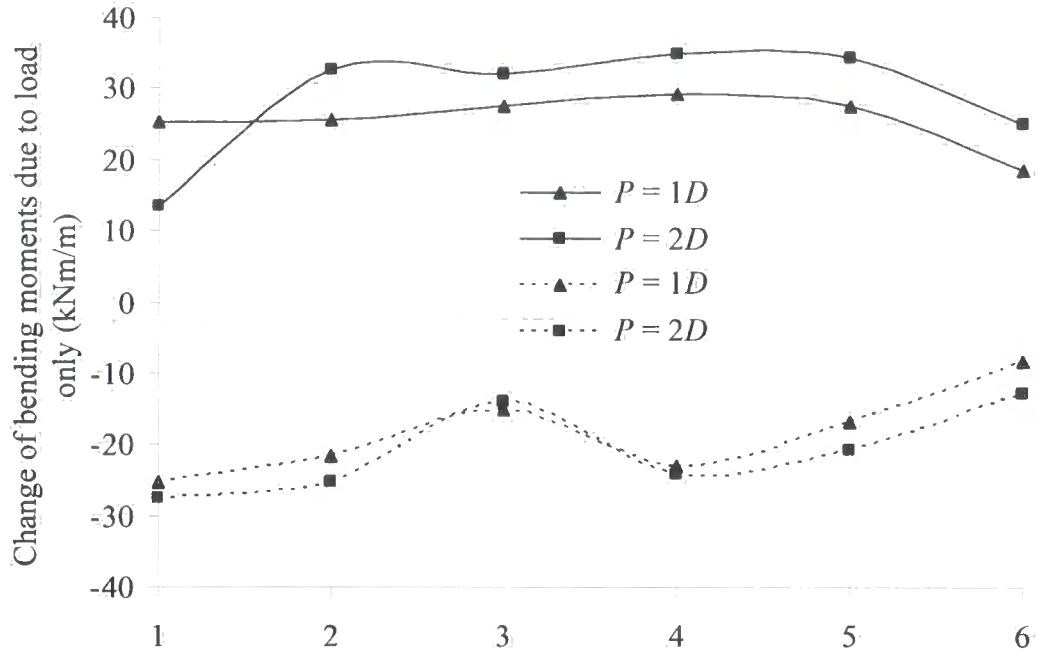

a) Regarding the first tunnel when $z_{0,1}$ = 15m

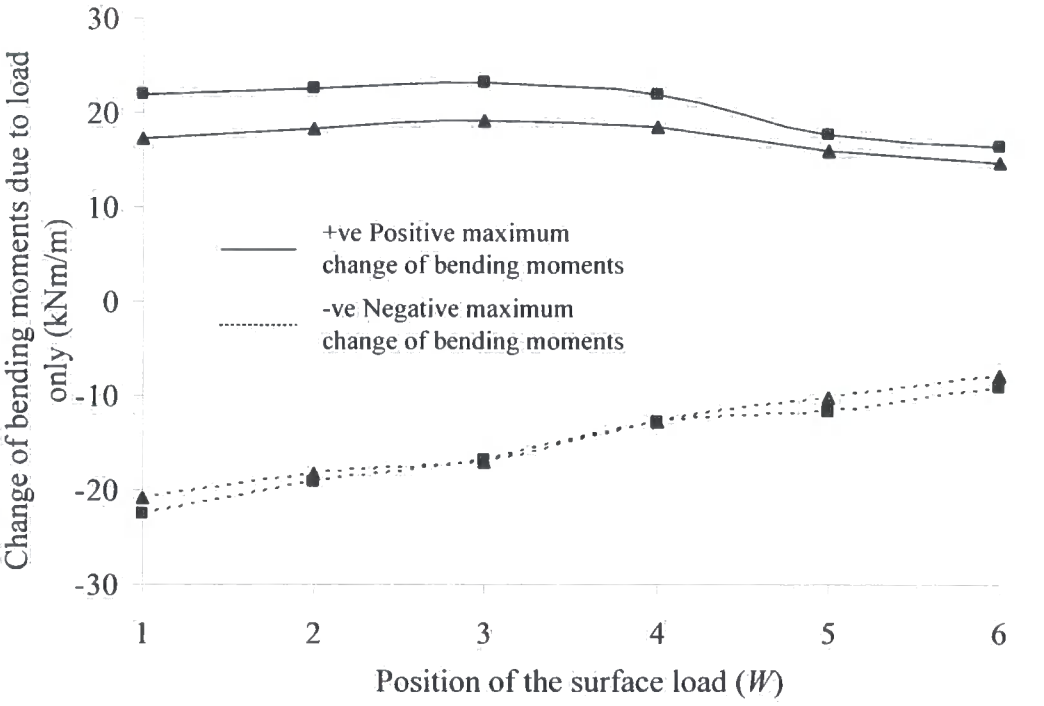

b) Regarding the first tunnel when $z_{0,1}$ = 20m

Figure 7.17. Maximum and minimum change of bending moments due to the effect of surface loading regarding the first tunnel for different surface loaded areas when $z_{0,1}$ = 15m and 20m.

7.4 Twin tunnels vertically aligned (case *TVD*)

7.4.1 Introduction

The cases of twin tunnels which are vertically aligned (P = piggy-back) and diagonally aligned (P = 0 and 1D) are presented in this section (case *TVD*). One of the meshes used for this geometric configuration is presented in Figure 7.18 where the depths to the tunnel axes are $z_{0,1}$ = 15m and $z_{0,2}$ = 23m. The pillar width and pillar depth are P = 0 and P_D = 1D respectively. The 3-D mesh consists of 7,190 ten-noded tetrahedra elements representing the soil and 384 six-noded triangles representing the tunnel lining, and there are 16,387 nodes. The details of analysis are the same to those described in Section 7.2.2. In this study the position of the first tunnel (named as upper in this parametric study) is fixed at $z_{0,1}$ = 15m (hence, its position will not be repeated hereafter), while that of the second tunnel (named as lower in this parametric study) varies. Six different surface loading positions (*W1* to *W6*), two different excavation depths of the lower tunnel ($z_{0,2}$ = 20m and 23m) and finally three different pillar widths (P = piggy-back, 0 and 1D) are modelled, to give a total of 36 analyses carried out in this parametric study.

7.4.2 Analysis results

Figure 7.19 depicts the ratio of the maximum surface settlements due to the effect of surface load over the tunnel diameter (S'_{max}/D) against the relative position of the surface load (W). Two different excavation depths for the lower tunnel are modelled ($z_{0,2}$ = 20m and 23m) and three different pillar widths (P = piggy-back, 0 and 1D). The thin lines refer to the shallow case while the dotted lines refer to the deepest case. The general pattern of these plots indicates that the position of the second tunnel does not significantly affect S'_{max}. Further to this, the maximum values of S'_{max} roughly occur when the surface load is directly applied above the upper tunnel (at *W2*). As the load shifts further away towards *W6* these values decrease regardless of the position of the second tunnel.

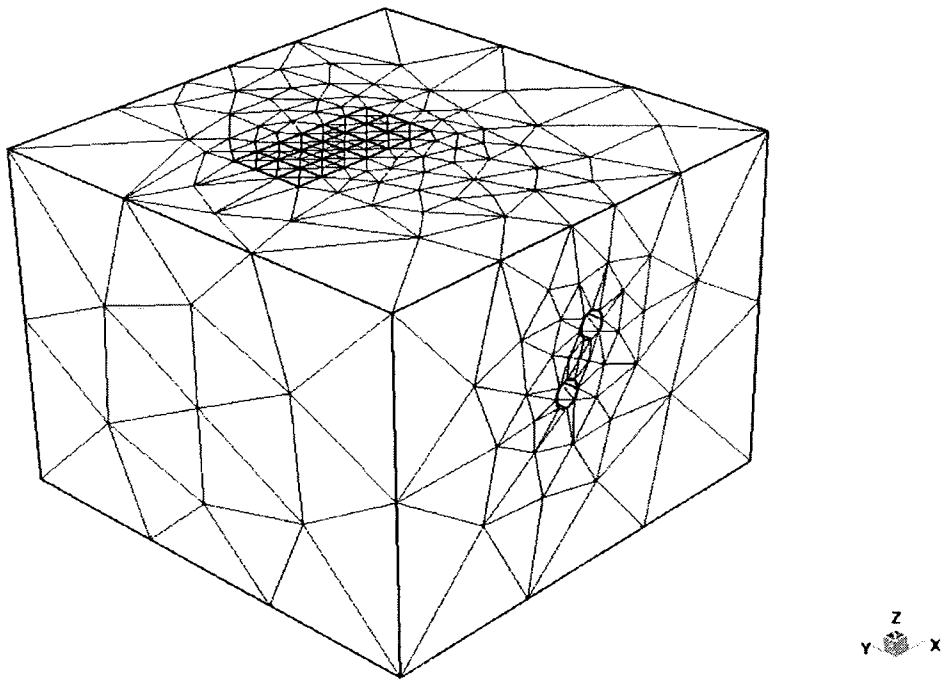

Figure 7.18. Generated mesh for the *TVD* case. The depths to the tunnel axes are $z_{0,1}$ = 15m and $z_{0,2}$ = 23m. The pillar width and pillar depth is P = 1D and P_D = 1D respectively.

Figure 7.20 shows the crown settlements produced solely by the surface load for the upper tunnel expressed as a percentage of the tunnel diameter against the longitudinal direction y. Six different loaded areas are analysed (*W1* to *W6*) while the pillar depth between the two tunnels is $P_D = D/4$ and the pillar width is P = piggy-back. These plots suggest only minor settlements along the longitudinal axis y, regardless of the position of the surface load. There is a line of symmetry for this particular geometric configuration along the vertical tunnel axis. Consequently it is expected that when the surface load is applied at *W1* or *W3* similar predictions should be generated. This is confirmed from this figure.

Figure 7.21 shows both tunnels' maximum crown settlements due to the effect of the load along the longitudinal y-axis expressed as a percentage of the tunnel diameter plotted against the relative position of the surface load (W). Three different pillar widths (P = piggy-back, 0 and 1D) and two different excavation depths of the second tunnel ($z_{0,2}$ = 20m and 23m) are modelled. Thin lines refer to the shallow case while dotted lines refer to the deeper case. The trend of these settlements regarding the

upper tunnel (see Figure 7.21a) indicates that as the pillar width increases so do the magnitudes of the crown settlements, regardless of the position of the lower tunnel. Figure 7.21b shows predictions regarding the lower tunnel. These predictions indicate that for a shallower excavation of the lower tunnel bigger values of crown settlements are produced. It seems that the closer the lower tunnel is driven to the upper the more these two tunnels interact. Hence, for the *TVD* case both the load and the position of the lower tunnel contribute to the interaction mechanism, unlike the *TH* case where only the surface load is a contributory factor. The upper tunnel's crown settlements seem always to be bigger than those predicted for the lower, regardless of the pillar width or depth.

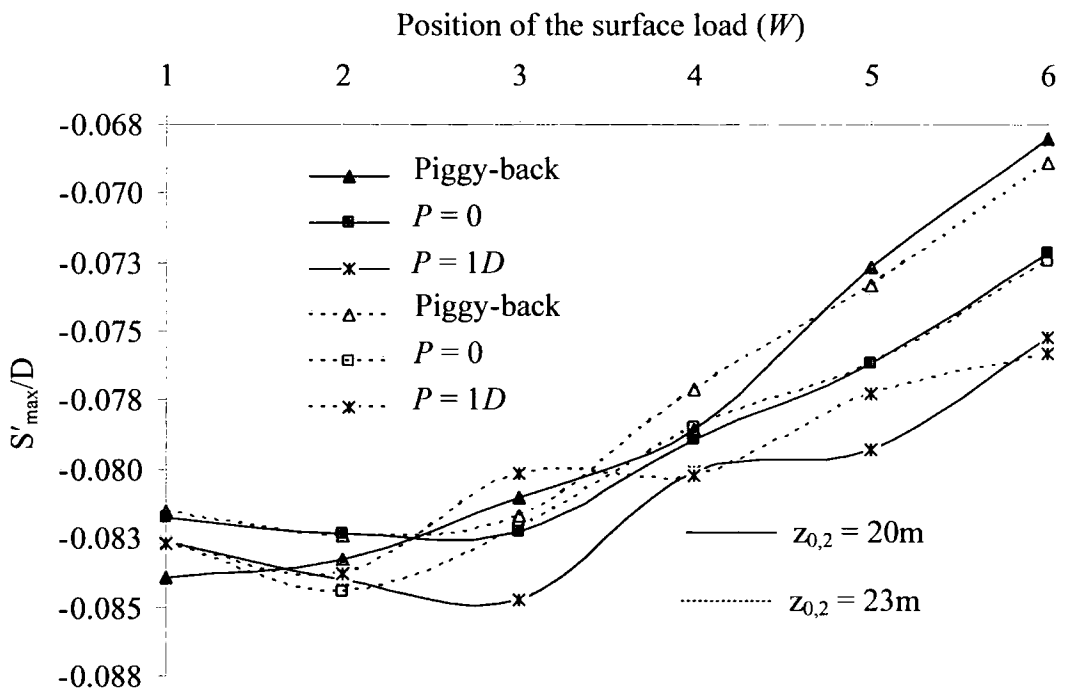

Figure 7.19. Plots of the maximum surface settlements due to surface loading against the position of the load for various excavation depths and pillar widths.

In Figure 7.22 the deformed shapes of both tunnel liners (scaled up) due to the effect of the load at a longitudinal distance of y = 17.5*D*/2 are plotted for two different excavation depths of the lower tunnel. The pillar width is P = piggy-back (i.e. the lower tunnel directly below the upper). The solid line represents the un-deformed shape of the tunnels prior to any loading stage. Once more, similar to the single tunnel case, the only observed movement is translation along both the vertical and the horizontal axes. The upper tunnel deforms in the same way regardless of the position

of the lower tunnel. As for the lower tunnel, slightly bigger deformations are predicted for shallower excavations ($z_{0,2}$ = 20m). These findings are further supported by the predictions presented in Figure 7.21.

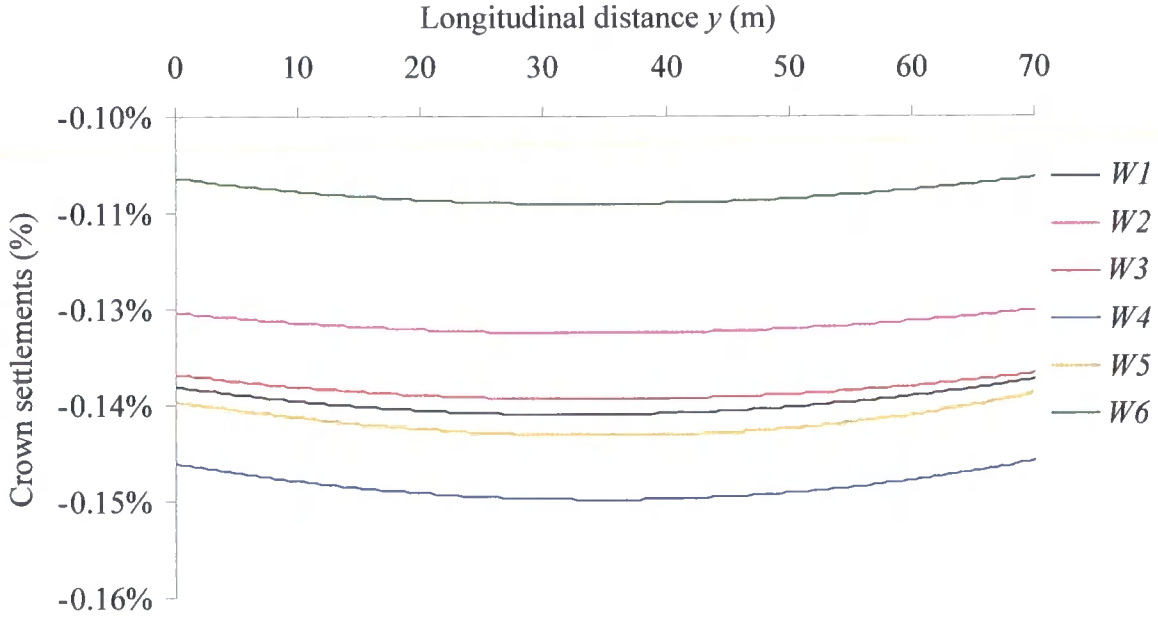

Figure 7.20. Crown settlements expressed as a percentage of the tunnel diameter along the longitudinal axis regarding the upper tunnel, when the lower tunnel is driven at $z_{0,2}$ = 20m and the pillar width is P = piggy-back.

Figure 7.23 shows the interaction between the two tunnels (in the *TVD* cases) and the surface load, compared to the single tunnel case in terms of crown settlements. The upper tunnel's crown settlements are plotted on the vertical axis as a percentage of the single tunnel case against the position of the surface load (*W*). Three different pillar widths are modelled (P = piggy-back, 0 and 1D) when the lower tunnel is driven at $z_{0,2}$ = 20m. The plots indicate a considerable interaction (20%) when the pillar width is P = piggy-back (the lower tunnel lies exactly below the upper). The maximum of the latter plot occurs when the surface load is applied directly above the two tunnels (at *W*2). As the lower tunnel is driven further away from the upper (P = 0 and 1D) less interaction occurs. Especially for the case where P = 1D the predictions show almost no interaction, indicating that the upper tunnel can be considered as a single tunnel case. Interaction decreases in every case, as the load shifts away from the upper tunnel. This outcome is in accordance with the findings presented in Figures 7.21 and 7.22.

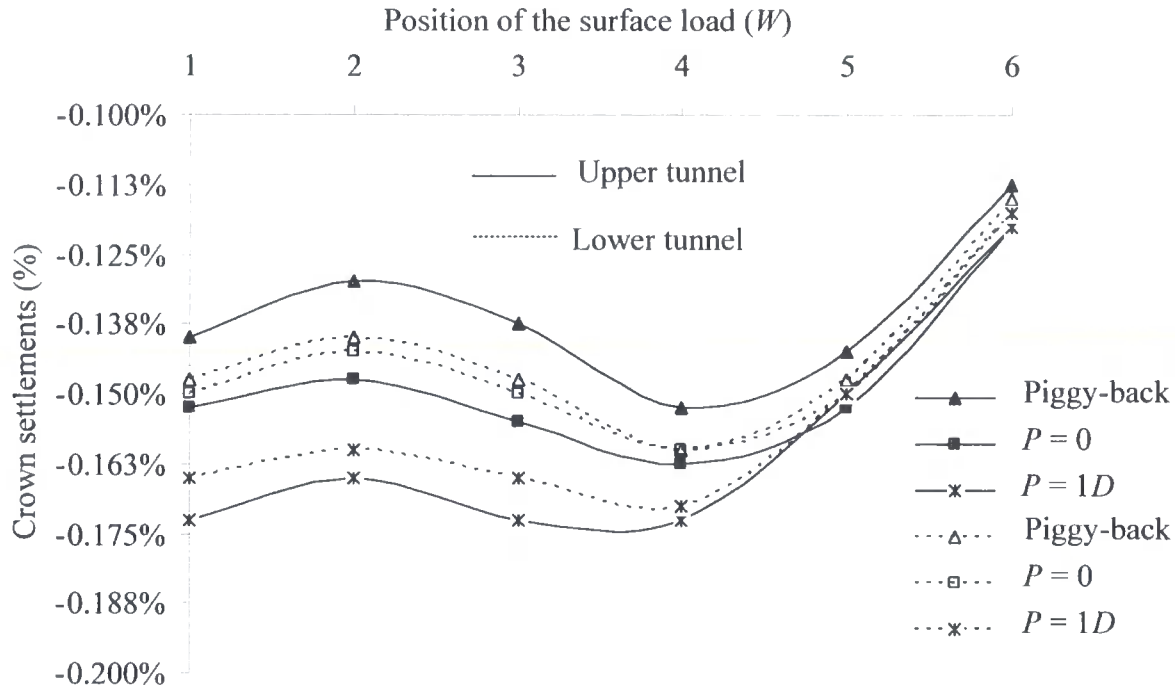

a) Regarding the upper tunnel

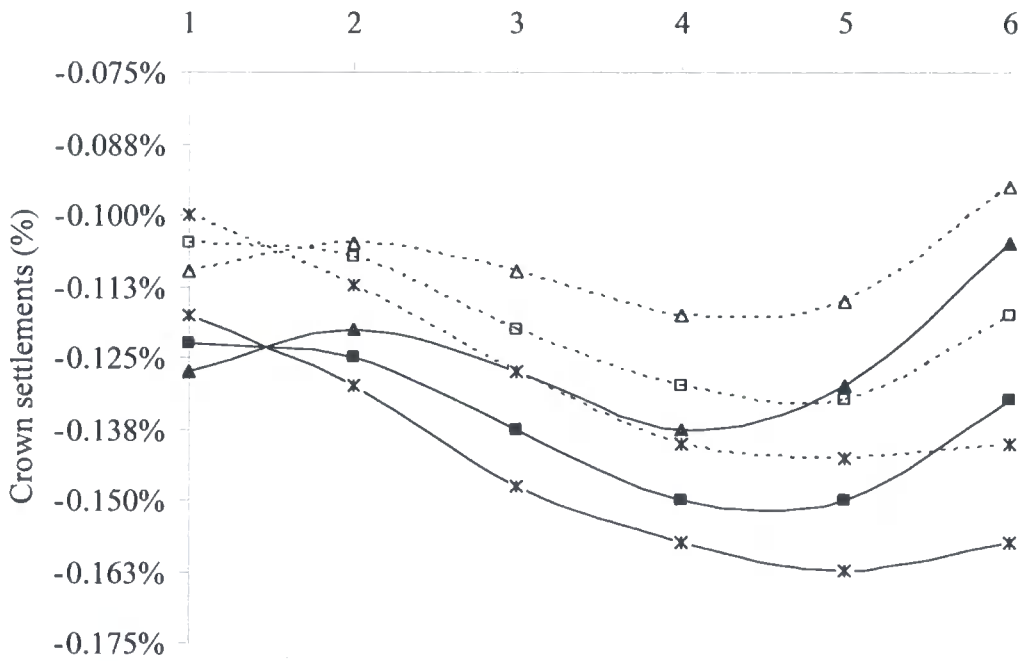

b) Regarding the lower tunnel

Figure 7.21. Maximum crown settlements expressed as a percentage of the tunnel diameter against the position of the surface loaded area for different excavation depths of the lower tunnel.

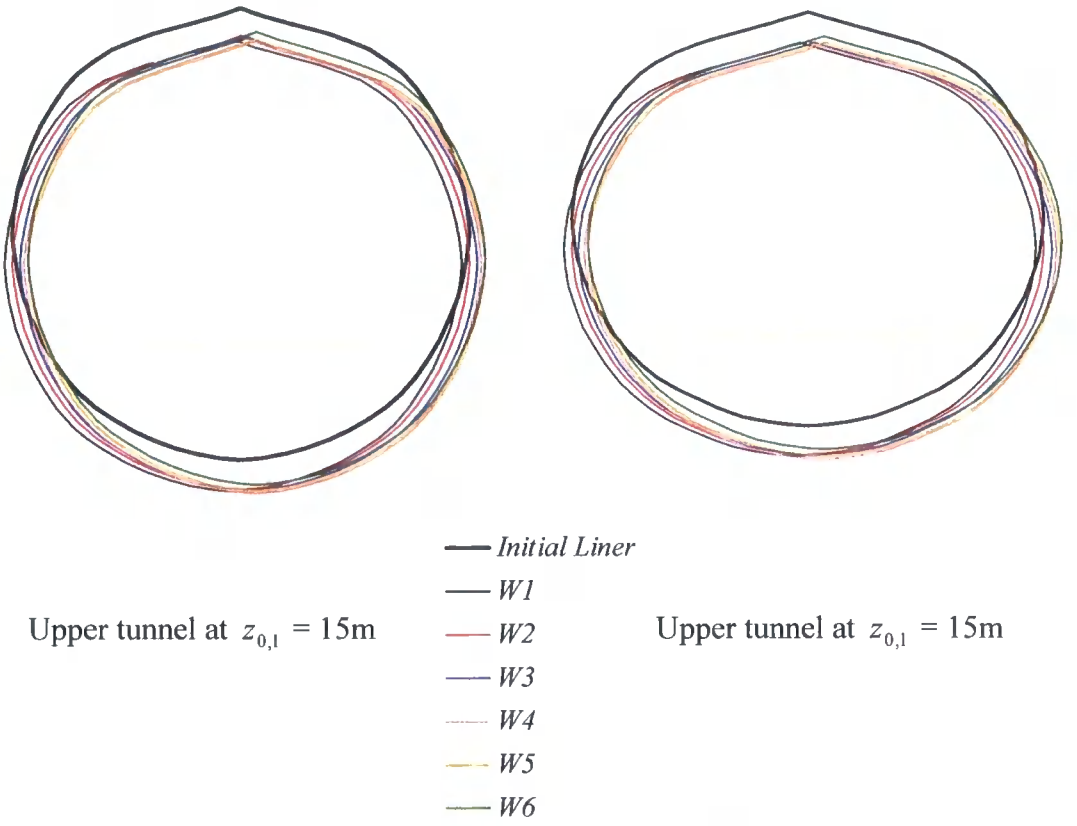

Figure 7.22. Deformed shape of the tunnels due to the surface loading when the second tunnel is driven at $z_{0,2}$ = 20m and 23m while P = piggy-back.

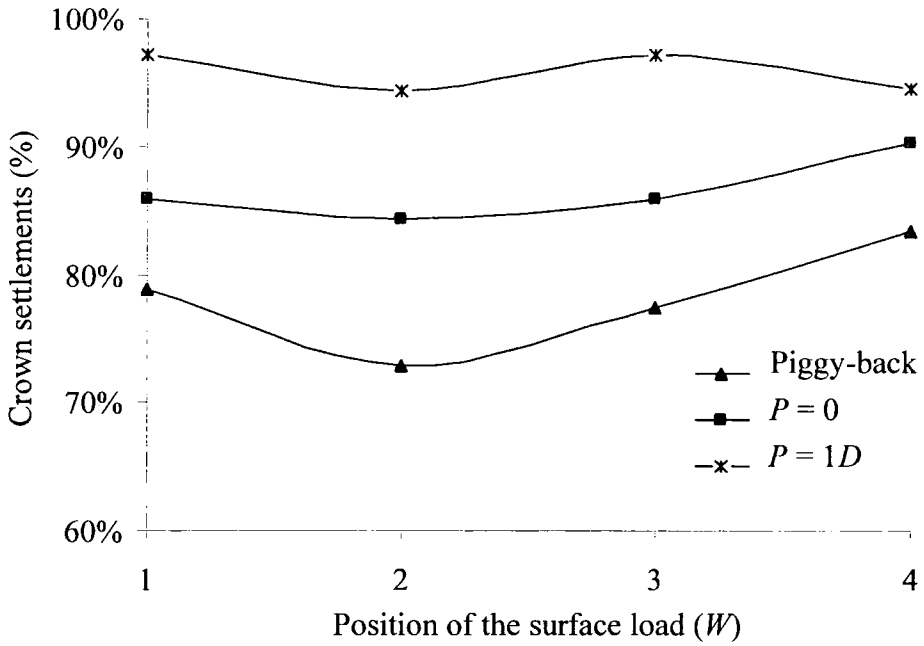

Figure 7.23. Plots of the crown settlements due to loading of the upper tunnel in the *TVD* case as a percentage of the single tunnel predictions for various surface loading areas when $z_{0,1}$ = 15m and $z_{0,2}$ = 20m.

The distribution of the bending moments (in kNm/m) around the tunnel liners just due to the effect of the surface load is plotted in Figure 7.24 for different positions of the surface load (*W*).The depth to the tunnel axis of the lower tunnel varies ($z_{0,2}$ = 20m and 23m), while the pillar width is *P* = piggy-back. The magnitudes of the bending moments always appear to be greater for the upper tunnel. The position of the lower tunnel does not seem significantly to affect the moment distribution in the upper tunnel liner. The positive maximum values of bending moments for the upper tunnel develop at approximately 225° and 45°. The negative maximum values on the other hand occur at 135°. These values are constant regardless of the position of the lower tunnel. The positive maximum values of bending moments for the lower tunnel this time develop between roughly 180° to 225° and between 315° and 0°. The negative maximum values occur between 90° to 135° and at 270°. The range remains the same regardless of the excavation depth. The values of bending moments (regarding the lower tunnel) slightly reduce though for deeper excavations.

Figure 7.25 show the previously mentioned positive maximum (thin lines) and negative maximum (dotted lines) values of the change of bending moments (in kNm/m) due to the surface load for the upper tunnel. Three different pillar widths are

modelled along with two different excavation depths ($z_{0,2}$ = 20m and 23m). These plots are almost parallel to the horizontal axis indicating that the bending moments are only marginally affected from the surface load when this is applied within the region of *W1* to *W5*. Further on (at *W6*) these changes of bending moments start to slightly reduce.

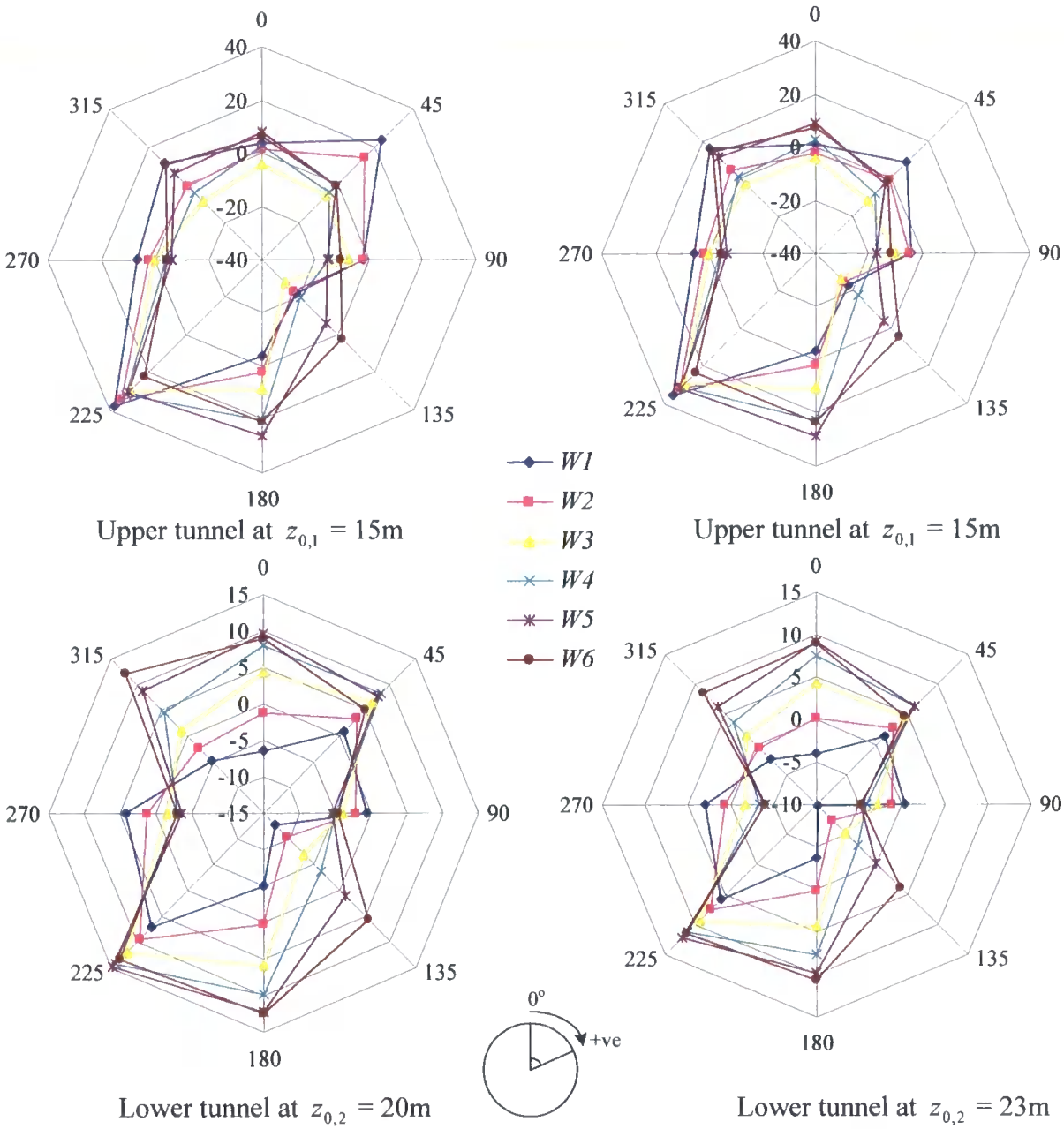

Figure 7.24. Change of bending moments due to the effect of surface loading for different surface loaded areas and different tunnel depths ($z_{0,2}$ = 20m and 23m). The axial axis refers to the distribution of bending moments (kNm/m) around the tunnel, while the circumferential axis refers to the angle around the tunnel.

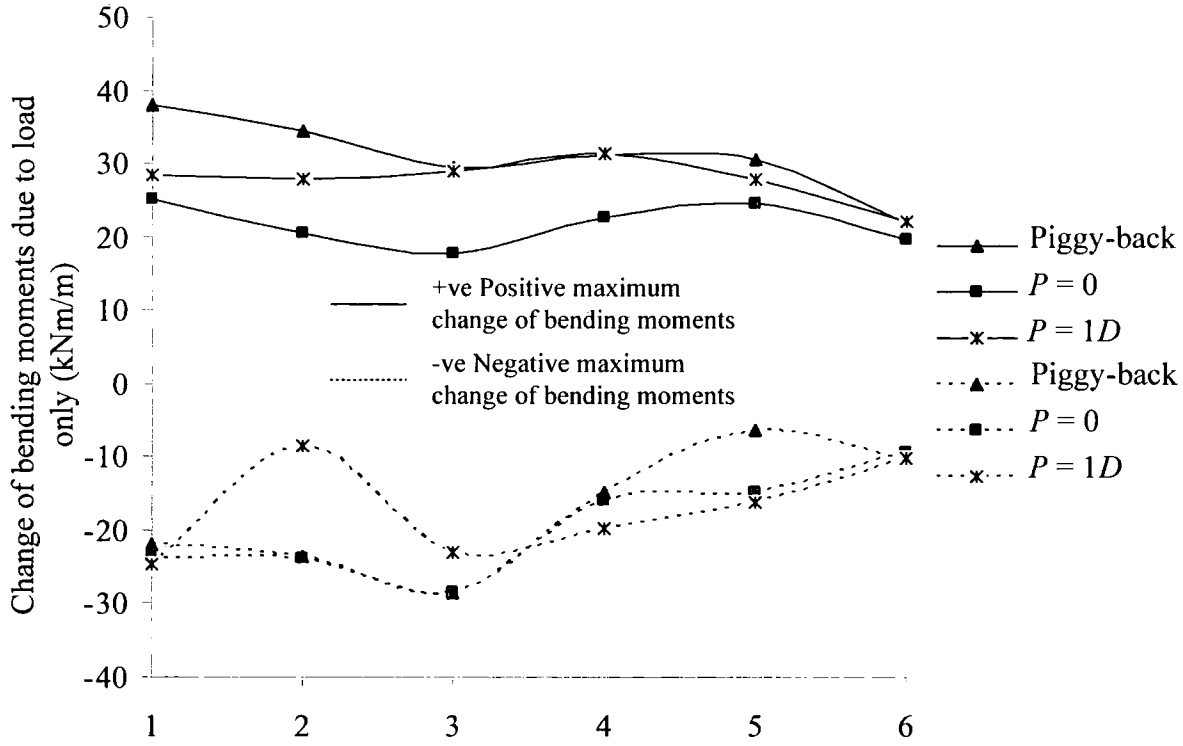

a) For the upper tunnel when $z_{0,2}$ = 20m

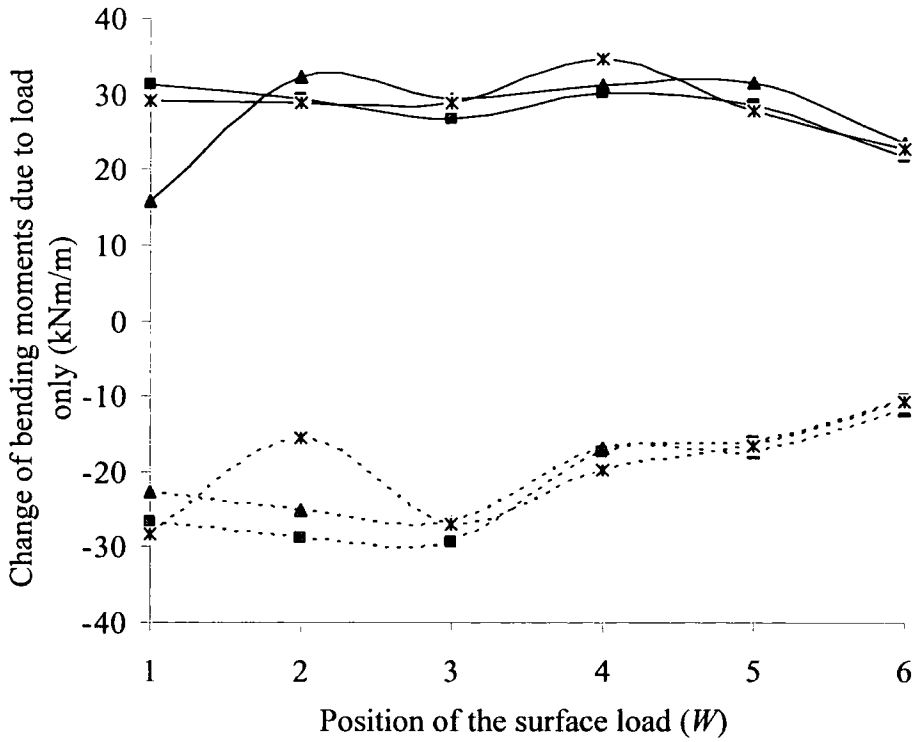

b) For the upper tunnel when $z_{0,2}$ = 23m

Figure 7.25. Maximum and minimum values of bending moments due to the effect of surface loading for different surface loaded areas when the lower tunnel is at $z_{0,2}$ = 20m and 23m.

7.5 Multiple tunnels (case *MHI*)

7.5.1 Introduction

In this section the case of multiple tunnels is analysed where one tunnel is inclined and the other is horizontally aligned (*MHI* case, see Figure 7.1). A parametric study is carried out varying the pillar width (P = 1D and 2D) and the position of the surface loaded area (*W1* to *W6*). A total of 12 analyses thus are performed. The position of the first tunnel (i.e the horizontal) is fixed at $z_{0,1}$ = 15m. The depth to the tunnel axis at the entrance of the second tunnel (i.e. the inclined) is $z_{0,2}$ = 15m, the inclination angle of which is 4° throughout this parametric study. This value is used to try to resemble the angle at which the tunnels dip from the surface to the ground to reach the service depth. The value of this angle usually varies but small values are preferred to ensure for a smooth rather than steep transition. Figure 7.26 shows one of the meshes used for this geometric configuration. The mesh consists of 5,379 ten-noded tetrahedra and 384 six-noded triangles. In terms of nodes the mesh consists of 12,109. The pillar width is P = 1D. The details of the 3-D FE analyses are the same as those presented in Section 7.2.2.

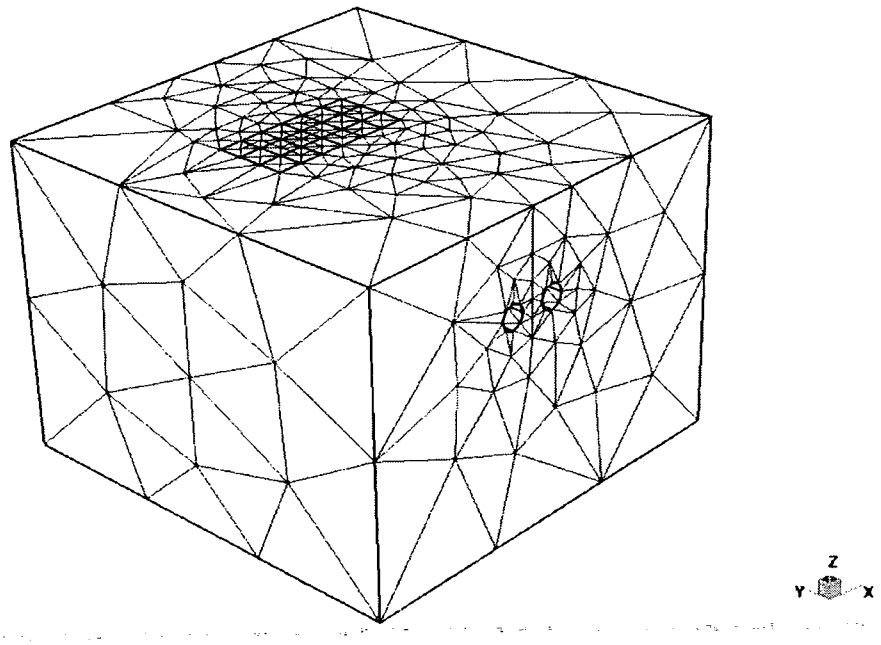

Figure 7.26. Generated mesh for the *MHI* case where the pillar width is P = 1D and the inclination angle of the second tunnel is 4°.

7.5.2 Analysis results

In Figure 7.27 the maximum surface settlements due to the effect of the load over the tunnel diameter (S'_{max}/D) are plotted on the vertical axis against the position of the surface load (W) for two different pillar widths. The thin line refers to the case where $P = 1D$ while the dotted line to the case where $P = 2D$. The maximum values of these plots occur when the surface load is applied at *W2* (directly above the first tunnel) and *W4* (roughly the region above the second tunnel), regardless of the position of the second tunnel. Further to this, the FE predictions indicate that as the load shifts further away from *W2* (towards *W6*), the values of the plot referring to the case where $P = 2D$ are always bigger than those referring to the $P = 1D$ case. This is explained as follows: the larger the clear space between the two tunnels ($P = 2D$) the more space the disturbed due to the surface load soil has to deform. Hence, the deeper the settlement trough and, as a consequence, the larger the predictions of S'_{max}.

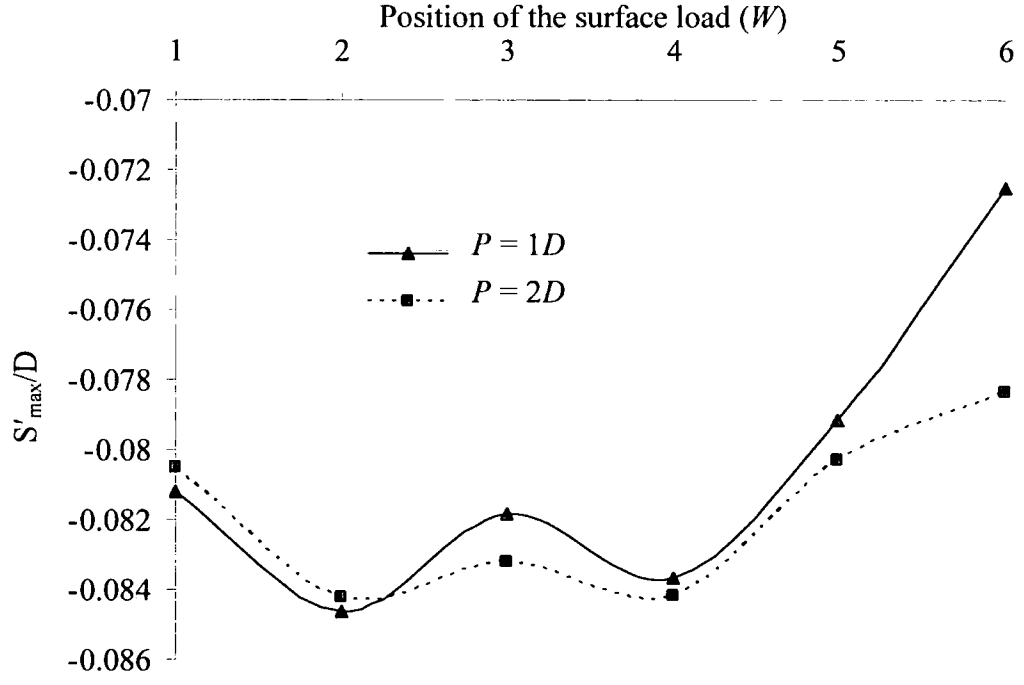

Figure 7.27. Plots of the ratio of the maximum surface settlements due to surface loading over the tunnel diameter against the position of the load for different pillar widths.

Figure 7.28 shows plots of the crown settlements due to the surface load expressed as a percentage of the tunnel diameter along the longitudinal y-axis regarding the horizontal tunnel for different loading positions (W). The pillar width is modelled to be $P = 1D$. In every case the maximum crown settlements approximately occur at a longitudinal distance of $y = 17.5D/2$ (i.e. the area where the load is applied). The difference between the maximum value of crown settlements compared to the minimum value, which occurs at y = 0 and $17.5D$ (i.e entrance and exit of the tunnels), is constant. This figure indicates that when the load is applied at the areas $W1$ and $W3$ (i.e. at a distance of $1D$ from each side of the horizontal tunnel), similar crown settlements occur. As the load shifts further away from the horizontal tunnel towards $W6$, these settlements reduce considerably.

In Figure 7.29 the maximum crown settlements due to the load expressed as a percentage of the tunnel diameter are plotted against the relative position of the surface loaded area (W) for two different pillar widths. Thin lines refer to the horizontal tunnel while dotted lines refer to the inclined tunnel. The trend of these plots for each tunnel is similar regardless of the pillar width. The horizontal tunnel seems to be more affected by the surface load when the latter is applied within the boundaries of $W1$ to $W4$ (crown settlements almost constant within the region of $W1$ to $W4$). As the load shifts further towards $W6$ the interaction between the load and the horizontal tunnel seems to fade, while the plot changes its gradient rapidly.

The deformed shapes of the tunnels (shown as coloured lines) due to the load (scaled up) in a plane normal to the longitudinal y-axis at a distance of $y = 17.5D/2$ are presented in Figure 7.30, for two different pillar widths. The solid line corresponds to the shape of the tunnels prior to any loading stage. Similar patterns of movements are observed to those described in Section 7.3.2. Hence, only vertical along with horizontal translation takes place without any change of the horizontal or the vertical tunnel diameter.

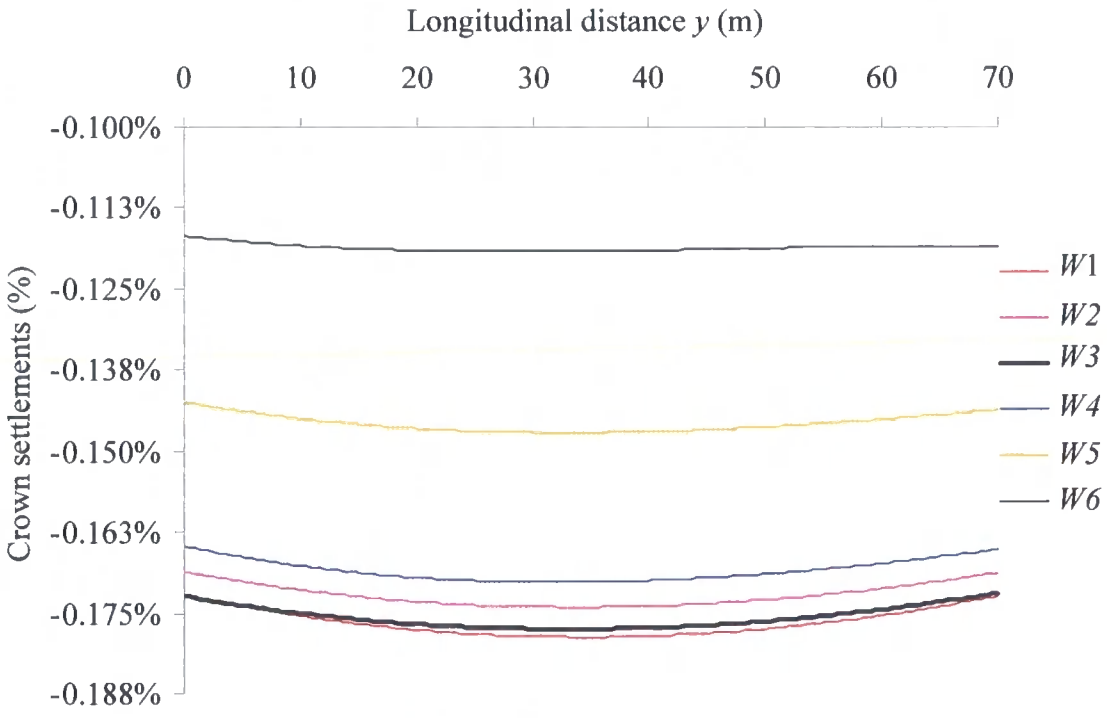

Figure 7.28. Crown settlements expressed as a percentage of the tunnel diameter along the longitudinal *y*-axis regarding the horizontal tunnel, when the pillar width is $P = 1D$.

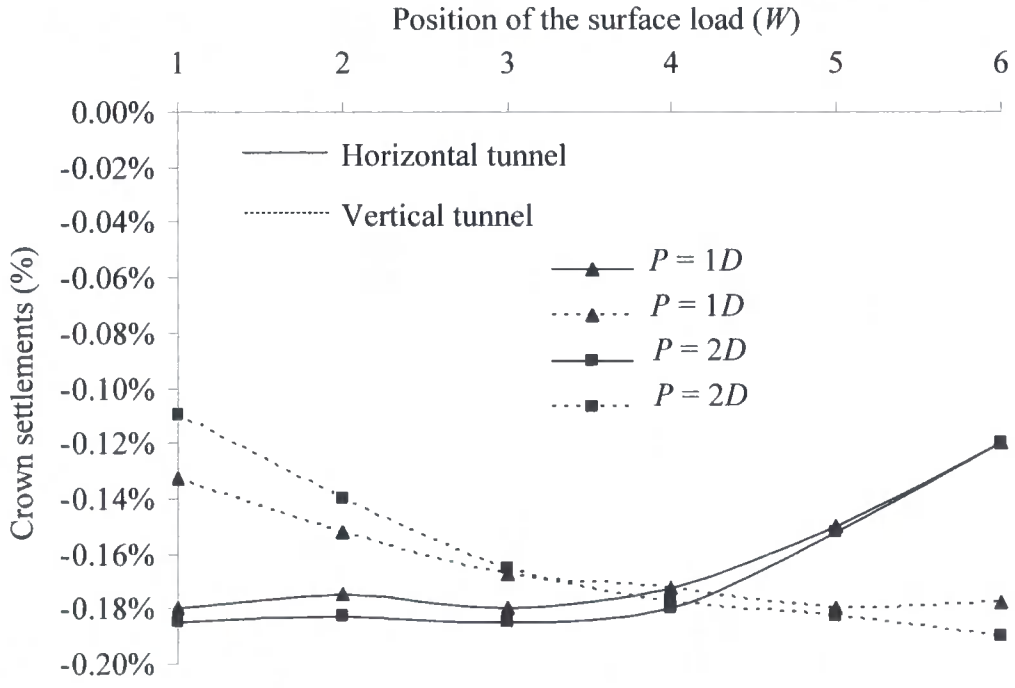

Figure7.29. Both tunnels maximum crown settlements expressed as a percentage of the tunnel diameter regarding the *MHI* case against the relative position of the surface loaded area for two different pillar widths.

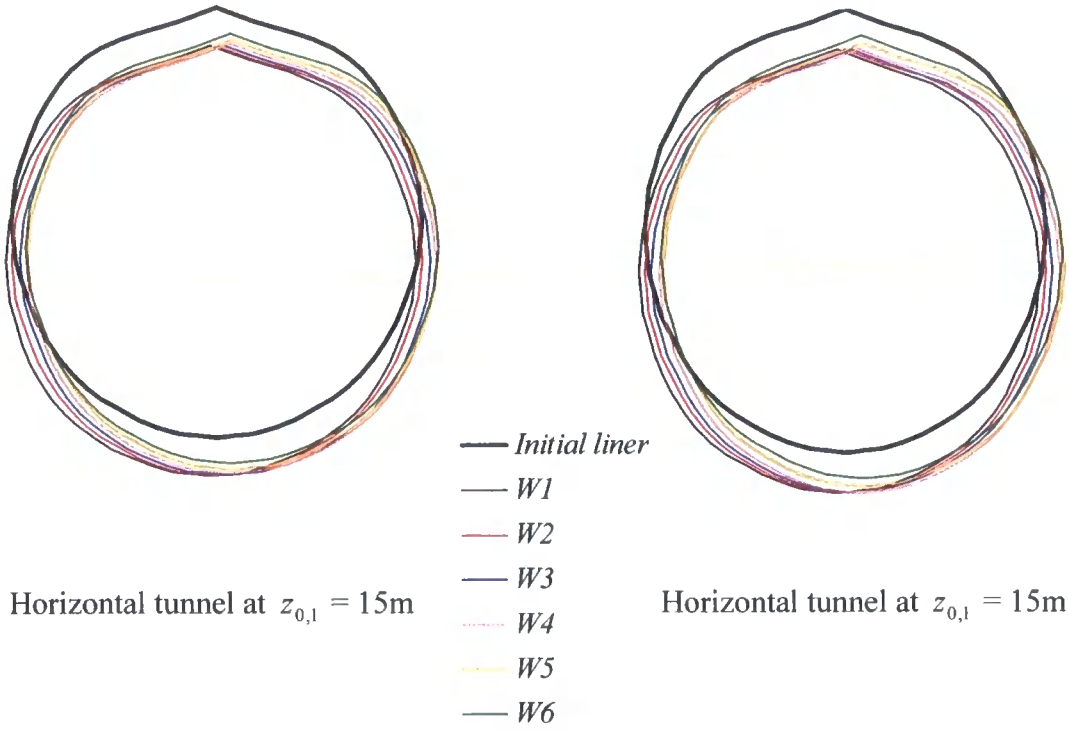

Horizontal tunnel at $z_{0,1} = 15$m

Horizontal tunnel at $z_{0,1} = 15$m

Inclined tunnel when $P = 1D$

Inclined tunnel when $P = 2D$

Figure 7.30. Deformed shape of the tunnels due to the surface loading for different pillar widths.

Figure 7.31 shows the interaction between the two tunnels for the *MHI* case and the surface load compared to the single tunnel case (*ST*). Crown settlement predictions of the first tunnel are plotted on the vertical axis as a percentage of the single tunnel case against the position of the load (*W*). Two different pillar widths are modelled ($P = 1D$ and $2D$). These plots are almost parallel to the horizontal axis when the surface load is applied within the region of *W1* to *W3*. This indicates that there is interaction (2% to 5%) in that area and the contributory factor is the load. Further from that area the gradients of these plots change. This indicates a reduction of the interaction mechanism. By comparing Figures 7.31 and 7.15 (regarding the *TH* case) it seems that they are almost identical. Thus, it can be said that the fact that the second tunnel is inclined in this geometric configuration does not alter the interaction mechanism in any way compared to the *TH* case where the second tunnel is horizontally aligned.

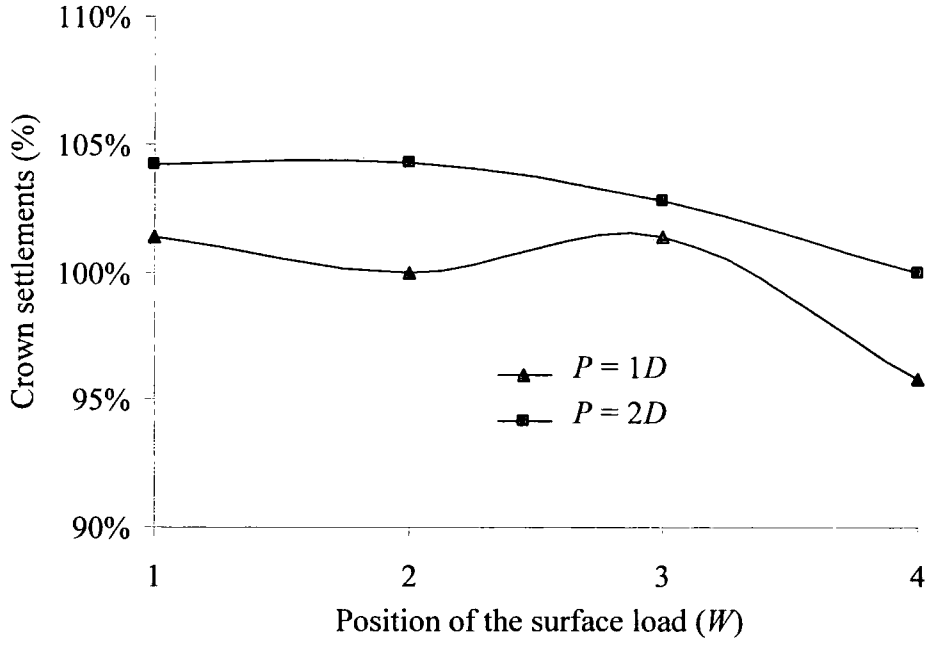

Figure 7.31. Plots of the crown settlements due to loading of the first tunnel in the *MHI* case as a percentage of the single tunnel predictions for various surface loading areas and two different pillar widths.

The distribution of the bending moments (in kNm/m) solely due to the effect of the surface load is presented in Figure 7.32 for both of the tunnels. The values presented in this figure are extracted from a normal to the longitudinal y-axis plane at a distance of $y = 17.5D/2$. The pillar width varies from $P = 1D$ to $2D$. Positive maximum values of bending moments regarding the horizontal tunnel develop between 180° and 225°. The negative maximum values on the other hand seem to appear at 135°. These

maxima correspond to the case where the surface load is applied between *W1* and *W3*. The position of the inclined tunnel only marginally seems to affect the bending moment distribution of the horizontal tunnel. The positive maximum values of bending moments for the inclined tunnel develop at 45° and 225°. The negative maximum values occur at 135°.

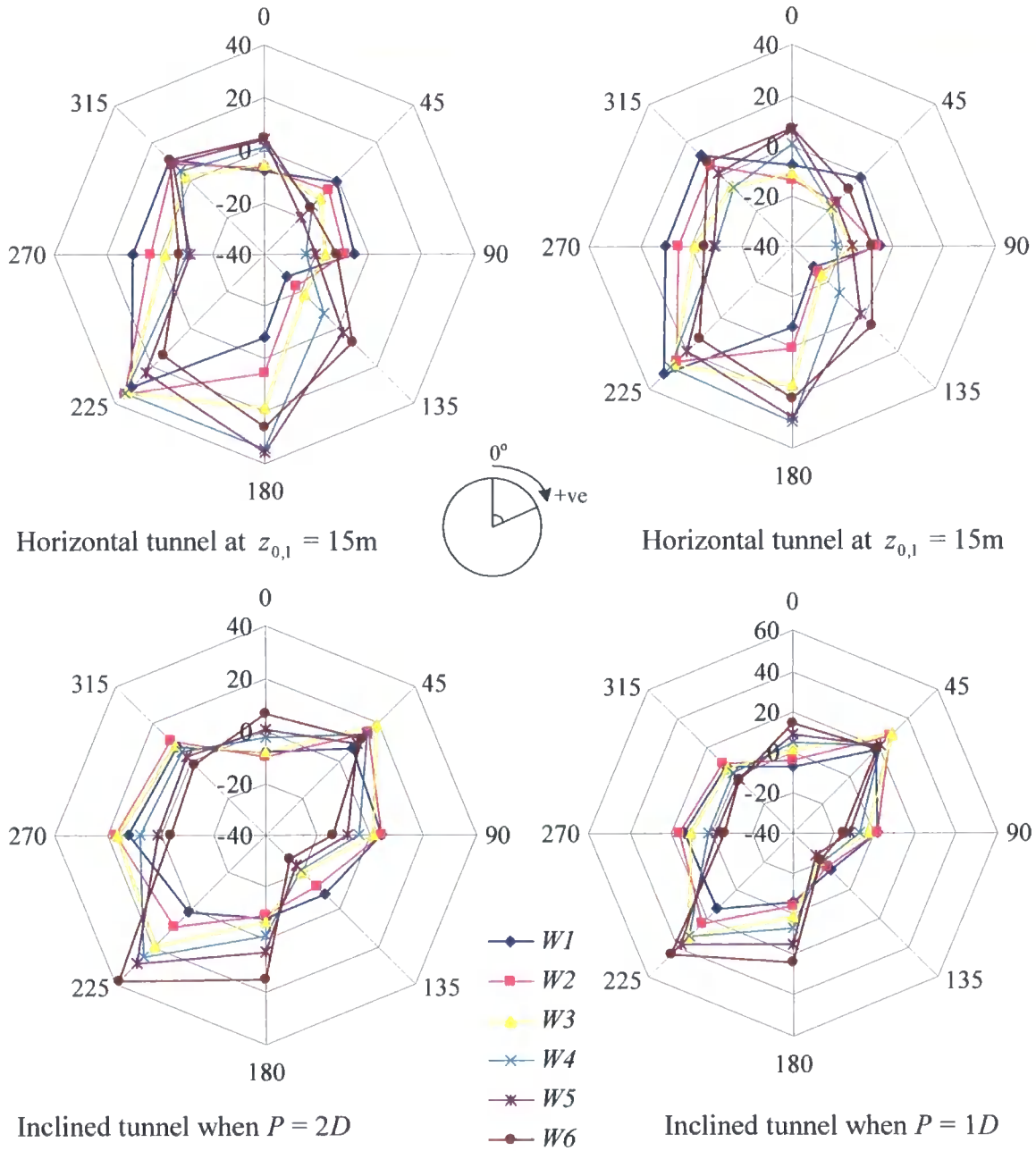

Figure 7.32. Change of bending moments due to the effect of surface loading for different surface loaded areas and different pillar widths (P = 1D and 2D). The axial axis refers to the distribution of bending moments (kNm/m) around the tunnel, while the circumferential axis refers to the angle around the tunnel.

Figure 7.33 shows the horizontal tunnel's positive (thin lines) and negative (dotted lines) maximum values of bending moments (in kNm/mm, on the vertical axis) due to the load on a plane normal to the longitudinal *y*-axis (at the mid-distance) against the relative position of the surface load (*W*). Two different pillar widths are modelled. The trend indicates that as the load shifts away from *W2* towards *W5*, the plotted values of bending moments seem to be constant (roughly parallel to the horizontal axis). At *W6* though the gradient of these plots changes slightly which indicates that interaction seems to reduce.

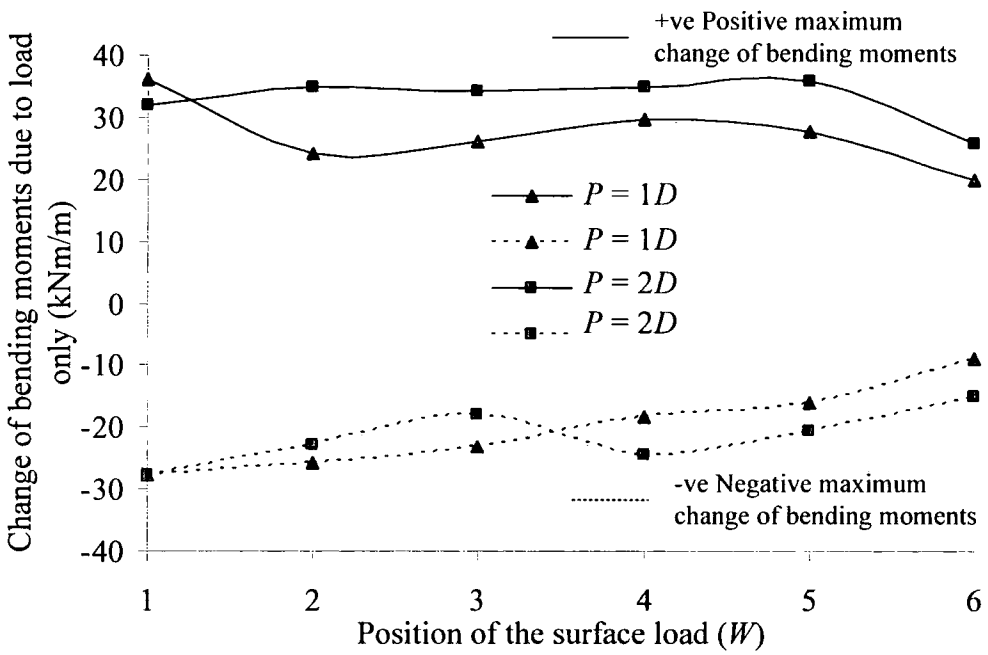

Figure 7.33. Positive and negative maximum values of bending moments due to the effect of surface loading of the horizontal tunnel for different surface loaded areas and different pillar widths.

7.6 Comparison of the *ST* case with the *TH*, *TVD* and *MHI* cases

In this section the 3-D FE predictions regarding the single tunnel case (*ST*) are compared with those regarding the *TH*, the *TVD* and the *MHI* cases. The reason for this comparison is to identify and to better understand the complex interaction mechanism between the two tunnels, the ground and the surface load in three dimensions. The comparison between the above mentioned cases is made in terms of the maximum surface settlements, the maximum crown settlements and the maximum

change of bending moments around the tunnel liner due to the surface load.

For the *TH* case the FE predictions regarding the first tunnel are roughly constant when the surface load is applied within the region of *W1* to *W4* (i.e. within a distance of $P \leq 2D$ from the first tunnel). Further from this area (*W5* and *W6*) these predictions are no longer constant. The first outcome from this comparison is that there is interaction within a region of $P \leq 2D$ from the first tunnel which can be attributed mainly to the surface load. Further from this area interaction seems to decrease. For deeper excavations the FE predictions seem to reduce as well. It appears that the position of the second tunnel within the domain is not such an influencing factor as the surface load for the current geometric configuration. The reason for this second outcome is that the general trend of the plots regarding the above mentioned three parameters is the same in both (*ST* and *TH*) cases.

The 3-D FE predictions regarding the lower tunnel in the *TVD* case confirm the above findings regarding the region where interaction mechanism is evident (*W*1 to *W*4). The maximum crown settlements regarding the *ST* case (Fig. 7.6) are similar to the *TVD* case when the lower tunnel is at $P = 1D$ from the upper (Fig. 7.21). This is an indication that there is almost no interaction between the two tunnels, the ground and the surface load at that distance. As a consequence the upper tunnel can be considered as single (i.e. greenfield conditions) beyond that pillar width ($P \geq 1D$). In this geometric configuration therefore, the interaction mechanism is affected by the surface load, the excavation depth and the position of the lower tunnel, unlike the *TH* case. The upper tunnel is greatly affected in the case where the lower is placed exactly beneath (piggy-back geometry) and at a pillar depth of $P_D = D/4$.

The maximum crown settlements regarding the horizontal tunnel (for the *MHI* case, (Fig. 7.29)) are similar to those predicted for the *ST* case (Fig. 7.6) when the surface load is applied within the region of *W*1 to *W*4. In general, the fact that the second tunnel is inclined, rather than horizontal (as in *TH* case) does not seem to affect considerably the predictions regarding the first tunnel (see Figures 7.15 and 7.31). The interaction mechanism is mainly affected by the surface load rather than the position of the second tunnel, similarly to the *TH* case.

7.7 Comparison between the 2-D and 3-D predictions using Strand7

Tunnelling is clearly a 3-D problem. Hence, 3-D FE analysis should be used rather than 2-D, given that the appropriate computer resources are available. Further to this, many published data are available comparing both 2-D and 3-D FE predictions of settlement with field data indicating that the 3-D predictions are closer to the field values and approximately two to three times smaller than the equivalent 2-D predictions (Dasari *et al.* 1996, Abdel-Meguid *et al.* 2002).

In this section, a comparison between the 2-D and the 3-D FE predictions, which are presented in Chapters 6 and 7 respectively, is performed when using the same commercial software (Strand7). The reason for this comparison is to try and find whether the type of FE analysis carried out (i.e. 2-D or 3-D) alters the predictions, i.e. to try and find whether it is possible to model the complex interaction mechanism between the surface load, the tunnels and the ground by using plane strain approximations.

The general trend of the plots regarding the maximum surface settlements due to the surface load, the distribution of the bending moments around the tunnel liners and the crown settlements due to the load is similar irrespective of the type (2-D or 3-D) of the FE analysis performed. However, the values of the plane strain analysis are always bigger than the equivalent 3-D. This is in agreement with the above mentioned published data. Further to this, the deformed shape of the tunnel liner due to the load along with the distribution of the bending moments reveal that the tunnel squats and rotates when performing 2-D analysis. The predictions regarding the tunnel shape when performing 3-D analysis though reveal a different type of deformation and different distribution of bending moments. This time the tunnel seems to move as a rigid body (no change of the vertical or the horizontal tunnel diameters) since the only kind of movement it undergoes is vertical and horizontal translation. According to Moore and Brachman (1994) the 2-D FE predictions regarding the hoop thrust and the bending moments are more conservative and of the wrong shape compared to the equivalent 3-D predictions. These findings are in agreement with the findings of this chapter.

When the surface load was applied within the region of *W*1 to *W*4 (i.e. $P \leq 2D$) interaction was evident. The same region was predicted in both types of FE analyses (i.e. 2-D and 3-D). In the 2-D FE analysis the surface load along with the excavation depth were the two significant factors for the interaction mechanism regardless of the tunnel geometric configuration. In the 3-D FE analysis these two factors were also identified regarding both the *TH* and the *MHI* cases, while for the *TVD* case the pillar width was a third factor contributing to the interaction. This was the case especially in the piggy-back geometry. However, as pillar width increased, interaction seemed to reduce.

The differences in the predictions between the different types of FE analyses (2-D and 3-D) are attributed to the following reasons:

- Different types of finite elements are used. Two-noded beam elements and six-noded triangles are used to model the tunnel lining and the ground respectively for the 2-D FE analyses, while six-noded thin shell elements and ten-noded tetrahedral elements are used to model the lining and the ground respectively for the 3-D analyses.
- The generated meshes differ in some extent. In particular the 2-D mesh is slightly denser than the equivalent 3-D.
- In the 3-D analysis the surface load is applied on a square patch. The plane strain approximation though indicates that the load is applied on an infinite stripe. Consequently the transfer of the surface load in the ground is greater in the 2-D analysis. Hence the predicted deformations are larger compared to the equivalent 3-D predictions where the ground and the tunnel liner seem to be stiffer.

The outcome from the above mentioned comparison between different types of FE analyses highlights the need to perform three dimensional rather than two dimensional FE analyses for the problem under investigation in this thesis since different predictions are produced for different dimensionality.

The objective of this project was not to compare the FE predictions with field data but to compare and evaluate the different methods themselves (for the reasons described in Sections 1.3 and 2.5.2). Thus a merely theoretical analysis in both Chapters 6 and 7 was performed for acquiring quality rather than quantity measurements.

Chapter 8

Achievements and conclusions

8.1 Introduction

It is the tunnel engineer's responsibility to ensure that the tunnel will be able to withstand any variations from the normal conditions which may put at risk a tunnel's functionality. Such variations may be caused by the complex interaction mechanism of soil-tunnel-structure. The need for this research was initiated from the failure of empirical methods to accurately account for this complex interaction mechanism which is commonly faced in urban areas where adjacent or overlying structures are built in close proximity to already driven tunnels. The aim of this research project was therefore to produce and evaluate tools for numerical modelling of the complex interaction mechanisms involved.

To fulfil this aim a series of objectives were set. The achievements and the conclusions drawn from these objectives are summarised in the following sections of this chapter. Limitations faced throughout this research are also discussed. Finally, recommendations for further research in the future to extend the scope of this project are given.

8.2 Conclusions

8.2.1 Numerical modelling

The first objective of this project was to make an assessment of the feasibility of

undertaking both detailed and accurate 3-D numerical modelling in terms of the available computer resources. It was found that in order to perform 3-D non-linear static analysis, using the commercial FE software Strand7, the optimum size of the problem should consist of less than 30,000 degrees of freedom (d.o.f).

Of the available approaches (e.g. empirical, analytical, physical) only numerical modelling has the ability to model the complex mechanism of soil-tunnel-structure interaction with accuracy. Further to this numerical modelling has the ability to perform parametric studies varying both geometric and material parameters of the domain. 13 2-D FE analyses were performed in Chapter 4 studying the effect of various parameters on the direction of the displacement vectors due to tunnelling under greenfield conditions. 162 2-D FE analyses and 80 3-D FE analyses were performed in Chapters 6 and 7 respectively studying the soil-tunnel-structure interaction mechanism. A better understanding of this mechanism was achieved. Consequently, a total of 255 analyses were carried out during this project. This number would not have been possible to undertake using another method.

8.2.2 Mesh generation using Gmsh

The second objective of this project was to try and reduce the amount of time spent during the pre-processing stage of tunnelling schemes when performing 3-D FE analysis. This main time-consuming activity being the generation of a suitable FE mesh. Discretisation can be broadly divided into structured and unstructured approaches. Many commercial FE packages use the former approach (e.g. Strand7). The shortcomings of using such mesh generators were presented in Chapter 5, the most important of which was meshing time. For complex geometries, in particular, meshing time tended to be prohibitive especially if an extended parametric study was required. It was shown that some time can be saved by re-meshing only a sub-section of the whole domain (e.g. around the tunnel) although care is needed to ensure coincidence of nodes.

Motivated by the need to generate a large number of meshes for a parametric study of tunnelling related problems, and overcome the difficulties produced by structured mesh generators (described above), a scheme based on parameterizing analyses was investigated using the freeware package Gmsh. This is a fully automated 3-D

unstructured tetrahedral mesh generator based on the Delauney triangulation algorithm.

In Chapter 5 a series of tests were performed using Gmsh in order to show the difference in philosophy to the structured approach and to find the optimum density of the generated meshes with respect to both the mesh quality and the time required to perform the FE analyses using Strand7. The outcome from these tests was that for a highly refined mesh the geometry of the domain did not affect the overall mesh quality. For a very coarse mesh, however, mesh quality was vastly affected by the geometry. Thus, as the size of the finite elements increased the overall mesh quality deteriorated while the time for the discretisation decreased. The use of areas of different densities within the same domain became the chosen approach to optimise the overall mesh quality and the amount of time required for the mesh generation. The beneficial impact of local refinement was therefore made obvious.

Then, the evaluation of the meshes used in Chapter 7 for the 3-D FE analyses took place. Limitations were imposed by Strand7 when performing non-linear static analysis regarding the size of the problem and consequently the quality of the mesh. The specific dimensions of the 3-D meshes were chosen to meet these restrictions. Gmsh used a shape measure (the aspect ratio γ) to validate the discretised domains. The overall mesh quality was characterised as "good" using this measure. The presence of a second tunnel within the domain (twin tunnel geometry) seemed to further increase the mesh quality. The reason was that the second tunnel introduced another dense area, similar to that of the first tunnel. However, the required time for the discretisation increased since the total number of the generated finite elements increased as well.

Finally, a code was investigated for generating meshes to model tunnel excavation (tunnel advance in consecutive steps) and lining instalments, even though tunnel excavation 3-D FE analyses were not performed. Gmsh proved to be a very flexible and powerful tool giving the user the opportunity to model not just horizontal tunnels but also inclined and intersecting tunnels.

8.2.3 Comparison of the different methods used

The next objective had to do with the comparison and evaluation of the different softwares used in this project. Two different commercial FE packages (Strand7 and Plaxis) were used to perform 2-D analyses to predict tunnel deformations due to surface loading in soft ground. 3-D analyses for the same problem were then performed to highlight the differences between the different types of analyses (2-D and 3-D). In both cases the dimensions of the domain, the soil and the tunnel lining properties were kept constant (apart from the soil dilation angle). The surface load was directly applied to the surface of the finite elements. No interface elements were used to model the existence of any type of foundations or treatment to the ground prior to loading. The magnitude of the load was also constant. Its magnitude was chosen to resemble the uniform stress of a 10-storey building, assuming a stress of 10 kN/m^2 per storey (BS 8002). This was rather an unrealistic case. However, it was chosen as a worse case scenario of an accidentally concentrated load. Tunnel excavation was not modelled. In both types of analyses performed (i.e. 2-D and 3-D) drained analysis is carried out. This implies that soil might experience elastic volume changes (in contrast to undrained analysis where no volume changes exist). The difference however to an undrained analysis is expected to be small in these studies. Further to this the objective of this project was not to compare the FE predictions with field data but to compare the different methods themselves. Thus a merely theoretical analysis in was performed.

2-D case

For the 2-D case (presented in Chapter 6), the same number of analyses were performed with each software (Strand7 and Plaxis) giving a total of 162 analyses. Parametric studies were carried out varying the depth of the tunnel axis (z_0), the pillar width (P), the pillar depth (P_D) and the position of the surface loaded area (W). Single tunnel analyses were performed first followed by twin tunnel analyses of various tunnel configurations (e.g. twin tunnels horizontally, vertically and diagonally aligned). The aim was to identify how the presence of the second tunnel affects the first tunnel and the minimum pillar width where interaction starts to reduce; i.e. the distance where predictions regarding the first tunnel (twin tunnel case) were similar to

those regarding the single tunnel case.

It was found that the deformed shape of the tunnel solely due to the effect of the surface load is squat (i.e. an increase of the horizontal diameter and decrease of the vertical) and rotation is evident anticlockwise opposing the position of the surface load. Similar predictions regarding the shape of the tunnel due to loading were made by Schroeder (2002). It was also found that the surface load and the excavation depth rather than the position of the second tunnel contributes to the interaction mechanism, regarding both the *TH* (twin tunnels horizontally aligned) and the *TVD* (twin tunnels vertically or diagonally aligned) cases. For the *TVD* case in particular, the presence of the second tunnel contributed to the interaction, particularly so when the lower tunnel lay exactly below the upper (piggy-back case). Finally, the interaction seemed to be constant when the surface load lay within a region of approximately $P \leq 2D$ from the first tunnel. Further from that distance, interaction seemed to reduce. The general trend from both FE packages was similar with small variations regarding the absolute values of the predictions. These variations were attributed to the following three factors:

- The domain problem was discritised differently between the two FE packages.
- Different types of finite elements were used to model the soil. Six-noded triangles and fifteen-noded triangles were used in Strand7 and Plaxis respectively to model the soil.
- Plastic potential function with associated flow was used in Strand7 while a plastic potential function with non-associated flow was used in Plaxis.

3-D case

The 2-D FE predictions produced by Strand7 were then compared with the equivalent 3-D predictions using the same package as presented in Chapter 7. In this way the complex interaction mechanisms of soil-tunnel-structure were modelled and studied in all three dimensions in space. Since the nature of tunnelling is 3-D it was suggested that this was a better way to model the problem under investigation.

The 3-D predictions regarding the deflected shape of the tunnel solely due to the effect of the surface load showed only small vertical translations. The shape of the tunnel did not alter nor did it rotate as was the case from the 2-D predictions. Similar

conclusions with the 2-D case were drawn however regarding the minimum distance where interaction reduces. Nevertheless the magnitudes of the 3-D predictions were smaller. Dasari *et al.*, (1996) and Abdel-Meguid *et al.*, (2002) came up with similar observations. The main reasons for this difference were attributed to the following factors:

- Different types of finite elements were used between the different types of the analyses.
- The 2-D generated mesh was slightly denser compared to the 3-D mesh.
- The surface load was concentrated within a square patch in the 3-D analysis while in the 2-D the approximation made indicated an infinite stripe. In the latter case therefore, the transfer of load in the ground was bigger. As a result more deformations were produced, in contrasts to the 3-D predictions where both the ground and the tunnel liner seemed to be stiffer. This shows that numerical analysis of this problem gives different predictions for different dimensionality and care is required.

8.2.4 On the direction of the deformation vectors

The last objective of this research was to attempt to clarify the ongoing conflict amongst researchers regarding the direction of the deformation vectors due to tunnelling in a greenfield site assuming plane strain conditions. The three main recorder approaches are the following:

- An empirical method presented by O'Reilly and New (1982) who introduced the following equation

$$H_x = \frac{x}{z_0} S_x \tag{8.1}$$

  For the validity of this equation the following assumption had to be made: the net displacement vector should be aligned with the tunnel CL. This assumption was studied in Chapter 4. They also tried to investigate which factors affected the shape of the settlement trough and the point of inflection *i*.
- An empirical method presented by Taylor (1995) who suggested that the net displacement vector is heading towards a point below tunnel invert

- Deanne and Bassett (1994) presented field data from the Heathrow Express Trial Tunnel indicating that the deformation vectors are heading somewhere inside the tunnel between the CL and the invert.

Four parametric studies were performed using Plaxis, varying the excavation depth, the tunnel diameter, the soil stiffness and finally the volume loss to assess which of these factors affected *i*. An isotropic linear elastic pre-yield model was used to model the tunnel liner. A simple elasto-plastic model was used for the soil. The plastic region was modelled using the Mohr-Coulomb failure criterion with non-associated flow. Thirteen analyses were carried out in total. These analyses showed a strong relation between the point of inflection *i* and z_0, E_{inc} and V_L. They failed though to strongly correlate *D* with *i*.

- When z_0 varied the net displacement vector was found to be either above the crown (cases z_0 = 14m and 34m) or between the CL and the invert (z_0 = 20m and 27m).
- When *D* varied the net displacement vector was always heading inside the tunnel but below CL.
- Finally when E_{inc} and V_L varied the angle of the net deformation vector increased with increasing values of E_{inc} and V_L.

The outcome from these 2-D FE analyses was that the direction of the surface deformation vectors depends on the specific soil conditions along with the geometry of the excavation. Therefore, a general rule regarding their direction cannot be extracted contrary to the suggestions of O'Reilly and New (1982) and Taylor (1995).

Another part of the analysis presented in Chapter 4 dealt with the assessment of calculating more accurately the trough width constant *K*. O'Reilly and New (1982) suggested that a value of K = 0.5 would suit most clay profiles. The most accurate way to calculate *K* was through the FE predictions (i.e. K_3). Further to this, for the particular soil profile used, a value of K = 0.6 was found to be closer to the FE predictions (i.e. K_3) rather than the empirical value of K = 0.5. The difference though is marginal.

The limitations from these analyses were that these predictions apply for the particular soil profile. Finally, plane strain approximations were assumed, while tunnelling is a 3-D process (Clough and Leca 1989). All three dimensions therefore have actually to be modelled for a more accurate representation of the real conditions.

8.3 Recommendations for further research

The aim of this research project was to provide tools for numerical modelling of tunnelling interactions, especially to practising engineers, and therefore contribute to the better understanding of the complex mechanism of soil-tunnel-structure interaction. Throughout this study new questions and implications have risen. Consequently recommendations are presented in this section to extend the scope of this research in the future.

- Tunnels, along with their permanent linings, appear in the mesh as if wished in place in the 3-D analyses presented in Chapter 7. Tunnel excavation and the advance of the tunnel face in successive increments were not modelled. Tunnel induced deformations and the change of stress around the tunnels therefore were not studied. Detailed and accurate simulation of the tunnel advance would make the FE predictions more realistic but considerably more time-consuming.

- The surface load, in the FE analyses presented in Chapters 6 and 7, was directly applied to the finite elements. No interface elements were used to model the existence of foundations or treatment to the ground prior to loading. These should be incorporated for a more realistic representation of the field conditions.

- The surface load was always applied perpendicular to the tunnel axis and the surface finite elements. The effects of the same load applied at a skew angle were not studied.

- Given that the required computer resources are available a more detailed and dense mesh can be generated for the analyses presented in Chapter 7.

- In the study presented in Chapter 5 it was possible to model various kinds of tunnelling geometries, mainly parallel or inclined (in one case) with the use of a

powerful mesh generator, Gmsh. However, tunnels passing each other at an angle or even intersecting tunnels were not analysed (meshes for these cases were generated though just for illustrative purposes to present the capabilities of Gmsh). Analyses can be carried out to investigate the effects of surface loading above tunnels intersection.

- Throughout this thesis a simple elasto-plastic constitutive model was used to represent soil behaviour mainly due to the small number of input parameters required and the availability of such constitutive models in both FE packages used (compatibility purpose). More sophisticated and advanced models can be used for a more accurate representation of real soil behaviour.

- Finally a horizontal surface profile was considered throughout this project. A future research could incorporate an inclined surface profile (slope) to study the effects of the extra surface weight on the tunnel and how tunnelling process along with the induced deformations would be affected by that weight.

Bibliography

Abdel-Meguid, M., Rowe, R.K., and Lo, K.Y. (2002) 3D effects of surface construction over existing subway tunnels. *Int. J. Geomech.* 2(4), pp. 447-469.

Addenbrooke, T.I. (1996) *Numerical analysis of tunnelling in stiff clay.* Ph.D. thesis. Imperial College, University of London.

Addenbrooke, T.I. and Potts, D.M. (2001) Twin tunnel interaction: surface and subsurface effects. *Int. J. Geomech.* 1(2), pp. 249-271.

Addenbrooke, T.I., Potts, D.M. and Puzrin, A.M. (1997) The influence of pre-failure soil stiffness on the numerical analysis of tunnel construction. *Géotechnique* 47(3), pp. 693-712.

Akagi, H., and Komiya, K. (1996) Finite element simulation of shield tunnelling processes in soft ground. In: *Geotechnical Aspects of Underground Construction in Soft Ground: proceedings of the International Conference of the TC28 of the ISSMGE, London, 15-17 June 2005.* Mair, R.J., and Taylor, R.N., (eds), Rotterdam: A.A. Balkema. pp. 447-452.

Atkinson, J.H. and Mair, R.J. (1981) Soil mechanics aspects of soft ground tunnelling. *Ground engineering* 14(5), pp. 20-28.

Atkinson, J.H. and Potts, D.M. (1977) Stability of a shallow circular tunnel in cohesionless soil. *Géotechnique* 27(2), pp. 203-215.

Attewell P.B. (1978) Ground movements caused by tunnelling in soil. In: *Procs. Of Conf. on large ground movements and structures, UWIST/July 1977*, pp. 812-948.

Attewell, P.B. and Farmer, I.W. (1974a) Ground disturbance caused by shield tunnelling in a stiff, overconsolidated clay. *Engineering Geology* 8(4), pp.361-381.

Attewell, P.B. and Farmer, I.W. (1974b) Ground deformations resulting from shield tunnelling in London Clay. *Canad. Geotech. J.* 11(3), pp. 380-395.

Attewell, P.B. and Woodman, J.P. (1982) Predicting the dynamics of ground settlement and its derivatives caused by tunnelling in soil. *Ground Engineering* 15(8), pp. 13-22.

Attewell, P.B., Yeates, J. and Selby, A.R. (1986) *Soil movements induced by tunnelling and their effects on pipelines and structures.* Glasgow: Blackie.

Augarde, C.E. (1997) *Numerical modelling of tunnelling processes for assessment of damage to buildings.* D.Phil. thesis. University of Oxford.

Augarde, C.E. and Burd, H.J. (2001) Three-dimensional finite element analysis of lined tunnels. *Int. J. Numer. Anal. Meth. Geomech* 25(3), pp. 243-262.

Augarde, C.E., Burd, H.J. and Houlsby, G.T. (1998) Some experiences of modelling tunnelling in soft ground using three-dimensional finite elements. In: *Application of Numerical Methods to Geotechnical Problems: proc. 4th European Conf. Num. Meth. Geotech. Engng - NUMGE98, Udine, Italy, 14-16 October 1998.*Cividini, A.(ed), Springer: Italy. pp. 603-612.

Augarde, C.E., Burd, H.J. and Houlsby, G.T. (2005) Discussion on: The influence of building weifht on tunnelling-induced ground and building deformation. *Soils and Foundations* 45(4), pp. 166-169.

Augarde, C.E., Lyamin, A.V. and Sloan, S.W. (2003) Stability of an undrained plane strain heading revisited. *Computers and Geotechnics* 30(5), pp. 419-430.

Barakat, M.A. (1996) *Measurements of ground settlement and building deformations due to tunnelling.* Ph.D. thesis. Imperial College, University of London.

Barratt, D.A., O'Reilly, M.P., and Temporal, J. (1994) Long term measurements of loads on tunnel linings in overconsolidated clay. In: *Tunnelling '94: proc. 7th Int. Symp. of Inst. of Mining and Metallurgy and British Tunnelling Society*, London, pp. 469-481.

Barratt, D.A. and Tyler, R.G. (1976) Measurements of ground movement and lining behaviour on the London Underground at Regents Park. In: Transport and Road Research Laboratory Report LR684, UK.

Bartlett, J.V. and Bubbers, B.L. (1970) Surface movements caused by bored tunnelling. *Conference on "subway construction"*, Budapest - Balatonfured. Pp. 513-539.

Bell, R.W., Houlsby, G.T. and Burd, H.J. (1993) Suitability of three-dimensional finite elements for modelling material incompressibility using exact integration. *Commun. Numer. Meth. Engng.* 9(4), pp. 313-329.

Bernat, S., Cambou, B. (1998) Soil-structure interaction in shield tunnelling in soft soil. *Computers and Geotechnics* 22(3), pp. 221-242.

Blom, C.B.M., Horst, E.J. van der and Jovanovic, P.S. (1999) Three dimensional structural analyses of the shield driven "Green-Heart" tunnel of the high speed line south. *Tunnels and Underground Space Technology* 14(2), pp. 217-224.

Bloodworth, A.G. (2002) *Three dimensional analysis of tunnelling effects on structures to develop design methods.* D.Phil. thesis. University of Oxford.

Boon, S.J. (1996) Ground-movement-related building damage. *J. Geotech. Engng.* 122(11), pp. 886-896.

Boscardin, M.D. and Cording, E.J. (1989) Building response to excavation-induced settlement. *J. Geotech. Engng.* 115(1), pp. 1-21.

Bowers, K.H. and Moss, N.A. (2006) Settlement due to tunnelling on the CTRL London Tunnels. In: *Geotechnical Aspects of Underground Construction in Soft Ground: proceedings of the 5th International Conference of the TC28 of the ISSMGE, Amsterdam, 15-17 June 2005.* Bakker, K.J., Bezuijen, A., Broere, W. and Kwast, E.A., (eds), London: Taylor & Francis. pp. 203-209.

Bowers, K.H., and Redgers, J.D. (1996) Discussion: Observations of lining load in a London clay tunnel. In: *Geotechnical Aspects of Underground Construction in Soft Ground: proceedings of the International Conference of the TC28 of the ISSMGE, London, UK, 15-17 April 1996.* Mair, R.J., and Taylor, R.N., (eds), Rotterdam: A.A. Balkema. pp. 335.

Britannica (2007) [online] Available from: http://www.britannica.com/eb/article-72434/tunnels-and-underground-excavations

British Standards Institution (1994) BS 8002: Code of Practise for Earth retaining Structures.

Broms, B.B. and Bennermark, H. (1967) Stability of clay in vertical openings. *J. Soil Mech. and Found. Division ASCE* 193(SM1), pp. 71-94.

Brown, P., and Booker, J. (1985) Finite element analysis of excavation. *Computers and Geotechnics* 1(3), pp. 207-220.

Burd, H.J., Houlsby, G.T., Augarde, C.E. and Liu, G. (2000) Modelling tunnelling-induced settlement of masonry buildings. *Proc. ICE Geotech. Engng* 143(1), pp. 17-29.

Burghignoli, A., Lacarbonara, W., Soccodato, F.M., Vestroni, F. and Viggiani, G. (2006) A study of the response of monumental and historical structures to tunnelling. In: *Geotechnical Aspects of Underground Construction in Soft Ground: proceedings of the 5th International Conference of the TC28 of the ISSMGE, Amsterdam, 15-17 June 2005*, Bakker, K.J., Bezuijen, A., Broere, W. and Kwast, E.A., (eds), London: Taylor & Francis. pp. 487-493.

Burland, J.B. (1989) Ninth Lauritis Bjerrum Memorial Lecture: "Small is beautifull"- the stiffness of soils at small strains. *Can. Geotech. J.* 26(4), pp. 499-516.

Burland, J.B. (2001) Results of the research. In: Burland, J.B., Standing, J.R. and Jardine, F.M. eds., *Building response to tunnelling. Case studies from construction of the Jubilee Line Extension.* London: Thomas Telford, 2001, pp. 315-344.

Butterfield, R. (1999) Dimensional analysis for geotechnical engineers. *Géotechnique* 49(3), pp 357-366.

Calladine, C.R. (1969) *Engineering Plasticity.* Oxford: Pergamon Press.

Clayton, C.R.I., Van Der Berg, J.P. and Thomas, A.H. (2006) Monitoring and displacements at Heathrow Express Terminal 4 station tunnels. *Géotechnique* 56(5), pp. 323-334.

Clough, G.W. and Leca, E. (1989) With focus on the use of finite element methods for soft ground tunnelling. Colloque Int. sur Tunnels et micro-tunnels en terrain Meuble: du chantier a la theorie. Paris, Presses de l'ecole national des pot et chausses.pp. 531-573.

Clough, R.W. (1960) The Finite Element method In Plane Stress Analysis. *Proc. 2nd ASCE Conf. on Electronic Computation, Pittsburg, Pa.*

Cook, R.D. (1982a) *Concepts and Applications Of Finite Element Analysis.* 2nd ed. New York: John Wiley & Sons, Inc.

Cook, R.D. (1995b) *Finite Element Modelling For Stress Analysis.* New York: John Wiley & Sons, Inc.

Cooper, M.L., Chapman, D.N., Rogers, C.D.F. and Chan, H.C. (2002) Movements in the Piccadilly line tunnels due to the Heathrow express construction. *Géotechnique* 52(4), pp. 243-257.

Cording, E.J. and Hansmire, W.H. (1975) Displacements around soft ground tunnels. In: *5th Pan American Conf. on Soil Mech. and Found. Engng. Buenos Aires, 1975*, pp. 571-632.

Courant, R. (1943) Variational methods for solution of problems of equilibrium and vibration. *Bull. Am. Math. Soc.* 49(1), pp. 1-43.

Craig, R.F. (1992) *Soil Mechanics.* 5th ed. London: Chapman&Hall.

Dasari, G.R., Rawlings, C.G., and Bolton, M.D. (1996) Numerical modelling of a NATM tunnel construction in London Clay. In: *Geotechnical Aspects of Underground Construction in Soft Ground: proceedings of the International Conference of the TC28 of the ISSMGE, London, UK, 15-17 April 1996.* Mair, R.J., and Taylor, R.N., (eds), Rotterdam: A.A. Balkema. pp. 491-496.

Davis, E.H., Gunn, M.J. and Seneviratnes, H.N. (1980) The stability of shallow tunnels and underground openings in cohesive materials. *Géotechnique* 30(4), pp. 397-416.

Day, R.A. and Potts, D.M. (1994) Zero thickness interface elements-numerical stability and application. *Int. J. Numer. Anal. Meth. Geomech.* 18(10), pp. 689-708.

Deane, A.P. and Bassett, R.H. (1995) The Heathrow Express Trial Tunnel. *Proc. ICE Geotech. Engng.* 113, pp. 144-156.

Dias, D., Kastner, R., and Maghazi, M. (2000) Three dimensional simulation of slurry shield in tunnelling. In: *Geotechnical Aspects of Underground Construction in Soft Ground: proceedings of the 4th International Conference of the TC28 of the ISSMGE*, Kusakabe, O., Fujita, K. and Miyazaki,Y., (eds), Rotterdam: Balkema. pp. 351-356.

Doležalová, M. (2001) Tunnel complex unloaded by deep excavation. *Computers and Geotechnics* 28(6-7), pp. 469-493.

Duddeck H and Erdmann J. (1982) Structural design models for tunnels. Tunnelling 82, pp 83-91, Proceedings, London.

Egger, P. (2000) Design and construction aspects of deep tunnels (with particular emphasis on strain softening rocks). *Tunnelling and Underground Space Technology* 15(4), pp. 403-408.

Einstein, H.H. and Schwartz, C.W. (1979) Simplified analysis for tunnel supports. *J. Geotech. Engng. division*, 105(4), pp. 499-518.

El-Nahhas, F., El-Kadi, F. and Ahmed, A. (1992) Interaction of tunnel linings and soft ground. *Tunneling and Underground Space Technology* 7(1), pp. 33-43.

Fernando, N.S.M., Small, J.C. and Carter, J.P. (1996) Elastic analysis of buried structures subject to three-dimensional surface loading. *Int. J. Numer. Anal. Meth. Geomech.* 20(5), pp. 331-349.

Field, D.A. (2000) Qualitative measures for initial meshes. *Int. J. Numer. Meth. Engng.* 47(4), pp. 887-906.

Franzius, J.N. (2003) *Behaviour of buildings due to tunnel induced subsidence.* Ph.D. thesis. Imperial College, University of London.

Franzius, J.N., Potts, D.M. and Burland, J.B. (2005) The influence of soil anisotropy and K_0 on ground surface movements resulting from tunnel excavation. *Géotechnique* 55(3), pp. 189-199.

Franzius, J.N., Potts, D.M. and Burland, J.B. (2006) Twist behaviour of building due to tunnel induced ground movement. In: *Geotechnical Aspects of Underground Construction in Soft Ground: proceedings of the 5th International Conference of the TC28 of the ISSMGE, Amsterdam, 15-17 June 2005.* Bakker, K.J., Bezuijen, A., Broere, W. and Kwast, E.A., (eds), London: Taylor & Francis. pp. 107-113.

Frey, P.J. and George, P.L. (2000) *Mesh generation application to finite elements.* Oxford: Hermes Science Publishing.

Frischmann, W.W., Hellings, J.E., Gittoes, G. and Snowden, C. (1994) Protection of the Mansion House against damage caused by ground movements due to Docklands light railway extension. *Proc. Instn. Civ. Engrs. Geotech. Engng.* 107(2), pp. 65-76.

Galli, G., Grimaldi, A. and Leonardi A. (2004) Three-dimansional modelling of tunnel excavation and lining. *Computers and Geotechnics* 31(3), pp. 171-183.

Gens, A., Ledesma, A. and Alonso, E.E. (1996) Estimation of parameters in geotechnical backanalysis-II. Application to a tunnel excavation problem. *Computers and Geotechnics*, 18(1), pp. 29-46.

Ghaboussi, J. and Ranken, R.E (1977) Interaction between two parallel tunnels. *Int. J. Numer. Anal. Meth. Geomech.* 1(1), pp. 75-103.

Glossop, N.H. and O'Reilly, M.P. (1982) Settlement caused by tunnelling through soft marine silty clay. *Tunnels & Tunnelling* 14(9), pp. 13-16.

Gourvenec, S.M., Mair, R.J., Bolton, M.D. and Soga, K. (2005) Ground conditions around an old tunnel in London clay. *Geotech. Engng.* 158(1), pp.25-33.

Gunn, M. (1993) The prediction of surface settlement profiles due to tunnelling. In: *Predictive Soil Mechanics: proceedings of the Wroth Memorial Symposium, Oxford, 27-29 July 1992.* Houlsby, G.T. and Schofield, A.N. (eds), London: Thomas Telford. pp. 304-316.

Geuzaine, C. and Remacle, J.F. (2005) [online] Available from: http://www.geuz.org/gmsh/

Gosz, M.R. (2006) *Finite Element Method. Applications in Solids, Structures and Heat Transfer.* Boca Raton: Taylor and Francis Group.

Hansmire, W.H. (1984) Example analysis for circular tunnel lining. In: *Tunnelling in soil and rock: proceedings of two sessions of GEOTECH '84*, pp. 30-45.

Hellawell, E.E., Hawley, J., Pooley, J., Eskesen, S.D., Garrod, B. and Leggett, M. (2001) Metros under construction around the world. *Proc. ICE Geotech. Engng.* 149(1), pp. 29-39.

Houlsby, G.T., Liu, G. and Augarde, C.E. (2000) A tying scheme for imposing displecament constraints in finite element analysis. *Commun. Numer. Meth. Engng.* 16(10), pp. 721-732.

Huebner, K.H., Thornton, E.A. and Byrom, T.G. (1995) *The Finite Element Method For Engineers.* 3rd ed. New York: John Wiley & Sons, Inc.

Jardine, R.J., Potts, D.M., Foorie, A.B. and Burland, J.B.(1986) Studies of the influence of non-linear stress-strain characteristics in soil-structure interaction. *Géotechnique* 36(3), pp. 377-396.

Jenck, O. and Dias, D. (2006) Tunnelling on urban areas: 3D numerical analysis of soil/structure interaction. In: *Geotechnical Aspects of Underground Construction in Soft Ground: proceedings of the 5th International Conference of the TC28 of the ISSMGE, Amsterdam, 15-17 June 2005.* Bakker, K.J.,

Bezuijen, A., Broere, W. and Kwast, E.A., (eds), London: Taylor & Francis. pp. 535-541.

Karakus, M. and Fowell, R.J. (2003) Effects of different tunnel face advance excavation on the settlement by FEM. *Tunnelling and Underground Space Technology* 18(5), pp. 513-523.

Kettil, P., Ekevid, T. and Wiberg, N. E. (2003) Towards fully mesh adaptive FE-simulations in 3D using multi-grid solver. *Computers and Structures* 81(8-11), pp. 735-746.

Kim, S.H., Burd, H.J. and Milligan, G.W.E. (1998) Model testing of closely spaced tunnels in clay. *Géotechnique* 48(3), pp. 375-388.

Kimura, T. and Mair, R.J. (1981) Centrifugal testing of model tunnels in soft clay. In: *Proc. 10th Conf. Soil Mech. And Found. Engng., Stockholm, 1981,* Vol. 1, Session 2, pp. 319-322.

Koungelis, D.K. and Augarde, C.E. (2004) Interaction between multiple tunnels in soft ground. In: *Developments in Mechanics of Structures and Materials: procs. 18th Australasian Conference on the Mechanics of Structures and Materials, Perth, Australia, December 1-3, 2004.* Deeks, and Hao, (eds), London: Taylor and Francis. Vol.2, pp. 1031-1036.

Lambe, T.W. (1973) Predictions in soil engineering. *Géotechnique* 23(2), pp. 149-202.

Lee, S.W. (2002) The use of compensation grouting in tunnelling: a case study. *Proc. ICE Geotch. Engng* 155(2), pp. 101-109.

Lee, K.M. and Rowe, R.K. (1989) Deformation caused by surface loading and tunnelling: the role of elastic anisotropy. *Géotechnique* 39(1), pp. 125-140.

Lee, K.M. and Rowe, R.K. (1991) An analysis of three-dimensional ground movements: the Thunder Bay tunnel. *Can. Geotech. J.* 28(1), pp. 25-41.

Lee, K.M., Rowe, R.K. and Lo, K.Y. (1992) Subsidence owing to tunnelling. I: Estimating the gap parameter. *Can. Geotech. J.* 29(6), pp. 929-940.

Liu, G.R. (2003) *Mesh free methods.* London: CRC Press.

Loganathan, N. and Poulos, H.G. (1988) Analytical prediction for tunnelling induced ground movements in clay. *J. Geotech.Geoenv. Engng.* 124(9), pp. 846-856.

London's transport museum (2007) [online] Available from: http://www.ltmuseum.co.uk/learning/online_resources/ecobus_omnibus/pg/1851c.htm

Macklin, S.R. (1999) The prediction of volume loss due to tunnelling in overconsolidated clay based on heading geometry and stability number. *Ground Engng.* 32(4), pp. 30-33.

Mair, R.J., Gunn, M.J. and O'Reilly, M.P. (1981) Ground movements around shallow tunnels in soft clay. In: *Procs 10th Int. Conf. Soil Mech. And Found. Eng., Stockholm, June 1981,* Rotterdam: Balkema., Vol. 1, pp. 323-328.

Mair, R.J. and Taylor, R.N. (1993) Prediction of clay behaviour around tunnels using plasticity solutions. In: *Predictive soil mechanics: proc. Wroth Memorial Symposium. 1993.* London: Thomas Telford. pp. 449-463.

Mair, R.J. and Taylor, R.N. (1997) Bored tunnelling in the urban environment. In: *Procs 14th Int. Conf. Soil Mech. And Found. Engng.,* Balkema, *1997*, pp. 2353-2385.

Mair, R.J., Taylor, R.N. and Bracegirdle, A. (1993) Subsurface settlement profiles above tunnels in clay. *Géotechnique* 43(2), pp. 315-320.

Martos, F. (1958) Concerning an approximate equation of the subsidence trough and its time factors. In: *Int. Strata Control Congress, Leipzig, 1958*, pp. 191-205.

McCune, R.W., Armstrong, C.G. and Robinson, D.J. (2000) Mixed-dimensional coupling in finite element models. *Int. J. Num. Meth. Engng.* 49(6), pp. 725-750.

Moore, I.D. (1987a) The elastic stability of shallow buried tubes. *Géotechnique* 37(2), pp. 151-161.

Moore, I.D. (1987b) Response of buried cylinders to surface loads. *J. Geotech. Engng.* 113(7), pp. 758-773.

Moore, I.D., and Brachman, R.W. (1994) Three-dimensional analysis of flexible circular culverts. *J. Geotech. Engng.* 120(10), pp. 1829-1844.

Morgan, H.D. and Bartlett, J.V. (1969) The Victoria Line: tunnel design. *Proc. ICE,* Supplement, Paper 72703, pp. 377-395.

Mroueh, H. and Shahrour, I (1999) Use of sparse iterative methods for the resolution of three-dimensional soil-structure interaction problems. *Int. J. Num. Anal. Meth. Geomech.*, 23(15), pp. 1961-1975.

Mroueh, H. and Shahrour, I (2003) A full 3D finite element analysis of tunnelling-adjacent structures interaction. *Computers and Geotechnics* 30(3), pp. 245-253.

Muir Wood, A.M. (1975) The circular tunnel in elastic ground. *Géotechnique* 25(1), pp. 115-127.

Naylor, D.J. (1999) Filling space with tetrahedral. *Int. J. Numer. Meth. Engng.* 44(10), pp. 1383-1395.

New, B.M. and Bowers, K.H. (1994) Ground movement model validation at the Heathrow express trial tunnel. In: *Tunnelling 94: proc. 7th Int. Symp. of Inst. Of Mining and Metallurgy and British Tunnelling Society, 1994,* pp. 310-329.

New, B.M. and O'Reilly, M.P. (1992) Tunnelling induced ground movements; predicting treir magnitude and effects. In: *Procs. 4th Int. Conf. Ground Movements and Structures, Cardiff July 1991*, Geddes. pp. 671-697.

Nyren, R.J. (1998) *Field measurements above twin tunnels in London Clay.* Ph.D. thesis. Imperial College, University of London.

Oettl, G., Stark, R.F., and Hofstetter, G. (1998) A comparison of elastic-plastic soil models for 2D FE analyses of tunnelling. *Computers and Geotechnics* 23(1-2), pp. 19-38.

Ono, K. and Yamada, M. (1993) Analysis of the arching action in granular mass. *Géotechnique* 43(1), pp. 105-120.

O'Reilly, M.P. and New, B.M. (1982) Settlements above tunnels in the United Kingdom - Their magnitude and prediction. In: *Tunnelling '82 The Institution of Mining and Metallurgy 1982,* pp. 173-181.

O'Rourke, T.D. (1984) Guidelines for tunnel lining design. Published by ASCE, Technical committee on tunnel lining design of the Underground Technology Research Council.

Osman, A.S., Bolton, M.D. and Mair, R.J. (2006) Predicting 2D ground movements around tunnels in undrained clay. *Géotechnique* 56(9), pp. 597-604.

Osman, A.S., Mair, R.J. and Bolton, M.D. (2006) On the kinematics of 2D tunnel collapse in undrained clay. *Géotechnique* 56(9), pp. 585-595.

Panet, M., and Guenot, A. (1982) Analysis of convergence behind the face of a tunnel. In: *Tunnelling '82, The Institution of Mining and Metallurgy, London,* pp. 197-204.

Peck, R.B. (1969) Deep excavations and tunnelling in soft ground. In: *7th Int. Conf. Soil Mech. and Found. Engng, Mexico, 1969*, pp. 225-290.

Peck, R.B. (1984) State of the art: soft-ground tunnelling. In: *Tunnelling in soil and rock: proceedings of two sessions of GEOTECH '84*, pp 1-11.

Pöttler, R. (1992) Technical note on practical applications: Three-dimensional modelling of junctions at the channel tunnel project. *Int. J. Numer. Anal. Meth. Geomech.* 16(9), pp. 683-695.

Potts, D.M. (2003) Numerical analysis: a virtual dream or practical reality? *Géotechnique* 53(6), pp. 535-573.

Potts, D.M., Axelsson, K., Grande, L., Schweiger, H. and Long, M. eds. (2002) *Guidelines for the use of the advanced numerical analysis.* London: Thomas Telford.

Potts, D.M. and Zdravkovic, L. (1999) *Finite element analysis in geotechnical engineering: Theory.* London: Thomas Telford.

Potts, D.M. and Zdravkovic, L. (2001) *Finite element analysis in geotechnical engineering: Application.* London: Thomas Telford.

Puzrin, A.M. and Burland, J.B. (1998) Non linear model of small strain behaviour of soils. *Géotechnique* 48(22), pp. 217-233.

Rankin W.J. (1988) Ground movements resulting from urban tunnelling: predictions and effects. Engineering Geology of Underground Movements, Geological Society Engineering Geology Special Publication No. 5, Bell F.G., Culshaw M.G., Cripps J.C. and Lovell M.A. (eds), London, pp. 79-92.

Rowe, R.K. and Kack, G.J. (1983) A theoretical examination of the settlements induced by tunnelling: four case histories. *Can. Geotech. J.* 20(2), pp. 299-314.

Rowe, R.K. and Lee, K.M. (1992) An evaluation of simplified techniques for estimating three-dimensional undrained ground movements due to tunnelling in soft soils. *Can. Geotech. J.* 29(1), pp. 39-52.

Rowe, R.K., Lo, K.Y. and Kack, G.J. (1983) A method of estimating surface settlement above tunnels constructed in soft ground. *Can. Geotech. J.* 20(1), pp. 11-22.

Sagaseta, C. (1987) Analysis of undrained soil deformation due to ground loss. *Géotechnique* 37(3), pp. 301-320.

Schroeder, F.C. (2002) *The influence of bored piles on existing tunnels.* Ph.D. thesis. Imperial College, University of London.

Schroeder, F.C., Potts, D.M. and Addenbrooke, T.I. (2004) The influence of pile group loading on existing tunnels. *Géotechnique* 54(6), pp. 351-362.

Senechal, M. (1981) Which tetrahedral fill space? *Mathematics magazine* 54(5), pp. 227-243.

Simpson, B., O'Riordan, N.J. and Croft, D.D. (1979) A computer model for the analysis of ground movements in London Clay. *Géotechnique* 29(2), pp. 149-175.

Simpson, B., Atkinson, J.H. and Jovičić, (1996) The influence of anisotropy on calculations of ground settlements above tunnels. In: *Geotechnical Aspects of Underground Construction in Soft Ground: proceedings of the 2nd International Conference of the TC28 of the ISSMGE, London, UK, 15-17 April*

1996. Mair, R.J., and Taylor, R.N., (eds), Rotterdam: A.A. Balkema. pp. 591-594.

Soliman, E., Duddeck, H. and Ahrens, H. (1993) Two and three-dimensional analysis of closely spaced double-tubed tunnels. *Tunnelling and Underground Space Technology.* 18(1), pp. 13-18.

Spasojevic, A.D., Mair, R.J. and Gumbel J.E. (2007) Centrifuge modelling of the effects of soil loading on flexible sewer liners. *Géotechnique* 57(4), pp. 331-341.

Standing, J.R. and Burland, J.B. (2006) Unexpected tunnelling volume losses in the Westminster area, London. *Géotechnique* 56(1), pp. 11-26.

Standing, J.R., Farina, M. and Potts, D.M. (1998) The prediction of tunnelling induced building settlements-A case study. In: *Tunnels and Metropolises: proc. of the World Tunnel Congress '98. Sao Paulo/Brazil,* pp. 1053-1058.

Standing, R.J., Nyren, R.J., Longworth, T.I. and Burland, J.B. (1996) The measurement of ground movements due to tunnelling at two control sites along the Jubilee Line Extension. In: *Geotechnical Aspects of Underground Construction in Soft Ground: proc. of the 2nd International Conference of the TC28 of the ISSMGE, London 15-17 April 1996.* Mair, R.J., and Taylor, R.N., (eds), Rotterdam: A.A. Balkema. pp. 751-756.

Swoboda, G. (1979) Finite element analysis of the New Austrian tunnelling Method (NATM). In: *Proc. 3rd Int. Conf. Num. Meth. Geomech., Aachen,* Vol. 2, pp. 581.

Swoboda, G. and Abu-Krisha, A. (1999) Three dimensional numerical modelling for TBM tunnelling in consolidated clay. *Tunnels and Underground Space Technology* 14(3), pp. 327-334.

Thompson J.F., Soni B.K. and Weatherill N.P. (1999) *Handbook of grid generation.* CRS Press, Boca Raton, USA.

Topping, B.H.V., Muylle, J., Ivanyi, P., Putanowicz, R. and Cheng, B. (2004) *Finite Element Mesh Generation.* Stirling, Scotland: Saxe-Coburg. ISBN 1874672105.

Turner, M., Clough, R., Martin, H. and Topp, L. (1956) Stiffness and deflection analysis of complex structures. *J. Aeronaut. Sci.* 23(9), pp. 805-823.

Vermeer, P.A., Bonnier, P.G. and Moller, S.C. (2002) On a smart use of 3D-FEM in tunnelling. In: *Proc. of the 8th Int. Symp. Num. Models Geomech – NUMOG VIII, Rome, 10-12 April 2002.* Rotterdam: Balkema. pp. 361-366.

Verruijt, A. and Booker, J.R. (1996) Surface settlement due to deformation of a tunnel in an elastic half plane. *Géotechnique* 46(4), pp. 753-756.

Watkins, R.K., and Anderson, L.R. (2000) *Structural mechanics of buried pipes.* Washington D.C: CRC Press LLC.

Ward, W.H. (1969) Discussion on Peck, R.B., Deep excavations and tunnelling in soft ground. In: *Proc, 7th Int. Conf. Soil Mech. And Found. Engng., Mexico,* 1969, Vol. 3, pp. 320-325.

Ward, W.H. and Thomas, H.S.H. (1965) The development of the earth loading and deformation in tunnel linings in London Clay. In: *Proc 6th Int. Conf. Soil Mech. And Found. Engng., Toronto,* Vol. 2, pp. 432-436.

Wongsaroj, J., Soga, K. and Mair, R. J. (2007) Modelling of long-term ground response to tunnelling under St. James's Park, London. *Géotechnique* 57(1), pp. 75-90.

Yamaguchi, I., Yamazaki, I. and Kiritani, Y. (1998) Study of ground-tunnel interactions of four shield tunnels driven in close proximity, in relation to design and construction of parallel shield tunnels. *Tunnelling and Underground Space Technology* 13(3), pp. 289-304.

Yeow, H.C., Wong, C., Pillai, A. and Simpson, B. (2005) The use of a substructure method and three dimensional finite element modelling in assessment of damage due to underground tunnelling. In: *Proceedings of the 11th International conference of the IACMAG, Turin, 19-24 June 2005,* Patron (ed.) Bologna, Vol. 2, pp 711-718.

Yongjie Zhang, Chandrajit Bajaj and Bong-Soo Sohn (2005) 3D finite element meshing from imaging data. *Comp. Meth. Ap. Mech. Engng* 194(48-49), pp. 5083-5106.

Appendix A

Equal size of finite elements

```
/*********************************************************************
 *
 *  Gmsh file esfe.txt
 *
 *  Equal Size of Finite Elements
 *
 *********************************************************************/

D = 4;                  //Tunnel diameter
X = 8*D;                //Dimension of the domain along the x axis
Y = 5*D;                //Dimension of the domain along the y axis
Z = 5*D;                //Dimension of the domain along the z axis
ChL1 = D/5;             //Size of the elements at the boundaries
ChL2 = D/5;             //Size of the elements around the tunnel and at the foundations
x1=X/2;//+X/2-21*D/40;          //Parameter which shifts the tunnel axis horizontally
z1=Z/2;//+Z/2-21*D/40;          //Parameter which shifts the tunnel axis vertically
k1=0;                   //Parameter which shifts the end of the tunnel only along the z axis

// Points at the boundaries of the domain
Point (1) = {0, 0, 0, ChL1};          Point (2) = {X, 0, 0, ChL1};
Point (3) = {X, Y, 0, ChL1};          Point (4) = {0, Y, 0, ChL1};
Point (5) = {0, 0, Z, ChL1};          Point (6) = {X/2-6, 0, Z, ChL2};
Point (7) = {X/2+6, 0, Z, ChL2};      Point (8) = {X, 0, Z, ChL1};
Point (9) = {X, Y, Z, ChL1};          Point (10) = {X/2+6, Y, Z, ChL2};
Point (11) = {X/2-6, Y, Z, ChL2};     Point (12) = {0, Y, Z, ChL1};

//Points at the tunnel entrance
Point (13) = {x1, 0, z1, ChL2};           Point (14) = {x1, 0, z1 + D/2, ChL2};
Point (15) = {x1 - D/2, 0, z1, ChL2};     Point (16) = {x1, 0, z1 - D/2, ChL2};
Point (17) = {x1 + D/2, 0, z1, ChL2};

//Points at the tunnel exit
Point (18) = {x1, Y, z1 + k1, ChL2};          Point (19) = {x1, Y, z1 + D/2 + k1, ChL2};
Point (20) = {x1 - D/2, Y, z1 + k1, ChL2};    Point (21) = {x1, Y, z1 - D/2 + k1, ChL2};
Point (22) = {x1 + D/2, Y, z1 + k1, ChL2};

//Creating the boundaries of the domain
Line (1) = {1, 2};      Line (2) = {2, 3};
Line (3) = {3, 4};      Line (4) = {4, 1};
Line (5) = {5, 6};      Line (6) = {6, 7};
Line (7) = {7, 8};      Line (8) = {8, 9};
Line (9) = {9, 10};     Line (10) = {10, 11};
Line (11) = {11, 12};   Line (12) = {12, 5};
Line (13) = {1, 5};     Line (14) = {2, 8};
Line (15) = {3, 9};     Line (16) = {4, 12};

//Creating the entrance opening
Circle (17) = {14, 13, 15};   Circle (18) = {15, 13, 16};
Circle (19) = {16, 13, 17};   Circle (20) = {17, 13, 14};

//Creating the exit opening
Circle (21) = {19, 18, 20};   Circle (22) = {20, 18, 21};
```

```
Circle (23) = {21, 18, 22};  Circle (24) = {22, 18, 19};

//Connecting the entrance and exit of the tunnel
Line (25) = {14, 19};  Line (26) = {15, 20};
Line (27) = {16, 21};  Line (28) = {17, 22};

//Create the "Surfaces" of the domain
Line Loop (49) = {17, 18, 19, 20}; //Plane Surface (50) = {49};
Line Loop (51) = {21, 22, 23, 24}; //Plane Surface (52) = {51};

Line Loop (57) = {-13, 1, 14, -7, -6, -5}; Plane Surface (58) = {57, 49};
Line Loop (59) = {-14, 2, 15, -8}; Plane Surface (60) = {59};
Line Loop (61) = {-15, 3, 16, -11, -10, -9}; Plane Surface (62) = {61, 51};
Line Loop (63) = {-16, 4, 13, -12}; Plane Surface (64) = {63};
Line Loop (65) = {1, 2, 3, 4}; Plane Surface (66) = {65};
Line Loop (67) = {-11, -10, -9, -8, -7, -6, -5, -12}; Plane Surface (68) = {67};

//Create the "Surfaces" of the tunnel
Line Loop (69) = {17, 26, -21, -25}; Ruled Surface (70) = {69};
Line Loop (71) = {18, 27, -22, -26}; Ruled Surface (72) = {71};
Line Loop (73) = {19, 28, -23, -27}; Ruled Surface (74) = {73};
Line Loop (75) = {20, 25, -24, -28}; Ruled Surface (76) = {75};

//Create the boundaries of the domain
Physical Surface (1) = {58};
Physical Surface (2) = {60};
Physical Surface (3) = {62};
Physical Surface (4) = {64};
Physical Surface (5) = {66};

//Create the boundaries of the tunnel
Physical Surface (6) = {70};
Physical Surface (7) = {72};
Physical Surface (8) = {74};
Physical Surface (9) = {76};

//Create the volume of the domain
Surface Loop (1) = {58, 60, 62, 64, 66, 68, 70, 72, 74, 76};
Volume (1) = {1};
```

Appendix B

Single tunnel geometry

```
/*********************************************************************
 *
 *  Gmsh file stg.txt
 *
 *  Single Tunnel Geometry
 *
 *********************************************************************/

D = 4;          //Tunnel diameter
DD=4;           //Size of the foundations
X = 17.5*D;     //Dimension of the domain along the x axis
Y = 17.5*D;     //Dimension of the domain along the y axis
Z = 12.5*D;     //Dimension of the domain along the z axis
ChL1 = 18;      //Size of the elements at the boundaries
ChL2 = 3;       //Size of the elements around the tunnel
ChL3 = 9;       //Size of the transition elements
ChL4 = 3;       //Size of the elements around at the foundations
x1=X/2;         //Parameter which shifts the tunnel axis horizontally
z1=Z-15;        //Parameter which shifts the tunnel axis vertically
k1=0;           //Parameter which shifts the end of the tunnel only along the z axis

//Points at the tunnel entrance
Point (1) = {x1, 0, z1, ChL2};       Point (2) = {x1, 0, z1+D/2, ChL2};
Point (3) = {x1-D/2, 0, z1, ChL2};   Point (4) = {x1, 0, z1-D/2, ChL2};
Point (5) = {x1+D/2, 0, z1, ChL2};

//Points at the tunnel exit
Point (6) = {x1, Y, z1+k1, ChL2};       Point (7) = {x1, Y, z1+k1+D/2, ChL2};
Point (8) = {x1-D/2, Y, z1+k1, ChL2};   Point (9) = {x1, Y, z1+k1-D/2, ChL2};
Point (10) = {x1+D/2, Y, z1+k1, ChL2};

//Points at the boundaries of the domain
Point (19) = {0, 0, 0, ChL1};        Point (20) = {X, 0, 0, ChL1};
Point (21) = {X, Y, 0, ChL1};        Point (22) = {0, Y, 0, ChL1};
Point (23) = {0, 0, Z, ChL1};        Point (24) = {X/2-D, 0, Z, ChL3};
Point (25) = {X/2+D, 0, Z, ChL3};    Point (26) = {X, 0, Z, ChL1};
Point (27) = {X, Y, Z, ChL1};        Point (28) = {X/2+D, Y, Z, ChL3};
Point (29) = {X/2-D, Y, Z, ChL3};    Point (30) = {0, Y, Z, ChL1};

//Points at the foundations
Point (64) = {X/2-2.5*DD, Y/2-DD/2, Z, ChL4};
Point (65) = {X/2-1.5*DD, Y/2-DD/2, Z, ChL4};
Point (66) = {X/2-0.5*DD, Y/2-DD/2, Z, ChL4};
Point (67) = {X/2+0.5*DD, Y/2-DD/2, Z, ChL4};

Point (72) = {X/2-2.5*DD, Y/2+DD/2, Z, ChL4};
Point (73) = {X/2-1.5*DD, Y/2+DD/2, Z, ChL4};
Point (74) = {X/2-0.5*DD, Y/2+DD/2, Z, ChL4};
Point (75) = {X/2+0.5*DD, Y/2+DD/2, Z, ChL4};

Point (80) = {X/2-2.5*DD, Y/2+1*DD+DD/2, Z, ChL4};
Point (81) = {X/2-1.5*DD, Y/2+1*DD+DD/2, Z, ChL4};
```

```
Point (82) = {X/2-0.5*DD, Y/2+1*DD+DD/2, Z, ChL4};
Point (83) = {X/2+0.5*DD, Y/2+1*DD+DD/2, Z, ChL4};

Point (88) = {X/2-2.5*DD, Y/2+2*DD+DD/2, Z, ChL4};
Point (89) = {X/2-1.5*DD, Y/2+2*DD+DD/2, Z, ChL4};
Point (90) = {X/2-0.5*DD, Y/2+2*DD+DD/2, Z, ChL4};
Point (91) = {X/2+0.5*DD, Y/2+2*DD+DD/2, Z, ChL4};

//Connecting the entrance and exit of the tunnel
Line (1) = {2, 7};   Line (2) = {3, 8};
Line (3) = {4, 9};   Line (4) = {5, 10};

//Creating the entrance opening
Circle (9) = {2, 1, 3};    Circle (10) = {3, 1, 4};
Circle (11) = {4, 1, 5};   Circle (12) = {5, 1, 2};

//Creating the exit opening
Circle (13) = {7, 6, 8};    Circle (14) = {8, 6, 9};
Circle (15) = {9, 6, 10};   Circle (16) = {10, 6, 7};

//Creating the boundaries of the domain
Line (25) = {19, 20};   Line (26) = {20, 21};
Line (27) = {21, 22};   Line (28) = {22, 19};

Line (29) = {23, 24};   Line (30) = {24, 25};
Line (31) = {25, 26};   Line (32) = {26, 27};
Line (33) = {27, 28};   Line (34) = {28, 29};
Line (35) = {29, 30};   Line (36) = {30, 23};

Line (37) = {23, 19};   Line (38) = {26, 20};
Line (39) = {27, 21};   Line (40) = {30, 22};

//Creating the foundations
Line (63) = {64, 65};   Line (64) = {65, 66};
Line (65) = {66, 67};

Line (70) = {72, 73};   Line (71) = {73, 74};
Line (72) = {74, 75};

Line (77) = {80, 81};   Line (78) = {81, 82};
Line (79) = {82, 83};

Line (84) = {88, 89};   Line (85) = {89, 90};
Line (86) = {90, 91};

Line (96) = {88, 80};   Line (97) = {80, 72};
Line (98) = {72, 64};

Line (102) = {89, 81};   Line (103) = {81, 73};
Line (104) = {73, 65};

Line (108) = {90, 82};   Line (109) = {82, 74};
Line (110) = {74, 66};

Line (114) = {91, 83};   Line (115) = {83, 75};
Line (116) = {75, 67};

//Creating loops for the tunnel
Line Loop (1) = {9, 10, 11, 12};    Line Loop (3) = {13, 14, 15, 16};
```

```
Line Loop (5) = {9, 2, -13, -1};    Line Loop (6) = {10, 3, -14, -2};
Line Loop (7) = {11, 4, -15, -3};   Line Loop (8) = {12, 1, -16, -4};

//Creating loops for the boundaries of the domain
Line Loop (13) = {25, 26, 27, 28};   Line Loop (14) = {29, 30, 31, 32, 33, 34, 35, 36};

Line Loop (15) = {37, 25, -38, -31, -30, -29};   Line Loop (16) = {38, 26, -39, -32};
Line Loop (17) = {39, 27, -40, -35, -34, -33};   Line Loop (18) = {40, 28, -37, -36};

//Creating loops for the foundations
Line Loop (41) = {63, -104, -70, 98};
Line Loop (42) = {64, -110, -71, 104};
Line Loop (43) = {65, -116, -72, 110};

Line Loop (48) = {70, -103, -77, 97};
Line Loop (49) = {71, -109, -78, 103};
Line Loop (50) = {72, -115, -79, 109};

Line Loop (55) = {77, -102, -84, 96};
Line Loop (56) = {78, -108, -85, 102};
Line Loop (57) = {79, -114, -86, 108};

Line Loop (61) = {63, 64, 65, -116, -115, -114, -86, -85, -84, 96, 97, 98};

//Creating surfaces for the tunnel
//Plane Surface (1) = {1};   //Plane Surface (2) = {3};
Ruled Surface (3) = {5};    Ruled Surface (4) = {6};
Ruled Surface (5) = {7};    Ruled Surface (6) = {8};

//Creating surfaces for the boundaries of the domain
Plane Surface (13) = {13};        Plane Surface (14) = {14, 61};
Plane Surface (15) = {15, 1};     Plane Surface (16) = {16};
Plane Surface (17) = {17, 3};     Plane Surface (18) = {18};

//Creating surfaces for the foundations
Plane Surface (41) = {41};
Plane Surface (42) = {42};
Plane Surface (43) = {43};

Plane Surface (48) = {48};
Plane Surface (49) = {49};
Plane Surface (50) = {50};

Plane Surface (55) = {55};
Plane Surface (56) = {56};
Plane Surface (57) = {57};

Plane Surface (61) = {61};

//Creating physical surfaces for the tunnel
//Physical Surface (1) = {1};   //Physical Surface (2) = {2};
Physical Surface (3) = {3};     Physical Surface (4) = {4};
Physical Surface (5) = {5};     Physical Surface (6) = {6};

//Creating physical surfaces for the boundaries of the domain
Physical Surface (13) = {13};   Physical Surface (14) = {14};
Physical Surface (15) = {15};   Physical Surface (16) = {16};
Physical Surface (17) = {17};   Physical Surface (18) = {18};

//Creating physical surfaces for the foundations
```

```
Physical Surface (41) = {41};
Physical Surface (42) = {42};
Physical Surface (43) = {43};

Physical Surface (48) = {48};
Physical Surface (49) = {49};
Physical Surface (50) = {50};

Physical Surface (55) = {55};
Physical Surface (56) = {56};
Physical Surface (57) = {57};

Physical Surface (61) = {61};

//Creating the volume of the domain
Surface Loop (1) = {13, 14, 15, 16, 17, 18, 3, 4, 5, 6, 41, 42, 43, 48, 49, 50, 55, 56, 57};
Volume (1) = {1};
Physical Volume (1) = {1};
```

Appendix C

Twin tunnel geometry

```
/*********************************************************************
*
*  Gmsh file ttg.txt
*
*  Twin Tunnel Geometry
*
*********************************************************************/

D = 4;              //Tunnel diameter
DD = 4;             //Size of the foundations
X = 17.5*D;         //Dimension of the domain along the x axis
Y = 17.5*D;         //Dimension of the domain along the y axis
Z = 12.5*D;         //Dimension of the domain along the z axis
ChL1 = 18;          //Size of the elements at the boundaries
ChL2 = 3;           //Size of the elements at the tunnels and the foundations
ChL3 = 9;           //Size of the transition elements
x1 =X/2;            //Parameter which shifts the right tunnel axis horizontally
z1 =Z-15;           //Parameter which shifts the right tunnel axis vertically
k1 = 0;             //Parameter which shifts the end of the right tunnel only along the z axis
f = 2*D;            //Pillar width
x2 =X/2-f;          //Parameter which shifts the left tunnel axis horizontally
z2 = Z-15;          //Parameter which shifts the left tunnel axis vertically
k2 = 0;             //Parameter which shifts the end of the left tunnel only along the z axis

//Points at the right tunnel entrance
Point (1) = {x1, 0, z1, ChL2};        Point (2) = {x1, 0, z1+D/2, ChL2};
Point (3) = {x1-D/2, 0, z1, ChL2};    Point (4) = {x1, 0, z1-D/2, ChL2};
Point (5) = {x1+D/2, 0, z1, ChL2};

//Points at the right tunnel exit
Point (6) = {x1, Y, z1+k1, ChL2};        Point (7) = {x1, Y, z1+D/2+k1, ChL2};
Point (8) = {x1-D/2, Y, z1+k1, ChL2};    Point (9) = {x1, Y, z1-D/2+k1, ChL2};
Point (10) = {x1+D/2, Y, z1+k1, ChL2};

//Points at the boundaries of the domain
Point (19) = {0, 0, 0, ChL1};          Point (20) = {X, 0, 0, ChL1};
Point (21) = {X, Y, 0, ChL1};          Point (22) = {0, Y, 0, ChL1};
Point (23) = {0, 0, Z, ChL1};          Point (24) = {X/2-D, 0, Z, ChL3};
Point (25) = {X/2+D, 0, Z, ChL3};      Point (26) = {X, 0, Z, ChL1};
Point (27) = {X, Y, Z, ChL1};          Point (28) = {X/2+D, Y, Z, ChL3};
Point (29) = {X/2-D, Y, Z, ChL3};      Point (30) = {0, Y, Z, ChL1};

//Points at the left tunnel entrance
Point (31) = {x2-f, 0, z2+k2, ChL2};
Point (32) = {x2-f, 0, z2+k2+D/2, ChL2};
Point (33) = {x2-D/2-f, 0, z2+k2, ChL2};
Point (34) = {x2-f, 0, z2+k2-D/2, ChL2};
Point (35) = {x2+D/2-f, 0, z2+k2, ChL2};

//Points at the left tunnel exit
Point (36) = {x2-f, Y, z2+k2, ChL2};
Point (37) = {x2-f, Y, z2+k2+D/2, ChL2};
```

```
Point (38) = {x2-D/2-f, Y, z2+k2, ChL2};
Point (39) = {x2-f, Y, z2+k2-D/2, ChL2};
Point (40) = {x2+D/2-f, Y, z2+k2, ChL2};

//Points at the foundations
Point (62) = {X/2-4.5*DD, Y/2-DD/2, Z, ChL4};
Point (63) = {X/2-3.5*DD, Y/2-DD/2, Z, ChL4};
Point (64) = {X/2-2.5*DD, Y/2-DD/2, Z, ChL4};
Point (65) = {X/2-1.5*DD, Y/2-DD/2, Z, ChL4};
Point (66) = {X/2-0.5*DD, Y/2-DD/2, Z, ChL4};
Point (67) = {X/2+0.5*DD, Y/2-DD/2, Z, ChL4};
Point (68) = {X/2+1.5*DD, Y/2-DD/2, Z, ChL4};

Point (70) = {X/2-4.5*DD, Y/2+DD/2, Z, ChL4};
Point (71) = {X/2-3.5*DD, Y/2+DD/2, Z, ChL4};
Point (72) = {X/2-2.5*DD, Y/2+DD/2, Z, ChL4};
Point (73) = {X/2-1.5*DD, Y/2+DD/2, Z, ChL4};
Point (74) = {X/2-0.5*DD, Y/2+DD/2, Z, ChL4};
Point (75) = {X/2+0.5*DD, Y/2+DD/2, Z, ChL4};
Point (76) = {X/2+1.5*DD, Y/2+DD/2, Z, ChL4};

Point (78) = {X/2-4.5*DD, Y/2+1*DD+DD/2, Z, ChL4};
Point (79) = {X/2-3.5*DD, Y/2+1*DD+DD/2, Z, ChL4};
Point (80) = {X/2-2.5*DD, Y/2+1*DD+DD/2, Z, ChL4};
Point (81) = {X/2-1.5*DD, Y/2+1*DD+DD/2, Z, ChL4};
Point (82) = {X/2-0.5*DD, Y/2+1*DD+DD/2, Z, ChL4};
Point (83) = {X/2+0.5*DD, Y/2+1*DD+DD/2, Z, ChL4};
Point (84) = {X/2+1.5*DD, Y/2+1*DD+DD/2, Z, ChL4};

Point (86) = {X/2-4.5*DD, Y/2+2*DD+DD/2, Z, ChL4};
Point (87) = {X/2-3.5*DD, Y/2+2*DD+DD/2, Z, ChL4};
Point (88) = {X/2-2.5*DD, Y/2+2*DD+DD/2, Z, ChL4};
Point (89) = {X/2-1.5*DD, Y/2+2*DD+DD/2, Z, ChL4};
Point (90) = {X/2-0.5*DD, Y/2+2*DD+DD/2, Z, ChL4};
Point (91) = {X/2+0.5*DD, Y/2+2*DD+DD/2, Z, ChL4};
Point (92) = {X/2+1.5*DD, Y/2+2*DD+DD/2, Z, ChL4};

//Connecting the entrance and exit of the right tunnel
Line (1) = {2, 7};    Line (2) = {3, 8};
Line (3) = {4, 9};    Line (4) = {5, 10};

//Creating the entrance opening of the right tunnel
Circle (9) = {2, 1, 3};     Circle (10) = {3, 1, 4};
Circle (11) = {4, 1, 5};    Circle (12) = {5, 1, 2};

//Creating the exit opening of the right tunnel
Circle (13) = {7, 6, 8};     Circle (14) = {8, 6, 9};
Circle (15) = {9, 6, 10};    Circle (16) = {10, 6, 7};

//Creating the boundaries of the domain
Line (25) = {19, 20};    Line (26) = {20, 21};
Line (27) = {21, 22};    Line (28) = {22, 19};

Line (29) = {23, 24};    Line (30) = {24, 25};
Line (31) = {25, 26};    Line (32) = {26, 27};
Line (33) = {27, 28};    Line (34) = {28, 29};
Line (35) = {29, 30};    Line (36) = {30, 23};

Line (37) = {23, 19};    Line (38) = {26, 20};
Line (39) = {27, 21};    Line (40) = {30, 22};
```

```
//Creating the entrance opening of the left tunnel
Circle (41) = {32, 31, 33};  Circle (42) = {33, 31, 34};
Circle (43) = {34, 31, 35};  Circle (44) = {35, 31, 32};

//Creating the exit opening of the left tunnel
Circle (45) = {37, 36, 38};  Circle (46) = {38, 36, 39};
Circle (47) = {39, 36, 40};  Circle (48) = {40, 36, 37};

//Connecting the entrance and exit of the right tunnel
Line (49) = {32, 37};  Line (50) = {33, 38};
Line (51) = {34, 39};  Line (52) = {35, 40};

//Creating the foundations
Line (61) = {62, 63};  Line (62) = {63, 64};
Line (63) = {64, 65};  Line (64) = {65, 66};
Line (65) = {66, 67};  Line (66) = {67, 68};

Line (68) = {70, 71};  Line (69) = {71, 72};
Line (70) = {72, 73};  Line (71) = {73, 74};
Line (72) = {74, 75};  Line (73) = {75, 76};

Line (75) = {78, 79};  Line (76) = {79, 80};
Line (77) = {80, 81};  Line (78) = {81, 82};
Line (79) = {82, 83};  Line (80) = {83, 84};

Line (82) = {86, 87};  Line (83) = {87, 88};
Line (84) = {88, 89};  Line (85) = {89, 90};
Line (86) = {90, 91};  Line (87) = {91, 92};

Line (96) = {88, 80};  Line (97) = {80, 72};
Line (98) = {72, 64};

Line (102) = {89, 81};  Line (103) = {81, 73};
Line (104) = {73, 65};

Line (108) = {90, 82};  Line (109) = {82, 74};
Line (110) = {74, 66};

Line (114) = {91, 83};  Line (115) = {83, 75};
Line (116) = {75, 67};

Line (120) = {92, 84};  Line (121) = {84, 76};
Line (122) = {76, 68};

Line (126) = {87, 79};  Line (127) = {79, 71};
Line (128) = {71, 63};

Line (129) = {86, 78};  Line (130) = {78, 70};
Line (131) = {70, 62};

//Creating loops for the right tunnel
Line Loop (1) = {9, 10, 11, 12};  Line Loop (3) = {13, 14, 15, 16};

Line Loop (5) = {9, 2, -13, -1};  Line Loop (6) = {10, 3, -14, -2};
Line Loop (7) = {11, 4, -15, -3};  Line Loop (8) = {12, 1, -16, -4};

//Creating loops for the boundaries of the domain
Line Loop (13) = {25, 26, 27, 28};  Line Loop (14) = {29, 30, 31, 32, 33, 34, 35, 36};
```

```
Line Loop (15) = {37, 25, -38, -31, -30, -29};   Line Loop (16) = {38, 26, -39, -32};
Line Loop (17) = {39, 27, -40, -35, -34, -33};   Line Loop (18) = {40, 28, -37, -36};

//Creating loops for the left tunnel
Line Loop (19) = {41, 42, 43, 44};   Line Loop (20) = {45, 46, 47, 48};

Line Loop (21) = {41, 50, -45, -49};   Line Loop (22) = {42, 51, -46, -50};
Line Loop (23) = {43, 52, -47, -51};   Line Loop (24) = {44, 49, -48, -52};

//Creating loops for the foundations
Line Loop (40) = {62, -98, -69, 128};    Line Loop (41) = {63, -104, -70, 98};
Line Loop (42) = {64, -110, -71, 104};   Line Loop (43) = {65, -116, -72, 110};
Line Loop (44) = {66, -122, -73, 116};

Line Loop (47) = {69, -97, -76, 127};    Line Loop (48) = {70, -103, -77, 97};
Line Loop (49) = {71, -109, -78, 103};   Line Loop (50) = {72, -115, -79, 109};
Line Loop (51) = {73, -121, -80, 115};

Line Loop (54) = {76, -96, -83, 126};    Line Loop (55) = {77, -102, -84, 96};
Line Loop (56) = {78, -108, -85, 102};   Line Loop (57) = {79, -114, -86, 108};
Line Loop (58) = {80, -120, -87, 114};

Line Loop (61) = {61, -128, -68, 131};   Line Loop (62) = {68, -127, -75, 130};
Line Loop (63) = {75, -126, -82, 129};

Line Loop (64) = {61, 62, 63, 64, 65, 66, -122, -121, -120, -87, -86, -85, -84, -83, -82, 129, 130, 131};

//Creating surfaces for the right tunnel
//Plane Surface (1) = {1};   //Plane Surface (2) = {3};
Ruled Surface (3) = {5};   Ruled Surface (4) = {6};
Ruled Surface (5) = {7};   Ruled Surface (6) = {8};

//Creating surfaces for the left tunnel
//Plane Surface (7) = {19};   //Plane Surface (8) = {20};
Ruled Surface (9) = {21};    Ruled Surface (10) = {22};
Ruled Surface (11) = {23};   Ruled Surface (12) = {24};

//Creating surfaces for the boundaries of the domain
Plane Surface (13) = {13};          Plane Surface (14) = {14, 64};
Plane Surface (15) = {15, 1, 19};   Plane Surface (16) = {16};
Plane Surface (17) = {17, 3, 20};   Plane Surface (18) = {18};

//Creating surfaces for the foundations
Plane Surface (40) = {40};   Plane Surface (41) = {41};
Plane Surface (42) = {42};   Plane Surface (43) = {43};
Plane Surface (44) = {44};

Plane Surface (47) = {47};   Plane Surface (48) = {48};
Plane Surface (49) = {49};   Plane Surface (50) = {50};
Plane Surface (51) = {51};

Plane Surface (54) = {54};   Plane Surface (55) = {55};
Plane Surface (56) = {56};   Plane Surface (57) = {57};
Plane Surface (58) = {58};

Plane Surface (61) = {61};   Plane Surface (62) = {62};
Plane Surface (63) = {63};

Plane Surface (64) = {64};
```

```
//Creating physical surfaces for the right tunnel
Physical Surface (1) = {1};  Physical Surface (2) = {2};
Physical Surface (3) = {3};  Physical Surface (4) = {4};
Physical Surface (5) = {5};  Physical Surface (6) = {6};

//Creating physical surfaces for the left tunnel
Physical Surface (7) = {7};      Physical Surface (8) = {8};
Physical Surface (9) = {9};      Physical Surface (10) = {10};
Physical Surface (11) = {11};  Physical Surface (12) = {12};

//Creating physical surfaces for the boundaries of the domain
Physical Surface (13) = {13};     Physical Surface (14) = {14};
Physical Surface (15) = {15};     Physical Surface (16) = {16};
Physical Surface (17) = {17};     Physical Surface (18) = {18};

//Creating physical surfaces for the foundations
Physical Surface (40) = {40};     Physical Surface (41) = {41};
Physical Surface (42) = {42};     Physical Surface (43) = {43};
Physical Surface (44) = {44};

Physical Surface (47) = {47};  Physical Surface (48) = {48};
Physical Surface (49) = {49};  Physical Surface (50) = {50};
Physical Surface (51) = {51};

Physical Surface (54) = {54};  Physical Surface (55) = {55};
Physical Surface (56) = {56};  Physical Surface (57) = {57};
Physical Surface (58) = {58};

Physical Surface (61) = {61};  Physical Surface (62) = {62};
Physical Surface (63) = {63};

Physical Surface (64) = {64};

//Creating the volume of the domain
Surface Loop (1) = {13, 14, 15, 16, 17, 18, 3, 4, 5, 6, 40, 41, 42, 43, 44, 47, 48, 49, 50, 51, 54, 55, 56,
57, 58, 61, 62, 63, 9, 10, 11, 12};
Volume (1) = {1};
Physical Volume (1) = {1};
```

Appendix D

Excavation of a single tunnel geometry

```
/*********************************************************************
 *
 *  Gmsh file estg.txt
 *
 *  Excavation of a Single Tunnel Geometry
 *
 *********************************************************************/
//I have to take care that loop.txt file should be in the same directory with estg.txt

// Defining some parameters and characteristic lengths:

D = 4;          //Tunnel diameter
DD = 4;         //Size of the foundations
X = 17.5*D;     //Dimension of the domain along the x axis
Y = 17.5*D;     //Dimension of the domain along the y axis
Z = 12.5*D;     //Dimension of the domain along the z axis
ChL1 = 18;      //Size of the elements at the boundaries
ChL2 = 2;       //Size of the elements inside and around the tunnel
ChL3 = 9;       //Size of the transition elements
ChL4 = 3;       //Size of the elements at the foundations
x1=X/2;         //Parameter which shifts the tunnel axis horizontally
z1=Z-15;        //Parameter which shifts the tunnel axis vertically
k1=0;           //Parameter which shifts the end of the tunnel only along the z axis


//Points at the boundaries of the domain
Point (1) = {0, 0, 0, ChL1};              Point (2) = {X, 0, 0, ChL1};
Point (3) = {X, Y, 0, ChL1};              Point (4) = {0, Y, 0, ChL1};
Point (5) = {0, 0, Z, ChL1};              Point (6) = {X/2-15, 0, Z, ChL3};
Point (7) = {X/2+15, 0, Z, ChL3};         Point (8) = {X, 0, Z, ChL1};
Point (9) = {X, Y, Z, ChL1};              Point (10) = {X/2+15, Y, Z, ChL3};
Point (11) = {X/2-15, Y, Z, ChL3};        Point (12) = {0, Y, Z, ChL1};

//Points at the tunnel entrance
Point (13) = {x1, 0, z1, ChL2};           Point (14) = {x1, 0, z1+D/2, ChL2};
Point (15) = {x1-D/2, 0, z1, ChL2};       Point (16) = {x1, 0, z1-D/2, ChL2};
Point (17) = {x1+D/2, 0, z1, ChL2};

//Points at the tunnel exit
Point (18) = {x1, Y, z1+k1, ChL2};        Point (19) = {x1, Y, z1+D/2+k1, ChL2};
Point (20) = {x1-D/2, Y, z1+k1, ChL2};    Point (21) = {x1, Y, z1-D/2+k1, ChL2};
Point (22) = {x1+D/2, Y, z1+k1, ChL2};

//Points at the foundations
Point (64) = {X/2-2.5*DD, Y/2-DD/2, Z, ChL4};
Point (65) = {X/2-1.5*DD, Y/2-DD/2, Z, ChL4};
Point (66) = {X/2-0.5*DD, Y/2-DD/2, Z, ChL4};
Point (67) = {X/2+0.5*DD, Y/2-DD/2, Z, ChL4};

Point (72) = {X/2-2.5*DD, Y/2+DD/2, Z, ChL4};
Point (73) = {X/2-1.5*DD, Y/2+DD/2, Z, ChL4};
Point (74) = {X/2-0.5*DD, Y/2+DD/2, Z, ChL4};
```

```
Point (75) = {X/2+0.5*DD, Y/2+DD/2, Z, ChL4};

Point (80) = {X/2-2.5*DD, Y/2+1*DD+DD/2, Z, ChL4};
Point (81) = {X/2-1.5*DD, Y/2+1*DD+DD/2, Z, ChL4};
Point (82) = {X/2-0.5*DD, Y/2+1*DD+DD/2, Z, ChL4};
Point (83) = {X/2+0.5*DD, Y/2+1*DD+DD/2, Z, ChL4};

Point (88) = {X/2-2.5*DD, Y/2+2*DD+DD/2, Z, ChL4};
Point (89) = {X/2-1.5*DD, Y/2+2*DD+DD/2, Z, ChL4};
Point (90) = {X/2-0.5*DD, Y/2+2*DD+DD/2, Z, ChL4};
Point (91) = {X/2+0.5*DD, Y/2+2*DD+DD/2, Z, ChL4};

//Creating the boundaries of the domain
Line (1) = {1, 2};        Line (2) = {2, 3};
Line (3) = {3, 4};        Line (4) = {4, 1};
Line (5) = {5, 6};        Line (6) = {6, 7};
Line (7) = {7, 8};        Line (8) = {8, 9};
Line (9) = {9, 10};       Line (10) = {10, 11};
Line (11) = {11, 12};     Line (12) = {12, 5};
Line (13) = {1, 5};       Line (14) = {2, 8};
Line (15) = {3, 9};       Line (16) = {4, 12};

//Creating the entrance opening
Circle (17) = {14, 13, 15};    Circle (18) = {15, 13, 16};
Circle (19) = {16, 13, 17};    Circle (20) = {17, 13, 14};

//Creating the exit opening
Circle (21) = {19, 18, 20};    Circle (22) = {20, 18, 21};
Circle (23) = {21, 18, 22};    Circle (24) = {22, 18, 19};

//Creating the foundations
Line (63) = {64, 65};  Line (64) = {65, 66};
Line (65) = {66, 67};

Line (70) = {72, 73};  Line (71) = {73, 74};
Line (72) = {74, 75};

Line (77) = {80, 81};  Line (78) = {81, 82};
Line (79) = {82, 83};

Line (84) = {88, 89};  Line (85) = {89, 90};
Line (86) = {90, 91};

Line (96) = {88, 80};  Line (97) = {80, 72};
Line (98) = {72, 64};

Line (102) = {89, 81};  Line (103) = {81, 73};
Line (104) = {73, 65};

Line (108) = {90, 82};  Line (109) = {82, 74};
Line (110) = {74, 66};

Line (114) = {91, 83};  Line (115) = {83, 75};
Line (116) = {75, 67};

//Creating loops for the tunnel
Line Loop (1) = {17, 18, 19, 20};    //Plane Surface (1) = {1};
Line Loop (2) = {21, 22, 23, 24};    //Plane Surface (2) = {2};

Line Loop (3) = {-13, 1, 14, -7, -6, -5}; Line Loop (4) = {-14, 2, 15, -8};
```

```
Line Loop (5) = {-15, 3, 16, -11, -10, -9}; Line Loop (6) = {-16, 4, 13, -12};
Line Loop (7) = {1, 2, 3, 4}; Line Loop (8) = {-11, -10, -9, -8, -7, -6, -5, -12};

//Creating loops for the foundations
Line Loop (41) = {63, -104, -70, 98};     Line Loop (42) = {64, -110, -71, 104};
Line Loop (43) = {65, -116, -72, 110};

Line Loop (48) = {70, -103, -77, 97};     Line Loop (49) = {71, -109, -78, 103};
Line Loop (50) = {72, -115, -79, 109};

Line Loop (55) = {77, -102, -84, 96};     Line Loop (56) = {78, -108, -85, 102};
Line Loop (57) = {79, -114, -86, 108};

Line Loop (61) = {63, 64, 65, -116, -115, -114, -86, -85, -84, 96, 97, 98};

//Creating surfaces for the boundaries of the domain
Plane Surface (3) = {3, 1};     Plane Surface (4) = {4};
Plane Surface (5) = {5, 2};     Plane Surface (6) = {6};
Plane Surface (7) = {7};        Plane Surface (8) = {8, 61};

//Creating surfaces for the foundations
Plane Surface (41) = {41}; Plane Surface (42) = {42};
Plane Surface (43) = {43};

Plane Surface (48) = {48}; Plane Surface (49) = {49};
Plane Surface (50) = {50};

Plane Surface (55) = {55}; Plane Surface (56) = {56};
Plane Surface (57) = {57};

Plane Surface (61) = {61};

Include "loop.txt";  //loop.txt file should be in the same directory with the current file

//Creating physical surfaces for the boundaries of the domain
Physical Surface (1) = {3}; Physical Surface (2) = {4};
Physical Surface (3) = {5}; Physical Surface (4) = {6};
Physical Surface (5) = {7}; Physical Surface (6) = {8};

//Creating physical surfaces for the foundations
Physical Surface (7) = {41}; Physical Surface (8) = {42};
Physical Surface (9) = {43};

Physical Surface (10) = {48}; Physical Surface (11) = {49};
Physical Surface (12) = {50};

Physical Surface (13) = {55}; Physical Surface (14) = {56};
Physical Surface (15) = {57};

Physical Surface (16) = {61};

//Creating the volume of the domain
Surface Loop (3000) = {3, 4, 5, 6, 7, 8, 41, 42, 43, 48, 49, 50, 55, 56, 57, 132, 134, 136, 138, 176, 178,
180, 182, 220, 222, 224, 226, 264, 266, 268, 270, 308, 310, 312, 314, 352, 354, 356, 358, 396, 398,
400, 402, 440, 442, 444, 446, 484, 486, 488, 490, 528, 530, 532, 534, 572, 574, 576, 578, 616, 618,
620, 622, 660, 662, 664, 666, 704, 706, 708, 710};
Volume (100) = {3000};
Physical Volume (1) = {100};
```

```
/*********************************************************************
 *
 *  Gmsh file loop.txt
 *
 *  Division of the tunnel into smaller volumes
 *  Add this file to the same working directory with the estg.txt file
 *********************************************************************/

ChL2 = 2;          //Size of the elements in and around the tunnel
Ur = 5;            //Unsupported length of excavation
D = 4;             //Tunnel diameter
X = 17.5*D;        //Dimension of the domain along the x axis
Y = -Ur;           //Dimension of the domain along the y axis
Z = 12.5*D;        //Dimension of the domain along the z axis
x1=X/2;            //Parameter which shifts the tunnel axis horizontally
z1=Z-15;           //Parameter which shifts the tunnel axis vertically

//Create a Function
Function CirclePlanes

//Points at the tunnel entrance
p1 = newp; Point (p1) = {x1, Y, z1, ChL2};          p2 = newp; Point (p2) = {x1, Y, z1 + D/2, ChL2};
p3 = newp; Point (p3) = {x1 - D/2, Y, z1, ChL2};    p4 = newp; Point (p4) = {x1, Y, z1 - D/2, ChL2};
p5 = newp; Point (p5) = {x1 + D/2, Y, z1, ChL2};

//Points at the exit of the first volume
p6 = newp; Point (p6) = {x1, Y+Ur, z1, ChL2};       p7 = newp; Point (p7) = {x1, Y+Ur, z1+D/2, ChL2};
p8 = newp; Point (p8) = {x1 - D/2, Y+Ur, z1, ChL2}; p9 = newp; Point (p9) = {x1, Y+Ur, z1-D/2, ChL2};
p10 = newp; Point (p10) = {x1 + D/2, Y+Ur, z1, ChL2};

//Creating the entrance opening
c1 = newreg; Circle (c1) = {p2, p1, p3};   c2 = newreg; Circle (c2) = {p3, p1, p4};
c3 = newreg; Circle (c3) = {p4, p1, p5};   c4 = newreg; Circle (c4) = {p5, p1, p2};

//Creating the exit opening of the first volume
c5 = newreg; Circle (c5) = {p7, p6, p8};    c6 = newreg; Circle (c6) = {p8, p6, p9};
c7 = newreg; Circle (c7) = {p9, p6, p10};   c8 = newreg; Circle (c8) = {p10, p6, p7};

//Connecting the opening and the exit of the first volume
l1 = newreg; Line (l1) = {p2, p7};     l2 = newreg; Line (l2) = {p3, p8};
l3 = newreg; Line (l3) = {p4, p9};     l4 = newreg; Line (l4) = {p5, p10};

//Creating loops and surfaces for the first volume
ll1 = newreg; Line Loop (ll1) = {c1, c2, c3, c4};   ps1 = news; Plane Surface (ps1) = {ll1};

ll3 = newreg; Line Loop (ll3) = {l1, c5, -l2, -c1};
rs1 = newreg; Ruled Surface (rs1) = {ll3}; Printf("Ruled surface rs1= %g " , rs1) ;
ll4 = newreg; Line Loop (ll4) = {l2, c6, -l3, -c2};   rs2 = newreg; Ruled Surface (rs2) = {ll4};
ll5 = newreg; Line Loop (ll5) = {l3, c7, -l4, -c3};   rs3 = newreg; Ruled Surface (rs3) = {ll5};
ll6 = newreg; Line Loop (ll6) = {l4, c8, -l1, -c4};   rs4 = newreg; Ruled Surface (rs4) = {ll6};

Extrude  Surface { ps1, { 0, Ur, 0 }};

Return                  //End of the Function

For (1:14)              //Generate the loop
Y += Ur ;
Call CirclePlanes ;
EndFor
```

Appendix E

Unrealistic tunnel scheme – spiral shape

```
/*********************************************************************
 *
 *  Gmsh file spiral.txt
 *
 *  Unrealistic tunnel scheme – spiral shape
 *
 *********************************************************************/

// Defining some parameters and characteristic lengths:

x= 64;
y= 40;
z= 40;
D= 4.173;
m =1;
pi = 3.14;

//begininge hole
Point(1) = {x/2,  0,  2*z/3,  m} ;          Point(2) = {x/2,  0,  2*z/3 + D/2,  m} ;
Point(3) = {x/2 - D/2,  0,  2*z/3,  m} ;    Point(4) = {x/2,  0,  2*z/3 - D/2,  m} ;
Point(5) = {x/2 + D/2,  0,  2*z/3,  m} ;

Circle (1) = {2, 1, 3};  Circle (2) = {3, 1, 4};
Circle (3) = {4, 1, 5};  Circle (4) = {5, 1, 2};

Line Loop (5) = {1, 2, 3, 4};    Plane Surface (6) = {5};

tmp[] = Extrude Surface {6, {0, 10, 0}};;
Printf("NewSurface= %g " , tmp[0]) ;
tmp[] = Extrude Surface { tmp[0], {0, 0, 1}, { x/2 - D/2,  10,  2*z/3,  m }, pi/180 * 90 };;
Printf("NewSurface= %g " , tmp[0]) ;
tmp[] = Extrude Surface { tmp[0], { 0, -1, 0 }, {29.915,  12.086,  24.58,  m }, pi/180 * 25 };;
Printf("NewSurface= %g " , tmp[0]) ;
tmp[] = Extrude Surface {tmp[0], {-12, 0, -7}};;
Printf("NewSurface= %g " , tmp[0]) ;
tmp[] = Extrude Surface {tmp[0], { 0, 1, 0 }, {15.6,  12.086,  21.9,  m }, pi/180 * 25 };;
Printf("NewSurface= %g " , tmp[0]) ;
tmp[] = Extrude Surface {tmp[0], { 0, 0, 1 }, {16.3,  9.5, 19.093,  m }, pi/180 * 90 };;
Printf("NewSurface= %g " , tmp[0]) ;
tmp[] = Extrude Surface { tmp[0], {0, -10, 0}};;
Printf("NewSurface= %g " , tmp[0]) ;
tmp[] = Extrude Surface {tmp[0], { 0, 0, 1 }, {16.6, -0.4999,  19.09,  m }, pi/180 * 90 };;
Printf("NewSurface= %g " , tmp[0]) ;
tmp[] = Extrude Surface {tmp[0], {12.5, 0, 0}};;
Printf("NewSurface= %g " , tmp[0]) ;
tmp[] = Extrude Surface {tmp[0], { 0, 0, 1 }, {29.527, -0.7,  19.09,  m }, pi/180 * 90 };;
Printf("NewSurface= %g " , tmp[0]) ;
tmp[] = Extrude Surface {tmp[0], {0, 11, 0}};;
Printf("NewSurface= %g " , tmp[0]) ;
tmp[] = Extrude Surface {tmp[0], { 0, 0, 1 }, {29.6,  10.3,  19.09,  m }, pi/180 * 90 };;
Printf("NewSurface= %g " , tmp[0]) ;
tmp[] = Extrude Surface {tmp[0], { 0, -1, 0 }, {29.609,  12.914,  16.5,  m }, pi/180 * 25 };;
```

```
Printf("NewSurface= %g " , tmp[0]) ;
tmp[] = Extrude Surface {tmp[0], {-12, 0, -7}};;
Printf("NewSurface= %g " , tmp[0]) ;
tmp[] = Extrude Surface {tmp[0], { 0, 1, 0 }, {15.1, 12.914,  14.1,  m }, pi/180 * 25 };;
Printf("NewSurface= %g " , tmp[0]) ;
tmp[] = Extrude Surface {tmp[0], { 0, 0, 1 }, {15.423, 10.228,  11.4,  m }, pi/180 * 90 };;
Printf("NewSurface= %g " , tmp[0]) ;
tmp[] = Extrude Surface {tmp[0], {0, -11, 0}};;
Printf("NewSurface= %g " , tmp[0]) ;
tmp[] = Extrude Surface {tmp[0], { 0, 0, 1 }, {15.3, -0.77,  11.4,  m }, pi/180 * 90 };;
Printf("NewSurface= %g " , tmp[0]) ;
tmp[] = Extrude Surface {tmp[0], {14, 0, 0}};;
Printf("NewSurface= %g " , tmp[0]) ;
tmp[] = Extrude Surface {tmp[0], { 0, 0, 1 }, {29.3, -0.7,  11.4,  m }, pi/180 * 90 };;
Printf("NewSurface= %g " , tmp[0]) ;
tmp[] = Extrude Surface {tmp[0], {0, 11, 0}};;
Printf("NewSurface= %g " , tmp[0]) ;
tmp[] = Extrude Surface {tmp[0], { 0, 0, 1 }, {29.347, 10.301,  11.4,  m }, pi/180 * 90 };;
Printf("NewSurface= %g " , tmp[0]) ;
tmp[] = Extrude Surface {tmp[0], { 0, -1, 0 }, {29.062, 12.887,  9.37,  m }, pi/180 * 25 };;
Printf("NewSurface= %g " , tmp[0]) ;
tmp[] = Extrude Surface {tmp[0], {-12, 0, -7}};;
Printf("NewSurface= %g " , tmp[0]) ;
tmp[] = Extrude Surface {tmp[0], { 0, 1, 0 }, {15.269, 12.887,  6.28,  m }, pi/180 * 25 };;
Printf("NewSurface= %g " , tmp[0]) ;
tmp[] = Extrude Surface {tmp[0], { 0, 0, 1 }, {15.528, 10.101,  4.07,  m }, pi/180 * 90 };;
Printf("NewSurface= %g " , tmp[0]) ;
tmp[] = Extrude Surface {tmp[0], {0, -10.5, 0}};;
Printf("NewSurface= %g " , tmp[0]) ;
tmp[] = Extrude Surface {tmp[0], { 0, 0, 1 }, {15.128, -0.398,  4.07,  m }, pi/180 * 90 };;
Printf("NewSurface= %g " , tmp[0]) ;
tmp[] = Extrude Surface {tmp[0], {7, 0, 0}};;
Printf("NewSurface= %g " , tmp[0]) ;
```